BOTSWANA INTERNATIONAL UNIVERSITY OF SCIENCE & TECHNOLOGY

Faculty of Sciences

Department of Physics and Astronomy

Student email: Kebadiretse.lefatshe@studentmail.biust.ac.bw

Phone number: +267 75165931

MODIFICATION OF STRUCTURAL, MORPHOLOGICAL AND OPTICAL PROPERTIES OF ZnO NANORODS THROUGH ION IMPLANTATION FOR OPTOELECTRONIC APPLICATIONS

by

KEBADIRETSE LEFATSHE

Student ID number: 14100843

BSc (Physics and Radiation Health) (UB), MSc (Physics) (BIUST)

A Thesis Submitted to the Faculty of Sciences in Fulfilment of the Requirements for the Award of the Doctor of Philosophy in Physics of BIUST

Supervisor(s): Prof Cosmas M. Muiva

Department of Physics and Astronomy

Faculty of Science, BIUST

E-mail Address: muivac@biust.ac.bw

Co-Supervisor(s): Dr Morgan Madhuku

Tandem and Accelerator Mass Spectrometry

iThemba LABS

E-mail Address: m.madhuku@ilabs.nrf.ac.za

December, 2023

TABLE OF CONTENTS

DECLARATION REGARDING THE WORK AND COPYRIGHT vi

ABSTRACT vii

ACKNOWLEDGEMENTS viii

LIST OF PUBLICATIONS ix

LIST OF FIGURES x

LIST OF TABLES xvi

LIST OF SYMBOLS AND ABBREVIATIONS xviii

DEDICATION xx

CHAPTER 1: INTRODUCTION 1

1.1 Overview 1
1.2 Motivation of the study 1
1.3 Statement of the problem 2
1.4 Research objectives 4
1.5 Thesis outline 5

CHAPTER 2: LITERATURE REVIEW 6

2.1 Overview 6
2.2 Nanostructured ZnO 8
2.3 Review on current research on synthesis and applications of ZnO nanorods 9
2.3.1 Synthesis of ZnO NRs 9
2.3.2 Applications of ZnO NRs 11
2.4 Ion beam induced effects for the modification of the properties of ZnO NRs 12

CHAPTER 3: EXPERIMENTAL METHODS AND TECHNIQUES 17

3.1 Overview 17
3.2 Sample Fabrication 17
3.2.1 Synthesis of the ZnO seed layer 17
3.2.2 Synthesis of the ZnO nanorods 19

3.3 Ion implantation 22
3.4 Characterization techniques 26
3.4.1 X-ray diffraction (XRD) technique 26
3.4.2 Rutherford backscattering spectrometry (RBS) 30
3.4.3 Raman spectroscopy 33
3.4.4 Fourier transform infrared (FTIR) Spectroscopy 35
3.4.5 Field emission scanning electron microscopy (FESEM) 37
3.4.6 Energy dispersive X-ray spectroscopy (EDX) 39
3.4.7 Atomic force microscopy (AFM) 39
3.4.8 X-ray photoelectron spectroscopy (XPS) 40
3.4.9 Ultraviolet/visible/near infrared (UV/VIS/NIR) spectroscopy 42

CHAPTER 4: SIMULATIONS OF THE INTERACTIONS OF CARBON AND SILVER IONS WITH ZnO 49

4.1. Overview 49
4.2 Binary-collision-approximation (BCA) 49
4.3 Stopping Power 49
4.4 SRIM/TRIM simulation of Ag^+ and C^+ ions on ZnO films 52
4.4.1 Collision cascades 52
4.4.2 Ion distribution 53
4.4.3 Energy Loss to Ionization 54
4.4.4 Phonon production 54
4.4.5 Ion-recoil distribution 55
4.4.6 Ionization profile 56
4.4.7 Collision events 57
4.4.8 Energy lost to recoil 58

CHAPTER 5: RESULTS AND DISCUSSION I- Optimization of the chemical deposition (CBD) method 61

5.1 Overview 61
5.2 Microstructural analysis 61
5.2.1 X-ray diffraction (XRD) Analysis 61
5.2.2 Raman analysis 63
5.3 Morphological Studies 64

5.4 Optical studies....65
5.4.1 X-ray photoelectron spectroscopy (XPS) analysis....65
5.4.2 Transmittance....67
5.4.3 Optical band gap (E_g)....68
5.4.4 Urbach energies....71
5.4.5 Spectral dispersion parameters....71
5.4.6 Dielectric parameters....75

CHAPTER 6: RESULTS AND DISCUSSION II- Ag^+ ion implanted ZnO nanorods....79

6.1 Overview....79
6.2 Crystalline structure analysis....79
6.2.1 X-ray Diffraction (XRD) analysis....79
6.2.2 Raman analysis....85
6.2.3 Fourier Transform Infrared (FTIR) analysis....86
6.3 Morphological Analysis....87
6.3.1 Field Emission Scanning Electron Microscopy (FESEM)....87
6.3.2 Elemental analysis....88
6.3.3 Atomic Force Microscopy (AFM)....90
6.4 Optical Analysis....92
6.4.1 Absorbance....92
6.4.2 Extinction (k_x) coefficients....93
6.4.3 Optical band gap....94
6.4.4 Urbach energy....97
6.4.5 Skin depth and optical conductivity....98

CHAPTER 7: RESULTS AND DISCUSSION III- Carbon ion implanted ZnO NRs....101

7.1 Overview....101
7.2 Structural Studies of Carbon ion implanted ZnO....101
7.2.1 XRD analysis....101
7.2.2 Raman analysis....106
7.2.3 FTIR....108
7.3 Morphological Analysis....109
7.3.1 Field Emission Scanning Electron Microscopy (FESEM)....109
7.3.2 Atomic Force Microscopy (AFM)....111

7.4 Optical properties of C^+ ion implanted ZnO NRS 112
7.4.1 Absorbance 112
7.4.2 Absorption (α) and extinction coefficient (k_x) 114
7.4.3 Optical band gap 114
7.4.4 Urbach energy 116
7.4.5 Skin depth and optical conductivity 117

CHAPTER 8: RESULTS AND DISCUSSION IV- Silver (Ag^+) and Carbon (C^+) co-implanted ZnO nanorods 121

8.1 Overview 121
8.2 Structural properties 121
8.2.1 X-ray diffraction (XRD) studies 121
8.2.2 Raman Spectroscopy 125
8.2.3 FTIR 128
8.3 Morphological analysis 129
8.3.1 FESEM and AFM 129
8.4 Optical Properties 131
8.4.1 Absorbance 131
8.4.2 Extinction coefficient 132
8.4.3 Band gap determination 133
8.4.4 Urbach energy 134
8.4.5 Skin depth and Optical conductivity 135

CHAPTER 9: SUMMARY, CONCLUSIONS AND RECOMMENDATIONS 139

REFERENCES 142

APPENDIX A: SUPPLEMENTARY DATA 174

APPENDIX B: PHOTOGRAPHS OF SOME OF THE USED EQUIPMENT 176

APPENDIX C: PUBLICATIONS 179

DECLARATION REGARDING THE WORK AND COPYRIGHT

Candidate: KEBADIRETSE LEFATSHE

Student ID: 14100843

Thesis Title: MODIFICATION OF STRUCTURAL, MORPHOLOGICAL AND OPTICAL PROPERTIES OF ZnO NANOSTRUCTURES THROUGH ION IMPLANTATION FOR OPTOELECTRONIC APPLICATIONS

I, **Kebadiretse Lefatshe**, certify that the Thesis is all my own original work and that I have not obtained a degree in this University or elsewhere on the basis of any of this work. This thesis is copyright material protected under the Berne Convention, the Copyright and Neighbouring Rights Act, Act. No. 8 of 2000 and other international and national enactments, in that behalf, on intellectual property. It must not be reproduced by any means, in full or in part, except for short extracts in fair dealing; for researcher private study, critical scholarly review or discourse with an acknowledgement, without the written permission of the office of the Postgraduate School, on behalf of both the author and the BIUST.

Signed: ---------- Date: 01/12/2023 ----------

Primary Supervisor: Prof. COSMAS MUIVA

I, the Candidate's **Primary Supervisor**, hereby confirm that I have inspected the above titled thesis and, to the best of my knowledge, it is based on the original work of the candidate.

Signed: ---------- Date: 01/12/2023 ----------

ABSTRACT

In this work, ion implantation was selected for its ability to induce lattice defects and imperfections thus modifying the properties of ZnO NRs. ZnO NRs were grown through the chemical bath deposition method and implanted with Ag^+ and C^+ ions. Ion implantation was carried out at room temperature at 50 KeV energy and various ion fluences from 1.0×10^{15} to 3.0×10^{16} ions/cm^2. Average penetration depths of 17.4 and 97.9 nm were estimated for Ag^+ and C^+ ions, respectively, using the stopping and range of ions in matter (SRIM) program. X-ray diffraction analysis revealed the hexagonal wurtzite structure of ZnO, with a preferential stacking along the c-axis. A variation of calculated microstructural parameters denoted the presence and effect of the implanted ions. Furthermore, Raman analysis results showed distinct features on phonon modes, which were strongly dependent on the ion species and the fluence of the implanted ions. These observed disparities signalled the presence of distortions and possible accumulation of defects as induced by ion implantation.

The UV/Vis/NIR spectroscope was used to measure the absorbance and transmittance of the samples. A shift of the absorption edges towards longer wavelengths was observed, implying a consequential decrease of the bandgap. The diminution of the optical band gap of implanted ZnO was ascribed to imperfect lattice and isolated impurity bands between the conduction and valence bands. In addition to the increased absorption of the visible light, a decreased band gap also enables quick photoexcitation of electrons, hence resulting in an increase in charge generation. These results highlight an effective strategy of extending the absorption of visible light through creating a disturbance of the structural periodicity. Such modified ZnO nanorods are efficient for the utilization of the abundant solar energy for photocatalytic environmental remediation and energy conversion applications.

ACKNOWLEDGEMENTS

Praise be to my God, Jehovah who carried me through and who made it all possible to complete this work. He is amazing! I wish to extend my utmost gratitude to several individuals who have played a role in this PhD work.

I am deeply thankful to my academic mentors; supervisor Prof Cosmas M. Muiva and co-supervisor Dr Morgan Madhuku. Thank you for the incredible support and mentorship. You both were literally a text away. I could text any of you after midnight and still get a response at that time. God bless you for me. With the same spirit I would also like to thank my spiritual mentors; Pastor Dr Godwill Gulubane and his beautiful wife Mrs Kitso Gulubane. They have been altruistic during this journey, devoting their time to pray for my studies, and my general well-being.

To the teaching and technical staff in the Department of Physics and Astronomy, BIUST, I'm truly thankful for your positive input in this research. My utmost appreciation also goes to Mr Rabalone, the chief technician Department of Geology for FESEM microscopy assistance; Dr Mamogo A. Masenya, and Mr Tony Miller both from iThemba LABS TAMS laboratory for their assistance with ion implantation and RBS measurements.

To Mr Comfort Sekga, Mr Charles Moditswe, Dr Jacob Kaavera, co-authors Ms Dineo P Sebuso and Mrs Phindani Dube- Nxumalo, and fellow physics postgraduate students, thank you for the support and encouragement that came in any shape and form. Last but not least, my family and friends, you guys have been understanding and supportive. Thank you for your incredible interminable love. I love you so much.

LIST OF PUBLICATIONS

Reviewed journal articles from this work

1. **K. Lefatshe**, C. Muiva, M. Madhuku, Effect of low energy Ag^{+} ion implantation on ZnO nanorods for enhanced visible light absorption-structural and optical analysis *Optical Materials 122* (2021), 111757

2. **K Lefatshe**, P Dube, D Sebuso, M Madhuku, C Muiva, Optical dispersion analysis of template assisted 1D-ZnO nanorods for optoelectronic applications *Ceramics International 47* (2021), 7407

Other reviewed journal articles related to this work

3. **Kebadiretse Lefatshe**, Genene T. Mola and Cosmas M. Muiva, Reduction of hazardous reactive oxygen species (ROS) production of ZnO through Mn inclusion for possible UV-radiation shielding application *Heliyon 6* (2020), e04186

LIST OF FIGURES

Figure 2.1: Different crystal structures for the ZnO polymorphs.

Figure 2.2: ZnO nanostructures of various morphologies.

Figure 3.1: Schematic diagram of a spray pyrolysis technique used for the growth of ZnO seed layers.

Figure 3.2: A flow chart representing the three steps in the growth and ion implantation of the ZnO nanorods.

Figure 3.3: A block diagram of the Varian 200-20A2F ion implanter.

Figure 3.4: Bragg's law (a) for real as well as (b) reciprocal space geometry.

Figure 3.5: The principle and scattering geometry of the RBS (a) and a schematic showing elastic collision of the projectile ion with the target atom (b).

Figure 3.6: The variation of the kinematic factor, k, at varying scattering θ angles as a function of target mass, for incident H ions.

Figure 3.7: Schematic diagram and pictures of the iThemba LABS 6 MeV Tandem accelerator.

Figure 3.8: Schematic Jablonski diagram illustrating different quantum energy transitions for Raman and Rayleigh scattering.

Figure 3.9: Schematic diagram to show parts of an FTIR spectrometer.

Figure 3.10: (a) Mechanisms of emission of secondary electrons (SE), backscattered electrons (BSE), and characteristic X-rays from atoms of the sample [3.47], (b) schematic representation of the FESEM system.

Figure 3.11: AFM operating principle.

Figure 3.12: Schematic diagram of photoemission process used for XPS., showing the excitation and emission of an electron as induced by the incident X-rays.

Figure 3.13: Possible electronic transitions occurring between molecular orbitals due to absorption of UV and visible light.

Figure 3.14: UV-vis spectrophotometer schematic for a double beam instrument.

Figure 4.1: XY ion simulations showing collision cascade initiated by 50 KeV (a) Ag^+ and (b) C^+ ions**.**

Figure 4.2: Depths of incident ions in ZnO using incident energy of 50 KeV (a)Ag^+ and (b) C^+.

Figure 4.3: Energy loss to target electrons upon 50 KeVeV Ag^+ and C^+ ion implantation.

Figure 4.4: The distribution of target phonons in ZnO films as produced by ions and recoils due to (a) Ag^+ and (b) C^+ ion implantation.

Figure 4.5: TRIM simulation of ion-recoil distribution of ZnO as induced by (a) Ag^+ and (b) C^+ ion distribution.

Figure 4.6: Plots of ionization of ZnO target material by (a) Ag^+ and (b) C^+ ions.

Figure 4.7: SRIM simulation of diferent collision events on ZnO target upon (a) Ag^+ ion and (b) C^+ ion implantantion.

Figure 4.8: TRIM plot of energy transferred to the recoil cascades, (a) Ag^+ and (b) C^+ on ZnO substrate.

Figure 5.1: XRD Patterns of surfactant free grown (SF-ZNR ZnO), ethylene glycol surfactant assisted ZnO (EG-ZNR) and polyethylene glycol surfactant assisted ZnO (PEG-ZNR).

Figure 5.2: Raman spectra of surfactant free grown ZnO nanorods (SF-ZNR ZnO), ethylene glycol surfactant assisted ZnO nanorods (EG-ZNR) and polyethylene glycol surfactant assisted ZnO nanorods (PEG-ZNR).

Figure 5.3: FESEM images of elongated ZnO nanorods prepared in surfactant free (A), EG (B) and PEG (C) templates.

Figure 5.4: (a) XPS wide spectra of SF-ZNR, EG-ZNR and PEG-ZNR. Narrow XPS spectra of (b) 2p core shell and (c) O1s. The insert on (a) is a bar chart showing the elemental atomic percentages of Zn and O in all the three samples.

Figure 5.5: The transmittance spectra of the SF-ZNR, EG-ZNR and PEG-ZNR.

Figure 5.6: Variation of $(\alpha h\nu)^2$ with photon energy, hv, for SF-ZNR, EG-ZNR and PEG-ZNR.

Figure 5.7: The derivative spectroscopy plot of SF-ZNR, EG-ZNR and PEG-ZNR nanorods.

Figure 5.8: Plot of $hv(2nk_x)^{1/2}$ vs hv for ZnO nanorods.

Figure 5.9: Variation of Ln α with the photon energy to determine the Urbach energies of the SF-ZNR, EG-ZNR and PEG-ZNR nanostructures. Linear fitted with Reg ≈1.

Figure 5.10: The refractive index of SF-ZNR, EG-ZNR and PEG-ZNR as a function of the wavelength.

Figure 5.11: The extinction coefficient of SF-ZNR, EG-ZNR and PEG-ZNR as a function of the wavelength.

Figure 5.12: Plot of the refractive index factor (WDD), $(n^2-1)^{-1}$ vs hv^2 for ZnO nanostructured films. Linear fits with Reg. ≈ 0.8.

Figure 5.13: Plot of n^2 vs λ^2 for the ZnO SF-ZNR, EG-ZNR and PEG-ZNR nanostructures. Linear fitted with Reg ≈ 1.

Figure 5.14: The spectral dependence of the (a) imaginary (ε_i) and (b) real components (ε_r) of the dielectric function for the ZnO NRs nanostructures.

Figure 6.1: Recorded XRD [a] wide range scans, [b] enlarged 002 peak and other dwarfed peaks [c] of pristine ZnO and Ag^+ implanted ZnO at different fluences ($1x10^{15}$, $2x10^{15}$, $3x10^{15}$, $1x10^{16}$ and $3x10^{16}$ ions/cm^2).

Figure 6.2: The variation of the lattice parameters a_p and c_p with fluence of Ag^+ ions.

Figure 6.3: Room temperature Raman spectra of pristine and Ag^+ implanted ZnO.

Figure 6.4: FTIR spectra of pristine ZnO and Ag^+ ion implanted ZnO films at fluences of $1x10^{15}$, $2x10^{15}$, $3x10^{15}$, $1x10^{16}$ and $3x10^{16}$ ions/cm^2.

Figure 6.5: Field emission scanning electron microscopy (FESEM) images of Ag^+ ion implanted ZnO at fluences of (a, b) 2.0 x 10^{15}, (c) 3.0 x 10^{15}, (d) 1.0 x 10^{16} and (e) 3.0 x 10^{16} ions/cm^2.

Figure 6.6: Elemental mapping images of Ag^+ ion implanted ZnO at fluence of 3.0 x 10^{15} ions/cm^2.

Figure 6.7: Three-dimensional (3D) AFM tapping mode images of low energy (a) pristine and Ag^+ ion implanted ZnO samples at fluences of (b) 1x 10^{15} (c) 2x 10^{15}, (d) 3x 10^{15}, (e) 1x 10^{16}, and (f) 3x 10^{16} ions/cm^2.

Figure 6.8: Absorbance spectra from pristine and Ag^+ ion implanted ZnO samples.

Figure 6.9: Strong dependence of the extinction coefficient (k_x) on Ag^+ ion fluence.

Figure 6.10: Tauc plots used to determine the optical band gap (E_g) of (a) pristine and (b) Ag^+ ion implanted ZnO films.

Figure 6.11: Ln α against photon energy for pristine and Ag^+ ion implanted ZnO NRs.

Figure 6.12: The variation of skin depth with the fluence of Ag^+ ions.

Figure 6.13: Optical conductivity as a function of the wavelength for Ag^+ ion implanted ZnO NRs.

Figure 7.1: 2θ XRD profiles of carbon implanted ZnO at fluences of 1.0 x10^{15} (CIIZ1), 2.0 x10^{15} (CIIZ2), 3.0 x10^{15} (CIIZ3), 1.0 x10^{16} (CIIZ4) and 3.0 x10^{16} ions/cm^2 (CIIZ5).

Figure 7.2: (a) Zoomed 002 peak and (b) a plot of the lattice parameter of pristine ZnO, CIIZ1 (1.0 x10^{15} ions/cm^2) CIIZ2 (2.0 x10^{15} ions/cm^2), CIIZ3 (3.0 x10^{15} ions/cm^2), CIIZ4(1.0 x10^{16} ions/cm^2), and CIIZ5 (3.0 x10^{16} ions/cm^2).

Figure 7.3: Wide range micro-Raman spectra of pristine and carbon implanted ZnO samples.

Figure 7.4: Individual enlarged parts of the Raman spectra of pristine and carbon implanted ZnO samples to illustrate the peak positions and symmetry of the observed vibrational modes.

Figure 7.5: FTIR spectra showing variation of the functional groups in carbon ion implanted ZnO at different fluences.

Figure 7.6: High magnification field FESEM micrographs of carbon implanted samples at 1.0 x 10^{15} (CIIZ1), 2.0 x 10^{15} (CIIZ2), 3.0 x 10^{15}(CIIZ3) and 1.0 x 10^{16} (CIIZ4).

Figure 7.7: EDX spectrum and elemental mapping analysis of ZnO NRs implanted with carbon ions at fluence 1.0 x10^{16} ions/cm^2.

Figure 7.8: 3D topography images of (a) pristine and carbon implanted samples (from b-f) at 1.0 x 10^{15}, 2.0 x 10^{15}, 3.0 x 10^{15}, 1.0 x 10^{16} and 3.0 x 10^{16} ions/cm^2.

Figure 7.9: Absorbance and transmittance spectra of pristine and 50 keV C^+ ion beam implanted ZnO thin films at various ion fluences.

Figure 7.10: Spectral (a) optical absorption and (b) extinction coefficients of virgin and 50 KeV C^+ ion beam implanted ZnO thin films with varying ion fluence.

Figure 7.11: Tauc plots for optical band gap determination for pristine and ZnO NR films implanted with carbon ions of fluences of 1.0 x10^{15}, 2.0 x10^{15}, 3.0 x10^{15}, 1.0 x10^{16} and 3.0 x10^{16} denoted as CIIZ1, CIIZ2, CIIZ3, CIIZ4 and CIIZ5, respectively.

Figure 7.12: Photon energy dependence of ln α for pristine and ZnO NR films implanted with carbon ions at fluences of 1.0 x10^{15}, 2.0 x10^{15}, 3.0 x10^{15}, 1.0 x10^{16} and 3.0 x10^{16} denoted as CIIZ1, CIIZ2, CIIZ3, CIIZ4 and CIIZ5, respectively.

Figure 7.13: Photon energy dependence of skin depth for pristine and ZnO NR films implanted with carbon ions at fluences of 1.0 x10^{15}, 2.0 x10^{15}, 3.0 x10^{15}, 1.0 x10^{16} and 3.0 x10^{16} denoted as CIIZ1, CIIZ2, CIIZ3, CIIZ4 and CIIZ5, respectively.

Figure 7.14: Photon energy dependence of skin depth for pristine and ZnO NR films implanted with carbon ions at fluences of 1.0 x10^{15}, 2.0 x10^{15}, 3.0 x10^{15}, 1.0 x10^{16} and 3.0 x10^{16} denoted as CIIZ1, CIIZ2, CIIZ3, CIIZ4 and CIIZ5 respectively.

Figure 8.1: (a-e) XRD profiles of the Ag^+-C^+ co-implanted ZnO films at varying fluences as labelled. (f) detailed inspection of the 002 peak of 1 x10^{15}, 2 x10^{15}, 3 x10^{15}, 1 x10^{16} and 3 x10^{16} ions/cm^2 Ag^+-C^+ co-implanted ZnO film.

Figure 8.2: A plot to show the change of (a) the 002 peak intensity and (b) the ion fluence for ZnO NRs samples co-implanted with Ag^+ and C^+ ions at 50 KeV.

Figure 8.3: Raman spectra measurements ZnO nanorods co-implanted with Ag^+ and C^+ ions, using fluences of 1×10^{15}, 2×10^{15}, 3×10^{15}, 1×10^{16} and 3×10^{16} ions/cm^2 (energy 50 KeV).

Figure 8.4: Infrared spectra of pristine and Ag^+-C^+ co-implanted ZnO NR at varying fluences of 1.0 $x10^{15}$, 2.0 $x10^{15}$, 3.0 $x10^{15}$, 1.0 $x10^{16}$ and 3.0 $x10^{16}$ ions/cm^2.

Figure 8.5: Top surface view FESEM and 3D AFM images showing the surface morphology of well-aligned ZnO nanorods implanted with varying fluences of Ag^+ and C^+ ions [(a and b)1.0 $x10^{15}$, (c) 3.0 $x10^{15}$, (d) 1.0 $x10^{16}$, (e) 2.0 $x10^{15}$, (f) 1.0 $x10^{16}$ and (g) 3.0 $x10^{16}$ ions/ cm^2].

Figure 8.6: Optical absorption spectra for pristine and Ag^+- C^+ co-implanted ZnO NRs thin films at various fluences.

Figure 8.7: Extinction coefficient (k_x) profiles of pristine and 50 KeV Ag^+-C^+ co-implanted ZnO NRs with varying ion fluences.

Figure 8.8: Tauc's plot for determining the optical band gap for pristine and 50 KeV Ag^+-C^+ co-implanted ZnO NRs with varying ion fluence.

Figure 8.9: Ln α plots for Pristine and Ag^+-C^+ co-implanted ZnO NRs at ion fluence of 1.0 $x10^{15}$, 2.0 $x10^{15}$, 3.0 $x10^{15}$, 1.0 $x10^{16}$ and 3.0 $x10^{16}$ ions/cm^2.

Figure 8.10: Variation of the skin depth parameter of Ag^+-C^+ co-implanted ZnO NRs.

Figure 8.11: A plot showing enhanced optical conductivity of Ag^+-C^+ co-implanted ZnO NRs.

Figure A1: Rutherford backscattering spectra of pristine and Ag^+ ion implanted ZnO NRs.

Figure A2: Rutherford backscattering spectra of pristine and C^+ ion implanted ZnO NRs.

Figure A3: Rutherford backscattering spectra of pristine and Ag^+-C^+ co-implanted ZnO NRs.

Figure B.1: The Varian-Extrion 200-20A2F Ion implanter.

Figure B.2: The Bruker dimension edge scan analyst for atomic force measurements.

Figure B.3: A picture of the Bruker D8 Advance XRD equipment used.

Figure B.4: A Zeiss MERLIN FESEM used for the examination of the surface morphology and elemental composition analysis.

Figure B.5: The Horiba Labram HR evolution Raman spectrometer.

Figure B.6: The Bruker Vertex 70v FTIR spectrophotometer.

LIST OF TABLES

Table 2.1: Summary of basic properties of ZnO.

Table 2.2: Current studies on the use of ion implantation technology to modify various properties of ZnO nanorods

Table 3.1: Optimum deposition parameters used during spray pyrolysis for seed layer growth.

Table 3.2: Summary of optimized parameters for the growth of ZnO nanorods through chemical deposition method.

Table 4. 1: Various calculated parameters of Ag^+ ion implantation using SRIM/TRIM simulation.

Table 4. 2: Various calculated parameters of C^+ ion implantation using SRIM/TRIM simulation.

Table 5.1: Calculated structural parameters of ZnO films from XRD analysis.

Table 5.2: Calculated energy gaps of the ZnO nanostructures using Tauc $[E_{g(Tauc)}]$, Derivative $[E_{g(ds)}]$, WDD $[E_{g(WDD)}]$ and 2nk $[E_{g(nk)}]$ models, single oscillator parameters (E_d and E_o) and Urbach energies $[E_u]$ of the samples.

Table 5.3: Static refractive index ($n_{(o)}$), high frequency dielectric constant ($n_{(o)}^2$), lattice dielectric constant (ε_L), plasma frequency (ω_p), carrier concentration to effective mass ratio (N/M*) and momenta (M_{-1} and M_{-3}).

Table 6.1: The 002-peak position (2θ), interplanar d-spacing (d), FWHM (β), crystallite size (D) and dislocation densities (δ) of pristine and Ag^+ implanted ZnO films.

Table 6.2: Various calculated microstructural parameters of Pristine and Ag implanted ZnO films.

Table 6. 3: Elemental composition of pristine and Ag^+ ion implanted ZnO.

Table 6.4: Surface statistical AFM analysis of the Ag^+ ion implanted films.

Table 6.5: Calculated optical band gaps (E_g) and refractive index (n) of pristine and Ag^+ ion implanted samples.

Table 7.1: Calculated lattice parameters of pristine and C^+ ion implanted ZnO films.

Table 7.2: The calculated bonding and crystallographic properties of pristine and C^+ ion implanted ZnO.

Table 7.3: Variation of AFM parameters for carbon ion implanted ZnO.

Table 7.4: Calculated optical band gaps (E_g) and refractive index (n) of pristine and Ag^+ ion implanted samples

Table 8.1: XRD extracted crystal parameters: the position of the 002 peak, interplanar spacing (d), FWHM (β), average crystallite size (D_s), and lattice parameters (a_p and c_p) for ZnO NR films co-implanted with Ag^+ and C^+ ions.

Table 8.2: XRD analysis microstructural parameters of Ag^+-C^+ co- implanted ZnO films.

Table 8.3: Raman active phonons and their corresponding wavenumber values as observed in pristine and Ag^+ and C^+ co-implanted ZnO nanorods.

Table 8.4: Direct optical band gap, E_g, and band tail energy, E_u, for pristine and implanted samples.

LIST OF SYMBOLS AND ABBREVIATIONS

A	Absorbance
Ag	Silver
AFM	Atomic force microscopy
a_p	Lattice parameter a
BCA	Binary-collision-approximation
c	Speed of electromagnetic waves
C	Carbon
c_p	Lattice parameter c
CB	Conduction band
CBD	Chemical Bath Deposition
d	Interatomic spacing
DOS	Density of States
E	Energy
EDX	Energy dispersive X-ray
E_g	Optical band gap
E_u	Urbach energy
eV	Electron volt
FESEM	Field emission scanning electron microscope
FTIR	Fourier Transform Infrared Spectroscopy
h	Plank's constant
hv	Photon energy
k	Extinction coefficient
n	Refractive index
nm	Nanometre
NRs	Nanorods
R	Reflectance
SMO	Semiconducting metal oxides
SRIM	Stopping and Range of Ions in Matter
t	Thickness
T	Transmittance
UV	Ultra-violet

VIS	Visible
WDD	Wemple-Didomenico
XPS	X-ray Photoelectron Spectroscopy
XRD	X-ray Diffraction
ZnO	Zinc Oxide
λ	Wavelength

DEDICATION

In good memory of my mother Mrs Nabo G. Lefatshe, you are dearly missed sthandwa sami

CHAPTER 1: INTRODUCTION

1.1 Overview

Over the years, Africa has been known to grasp on its discoveries of fossil fuels such as gas, coal and crude oil for energy supply. However, over-exploitation of already dwindling fossil fuel reserves, pollution and adverse environmental effects that arise from these activities, such as global warming constitute global concerns. Due to economic and limited performance benefits of primeval technologies, there is bourgeoning emphasis on exploring alternative solutions to address the escalating industrial expansion and societal lifestyle demands. The development of new innovations or technologies to modify the already existing materials should be done to ensure performance improvements. Over centuries, there has been extensive research interest on semiconductor technology [1-4]. This growing interest is attributed to the outstanding properties and functionalities of these materials. Semiconductors have been considered for numerous applications in the fields of energy harnessing, environmental (remediation, health and mining sectors) as well as fabrication of functional optical devices [1, 5-11]. However, a number of discrepancies and reliability limitations for commercial applications have been well documented [12]. One of them is the issue of instability, as quite a number of semiconductors have been reported to suffer from corrosion when exposed to photons [13]. Other than photo corrosion and issues of instability, detriments in semiconductor technology are mostly due to low photon absorption and high recombination effects [14]. The ability to tune/tailor the properties of semiconductors in order to enhance their performance has immensely contributed to their evolving implementation in the design of optoelectronic devices.

1.2 Motivation of the study

Among the wide range of known semiconductors, zinc oxide (ZnO) is one of the most attractive, significant and preferred materials due to several properties. Other than its wide band gap energy, which ranges between 3.3 to 3.4 eV, ZnO is mostly considered due to its abundancy, cost efficiency and non-toxicity [4, 8, 15]. Publications related to light harvesting and photoactivated applications of ZnO including degradation of toxins such as dyes,

pesticides, antibiotics, microbial photoinactivation and light to chemical energy conversion have hastily increased over the past two decades [16]. Augmented efficiencies are noted from the use of ZnO compared to the other semiconductors such as Titanium dioxide (TiO_2) [5], gallium compounds (e.g GaN) [17, 18] and indium compounds (e.g In_2O_3, InN) [19, 20]. ZnO's wideband gap of about 3.3 eV, makes it impractical for applications that involve visible light absorption [21]. Research is thus being focused on the modification of ZnO for solar light absorption, without limiting its other properties.

In recent years, there has been substantial research interest in controlled fabrication of ZnO nanoarchitectures of various dimensionalities [2, 22, 23]. The aspect of size and shape dependent properties is accentuated and pre-eminent. Nanostructured one dimensional (1D) semiconducting metal oxides such as nanoneedles, nanorods, nanowires, etc are a novel class of optically active materials, depicting enormous prospect for photocatalytic applications**.** ZnO nanorods (NRs) have been found to offer unique outstanding performance in energy conversion applications and fabrication of electronic devices, due to their stability and their large geometrical aspect ratio. Fabricating nanorods reduces segregation and improves crystalline quality and electron mobility thus making them better nanostructures for use in solar cells, micro lasers, optoelectronics and nonlinear optics [23, 24]. For the abovementioned reasons and others discussed in the later chapters, this thesis is devoted to the fabrication and modification of ZnO NRs films. Thin films have been found to be easy to subject to vigorous modification techniques as compared with bulk material [25, 26]. The co-implantation of light and heavy ions in ZnO NRs is rarely reported in literature.

1.3 Statement of the problem

Conventional diffusion doping has been utilized for introducing impurity elements (referred to as dopants) into the lattice of a target material. The main drawback with this is the challenge of random distribution of the dopants, thus difficulty in controlling their depth or location within the semiconducting metal oxide (SMO) system [27]. Tsuzuk et al [14] have fully elaborated the drawbacks of conventional diffusion doping and strongly emphasized the need to use a dopant with the same ionic radius or valence number as that of the host semiconductor, the lack of such compatibility may lead to the creation of recombination sites. The efficacy of the injected metal ions as dopants in SMO systems depends on whether they mediate for

separation of the photogenerated charges or facilitate the recombination of these charges [27]. Inconsistent results have been established on the effect of various metal ion dopants. Previous studies have reported the adoption of ion implantation for fabrication of functional devices as well as to modify the physical, chemical and related properties of functional materials including polymers and semiconductors [3, 6, 28]. This method provides a degree of control over ion concentration and depth distribution in the host matrix within the selectable energy and fluence of the implantation.

Various elements including metal and non-metals have been embedded in various metal oxides through the ion implantation technique to modify their physicochemical responses [6, 29]. Silver (Ag) is recognised for its remarkable optical property due to its increased efficiency of interaction with incident photons, which is attributed to the ability of noble metals to depict a strong selective localized surface plasmonic resonance (LSPR) effect, thus their ability to have a significant absorption in the visible and near infrared region [26, 30]. Henceforth, the existence of plasmon-active nanostructures on SMOs offers new optical properties. In coupling metal oxides with Ag^+, Fermi level equilibration occurs. At the junction of a metal and a semiconductor, there is a formation of an electrostatic layer known as a Schottky barrier. This barrier is effective for electron trapping thus restricting the flow back of electrons to the surface of metal oxides, hence reducing charge recombination [9]. Furthermore, the Schottky barrier enhances the formation of the reactive oxygen species (ROS) which thus promotes catalytic reactions. The possibility of synergic combination of the unique properties of the ZnO NRs target structure and the plasmonic response of noble-metal nanoparticles of Ag and C will enable the development of new approach for effective utilization of solar irradiation. Implantation of Ag^+ and C^+ ions into ZnO NRs can be optimized and diversified for various visible-light-induced applications. Parameters such as the ion fluence, implantation energy, pre and post implantation treatments as well as the type of ion species used can produce different effects on the crystal structure of a semiconductor and subsequently influence its optical properties. Currently, the utilization of low energy ions for both structural and optical modifications of ZnO nanorods, and their effect with respect to different implantation parameters have not been studied. Research on various parameters is necessary in order to establish optimum conditions.

1.4 Research objectives

The main aim of this work was to fabricate ZnO NRs and investigate the effects of Ag^+ and C^+ ion implantation on the optical response property of ZnO in the visible light region. Various parameters were investigated, including the ion mass through single implantation of silver (Ag) and carbon (C) as well as co-implanting the two species. The effect of ion fluence, was also studied for the ion species used.

To accomplish the overall goal of the study, the work has been grouped according to the following objectives;

1. To study the effect of Ag^+ ion implantation on the structural, morphological and optical properties of the ZnO nanorods.

2. To analyse the effect of C^+ ion implantation on the structural, morphological and optical properties of the ZnO nanorods.

3. To examine the effect of C^+ and Ag^+ ion co-implantation on the structural, morphological and optical properties of the ZnO nanorods.

1.5 Thesis outline

Chapter 1 is a brief introduction discussing the problem statement and the motivation of this research work. The research objectives are also stated in this chapter.

Chapter 2 presents a review on the basic properties of ZnO, its structure as well as applications. Moreover, different fabrication routes for ZnO NRs are discussed.

Chapter 3 gives an in-depth step by step description of the synthesis methods for sample preparation, and characterisation techniques used in this study. Details on the theories and principles for certain characterisation techniques are also discussed. Diverse methods and models employed to calculate structural and optical parameters are outlined.

Chapter 4 of this thesis is a detailed background, theory and physics on the subject of ion implantation, explaining the mechanisms and dynamics of ion-solid interaction, stopping power mechanisms and the resultant distortion and defects on the host lattice structure. Details and parameters regarding the stopping and range of ions in matter (SRIM) computing software are also discussed.

Chapters 5-8, the experimentally obtained results are analysed and further expanded. The effects of implanted ion species at varying fluence are discussed with relative to the impact on the structural, morphological and optical properties of ZnO NRs.

Chapter 9 gives the summary and recommendations for future work.

Appendix A shows RBS spectra measurements for Ag^+, C^+ and Ag^+-C^+ co implanted ZnO NR films.

Appendix B presents photographs of the different instruments used in the experiments.

CHAPTER 2: LITERATURE REVIEW

2.1 Overview

Zinc oxide is a group II-VI semiconductor, with a chemical formula ZnO. It exhibits three types of crystal structures, which are determined by the tetrahedrally coordinated bonding geometry. The arrangement of zinc (Zn) and oxygen (O) sublattices results in formation of either the cubic zinc-blende, a hexagonal wurtzite or rock salt crystal structures, depending on the assembling sequence of the bi-layers. These crystal structures of ZnO are shown in Figure 2.1. The wurtzite structure is the most common, as it is thermodynamically stable under ambient conditions [31, 32]. The wurtzite structure belongs to the P63mc space group. The asymmetrical nature of the hexagonal wurtzite and its enormous electromechanical coupling are responsible for the reported powerful pyroelectric and piezoelectric properties of ZnO [33].

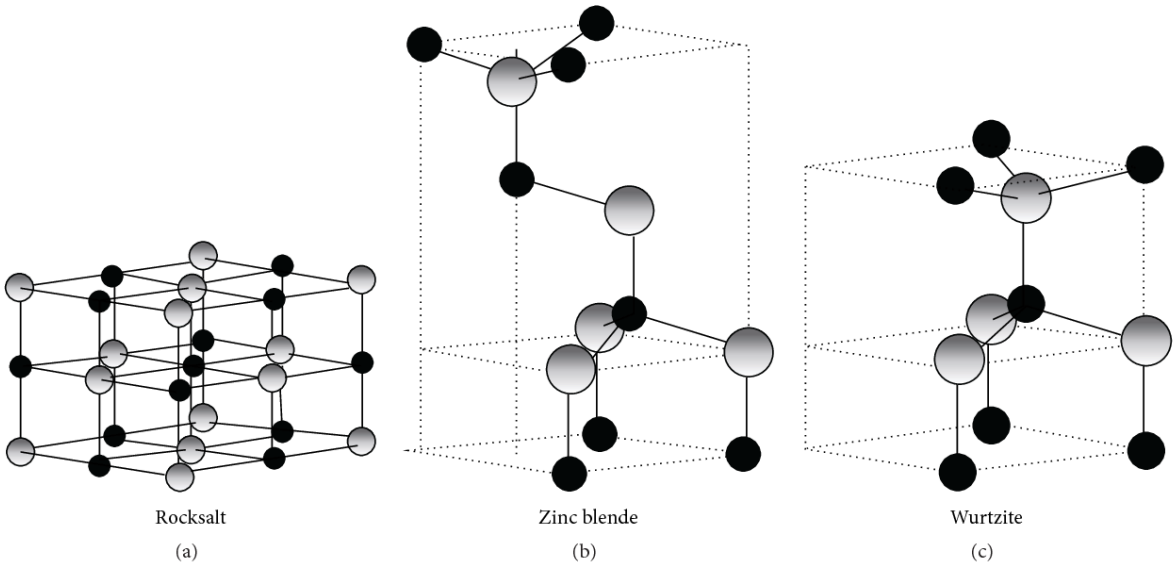


Figure 2.1: Different crystal structures for the ZnO polymorphs [34].

Since the emergence of heterogeneous catalysis, ZnO has been extensively employed for vast multifunctional photocatalytic applications including photocatalytic hydrogen production through water splitting [35, 36], environmental remediation [37, 38], and fuel generation from CO_2 reduction [39, 40]. The versatility of ZnO has been attributed to its abundance, non-toxic, inexpensiveness, as well as its diverse structural, electronic, and optical properties. Some of these basic properties of ZnO are summarised in Table 2.1.

Table 2.1: Summary of basic properties of ZnO [41-48].

Property	**Value**
Lattice parameter $a_p=b_p$	0.3248-0.3250 nm
Lattice parameter c_p	0.5204-0.5208 nm
Density	5.605 g/cm^3
Refractive index	2.0041, 2.008
Optical band gap	3.3 -3.4 eV, direct
Binding energy	60 MeV
Conductivity	0.6
Melting point	1975 ˚C
Boiling point	2360 ˚C
Solubility in water	0.0004%
Hardness	~5 Gpa
Specific gravity	5.5/5.7
Hole effective mass	0.59
Electron effective mass	0.24
Hole mobility	5-50 cm^2/Vs
Electron mobility	200 cm^2/Vs

2.2 Nanostructured ZnO

A comparison of nanomaterials with their bulk-sized counterparts, have demonstrated distinct properties owing to their dimensions. Continuous effort has been devoted towards modifying pre-existing technologies and building reconfigurable architectures for improved functionalities. Controlled synthesis of materials is important for the development of novel materials. The manipulation of the physio-chemical properties of materials, for instance, size, shape, surface area and crystal structure, is fundamental for discovering their potential as building blocks for design of functional devices. In their nano-dimensionalities, semiconductor properties are influenced by quantum-confinement effects [49]. Progress in synthesis of multi-dimensional, surface facet-selective ZnO nanostructures, for numerous applications in the health sector, energy harnessing, environmental remediation, as well as fabrication of functional devices is well recognised [50, 51]. Figure 2.2 shows diverse shapes of ZnO nanostructures such as nanocubes, nanoribbons and nanowires. Their vast applications are influenced by exceptional properties, including thermal stability, chemical stability, environmental benignity, large exciton energy and high electron mobility.

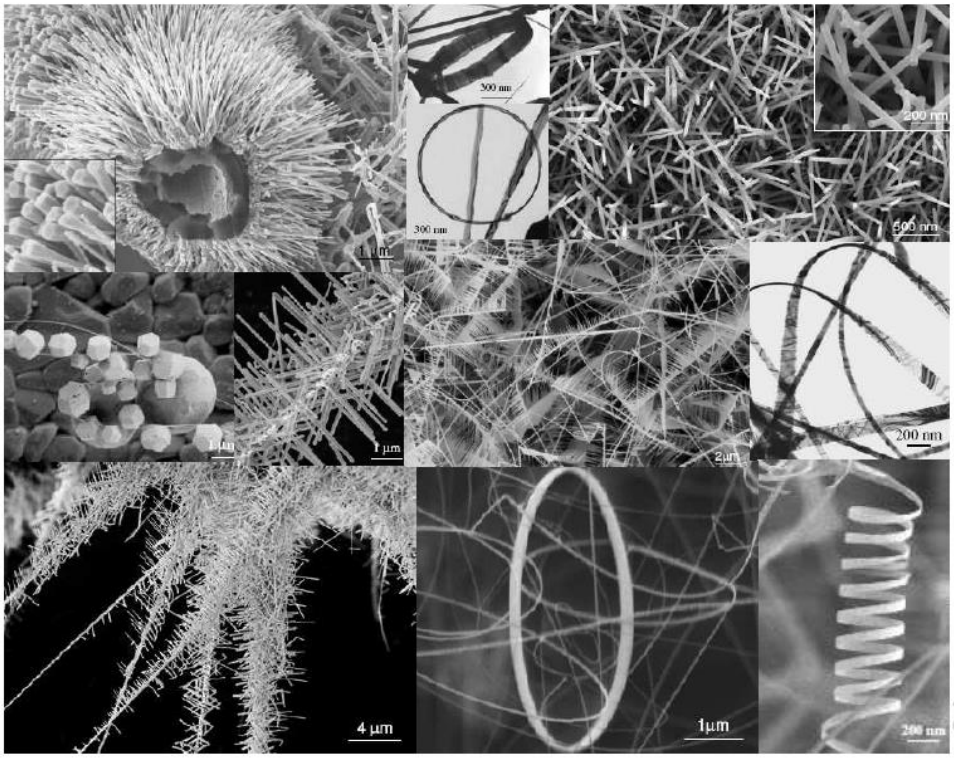


Figure 2.2: ZnO nanostructures of various morphologies [52].

One-dimensional (1D) semiconductor nanostructures are beneficial for various applications. This is accredited to their notable aspect ratio, high surface to volume ratio and their aptitude to necessitate effective electron transition [53]. ZnO nanorods have augmented properties and performance due to their stability, crystallinity, high surface area and improved electron transport. To emphasise the significance of nanostructure geometry, a study by Jaafar et al [54] compared two ZnO-based memory devices which were constructed using the same technique, with identical integral materials and electrodes. However, one device had ZnO nanorods, aligned vertically and the other had ZnO nanoparticles randomly dispersed, which were individually implanted inside a poly-methyl methacrylate (PMMA) material and inserted between two gold electrodes in a crossbar device arrangement. The disparities in the observed conduction and switching properties was attributed to the different nanostructure ZnO geometry. The switching in the nanoparticle device was associated with charge trapping and the formation of a space-charge field attributed to the distribution of the nanoparticles in the PMMA material whereas the switching of the nanorod device was attributed to the migration of the oxygen vacancies in an interfacial barrier region located at the end of these ZnO nanorods. A discrepancy has been reported regarding the properties of nanorods and nanoparticles, including optical, magnetic, catalytic and plasmonic properties, which are more enhanced to nanorods compared to nanoparticles [55-57].

2.3 Review on current research on synthesis and applications of ZnO nanorods

2.3.1 Synthesis of ZnO NRs

Due to the excellent properties exhibited by ZnO nanorods and potential applications, scientists have been prompted to develop various routes for synthesizing them. Elongated 1D ZnO nanorods have been investigated in photoactivated reactions including degradation of toxins such as dyes, pesticides, antibiotics, microbial photo-inactivation and light to chemical energy conversion [58-62]. While ZnO has a high electron mobility, the 1D nanorods enhances the electron mobility [24, 63]. Several techniques for the growth of ZnO nanorods are primarily categorised as either vapor-phase or solution-phase synthesis. The synthesis of such nanostructures is often done as either free standing in aqueous solutions (powders) or on flexible organic and inorganic substrates. The use of substrates in ZnO growth allows easy control of the direction of growth, for example the growth of vertically aligned ZnO nanorods. It also allows the simultaneous manipulation of the surface, interfacial, charge transport, and transfer properties of the nanorods, thus offering new opportunities to accomplish multi-

functionality for numerous applications. The next subsections are a discussion of existing methods that have been used for the growth of ZnO NRs thin films on glass substrates.

2.3.1.1 Vapor- phase synthesis

The vapor-phase synthesis involves the formation of vapor species through evaporation, chemical reduction, and gaseous reaction. The evaporated vapor is gradually condensed onto the surface of the substrate, stacking up to form a specific morphology. The disadvantage of this method emanates from the use of relatively high temperatures of about 500°C to 1500°C to generate the vapor. This technique also has a possibility of formation of intermediates, thus giving rise to unwanted impurities. Usually, the vapor phase method requires the use of a catalytic agent. Some of the methods that fall under the vapor phase category includes vapor liquid solid (VLS), chemical vapor deposition (CVD), vapor transport deposition (VTD), molecular beam epitaxy (MBE), metal organic chemical vapor deposition (MOCVD), physical vapor deposition (PVD), pulsed laser deposition (PLD), atomic layer deposition (ALD), and metal organic vapor phase epitaxy (MOVPE) [64-66].

2.3.1.2 Solution-phase synthesis

The solution phase-based synthesis routes have also been employed for growth of ZnO nanorods on substrates [67, 68]. Some of their advantages include their merit of simplicity, low temperature needed, scalability, and low cost. The relatively low temperatures permit use of a wide range of substrates including inorganic and organic substrates. Some of the mostly used solution-phase fabrication methods are the hydrothermal, chemical bath deposition (CBD), wet chemical precipitation, electrochemical deposition and the spray pyrolysis method [15, 69, 70]. Among other solution-phase routes, the CBD method offers a combination of cost-effectiveness, environmental benignity and equipment simplicity as compared to other methods. Furthermore, the CBD method offers the capability to generate high-density ZnO nanorods arrays of high crystal quality [71, 72]. The use of a nucleation surface for the chemical bath deposition results in a heterogeneous formation of ZnO NRs. Usually, a ZnO polycrystalline seed layer is used for this purpose. A seed layered substrate assists in construction of well- aligned and quality ZnO NRs. Techniques such as spray pyrolysis, dip coating, spin coating have been employed for the synthesis of seed layers on flexible substrates. As an optimisation attempt, the connection of the characteristics of the seed layer and the growth of ZnO NRs has been reported [73- 76].

The growth kinetics of ZnO NRs are highly dependent upon growth parameters, which can instantly be controlled thus easily manipulating the properties of the grown ZnO nanorod film. Previous studies have reported the influence of different parameters such as the growth temperature, duration of deposition, precursor type, precursor concentration, and pH of the precursor solutions on the uniformity, shape, growth direction, aspect ratio (length and diameter), and subsequent structure and optical properties of the grown ZnO NRs [76-81].

2.3.2 Applications of ZnO NRs

Owing to their exceptional structural, optical and piezoelectric properties, ZnO NRs are unremittingly being used in numerous applications from detection, photonics, field emission and in fabrication of functional devices [56, 60, 69, 76, 82]. As already mentioned, a very interesting recent direction in nanotechnology research is the use of ZnO NRs in light trapping related applications. The wide band gap of ZnO enables absorption of mostly the UV region of the electromagnetic spectrum. Literature reports on photoinduced applications of ZnO nanorods for degradation of pesticides, dyes, pharmaceuticals, as well as energy conversion [37, 83]. Due to a great potential of providing a direct transport pathway for photoexcited and effective light- harvesting efficiency, various endevors has been made to utilize ZnO nanorods in solar energy absorption. These include the fabrication of photoelectrochemical solar cells, dye-sensitized semiconductor single-crystal (DSCC) photoelectrodes, etc [52, 59, 74].

2.3.3 Modification of ZnO NRs

Considerable advancement towards enhanced efficacy and optimal performance of SMOs is attained through the implementation of numerous modification techniques. Doping with both metals and non-metals, combining with other SMOs, using dyes for sensitization, use of sacrificial agents, composites, polymer immobilization etc [51, 84-88] are often done to tune the electronic and optical properties of ZnO, hence achieving improved photoactivities. The dispersion of ZnO NRs on polymeric materials (e.g., cellulose), large surface area materials (e.g., graphene, activated carbon, carbon nanotubes) increases the specific surface area and number of active sites for photon absorption [89]. Doping with heterogeneous composites enhanced photoactivities by improving charge separation. However, some of these techniques have compromised the structure and other properties of ZnO nanorods.

Doping of SMOs encompasses incorporation of a slight proportion of impurities known as dopants, exclusively for modifying specific identified properties, without creating new phases or structures. Studies have revealed that the inclusion of dopants results in the disparity of properties and functionality of semiconducting metal oxides [14, 59, 90, 91]. Either wet chemical or ion beam assisted methods are often used for the doping process. Even though wet chemical conventional diffusion doping has been the most utilized method for inclusion of impurity elements to the host lattice, several detriments are reported. Diffusion doping often results in agglomeration of dopant elements on the surface of the SMOs, the agglomerates thus act as recombination centres [92]. Furthermore, issues of unpremeditated dispersal of the dopants within the SMO system are reported [93, 94]. The effect of doping is inspected through use of a wide-range of synthesis methods, various characterization techniques as well as analysis of these doped metal oxides for numerous applications. It was recently reported that inclusion of Mn^{2+} ions into ZnO decreased the crystallite size [95]. A blue shift in the optical bandgap and suppressed generation of reactive oxygen species (ROS) were observed, thus leading to reduced photocatalytic activity. Similar findings have been reported by Lesnik et al [96] and Tsuzuki et al [97]. Another study by Ullah et al [38] exhibited opposing results, as they noted augmented photocatalytic efficiency upon Mn doping. These inconsistent reports on dopants effect are thus associated to the location of dopants within the host lattice.

2.4 Ion beam induced effects for the modification of the properties of ZnO NRs

Ion beam technology is adopted as a technique to meet the challenges in the development of the semiconductor industry and usually categorised as either plasma immersion ion implantation (PIII), focused ion beams (FIBs), swift heavy ion irradiation (SHI), low and medium energy ion implantation. Ion implantation offers an opportunity to inject a controlled quantity of impurities at a precise depth within a semiconductor. This method does not rely on the solubility and diffusivity of the dopants [98]. It involves the injection of energetic dopant ions (E >1000 eV) on the host target. It has also been used for the fabrication of state-of-the-art semiconductors, as well as to modify existing properties of materials such as polymers, insulators, semiconductors, metals etc. Selective doping of the host with the element of interest via ion implantation eliminates the possibility of cross contamination and unintended impurities. The desired ion species are accelerated in an electrical field and implanted into the surface layer of the substrate to a depth of several micrometres. Controlling factors such as

dose, dopant depth and area localization during ion implantation method leads to precise doping [99].

Additionally, a series of parameters such as the type of ions, ion fluence, energy and/or post-implantation treatment does influence the degree of surface modification. The use of ion beam technology over the conventional diffusion doping for the modification of properties of SMOs enables selective enhancement of surface properties. This means that the bulk properties of the material can be left unchanged. Additionally, ion implantation allows the omnidirectional processing capability to tailor the surface properties of a material by introducing a myriad of diverse elements. Rare earth metals and transition metals, have been doped into semiconductors through the ion implantation method [100]. Besides metallic dopants, non-metals such as hydrogen, nitrogen, phosphorus and carbon have also been implanted onto the semiconductor lattice. Regardless of the advantages and evolving use of the ion implantation technique, few studies on the use of energetic ions to improve the properties of ZnO NRs have been reported. Park et al [101] have implanted nitrogen ions with energy of 120 KeV at two different beam fluences of 1×10^{16} and 1×10^{17} particles/cm^2. Results from their work indicated local structural damage and reduced crystallinity of the ZnO NRs upon nitrogen implantation. However, the damage was influenced by the ion beam fluence. Nitrogen ions of flux of 1×10^{17} particles/cm^2 were noted to cause shape deformation of the nanorods as they melted and produced tube-shaped nanostructures.

The effects of nitrogen ions on ZnO NRs have also been discussed by Wang et al [102]. Contradictory to the report by Park et al [101], the assimilation of the nitrogen ions at low energy of 30 KeV did not alter the morphology of the ZnO NRs. However, a red shift of the optical absorption edges towards longer wavelengths was noted. Additionally, the gradient N dopant distribution resulted in a terraced band structure and a built-in electric field. This phenomenon contributes to the enhanced separation efficiency of photogenerated electron-hole pairs in ZnO, as visible light PEC experiments showed higher efficiencies for N- implanted ZnO NRs. On the other hand, Cai et al [62] successfully implanted W^{6+} ions of varying fluences of 2.5×10^{14}, 1×10^{15}, and 5×10^{15} ions/cm^2, into ZnO nanorods without destroying the 1D nanostructure. The implanted films were then annealed at 500 ℃ for 2 hours. Structural analysis via XRD and Raman techniques revealed that the induced lattice disorder was dependent on the fluence of the W^{6+} ions. The optical analysis of the 50 KeV W^{6+} implanted ZnO displayed a gradual change in the position of the absorption cut-off edge. They explained

that the redshift was caused by the implanted W^{6+} ions, creating new impurity levels in the forbidden band of ZnO and thus resulting in reduction of the band gap of ZnO. It was also shown that the W^{6+} implanted ZnO NRs exhibited significant visible-light photoelectrochemical water-splitting performances. The photocurrent density of the implanted samples was noted to have increased by over 700 % as compared to the pristine ZnO NRs.

Transition metals are known for their extended visible light absorption, associated with the surface plasmon resonance (SPR) effect [103]. Macková et al [104] studied the distribution of Au ions and the induced damage in ZnO of various orientations. ZnO was implanted using 1 MeV Au^{+}, at fluence of 1.5×10^{16} ions/cm^2. The implanted samples were then annealed at 600 °C, at ambient atmosphere for an hour, followed by irradiating 10 MeV O^{3+} ions at fluence of 5×10^{14} ions/cm^2. Intensive analysis showed that Au^{+} induced disorder in the O sublattice. No additional strain was observed. However, following irradiation with O^{3+}, structural modifications such as compressive deformation and vertical strain were noted to be more enhanced, compared to those which were only implanted with Au^{+} ions.

The distribution of cobalt ions (Co^{+} and Co^{2+}) in vertically aligned ZnO NRs has been investigated by Park et al [105]. The fluence of the implanted cobalt ions were 1×10^{13} and 1×10^{15} ions/cm^2, at energies of 50 and 100 KeV, respectively, with subsequent post implantation annealing at varying temperatures from 400-650 ℃. The distribution of Co ions in ZnO NRs were found to be independent of the implantation energies and it was further observed that these ions primarily substituted the Zn sites. A systematic investigation by Wang et al [92] reported the effect of Cu^{2+} ions on the physicochemical and photoelectrochemical (PEC) properties of ZnO NR photoanodes. The study reports extended optical absorption edges of implanted ZnO NR arrays and an increase in the carrier density which resulted in significant water splitting activity under visible light irradiation.

Besides introducing impurities, the migration and distribution of the dopant ions through the host lattice generates strains, dislocations, structural transitions and defects which influence properties of SMOs. Inherent defects, such as interstitials, vacancies and anti-sites have been reported to impinge the geometric structures due to atomic rearrangement, thus altering the structural properties of ZnO [106]. The type and magnitude of formed defects are observed to be strongly influenced by the nature and fluence of the implanted ion species. The impact of the ions on defect evolution, accumulation and formation of defects complexes are found in

literature [107]. Azarov et al [108] reported a strong dependence of the defect's formation on ZnO due to implantation of various ion species. Self-ions, light ions, medium mass and heavy ions were implanted on ZnO NRs and a disparity in the defect accumulation was observed. Actually, heavy implants were noted to display a discrete two-stage behaviour of point defects and extended defects, respectively.

Most researchers have followed implantation with high temperature post annealing treatment [62, 104, 105, 108-111]. The core role of defects instigated by ion implantation is also mediated by post treatment procedures. Annealing post implantation is for crystalline quality recovery of the material and to help in the diffusion of the dopants for electrical conductivity, however unannealed defects have also been noted to augment optical properties of ZnO [106]. A summary of some recent studies on the modification of selected properties of ZnO NRs through ion implantation technique are as summarised in Table 2.2. Inspired by these previous studies and the inadequate available literature on concurrent ion implantation, we investigated how the simultaneous implantation of Ag^+ and C^+ ions influences both the structural characteristics and opto-response properties of ZnO nanorods (NRs). The evolution of probable modifications is investigated as a function of the varied fluences of the ions, utilizing a range of characterization techniques.

Table 2.2: Current studies on the use of ion implantation technology to modify various properties of ZnO nanorods. (The 5th column denotes whether a treatment procedure of any form was carried out on the samples post implantation.)

Targeted properties and applications	**Energy** (KeV)	**Fluence** (ions/cm^2)	**Ion species**	**Post treatment**	**Ref.**
Composition, structure and optical properties	80	2×10^{15}- 1×10^{16}	Sm	No	[100]
Photoluminescence properties	50	1.0×10^{14} ions/cm^2.	P	Yes	[109]
Ferromagnetism	250	$1\text{-}5 \times 10^{16}$	Mn, Co	Yes	[110]
Room temperature ferromagnetism	100	1×10^{16}	Cu	Yes	[111]
Photoelectrochemical water splitting under visible light	50	2.5×10^{14}-1×10^{15}	V	No	[112]
Fabrication of a p-n Homojunction	20	1×10^{16}	N	No	[113]
Photocatalytic degradation of Pharmaceuticals	100	5×10^{14}, 1×10^{15}, 5×10^{15}, and 1×10^{16}	N	No	[114]

CHAPTER 3: EXPERIMENTAL METHODS AND TECHNIQUES

3.1 Overview

Chapter 3 gives an in-depth description of the steps and procedures followed during the synthesis of ZnO nanorod films, followed by ion implantation. The reagents, concentrations of solutions and other parameters are described. ZnO seed-layers were grown on commercially available borosilicate glass substrates of dimension of (76 x 26 x 1.35) mm, through spray pyrolysis method. ZnO nanorods were later fabricated on the layered substrates via the adoption of the chemical bath deposition method. Various equipment was used to examine the structural, morphological and optical properties of the synthesised samples. The fundamental principles of these characterization techniques are discussed at length. Additionally, the theories and models used in the calculation of certain parameters are also expounded.

3.2 Sample Fabrication

All the necessary glassware and apparatus including beakers, glass substrates, conical flasks, measuring cylinders, spatula etc were thoroughly cleaned. Initially, the apparatus were soaked in liquid soap for 30 minutes and then scrubbed with a bottle brush. Subsequently, the glassware was then alternately sonicated with ethanol and acetone for an hour. Afterward it was rinsed twice with deionised water and left to air dry in a lint-free environment. The chemicals used in this work were purchased from Sigma Aldrich and were used in their pure form.

3.2.1 Synthesis of the ZnO seed layer

ZnO nanorods were synthesised on the prepared seed layer. The role played by the seed layer on the growth and alignment of nanorods has been reported [115, 116]. The seed layer serves as a substrate to facilitate the growth of ZnO nanostructures in the preferred orientation. This has been explained to be due to the reduced interface energy between the substrate and the crystal nuclei, which thus also reduces the nucleation barrier. In addition, the presence of a seed layer results in an increase in the surface roughness, which thus favours the growth of ZnO nanostructures. Due to their high energy, the crystalline interfaces between seeds absorbs particles or nuclei to lower the system energy, thus promoting nanorods growth. The ZnO

nanorod fabrication procedure commenced with the growth of a ZnO seed layer on clean borosilicate glass substrates. A simple home-assembled spray pyrolysis set up (shown in Figure 3.1) was used for the deposition of the ZnO seed layer.

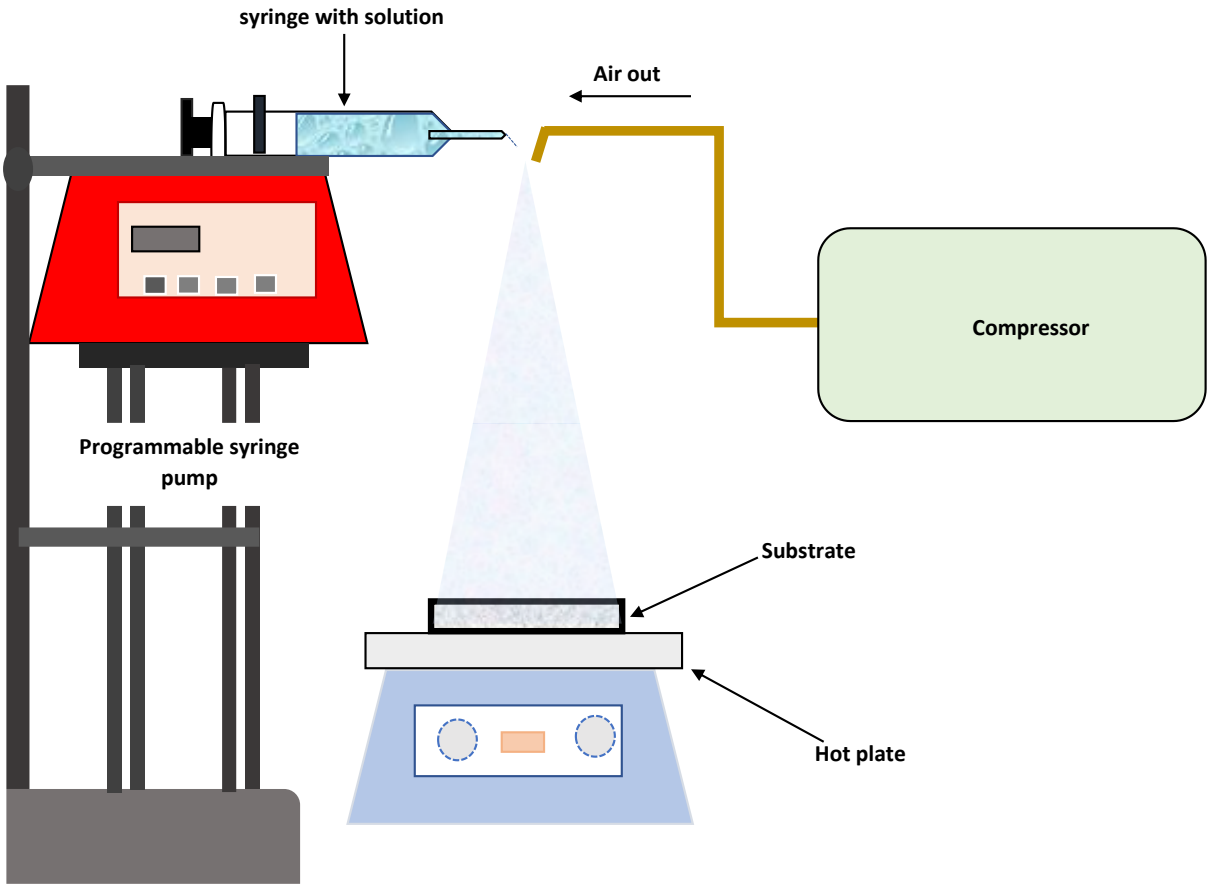


Figure 3.1: Schematic diagram of a spray pyrolysis technique used for the growth of ZnO seed layer.

A Zn^{2+} ion source solution was prepared from a stoichiometric zinc acetate dihydrate [Zn $(CH_3CO_2)_2.2H_2O$] salt. 0.55g of the salt was stirred in 100 mL of deionized water to form aqueous Zn^{2+} ion source solution. Few drops of glacial acetic acid (99% concentration) were added to the solution to avoid untimely precipitation, under continued stirring at room temperature. A sterile syringe was then loaded with the aqueous [Zn $(CH_3CO_2)_2.2H_2O$] solution, then deposited on the substrates with the aid of air from the compressor. The air serves to atomize the precursor solution, creating a very fine mist that can be evenly deposited on the glass substrates. Deposition was done at substrate temperature of 350 ℃. The seed layer substrates were then kept at this temperature for 20 minutes for annealing purpose. The samples

were stored in an air tight container for characterisation and growth of 1D structures. Optimum parameters for the growth of the seed layer are as summarised in Table 3.1.

Table 3.1: Optimum deposition parameters used during spray pyrolysis for seed layer growth.

Deposition parameter	**Optimum value**
Zn $(CH_3CO_2)_2.2H_2O$ [CAS 5970-45-6] concentration	0.025 M
Diameter of the syringe	20 mm
Volume of precursor solution sprayed	7.5 mL
Deposition temperature	350 ℃
Spray rate	0.5 mL/min
Spraying distance between nozzle and substrate	30 cm

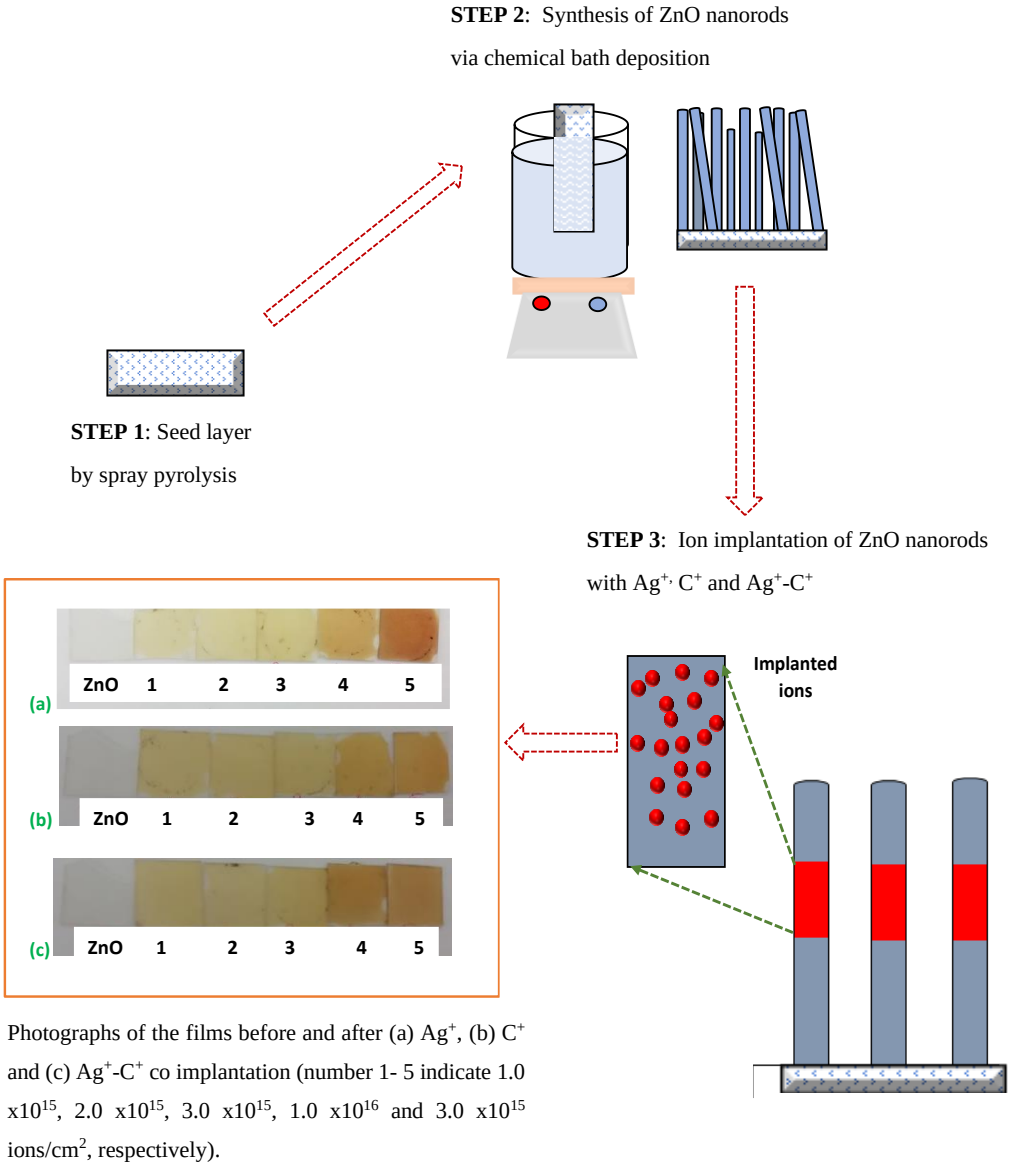
3.2.2 Synthesis of the ZnO nanorods

Subsequently, ZnO nanostructures were deposited on the prepared ZnO seed coatings through the chemical bath deposition (CBD) method [117, 118]. Table 3.2 shows the parameters for the growth of ZnO nanorods.

Table 3.2: Summary of optimized parameters for the growth of ZnO nanorods through chemical deposition method.

Deposition parameter	**Optimum value**
$Zn(NO_3)_2.6H_2O$ [CAS 10916-18-6] precursor concentration	0.05 M
Surfactant used and volume	Polyethylene glycol, 10 mL
Volume of precursor solution	50 Ml
Reducing agent and volume	Ammonia, 5 mL
Growth temperature	80 ℃
Growth time	1.5 hours
Post growth treatment	Annealing at 300 ºC for 3 hours

Typically, deionised water was used to prepare an aqueous solution of 0.05 M zinc nitrate hexahydrate [$Zn(NO_3)_2.6H_2O$]. 10 mL of the respective surfactant was added to the prepared solution and stirred for 20 minutes at room temperature to achieve a homogeneous solution and avoid formation of agglomerates [119]. About 5 mL of ammonia (NH_3) solution was then drop-wisely added to the solution, still under constant stirring. A white gelatine precipitate was observed immediately upon addition of ammonia solution, however, as more ammonia was added, the solution became less cloudy and colourless. The pre- synthesised seed layer films were then suspended in a 50 mL empty beaker, followed by adding this solution to the brim. The temperature of the solution was monitored and maintained at 80 ℃ throughout the procedure that lasted 1.5 hours. During the 1.5 hours the solution was not stirred to avoid mechanical abrasions on the growing 1D nanostructures. A summary of the fabrication route is as illustrated in Figure 3.2.



Photographs of the films before and after (a) Ag^+, (b) C^+ and (c) Ag^+-C^+ co implantation (number 1- 5 indicate 1.0 x10^{15}, 2.0 x10^{15}, 3.0 x10^{15}, 1.0 x10^{16} and 3.0 x10^{15} ions/cm^2, respectively).

Figure 3.2: A flow chart representing the three steps in the growth and ion implantation of the ZnO nanorods.

The growth mechanism of ZnO nanorods is proposed as follows.

1. Dissociation of the Zn $(NO_3)_2.6H_2O$ into Zn^{2+} and NO_3^- ions;

$$Zn(NO_3)_2.6H_2O\ (aq) \rightarrow Zn^{2+} + 2NO_3^{-3} + H_2O \qquad (3.1)$$

2. Reaction of ammonia with water, NH_3 is hydrolysed to form NH_4^+ and OH^- ions;

$$NH_3 + H_2O \rightarrow NH_4^+ + OH^- \quad (3.2)$$

3. The reaction of the OH^- ions with Zn^{2+} ions results in formation of $Zn(OH)_2$ complex ions The favoured adsorption of these ions on the (002) ZnO planes, allows formation of nanorods;

$$Zn^{2+} + 2NH^{4+} + 2OH^- \rightarrow 2Zn(OH)_2 + 2NH_3 \quad (3.3)$$

At the end of the stated time, the solution became clearer with some precipitates settling at the bottom of the beaker. The cloudy covered-slides were collected, gently dipped in de-ionized water for 2 minutes to remove the loose precipitate and dried for one hour at room temperature. The samples were then annealed in vacuum at 300 ℃ for 3 hours. During annealing the $(ZnOH)_2$ was oxidised to ZnO. The annealed samples were stored in an air tight sample storage for characterization and ion implantation.

3.3 Ion implantation

The bombardment of energetic ions onto host lattice results in crystal damage. The damage depends on the type of ions used, ion energy, ion mass number as well as ion fluence. Ion implantation remains one of the leading techniques in the fabrication and modification of functional semiconductors. As previously explained, this owes to the possibility to control the location of the dopants within the host lattice. Different properties have been modified through ion implantation, and improved efficiencies are documented. The basic operating principle of the ion implanter and experimental details for the implantation of the ZnO nanorod films are discussed in this section.

The vacuum chamber, ion-source, acceleration tube, mass analyzer and target chamber are the basic components of an ion implanter system. These components are responsible for the ion generation, beam formation, beam transport, ion purity and fluence control. The ion implanter system should be kept under high vacuum to allow efficient plasma generation and free ion beam transport. High vacuum also combats the occurrence of dispersion and contamination due to collisions with ambient gas molecules and previous source residue. Ion beams are

usually extracted from ion sources. A typical layout of the ion implanter is depicted in Figure 3.3.

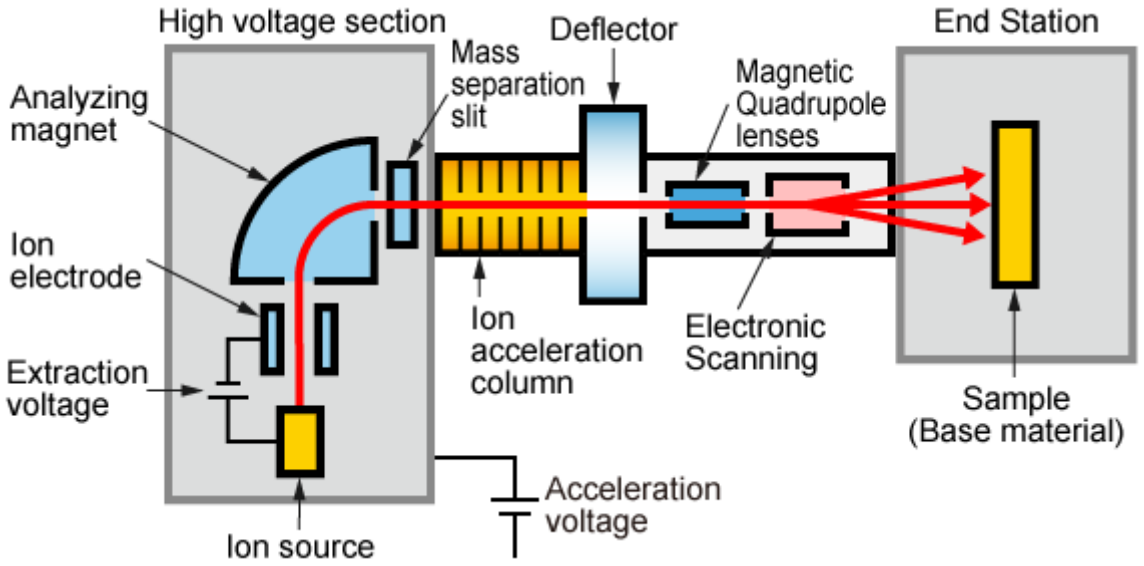


Figure 3.3: A block diagram of the Varian 200-20A2F ion implanter [120]**.**

The ions are mostly generated by electrical discharge of gases/vapor and solid sputtering. Ion implantation accelerator systems use different ion source. The Varian-Extrion model uses a Freeman arc discharge ion source. This type of an ion source is said to be versatile because it can provide high current and low emittance beams from most solid and gaseous species [121]. One important feature of the Freeman ion source is the hot tungsten filament that is heated to drive the arc discharge. A high filament current of approximately ~160 A is used for the heating process. Electrons are produced from a hot filament through thermionic emissions, followed by ionization of the dopant molecules to form an ion plasma. Electromagnetic fields are employed to extract ions from the ion source. The extraction process creates an ion beam, which is then collimated and accelerated to the mass analyzer at a specific kinetic energy (K.E) given by a simple equation 3.4, where m is the mass of the particle and **v** is the velocity of the particle.

$$\mathrm{K.E} = \frac{1}{2}\mathrm{m}\mathbf{v}^2 \qquad (3.4)$$

This energy is provided by the applied voltage. Since single charged ions are formed, the conservation of energy for an ion of charge q, accelerated through potential V and moving at velocity v can be written as:

$$\frac{1}{2}m\mathbf{v}^2 = qV \qquad (3.5)$$

There is always a possibility of the ion source producing more than one type of ion species. The current extracted from the ion source is entirely accelerated, loading the accelerator and thus resulting in elevated back-streaming of electrons and high levels of radiation are emitted [122]. It is then necessary to filter out other ions and remain with only the desired species. This filtration occurs in the mass analyzer also known as the mass spectrometer. The filtration process is based on atomic weights or ion masses. The mass separation is achieved by magnetic fields. The beam of ions enters the analyzing magnet from the ion source through a magnetic field (**B**) which is perpendicular to direction of the accelerated ions, they experience a force (**F**). This force is also perpendicular to the magnetic field and the direction of the moving charge (q) as given by equation 3.6;

$$\mathbf{F} = q(\mathbf{B} \times \mathbf{v}) \qquad (3.6)$$

The magnetic field results in a curving path of the ions, which consequently changes velocity (v) for the moving ions hence they experience a centripetal force equal to that given by equation 3.7;

$$\mathbf{F} = m\frac{\mathbf{v^2}}{R} \qquad (3.7)$$

Where m, **v** and R are the mass, velocity of the particle, and the radius of curvature, respectively.

Merging equation 3.6 and 3.7 gives a relation to determine R, for ions of mass m, charge q, in motion at a velocity v, perpendicular to the magnetic field.

$$R = \frac{m\mathbf{v}}{q\mathbf{B}} \qquad (3.8)$$

The mass to charge ratio, (m/q) is proportional to the radius of curvature R, so only ions of specific size will be allowed through a narrow resolving aperture into the accelerating tube. Lighter ions of smaller R or heavy ions of bigger R will travel along different paths as determined by their charge-to-mass ratios. However, some contaminants remain unseparated

due to their equivalent momentum. As the beam of selected ions enter the accelerating tube, they are accelerated to the desired energies which usually range from 25 KeV to 200 KeV for this specific ion implanter. Higher energies in the MeV range can be achieved for in other types of ion implanters. The acceleration tube encompasses electrodes which operate either in the drift mode, the post acceleration mode or the post deceleration mode. The mode of operation is influenced by the required implantation energy. For the drift mode the ion beam energy remains unchanged, whereas for the acceleration and deceleration modes the ion beam energy is increased or decreased respectively so as to attain the required implantation energy.

Regardless of the position of the target substrates, there is necessity for uniform distribution of the desired ion fluence over the surface area of target material. Since the beam is charged, beam manipulation can be achieved through beam deflection by electrostatic fields [122]. The electrostatic quadrupole triplet lens directs the ion beam to the target chamber, where it goes through a raster scanner assembly which consists of four electrostatic deflection plates, two vertical and two horizontals. The raster scanner assembly provides a uniform ion beam deposition. Only charged ions will be deflected in the vertical (Y) and horizontal (X) plates as they experience perpendicular forces due to the electric fields. The parallel beam plates sweep the beam across the specimen and results in implantation of a homogeneous desired fluence. The neutral particles are however not deflected; hence they will be removed by the horizontal plates as they carry a deflection bias voltage. A Faraday cup is used to integrate the extracted ion beam current [123].

SRIM (stopping and range of ions in matter) 2013 software was used to estimate the depth of the implanted ions, their nature of interaction with the host atoms as well as the damage cascade induced by the ions. More details on the SRIM simulations are discussed in chapter 4. The fabricated ZnO nanorod films were cut into 2 x 2 cm^2 pieces and mounted on the ion implanter sample holder end station. The ion implantation was conducted at the iThemba LABS Tandem and Accelerator Mass Spectrometry (TAMS) Laboratory (South Africa). Implantation was carried out at room temperature, without post treatment employed subsequent to ion implantation, at energy 50 KeV and at fluences of 1.0 $x10^{15}$, 2.0 $x10^{15}$, 3.0 $x10^{15}$, 1.0 $x10^{16}$ and 3.0 $x10^{16}$ ions/cm^2. Three sets of samples were implanted. The first set was implanted with Ag^+ ions, the second set with C^+ ions and, the third set was co-implanted with Ag^+ and C^+ ions.

3.4 Characterization techniques

Several analytical techniques; X-ray diffraction (XRD), Raman spectroscopy, Rutherford backscattering spectrometry (RBS), Fourier transform infrared (FTIR) spectroscopy, X-ray photoelectron spectroscopy (XPS), field emission scanning electron microscopy (FESEM), energy dispersive X-ray spectroscopy (EDX), atomic force microscopy (AFM), and ultraviolet/visible/near infrared **(**UV/VIS/NIR) spectroscopy were used to investigate the evolution of the structural, morphology and optical properties of the pristine and implanted samples. These techniques were accessed at different local and international laboratories and were employed before (i.e., on pristine samples) and after ion implantation. This subsection discusses the working principles, parameters and models for these techniques which were used in this research work. The specific instrumental parameters used during the measurements are also outlined.

3.4.1 X-ray diffraction (XRD) technique

The X-ray diffraction is a non- invasive, elastic scattering method used to probe a wide range of structural investigations. Different microstructural parameters, crystal orientations, internal crystal stresses/strain can be investigated from the analysis of patterns obtained from XRD measurements. Due to distinct unique fingerprints which produce diffraction peaks, unknown materials can also be identified by the use of the XRD technique. The X-ray compartment consists of a cathode ray tube which generates electromagnetic X-rays. The rays are filtered to produce monochromatic radiation and collimated towards the sample. When X-rays are incident on a crystal, they will scatter the electrons in all directions. This interaction of X-rays with atoms can either cause constructive or destructive interference patterns as the X-ray waves are scattered by crystal structures [124, 125]. Destructive interference results in no diffraction peaks, thus a restriction to study the crystallographic properties. On the other hand, following constructive interference, the diffracted rays will entail sharp interference maxima (peaks) with corresponding symmetry as in the distribution of atoms. XRD is the most appropriate technique to study interatomic distances in crystal frameworks. Constructive interferences obey Bragg's law (given by equation 3.9) which relates the wavelength (λ) of X-rays, to the diffraction angle (θ) and interplanar spacing (d) [126, 127].

$$n\lambda = 2d\sin\theta \qquad (3.9)$$

Bragg's law for real as well as reciprocal space geometry is illustrated in Figure 3.4, with X-rays striking on a crystal at an incident angle θ with respect to a certain crystal plane (hkl).

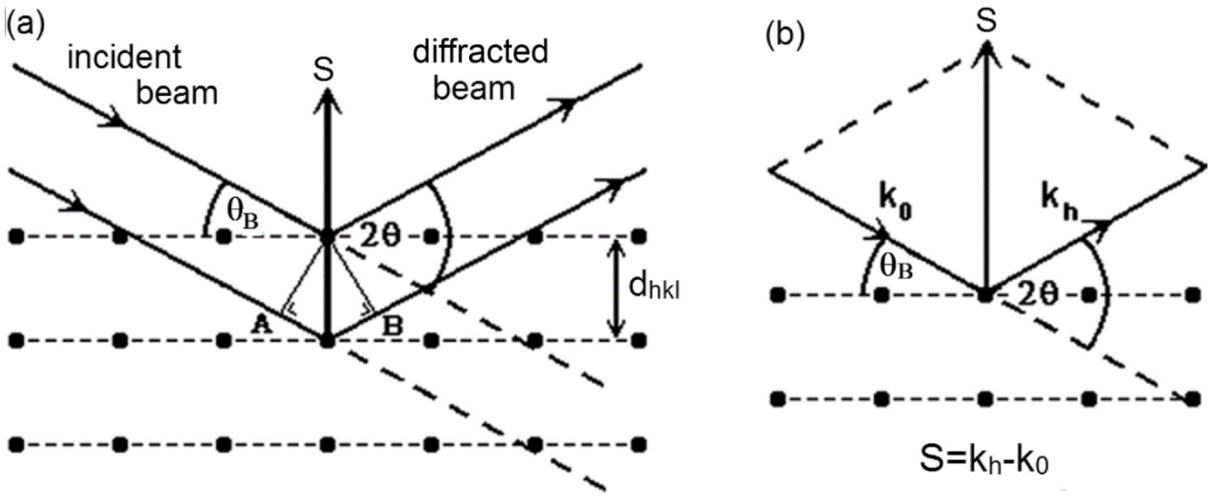


Figure 3.4: Bragg's law (a) for real as well as (b) reciprocal space geometry [127].

A Bruker advance D8 XRD diffractometer system equipped with a Lynxe detector was used in all XRD measurements. Monochromatic copper (Cu) Kα source with a wavelength λ=1.5418 Å was used for detailed XRD measurements of all the synthesised samples with current and voltage of 40 mA and 40 kV, respectively. The diffraction peaks were recorded in a continuous mode for a two theta (2θ) range of 20-80º, at a scanning rate of 0,02º/s. Pristine and ion implanted samples were measured under similar conditions. It was necessary to confirm the integration of the implanted ions into the ZnO framework using the XRD technique. The XRD was employed as the primary technique to also study any lattice alterations related to implantation damage as well as to investigate the lattice strain and dislocations from ion implantation. The measured XRD profiles were analysed with the Eva XRD software and further employed for calculation of various structural parameters.

The structural properties and impact of ions on the lattice of ZnO were assessed through calculation of various microstructural parameters using a series of equations [8, 128, 129]. Bragg's law, in equation 3.9 was used to determine the interplanar spacings (d) between the planes. An alteration of the d-spacing can indicate either expansion or contraction of the lattice [130]. Several methods were previously used to evaluate the grain size [8, 131, 132]. In this work, the X-ray line broadening method given by the Scherrer equation (equation 3.10) was

employed to calculate crystallite size (D_s) of the most prominent 002 peak, for the pristine and implanted samples.

$$D_s = \frac{K\lambda}{\beta Cos\theta} \quad (3.10)$$

where K the crystallite shape factor is 0.9, λ is the wavelength of the Cu K_α radiation of 1.5418 Å, β is the FWHM of the peak in radians, θ is the diffraction angle or peak position, also in radians.

Usually, dislocations arise during crystal growth or when the crystal is said to be distorted by stress [133]. The obtained D_s values were used in equation 3.11 to determine the variation of the dislocation density (δ) with fluence of the implanted ions.

$$\delta = \frac{1}{(D_s)^2} \quad (3.11)$$

To fortify the suggestion of possible lattice distortions, lattice parameters (a_p=b_p and c_p) were determined from equation 3.12 which relates the parameters to the interplanar d-spacing and the miller indices which are denoted by symbols hkl [134].

$$\frac{1}{d^2} = \frac{4}{3}\left[\frac{h^2+hk+k^2}{(a_p)^2}\right] + \frac{l^2}{(c_p)^2} \quad (3.12)$$

An imperfect semiconductor lattice is assumed to contain a concentration of intrinsic defects for example vacancies, self-interstitials, line defects, point defects, volume defects and planar defects. These are reported to induce positive strain in the implanted crystal layers. The lattice deformation was found to result solitarily in the out-of-plane direction, thus implying that the strain due to the implanted ions is perpendicular. The perpendicular stain will be referenced and discussed in this thesis. The degree of lattice distortion can be evaluated from the lattice strain using equation 3.13 [128]. The stress in the films was also calculated for pristine and implanted ZnO films. The stress in the films can be classified as either intrinsic or extrinsic stress. Intrinsic stress arise due to the presence of impurities and defects, while the latter is usually due to lattice and thermal coefficient mismatch between thin film and substrate. In this study, the samples were not annealed after ion implantation, hence it is suggested that there is some residual stress within the films. The presence of residual stress will be attributed to the variation of implanted ions within the ZnO lattice. The residual stress using the biaxial stress model as given by equation 3.14, respectively [128, 135, 136].

$$\varepsilon_{zz} = \frac{C_{impl} - C_{prist}}{C_{prist}} \quad (3.13)$$

$$\sigma_z = \frac{2C_{13}^2 - C_{33}(C_{11} + C_{12})}{C_{13}} . \varepsilon_{zz} \quad (3.14)$$

where c_{impl} is the lattice parameter c_p of the implanted ZnO crystal and c_{prist} is the lattice parameter c_p of the pristine ZnO lattice. For equation 3.14, the elastic stiffness of bulk ZnO; C_{11}, C_{12}, C_{13} and C_{33} are given as 209.7, 121.1, 105.1 and 210.9 GPa, respectively [128].

The impact of the presence of the implanted ions on the bonding of the atoms was investigated by calculating the bond length L. The second neighbouring bond length L_1, L_2 and L_3were also calculated from relations given by equation 3.15 to equation 3.18 [137, 138].

$$L = \sqrt{\left[\frac{a^2}{3} + (0.5 - u)^2 . c^2\right]} \quad (3.15)$$

$$L_1 = c(1 - \mu) \quad (3.16)$$

$$L_2 = \sqrt{a^2 + (\mu c)^2} \quad (3.17)$$

$$L_3 = \sqrt{\frac{4a^2}{3} + (0.5 - \mu)^2 . c^2} \quad (3.18)$$

where μ is the positional parameter which indicates the degree of atom displacement, and is calculated using equation 3.19. Symbols a and c denote the calculated lattice parameter

$$\mu = \frac{a^2}{3c^2} + 0.25 \quad (3.19)$$

A stacking fault is a two-dimensional imperfection caused by the non-alignment of one atomic plane with another. The probability of stalking faults was calculated using the relation given by equation 3.20

$$SF = \left[\frac{2\pi^2}{45(3\tan\theta)^{0.5}}\right] . \beta \quad (3.20)$$

where θ and β are the Bragg angle and FWHM of the 002 peak, respectively. These two parameters are given in unit of radians.

3.4.2 Rutherford backscattering spectrometry (RBS)

Rutherford backscattering spectrometry (RBS) technique is a quantitative technique widely used to investigate atomic depth distribution in the near surface regions. From the energy distribution of the backscattered alpha particles, elemental composition can be determined as a function of depth [139]. Therefore, the material's crystalline quality can be explored through RBS analysis. The degree of damage in a crystal is probed through the channelling effect. Also, the quantity of interstitial/substitutional elements in a lattice can be evaluated. RBS analysis depends on the kinematics of the scattering and the energy loss of the incident projectile upon interaction with the target atom [140].

Normally, a target is mounted in a vacuum chamber and impinged with energetic ions (usually in the MeV range). Alpha particles ($^4He^{2+}$) and protons are usually bombarded onto the target using electrostatic linear accelerators. An electrostatic repulsion occurs between the incoming projectile and target nuclei, resulting in an elastic backscattering of the ions [141]. The schematic of scattering dynamics is illustrated by Figure 3.5. Backscattering can only occur if the mass of the target atom is greater than that of the incident ion. The energy and number of the backscattered projectiles are then measured with a simple semiconductor surface barrier detector. An exchange of energy occurs between the scattered ions and the electrons on the surface of the detector, resulting in promotion of electrons from the valence band to the conduction band. An electron-hole pair is thus generated in the process. This electron- pairs are quantified to give the energy of the scattered ions.

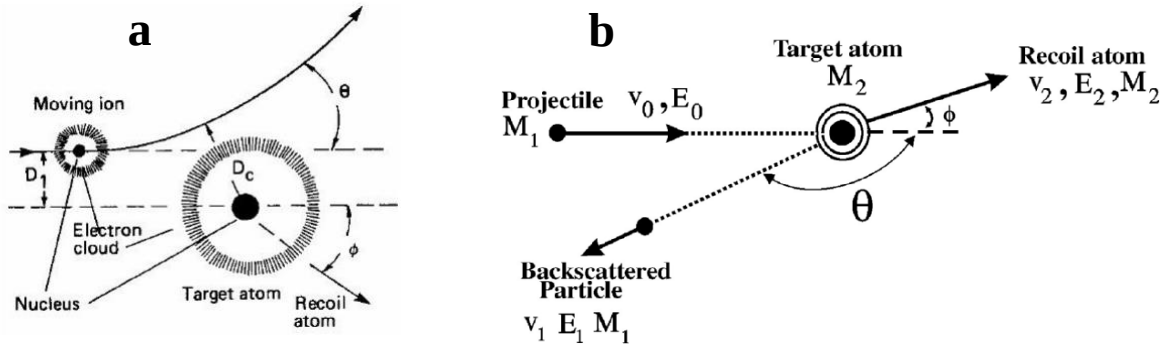


Figure 3.5: The principle and scattering geometry of the RBS (a) and a schematic showing elastic collision of the projectile ion with the target atom (b) [141].

Since this is an elastic process, the kinematics of the collision event between the energetic particle and the target are said to result in conservation of both the energy and momentum. The

energy (E_1) of the projectile particle after scattering by a target atom of mass M_2 can be determined from its initial energy (E_0) as given by equation 3.21 [140].

$$E_1 = k.E_0 \tag{3.21}$$

where the kinematic factor *k* is the ratio energies of the incident particle and that after the collision. This *k* is dependent on the mass of the incident particle, that of the target atom and the scattering angle, taking into consideration $M_1 < M_2$ for scattering angle θ. Also, the initial energy E_1 is so higher than the binding energy of the target atom and assuming they are no nuclear reactions and resonance, *k* is calculated using equation 3.22 [140, 142]

$$k = \left(\frac{M_1 \cos\theta \pm \sqrt{M_2^2 - M_1^2(\sin\theta)^2}}{M_1 + M_2} \right)^2 \tag{3.22}$$

where θ represents the scattering angle and M_2 is the mass of the target nucleus initially at rest. Figure 3.6 shows how at varying scattering angles the kinematic factor, *k*, changes as the mass of the target atom is varied. The kinematic factor is noted to increase monotonically as the scattering angle decreases.

The energy separation, ΔE_1, of backscattered particles for two unlike target elements with mass difference ΔM_2 can be calculated as;

$$\Delta E_1 = E_0 \frac{dk}{dM_2} \Delta M_2 \quad \rightarrow \quad \delta M_2 = \frac{\delta E}{E_0} \left(\frac{dk}{dM_2} \right)^{-1} \tag{3.23}$$

Equation 3.23 specifies that the mass resolution (δM_2) is reduced as the projectile energy E_1 increases. The mass resolution also reduces for elements with heavy mass, and there might also be an overlap between lighter elements with thick layers of the substrate of heavier elements.

The total energy loss, ΔE, is taken to be proportional to depth, t.

$$\Delta E = \Delta t \left(k \frac{dE}{dx_{in}} + \frac{1}{\cos\theta} \frac{dE}{dx_{out}} \right) \tag{3.24}$$

The elemental composition of the material can be deduced from RBS, using equation 3.25 [143];

$$Y = \sigma \Omega Q N \Delta t \tag{3.25}$$

where Y denotes the yield of scattered ions from a thin layer of thickness Δt, for a certain number of incident ions (Q) at a detector solid angle (Ω). The number of specimen atoms in atom/cm^2 is denoted N.

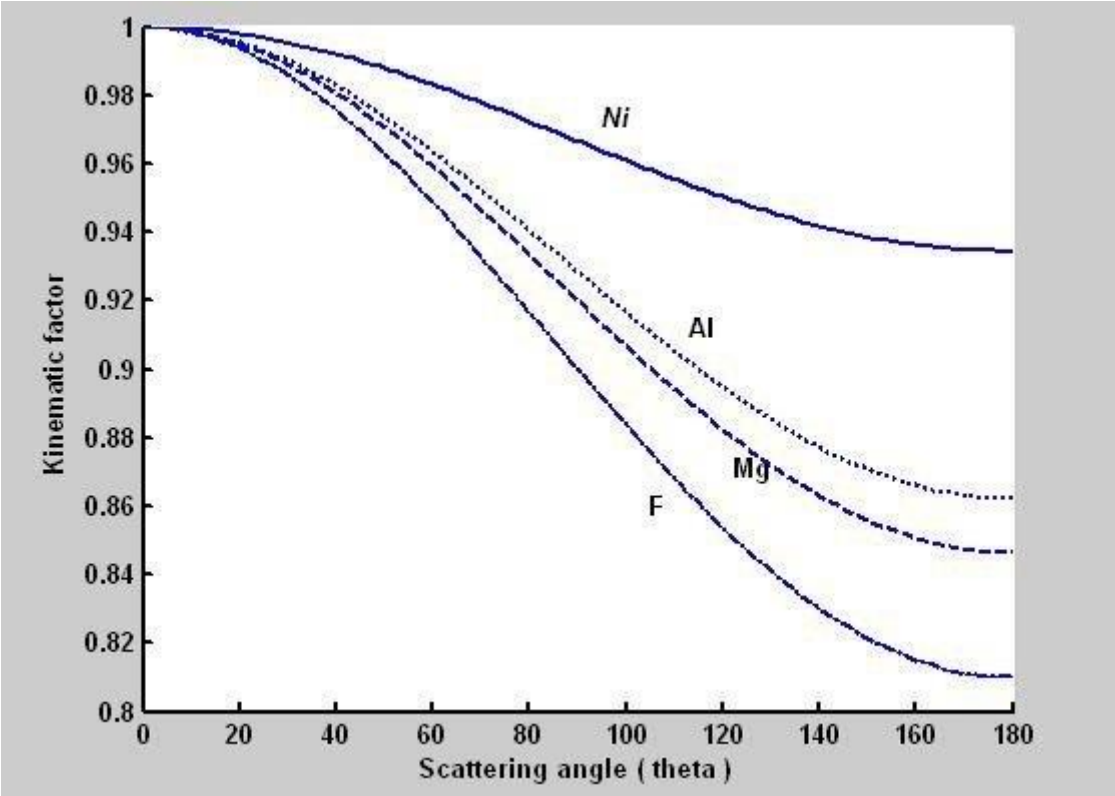


Figure 3.6: The variation of the kinematic factor, *k*, at varying scattering θ angles as a function of target mass, for incident H ions [144].

The film thicknesses, depth profiles and compositions of the pristine and ion implanted ZnO films were investigated by RBS, with a 6 MV Pelletron Tandem accelerator. The RBS measurements were performed at iThemba LABS, TAMS laboratory in South Africa.

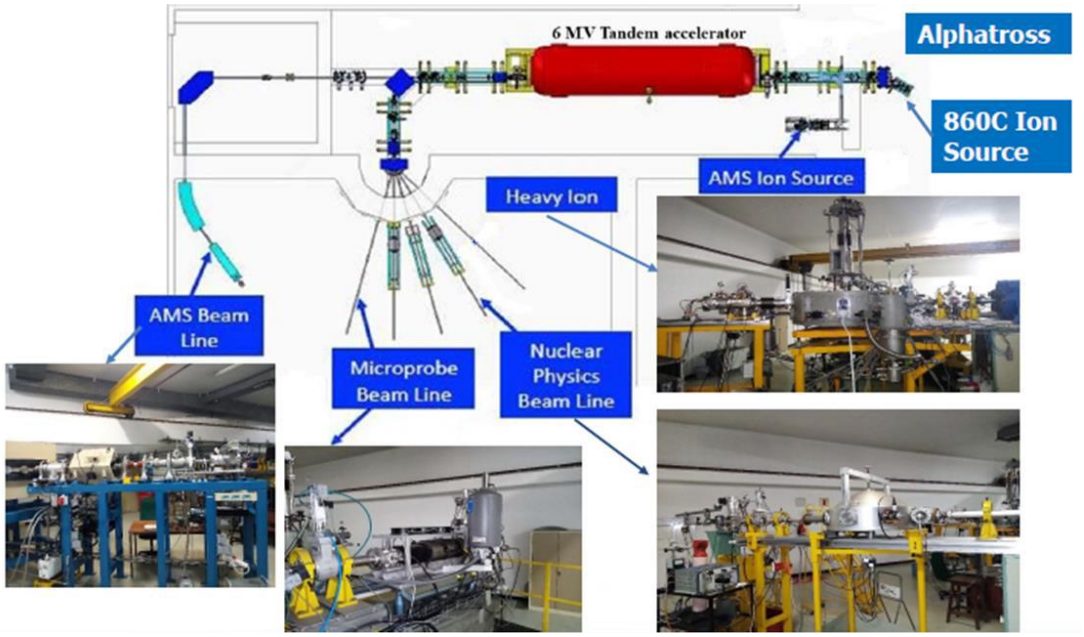


Figure 3.7: Schematic diagram and pictures of the iThemba LABS 6 MeV Tandem accelerator.

3.4.3 Raman spectroscopy

Interaction of light with matter is instrumental in spectrometric analysis. The non-invasive Raman spectroscopy technique has been employed on broad applications including medical diagnostics, material science, flow chemistry and bio-catalysis. In solid state physics, this technique is utilized to study the lattice dynamics and crystallographic orientations [145]. All materials possess a unique molecular fingerprint/signature, making it possible to use Raman spectroscopy for identification of unknown materials. Even though Fourier transform infrared (FTIR) spectroscopy and Raman techniques are often used as complimentary techniques, Raman spectroscopy offers quite a number of advantages over the FTIR. For our study the most outstanding merit of Raman spectroscopy is the ability to provide insight information on the lower frequency modes for inorganic- oxides (ZnO) which are often not easy to investigate through the use of the FTIR.

When photons interact with molecular electrons, there is an excitation of the material into an intermediate (virtual) state. This state is short lived such that the generated electron-phonon complex immediately re-emits a photon as scattered light, while leaving the electronic state of the material unchanged. Scattering of this light can either be classified as Rayleigh or Raman, depending on the relative energies of the incident and emitted photons [146]. Rayleigh scattering is basically an elastic scattering in which the energy of the incident and scattered photons is equal. However, inelastic scattering of light, which is known as the Raman

scattering, results in a promotion or demotion of photonic energy and frequency of the emitted light. Scattering of light that has gained extra energy from the molecules is known as Stokes scattering whereas the inverse is referred to as anti-Stokes, as depicted by Figure 3.8. Only a small portion of the light will experience inelastic light scattering as arbitrated by the electronic polarizability of the material. The difference between the incident photon energy and the energy of the Raman scattered photons is known as the Raman or frequency shift, and it is thus a measure of energy that induces transitions between different rotational and vibrational states in various materials. The disparities in the positions of the vibrational optical phonon modes and their intensities have been investigated to study the structural evolution upon ion implantation [146].

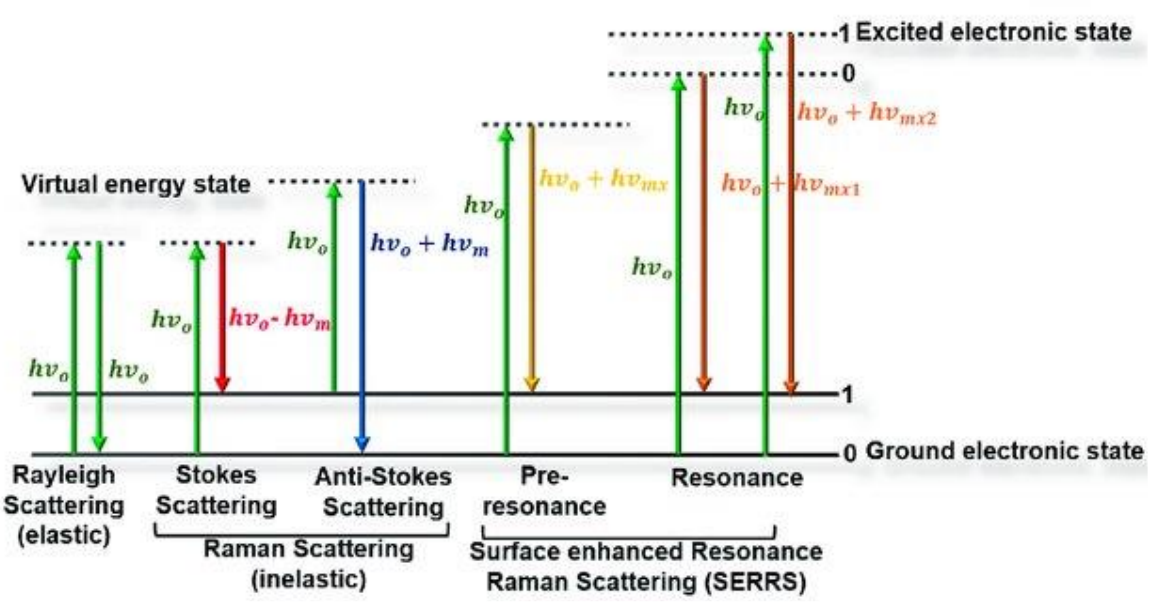


Figure 3.8: Schematic Jablonski diagram illustrating different quantum energy transitions for Raman and Rayleigh scattering [147].

Generally, longer wavelength of 532, 785, 830 and 1064 nm are used for the excitation of electrons. Laser diodes and mercury lamps are often used as monochromatic sources of light. The laser energy is transmitted to and collected from the sample by fibre optic cables, followed by elimination of the Rayleigh and anti-Stokes scattering by the edge filter. The light scattered through the Stokes process is then collimated on to a holographic grating and captured by a CCD detector.

A Horiba Labram HR Evolution Raman spectrometer was used to study the vibrational modes of the pristine and implanted ZnO samples. A diode laser of an excitation wavelength of 532

nm was used. Measurements were taken in the Raman shift of range of 50 to 1500 cm^{-1}, using an incident laser power of 2mW. An Olympus optical microscope of magnification BX50 was used. The spectra were saved in a text file and later plotted using the Origin8 Pro software.

The ZnO wurtzite structure belongs to the space group 46v C. According to the group theory, the phonon spectra of ZnO in the Γ point (centre of the Brillouin zone, which is defined as the Wigner-Seitz primitive cell of the reciprocal lattice) is characterised by six branches [148-150]. These Raman optical phonons with zero quasi-momentum at the Γ point (**k** = 0) are grouped as an irreducible representation of notations as $A_1+2B_1+E_1+2E_2$. The two non-polar E_2 modes are known as the E_{2low} and E_{2high}, and are associated to the vibration mode of the zinc and oxygen sub lattice atoms, respectively [151]. The $A_1 + E_1$ modes are both Raman and infrared active, the two nonpolar E_2 modes are only Raman active, and the two B_1 modes are both Raman and infrared silent.

3.4.4 Fourier transform infrared (FTIR) Spectroscopy

The Fourier transform infrared (FTIR) technique is highly sensitive and can be used to determine the quality of the sample. It is most suitable to study the presence of implanted ions in the SMO lattice, even at very low fluence. Measured spectral intensities depend on both sample morphology and chemistry [153]. Variations in the peak intensity, frequency or position and the symmetry of the absorption peaks is a key suggestion of the change in the material composition. FTIR spectroscopy relies on the analysis of infrared active vibrational modes. Different materials portray distinct infrared spectra showing absorption peaks which correspond mainly to overtones and combinations of fundamental vibrations between the bonds of the atoms making up that material [152]. It has been mostly used to identify the functional groups of different compounds, thus also identifying unknown materials. This technique can also be employed as an excellent tool for quantitative and compositional analysis, through a combination of modern software algorithms.

The three major parts of an FTIR spectrometer are the source, interferometer, and detector. The working principle of FTIR spectroscopy is as illustrated by the schematic diagram shown in Figure 3.9. A glowing black-body source emits a beam of IR radiation. The beam is collimated and directed through an aperture, and then goes through the interferometer. The interferometer consists of a beam splitter, a moving mirror, a stationary/sliding mirror and a timing laser.

Spectral encoding occurs in the interferometer. In the beam splitter the incident IR beam is divided. An ideal beam-splitter transmits and reflects 50% of the incident radiation. In this instance, approximately 50% of the light is refracted towards the fixed mirror and 50% is transmitted towards the moving mirror. Light is reflected from the two mirrors back to the beam splitter and recombine to give rise to a reconstructed beam which is optically referred to as an interference wave [154, 155]. The resulting interferogram is then steered toward the sample compartment where part of it is either absorbed, transmitted through or reflected off the surface of the sample. For a vibrational mode to absorb IR radiation, the vibrational motion associated with that mode must produce a change in the dipole moment of the molecule [156]. FTIR detectors are specially designed to observe interferograms as analogue signals, hence Fourier transformation algorithms are performed and the infrared spectrum is generated. The signal is converted as a function of retardation, to the frequency domain given by equation 3.26 [155];

$$S(v) = 2\int_0^{\infty} I(x)\, cos(2\pi vx)\, dx \qquad (3.26)$$

where I(x) represent the interferogram, v is wavenumber, x is the retardation and S(v) is the spectrum.

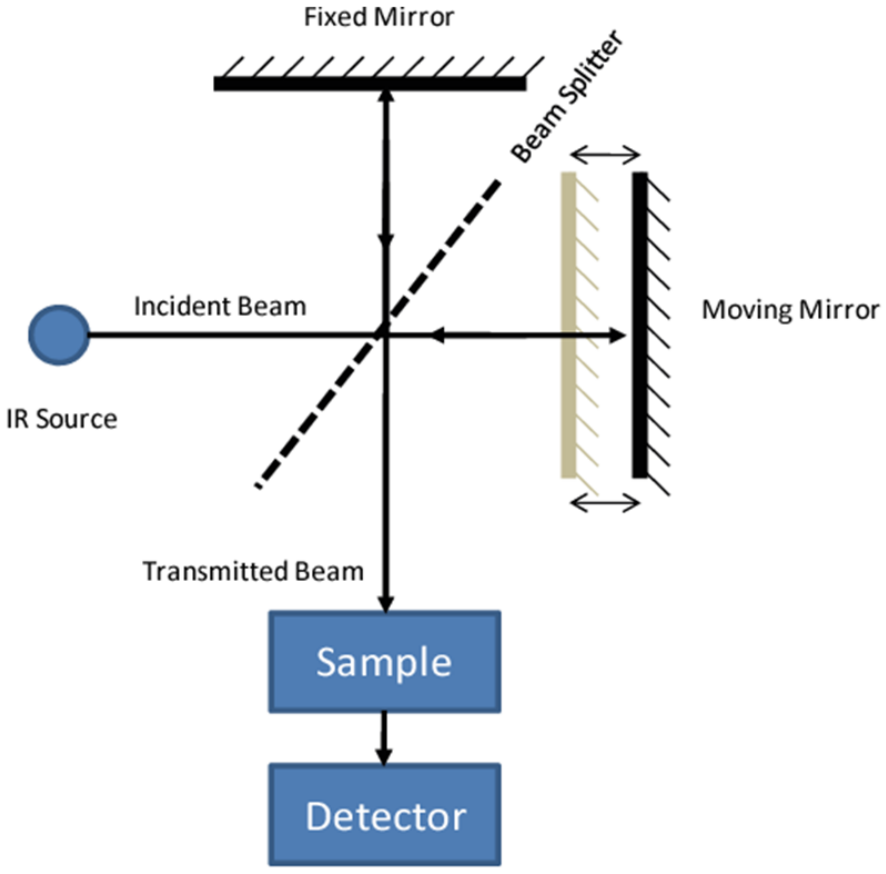


Figure 3.9: Schematic diagram to show parts of an FTIR [157].

A Bruker Vertex 70V FTIR spectrometer was used to investigate functional groups of the samples in order to study any variations in the Zn-O stretching modes upon introduction of either C^+ or Ag^+ ions. This instrument is equipped with a He-Ne laser that emits monochromatic infrared light with a wavelength of 633 nm. The spectra were acquired in the mid IR region, with a spectral range of 400-1500 cm^{-1} at nominal 4 cm^{-1} resolution. 128 scans were performed per sample to increase the signal-to-noise ratio. The instrument was equipped with a DLaTGS detector, and operated at room temperature in a transmission mode.

3.4.5 Field emission scanning electron microscopy (FESEM)

The surface morphology of materials is examined by the use of microscopes. Electron microscopes do offer better resolution images compared to optical microscopes [157]. This is attributed to the shorter wavelength of the electron beam which enables it to penetrate some few more microns beneath the surface of the sample. The degree of penetration depends on the density of the specimen as well as the accelerating voltage. The field emission scanning electron microscopy (FESEM) is often used to determine the morphology (shape and size), crystallographic properties, topography, composition, and other properties such as the electrical conductivity of materials. FESEM offers better imaging resolution compared to the conventional SEM, which often uses a heated tungsten source to generate electrons. However, the FESEM uses a high-energy beam of electrons which are liberated by a field emission source [157, 158]. These electrons are then accelerated in a high electrical field gradient, focused through a series of electromagnetic condenser lenses and then an objective lens to the specimen. The exchange of energy between the electron beam and the specimen results in elastic scattering and inelastic scattering thus emitting an assortment of high energy signals and electromagnetic radiation. The interaction of the incident beam of electrons with the specimen emits a variety of particles including backscattered electrons (BSE), secondary electrons (SE) and Auger electrons along with X-rays. The interaction processes as well as the schematic representation for the FESEM system are as illustrated in Figure 3.10.

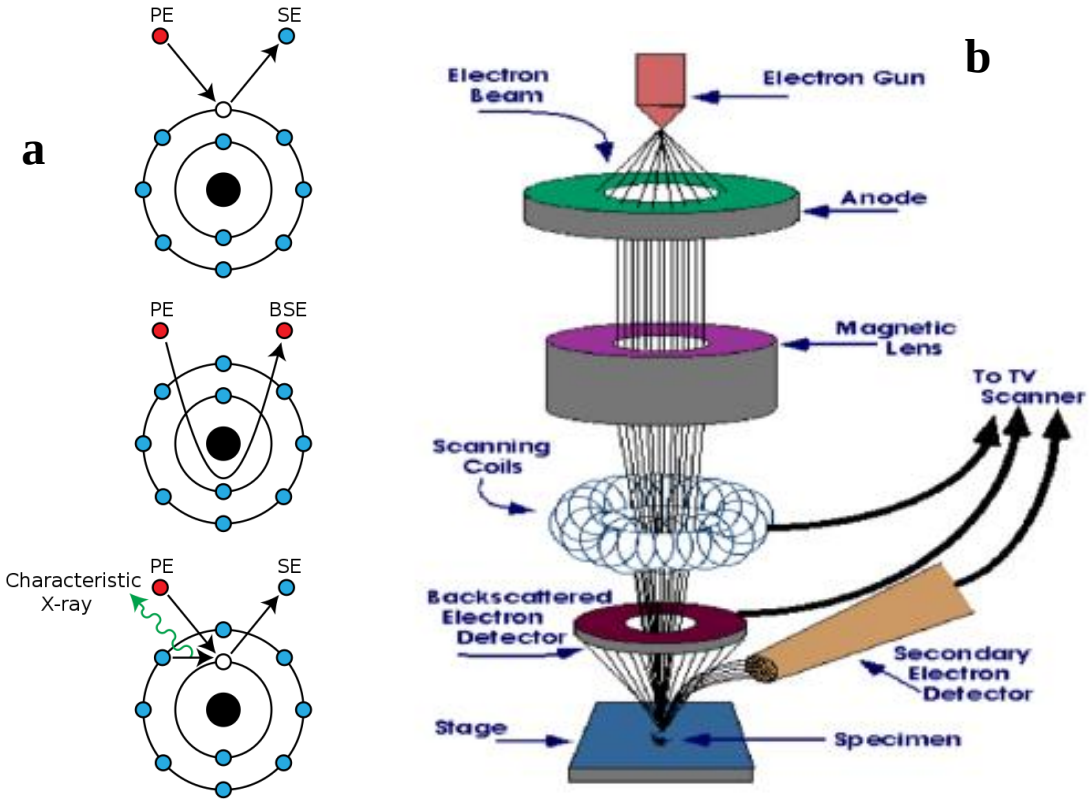


Figure 3.10: (a) Mechanisms of emission of secondary electrons (SE), backscattered electrons (BSE), and characteristic X-rays from atoms of the sample [159], (b) schematic representation of the FESEM system [159].

These signals are captured by the detectors and can be used to study the microstructural properties of the specimen. Secondary electrons are produced due to inelastic interaction of the primary electrons with loosely bound electrons in the atoms of the sample, resulting in the emission of electrons from the outer shells. These electrons are referred to as secondary electrons. Due to their low energies of 10-50 eV, secondary electrons are detected and mapped to study the surface topography of the specimen [158, 160].

For morphological studies, the FESEM experimental work for this research was conducted at the centre of analytical facilities, University of Stellenbosch in South Africa. The samples were first mounted on aluminium FESEM stubs by aid of a carbon double-sided adhesive tape. A thin layer of 10 nm of gold was then coated on the samples using a Leica EM ACE200 coater. Coating with a conductive layer prevents the build-up of charge, which might affect the quality of the images. A Zeiss MERLIN (Carl Zeiss Microscopy, Germany) FESEM was then used for

the examination of the surface morphology and elemental composition of the films. The electrons were accelerated at a voltage of 20 KeV and a beam current of 1.4 nA was used.

3.4.6 Energy dispersive X-ray spectroscopy (EDX)

Energy dispersive X-ray spectroscopy (EDX) is a quantitative analytical technique used for compositional elemental analysis of materials. As previously discussed, X-rays are also emitted upon interaction of energetic incident electrons with matter (see Figure 3.10). Bombardment of the sample with high energetic electrons results in the excitation of the inner shell electrons, ejecting it and resulting in the creation of a vacant electron hole in that inner shell. Since the inner shells ought to always be filled, an electron from an outer higher-energy state will then transition into the inner shell and recombine with the positively charged hole at the same time emitting energy in the form of X-rays. The generated X-rays are collected by the EDX detector which is usually housed in the FESEM compartment, and represented as a characteristic X-ray emission pattern indicating the available elements at their respective energies. The atomic percentages of the elements can also be evaluated from the spectra. In the present study, EDX analysis was used to study the purity and confirm the presence of implanted ions on the ZnO matrix. The EDX was done immediately after FESEM imaging as the EDX detector was attached to the Zeiss MERLIN SEM microscope. A voltage of 20kV was used to produce the X-rays.

3.4.7 Atomic force microscopy (AFM)

An atomic force microscope (AFM) is a non-optical or electron-optical microscope that rather uses the interatomic interactions between the probe and the surface of the samples to study the topology and morphology of materials [161]. It is known to be a very sensitive instrument, that its performance can be limited by external vibrations. Various parameters such as friction, hardness, elasticity, conductivity, magnetic forces, roughness and chemical functionality of materials can be estimated from AFM analysis. High-resolution images and study of local sites in air or liquid dispersions can also be attained through the use of the AFM technique. As such surface morphology of non-conducting samples like polymers, DNAs have been investigated using the AFM [162].

An AFM setup consists of a cantilever tip usually with a radius of 20-50 mm. The cantilever is designed with a very low spring constant to allow free movement in the x, y and z directions as controlled by a piezo-electric tube scanner. When the tip becomes in contact with surface, there is an attractive or repulsive force created. The force causes the cantilever to bend either towards or away from the surface, thus leading to a varying amount of laser light reflected into the photodiode.

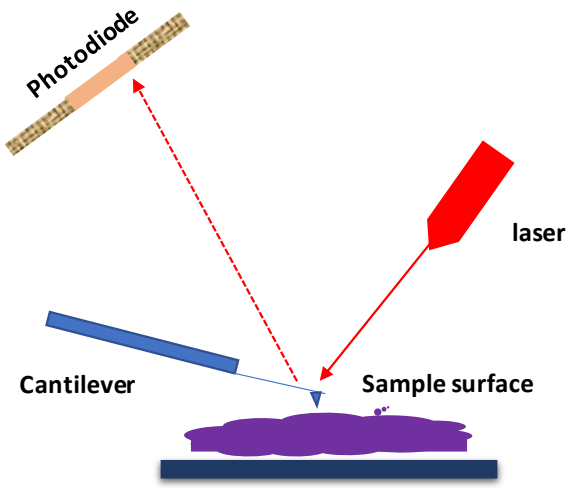


Figure 3.11: AFM operating principle.

The force between the tip/probe and the sample cannot be directly measured, it is calculated from the deflection of the cantilever according to Hooke' s law;

$$F = -kx \qquad (3.27)$$

where F is the force, k is the stiffness of the cantilever, and x is the distance the cantilever is bent.

A laser beam is used to detect and measure the cantilever deflections to or away from the surface of the sample. An incident beam is reflected on the surface of the cantilever and the divergence in the direction of the reflected beam signals the deflecting of the cantilever. The reflected signal is collected by the use of a position-sensitive photo diode (PSPD) which then convert them into 2D and 3D images.

3.4.8 X-ray photoelectron spectroscopy (XPS)

XPS is an analytical technique that measures the relative energies of electrons at an atomic and molecular level. It is often classified as a surface chemistry tool as it can be employed to characterize the nature of chemical bonds within materials or to study the elemental

composition of materials ranging from metals, ceramics, biomaterials, implants and polymers. The electronic structure and the density of the electronic states in semiconductors can also be studied by the use of the XPS.

The basic principle of XPS for quantitative analysis of surface composition is based on the photoelectric effect [146]. As shown by the schematic diagram in Figure 3.12, when a material is irradiated with monoenergetic photons of known high energies (usually soft X-rays are used), ionization takes place. This results in a systematic excitation and ejection of electrons from their bound state [146]. Due to the nuclear attraction forces, electrons in the inner sub shells (core electrons) will be difficult to eject due to the strong forces, whereas those in the other shells (valence electrons) are easier due to a lower binding energy. Complete transfer of the X-ray energy to a core level electron, results in the emission of photoelectrons [163]. Their kinetic energy is measured. In addition, not all emitted electrons will be collected by the electron analyser as some electrons are scattered inelastically. The photoelectric equation given by equation 3.28 [164] can then be used to calculate the electron binding energy of that certain material

$$E_b = E_p - (K.E + \varphi) \qquad (3.28)$$

where E_b is the binding energy, E_p is the energy of the incident photons usually calculated from $E=h\nu$; K.E is the kinetic energy of the ejected photoelectrons and φ is the combination of work function of the specific material and the instrument. The negligible contribution of the work function factor is usually ignored [163-165] and equation 3.28 simplifies to;

$$E_b = E_p - K.E \qquad (3.29)$$

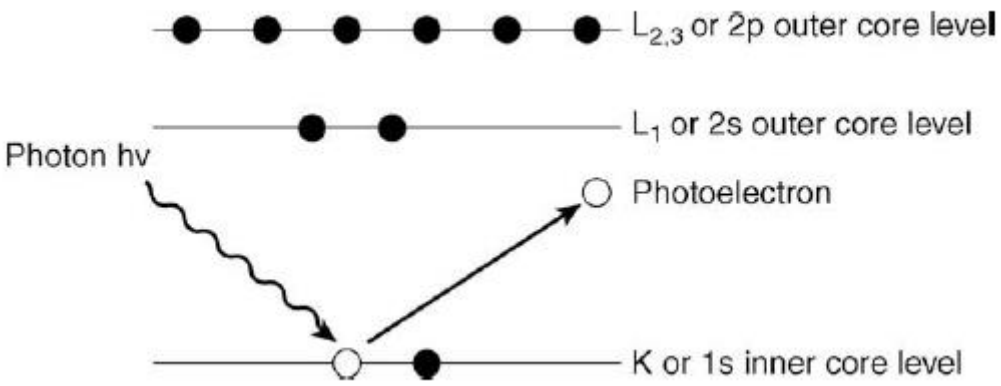


Figure 3.12: Schematic diagram of photoemission process used for XPS., showing the excitation and emission of an electron as induced by the incident X-rays [146].

The detector counts the number of photoelectrons at various kinetic energies. A typical XPS spectrum is a plot of the number of electrons detected at a specific binding energy. Each energy peak on the spectrum corresponds to a specific element. Only the lightest elements, hydrogen and helium atoms cannot be detected by the XPS technique. In addition to its inability to form a solid compound, helium has tiny cross-section for photoemission. Hydrogen also has an extremely small photoelectron cross-section and does not consist any core electrons which are essential for XPS detection [166]. The chemical states of the synthesised nanorods were investigated through core level measurements using a Kratos Axis Supra model X-ray photoelectron spectroscope. Further analysis of the XPS spectra were done using ESCApe software.

3.4.9 Ultraviolet/visible/near infrared (UV/VIS/NIR) spectroscopy

UV/VIS/NIR spectroscopy deals with three regions of the electromagnetic spectrum, that is the ultraviolet light (UV), visible light (VIS) and near-infrared (NIR). The wavelengths for these regions are; 180 to 400 nm, 400 to 800 nm, and 800 to 3200 nm for the UV, VIS and NIR, respectively [167, 168]. The UV/VIS/NIR spectroscopy can be used to quantify the light absorption, reflection, scattering and transmittance properties of a material. Molecules containing π-electrons or non-bonding electrons (n-electrons) do absorb energy from the incident light photons. The absorbed radiation induces electronic transitions from the ground state to a higher anti-bonding molecular orbitals or energy levels, thus resulting in any of the

four possible types of transitions (π–π*, n–π*, σ–σ*, and n–σ*) shown in Figure 3.13[169-171]. The UV/VIS/NIR measurements are usually given as a function of the wavelength.

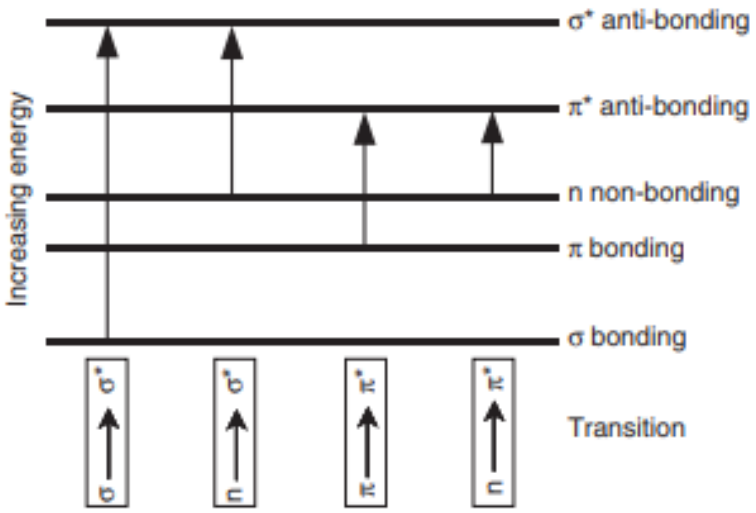


Figure 3.13: Possible electronic transitions occurring between molecular orbitals due to absorption of UV and visible light [171].

A typical single or double beam UV/VIS/NIR spectroscope, consists of a light source, a monochromator, a sample/reference chamber and a detector as displayed in Figure 3.14. Excluding cost and stability issues, the selection of the type of the light source mostly depends on the operational wavelength required for absorption by the material under investigation. A tungsten filament, xenon lamp, halogen lamps, gas discharge lamp, deuterium arc lamp, light emitting diodes can be used as the radiation sources. The principle of a double beam UV/VIS/NIR spectrophotometer is discussed. Typically, as a beam of light passes through the monochromator from the light source, it gets filtered into discrete wavelengths which are then allowed to singly pass to the slits. The slit only allows a small portion of the light to pass through upon which it gets split into a double beam. Through the aid of a series of mirrors, the other beam is directed to the reference chamber, while the other part goes to the sample compartment. Different intensities of light will pass through the sample and the reference, as influenced by the chromophores. The transmitted light from both the reference and the sample is captured and converted to interpretable electronic signals by the detectors. The detector is usually a charge -coupled device (CCD) or it can be a photomultiplier tube or a photodiode. The amount of the transmitted light is usually given by Beer-Lambert's law which basically defines the transmitted light as the ratio between the intensity of the transmitted light (I) and

the intensity of the incident light (I_0). Mathematically, Beer-Lambert's law [172, 173] can be expressed as:

$$T = \frac{I}{I_0} = e^{-\alpha t} \qquad (3.30)$$

where I is the intensity of the transmitted light, I_0 is the intensity of the incident light, α is the absorption coefficient and t is the thickness of the sample.

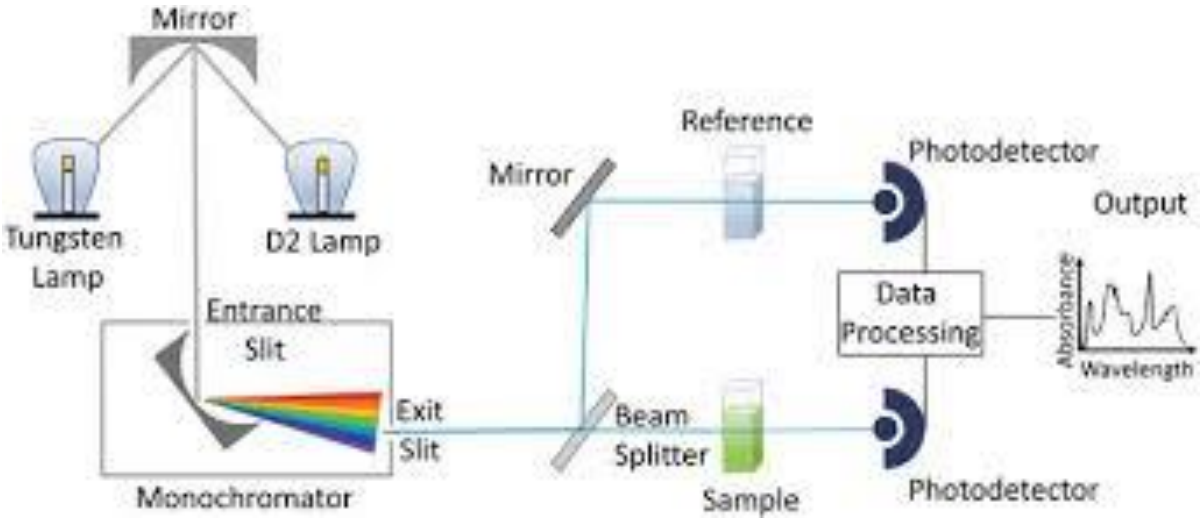


Figure 3.14: UV-vis spectrophotometer schematic for a double beam instrument [174].

For this work, both transmittance and absorbance of the pristine and ion implanted samples were measured using a double beam Lamba 750 Perkin-Elmer UV/VIS/NIR spectroscopy (see Appendix A for a picture). The measurements were taken in the spectral range of 300-1000 nm. A clean borosilicate glass was used as the reference. The measured absorbance and transmittance were analysed and further used to determine and deduce important optical parameters, such as absorption coefficient, extinction coefficient, linear refractive index, optical energy band gap, Urbach energy. and the optical conductivity. Several models were used for the calculation of these parameters. Comparing such optical parameters of pristine and ion implanted ZnO films will provide insight into any variations of the energy band structure, impurity levels, localized defects as well as the role of lattice vibrations.

3.4.9.1 Determination of the absorption coefficient (α) and extinction coefficient (k_x) and the linear refractive index

Rearrangement of the Beer Lambert's law gives equation 3.31 which can be used to determine the absorption coefficient (α);

$$\alpha = \frac{1}{t}.\ln\frac{1}{T} \qquad (3.31)$$

where t and T represent the film thickness and the measured transmittance, respectively.

To evaluate the extinction coefficient (k_x), which is a measure of the quantity of photons absorbed or/and scattered as light propagated in the material, equation 3.32 was used [175];

$$k_x = \frac{\alpha\lambda}{4\pi} \qquad (3.32)$$

Symbols k_x, α, λ, represent the extinction coefficient, the absorption coefficient and the wavelength of the photon, respectively.

Analysis of the refractive index (n) is remarkably paramount for many applications [176]. High refractive index materials are associated with incident light trapping (absorption) [177]. The model used to evaluate the refractive index is based on the physical thickness of the films, with a presumption of a ternary layered layer model; the substrate, the thin film and the incident medium. In the present case, the substrate was borosilicate glass, and the incident medium was air.

3.4.9.2 Determination of the energy bandgap [178-181].

The optical band gap energy, interpreted as the minimum required photon-excitation energy in a semiconductor, is a fundamental aspect of optical materials. The optical energy bandgap (E_g) was estimated from the well-known Tauc model simplified by equation 3.34. The extrapolation of the linear fragments of a Tauc plot of helps in the estimation of the bandgap.

$$\alpha hv = B\left(hv - E_g\right)^i \qquad (3.34)$$

The optical band was also evaluated through the derivative spectroscopy method. For this method, the transmittance of the ZnO nanostructures is differentiated with respect to the wavelength of transmission ($dT/d\lambda$) and the peak maxima (λ_{max}) deduced corresponds to the cut off wavelength of the samples [182]. Equation 3.35 is then used to calculate the Eg.

$$E_g = \frac{hc}{\lambda_{max}} \quad (3.35)$$

A plot of the $hv(2nk)^{1/2}$ vs the photon energy, hv was also used to find the band gap from extrapolating the linear segment of the plot.

$$hv\,(2nk_x)^{1/2} = hv - E_g \quad (3.36)$$

The symbols used in equation 3.34 to 3.36 are defined as follows: α is the absorption coefficient, h -Planck's constant, c- speed of light in vacuum, ν -frequency of incident photons, B is the band tailing parameter and i is the power index whether the semiconductor has a direct allowed/forbidden or indirect allowed/forbidden state. ZnO is a direct allowed transition semiconductor and i=1/2. n is the refractive index; k is the extinction coefficient. The values of E_g obtained from the four methods were denoted as $E_{g\,(Tauc)}$, $E_{g(ds)}$, $E_{g(2nk)}$ and $E_{g\,(WDD)}$, respectively.

3.4.9.3 Determination of the Urbach energy or absorption band tail

The Urbach energy, E_u is an estimation of the width of localized states associated with the conduction and valence bands, which extend inside the optical energy gap. Moreover, the Urbach energy also measures the degree of disorder in a semiconductor as a consequence of inclusion of an impurity in the film or lattice [183]. The following empirical formula estimates the dependence of the absorption coefficient α, on the photon energy [184, 185].

$$\alpha(hv) = a_o e^{\left(\frac{hv}{E_u}\right)} \quad (3.37)$$

The exponential behaviour is described by Urbach's law and can be written as;

$$Ln\alpha = ln\alpha_o + \frac{1}{E_u} hv \quad (3.38)$$

where α_o is a pre-exponential constant, E_u is the Urbach energy, α is the absorption coefficient, h -Planck's constant, ν -frequency of incident photons. A linear fit of Ln(α) against the photon energy (hv) gives the gradient. The inverse of the gradient equates to E_u, and the intercept is equal to $ln(\alpha_o)$.

3.4.9.4 Determination of the optical conductivity

The optical conductivity (σ_{opt}) is used to investigate the optical response of the synthesised materials. The optical conductivity of the samples was calculated using the relation;

$$\sigma_{opt} = \frac{\alpha nc}{4\pi} \quad (3.39)$$

Herein α, n, c are the absorption coefficient, refractive index and velocity of light in vacuum, respectively.

3.4.9.5 Determination of the dispersion and dielectric parameters

Dispersion parameters play a substantial role in the field of optical communications and in the fabrication of spectral analysis devices. The analysis of the dispersive refractive index of the ZnO thin films was performed through the concept of the single-effective oscillator model expressed by Wemple-Didomenico (WDD) [186]. This model explains that below the absorption band gap, the dispersion parameters (E_d, E_o) and the refraction index (n) are related through the following equation:

$$n^2 = 1 + \frac{E_o E_d}{E_o^2 - (hv)^2} \quad (3.40)$$

Where E_o and E_d represent the effective oscillator energy and the average force of the optical transitions, respectively. E_d is a measure of the average intensity of the inter-band optical transitions, that depends on chemical bonding and charge distribution within each unit cell, while E_o refers to the average excitation energy for electronic transitions [187].

Equation 3.40 can be rewritten as:

$$(n^2 - 1)^{-1} = \frac{E_o^2 - (hv)^2}{E_d E_O} = \frac{E_o}{E_d} - \frac{(hv)^2}{E_d E_o} \quad (3.41)$$

The values of E_o and E_d are thus deduced from the plot of $(n^2\text{-}1)^{-1}$ vs $(hv)^2$. The vertical intercept (E_o/E_d) and the slope of the plot $(1/E_oE_d)$ solved simultaneously give the required quantities E_o and E_d. .

The zero-frequency dielectric(ε_∞), also known as the static refractive index (n_o) is deduced when the photon energy (hv) is set to zero (hv=0) in the WDD equation 3.40, which then becomes;

$$n_{(o)} = \varepsilon_\infty = \left(1 + \frac{E_o}{E_d}\right)^{1/2} \quad (3.42)$$

The square of $n_{(o)}$ is known as the high frequency dielectric constant $(n_{(o)})^2$.

The high frequency dielectric constant, denoted ε_L is related to the refractive index (n) through the relation;

$$n^2 = \varepsilon_L - \left(\frac{e^2}{4\pi^2\varepsilon_o c^2}\right)\left(\frac{N}{M^*}\right)\lambda^2 \qquad (3.43)$$

where e is the electronic charge, ε_o is the permittivity of free space, c is the speed of light in a vacuum, N is the carrier concentration and M* is the charge carrier effective mass. A plot of n^2 vs λ^2 was used to deduce the values of ε_L and N/M* from the vertical intercept and the slope of the linear plot. The plasma frequency (ω_p) is defined as the resonant frequency for free electrons about their mean positions. Penn's theory [188] gives a relation:

$$2nk_x = \frac{\varepsilon_L \omega_p^2}{8\pi^2 c^3 \tau}\lambda^3 \qquad (3.44)$$

Where, the plasma frequency (ω_p) is calculated as;

$$\omega_p = \left(\frac{e^2 N}{\varepsilon_l \varepsilon_o M^*}\right)^{1/2} \qquad (3.45)$$

Another important relationship is the real **(ε_r)** and imaginary **(ε_i)** parts of the dielectric which are related to n and k through the following:

The relation between the real dielectric constant and the refractive index n is given by the Spitzer–Fan model;

$$\varepsilon_r = n^2 + k_x^2 \qquad (3.46)$$

$$\varepsilon_i = 2nk_x \qquad (3.47)$$

To evaluate the momenta M_{-1} and M_{-3}, the Wemple-Didomenico model is adopted. The calculated parameter, E_o and E_d were used to estimate M_{-1} and M_{-3} (moments of the optical spectra). These two parameters are used to express the inter-band transition strength and are evaluated using the following equations [189];

$$E_0^2 = \frac{M_{-1}}{M_{-3}}\ , \qquad (3.48)$$

$$E_d^2 = \frac{M_{-1}^3}{M_{-3}} \qquad (3.49)$$

The two equations above were rearranged to give

$$M_{-1} = \frac{E_d}{E_0} \qquad (3.50)$$

$$M_{-3} = \frac{M_{-1}}{E_0^2} \qquad (3.51)$$

CHAPTER 4: SIMULATIONS OF THE INTERACTIONS OF CARBON AND SILVER IONS WITH ZnO

4.1. Overview

The bombardment of a solid target with a beam of energetic particles results in partial backscattering of the injected particles from the surface layers, whilst the remaining fraction slows down through the target. The Stopping and Range of Ions in Matter (SRIM) software uses binary-collision-approximation (BCA) to study the trajectory of the energetic particle as it navigates and settles in the target atom. The BCA method also simulates the trajectory dynamics of the recoils in the host material. SRIM-2013 simulation was employed to simulate the interactions of Ag^+ and C^+ ions within the host, ZnO framework. Various parameters such as the dopant concentration of the implanted ions at varying fluences, vacancy density, total atom displacement and critical energy for both Ag^+ and C^+ ions were evaluated from the simulated data. A total of 99,999 incident ions were simulated.

4.2 Binary-collision-approximation (BCA)

Binary-collision-approximation (BCA) is based on Monte Carlo (MC) algorithms to simulate the interactions between the impinging energetic ions and the target material and the sequence of collisions sustained by the incoming ion. The BCA method is useful for estimating ion implantation profiles and the trajectory dynamics of the recoils in the host material at ion energies greater than roughly 1 KeV. The ion distribution in the target material is treated as a series of discrete collisions between two atoms [190]. The assumption on which the binary collision approximation is based is that all interactions within target atoms or between two-body encounters are considered. It is also assumed the recoil travels in a straight line between collision points in the framework, colliding with one individual atom at a time, hence resulting in binary collision [191-193]. For the BCA, random collision selections are combined with the observed stopping power, thus producing very precise computational calculations.

4.3 Stopping Power

The interaction of ions within the host atom causes the ions to lose energy and, thus, slowdown in the target matrix. Quantitative knowledge of stopping power and range is imperative for a vast number of applications including ion beam analysis, ion beam modification,

semiconductor fabrication, radiation therapy, nuclear engineering, etc [194, 195]. The amount of energy lost (dE) over a certain depth (dx), i.e., dE/dx, (where E is energy of ion and x is the penetration depth also known as the range) is known as stopping power. The SRIM simulations are used for determining the stopping power and range of ions in solids [196]. Ions lose their energy through various mechanisms; either electronic energy loss, nuclear energy loss or radiative energy loss. The radiative energy loss is often neglected, and consideration is made for energy lost due to partially screened Coulomb interactions between the incoming ions and bound electrons in the target which is termed as the electronic energy loss, and nuclear energy loss, defined as the energy lost due to elastic collisions between the incoming ions and the nuclei of the target atom. When all of the kinetic energy of the incoming ion is transferred to the target, it will cease moving.

The total stopping power is described as the summation of the contributions of electronic energy loss and nuclear energy loss given as [197]:

$$S = \frac{dE}{dx} = \left(\frac{dE}{dx}\right)_e + \left(\frac{dE}{dx}\right)_n \quad (4.1)$$

where e and n represent electronic and nuclear stopping powers, respectively. The energy transfer mechanisms between the incoming ion and the target atoms are very complex. Nuclear stopping power dominates at low energies while electronic stopping dominates in the high energy regime.

Nuclear stopping power results in elastic collision, hence the whole energy is transferred from the bombarded ion to the target atom, and both the energy and momentum are conserved. The elastic energy transferred T depends on the scattering angle θ through equation 4.2 [198]

$$T = \frac{4E_0 m_1 m_2}{(m_1+m_2)} \sin^2\frac{\theta}{2} = T_{max}\sin^2\frac{\theta}{2} \quad (4.2)$$

m_1 and m_2 represent the mass of the projectile and the stationary target atom, respectively, E_0 is the incident energy of the projectile and θ is the scattering angle in the center-of-mass frame.

The theoretical framework of nuclear stopping is treated as a classical collision between two charged particles. At small interatomic separations and high energies, screening effects are

taken to be negligible, hence V(r) reduces to repulsive Coulomb interaction between the nuclei, given as:

$$V(r) = \frac{Z_1 Z_2 e^2}{4\pi\varepsilon_0 r} \quad (4.3)$$

However, in ion implantation, there is screening of the charges at intermediate separations making it very complicated to describe accurately. A screening function $\Phi\left(\frac{r}{a}\right)$ between two interacting charges Z_1 and Z_2 is taken into consideration and the Coulomb potential is derived as [199]:

$$V(r) = \frac{Z_1 Z_2 e^2}{4\pi\varepsilon_0 r} \Phi\left(\frac{r}{a}\right) \quad (4.4)$$

The screening function $\Phi\left(\frac{r}{a}\right)$ depends on the electron density distribution of the two atoms, e represents the electronic charge, ε_0 is the permittivity of free space, Φ is the universal screening function, r is the interatomic distance, and a represents the empirical screening length in reference to the Bohr radius. Considering a collision between an energetic ion of mass M_1, atomic number Z_1 and of energy E_0 with a target of mass M_2, atomic number Z_2, the empirical screening length a is successively given by [200]:

$$a = \frac{0.885 a_0}{Z_1^{0.23} + Z_2^{0.23}} \quad (4.5)$$

where a_0 is the Bohr radius which is equals to 0.529 Å.

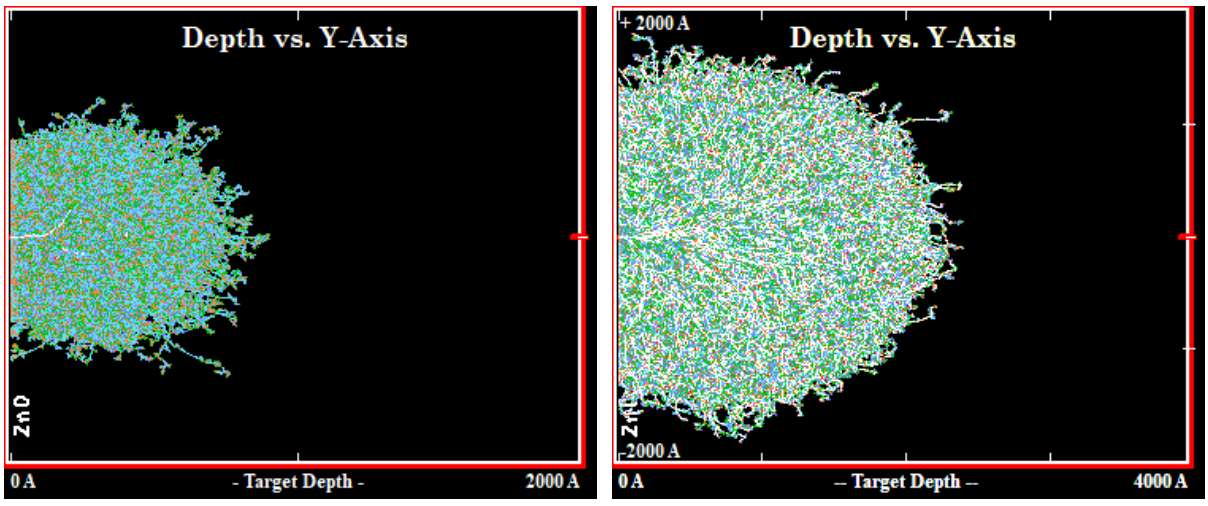
Compared to nuclear stopping power, quantitative description for electronic stopping power is far more complex. Various theories such as the LSS-theory (Lindhard, Scharff and Schiott) [201] for the slow-heavy ions and Bethe-Bloch formula for the swift ions have been proposed to quantify electronic stopping power [202]. Nuclear stopping power results in the movement of target atoms, thus creating imperfections such as point defects or complex defect clusters and small amorphous domains. Accumulation of point defects will distort the crystal lattice. Microstructural damage can be noted as phase transformation, dislocation loops, formation of voids and gas bubbles, volume swelling, etc. A combination of both the nuclear and electronic stopping power effects results in enhanced creation of such defects and damage accumulation.

SRIM-2013 was employed in this study to estimate the depth distribution and collision details of the implanted Ag^+ and C^+ ions.

4.4 SRIM/TRIM simulation of Ag^+ and C^+ ions on ZnO films

4.4.1 Collision cascades

As energetic incident ions sequentially collide with constituent atoms, the events may trigger amorphization, crystallization, phase transformation, crystal damage as well as alterations of the surface morphology of the target material. During elastic nuclear collisions, as the implanted ion strike a target atom, it will transfer a significant portion of its energy to the target nucleus. However, the magnitude of the transferred energy for elements of different atomic masses in the same target substrate differs. The transferred energy depends on the difference between the mass of the incident ion and that of the target atom. Taking into consideration the larger difference in the masses of the Ag^+ ion (106.6 amu) and C^+ ion (12 amu), the bombardment of ZnO lattice with Ag^+ or C^+ will possibly produce different cascades which are categorised into displacement collisions, vacancy production, replacement collisions and interstitial atoms. Figure 4.1 shows typical collision cascades as initiated by individual paths of incident ions and all the knock-ons, until all the energetic particles became stationary. The plots shown in Figure 4.1a and b illustrates a prediction of collision cascades in ZnO as initiated by the implantation of 50 KeV Ag^+ and C^+ ions, respectively at room temperature.



(a) **(b)**

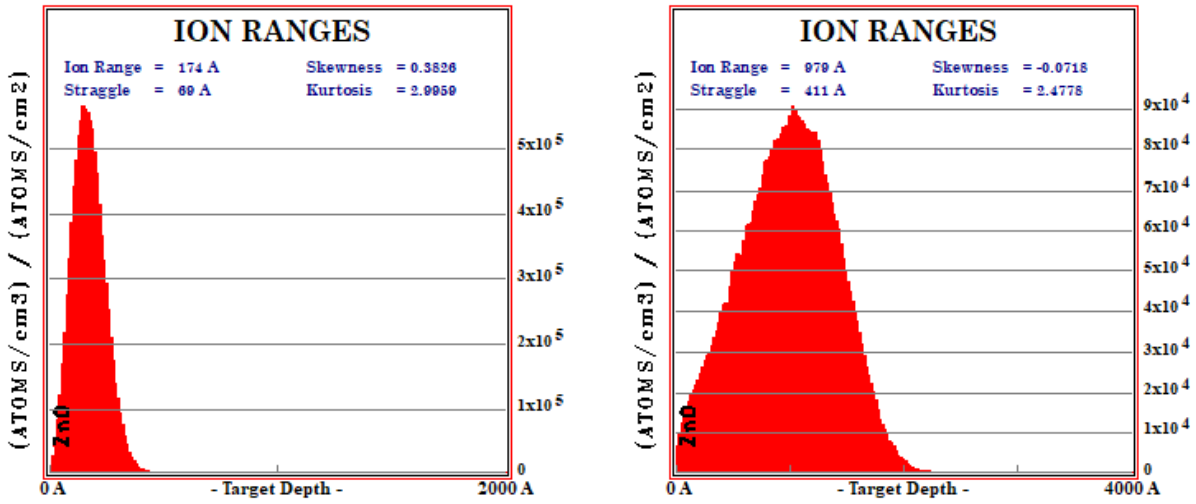
Figure 4.1: XY ion simulations showing collision cascade initiated by 50 KeV (a) Ag^+ and (b) C^+ ions.

4.4.2 Ion distribution

Figure 4.2 are the histograms which show the estimated average depths and distributions of the Ag^+ and C^+ ions in the ZnO matrix. The longitudinal mean projected ranges are noted to be much different for the two dopants. Expectedly the range is less for the heavy ion (Ag^+ = 17.4 nm) and more for the light ion (C^+ = 97.9 nm), indicating that C^+ ions can reach deeper regions than Ag^+ ions when implanted at the same energy. Despite the disparity in the estimated depth range, it is worth to note both the values are less than the thickness of the fabricated ZnO thin film, thus implying that all implanted ions will be deposited within the ZnO layer. The ion distribution plots were used to determine the dopant concentration for each ion using equation 4.6given as;

$$\text{dopant conc.} = (\text{fluence})(\text{peak value of the ion distribution plot}) \qquad (4.6)$$

The calculated values of the dopant concentrations for the Ag^+ and C^+ ions are given in column 2 of Tables 4.1 and 4.2.

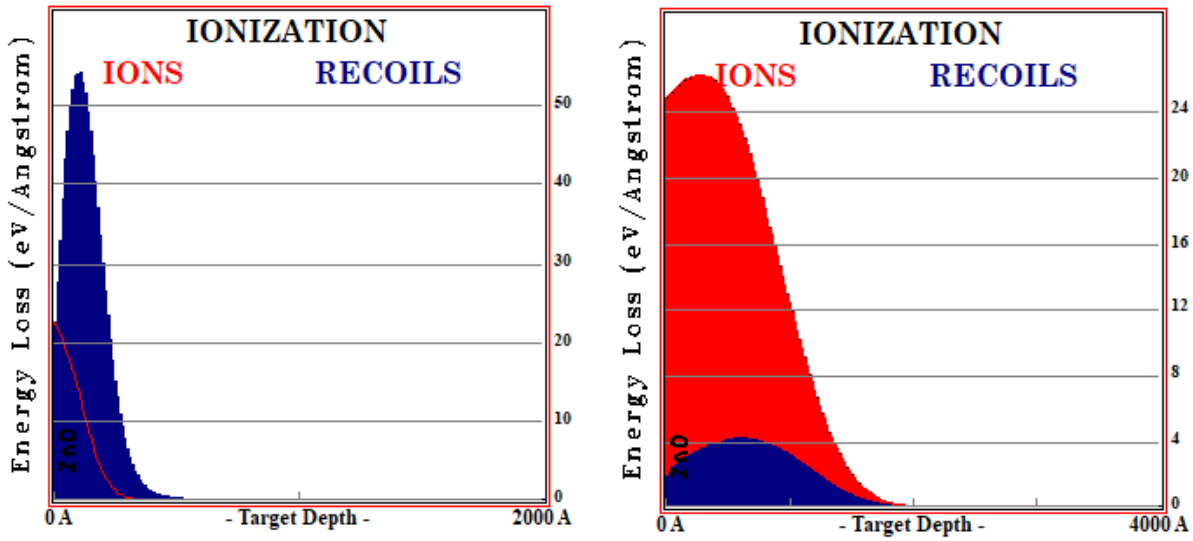


(a) **(b)**

Figure 4. 2: Depths of incident ions in ZnO using incident energy of 50 KeV (a)Ag^+ and (b) C^+.

4.4.3 Energy Loss to Ionization

Figure 4.3 shows a plot of the ionization from the incident Ag^+ and C^+ ions as well as from recoiling target atoms. As ions penetrate into the target material, they instantly interact with target electrons, individually or collectively. As shown, upon Ag^+ ion implantation, the ZnO electrons absorb energy from the recoil atoms compared to the fast-moving ions. A distinct situation is noted upon C^+ ion implantation, as the electrons tend to absorb a much higher fraction of energy from the ions than the recoil atoms.

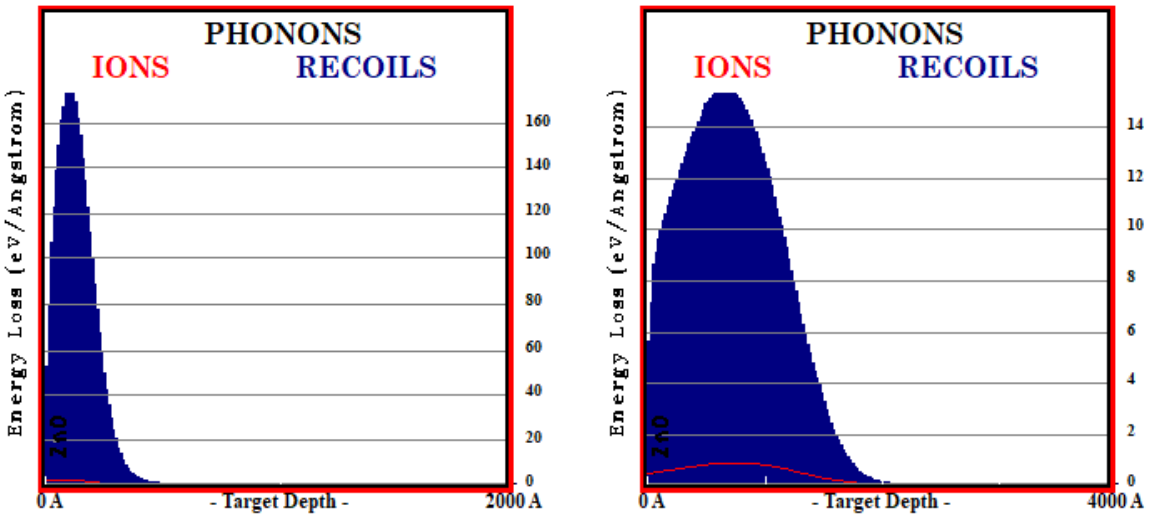


(a) **(b)**

Figure 4.3: Energy loss to target electrons upon 50 KeV Ag^+ and C^+ ion implantation.

4.4.4 Phonon production

Phonons are a collection of oscillations or vibrations of a lattice in a periodic atoms or molecules. Depending on the type of target material, the energy absorbed by the electrons is often dissipated as heat or phonons. Figure 4.4 shows the produced phonons in ZnO as it is implanted with Ag^+ or C^+ ions. As indicated by a very thin red line at the bottom of the plots, very minimum ion loss energy is transferred to phonon for both cases, that is for Ag^+ and C^+ ion implantation, thus implying phonon production is predominantly attributed to the loss of kinetic energy by recoiling target atoms.

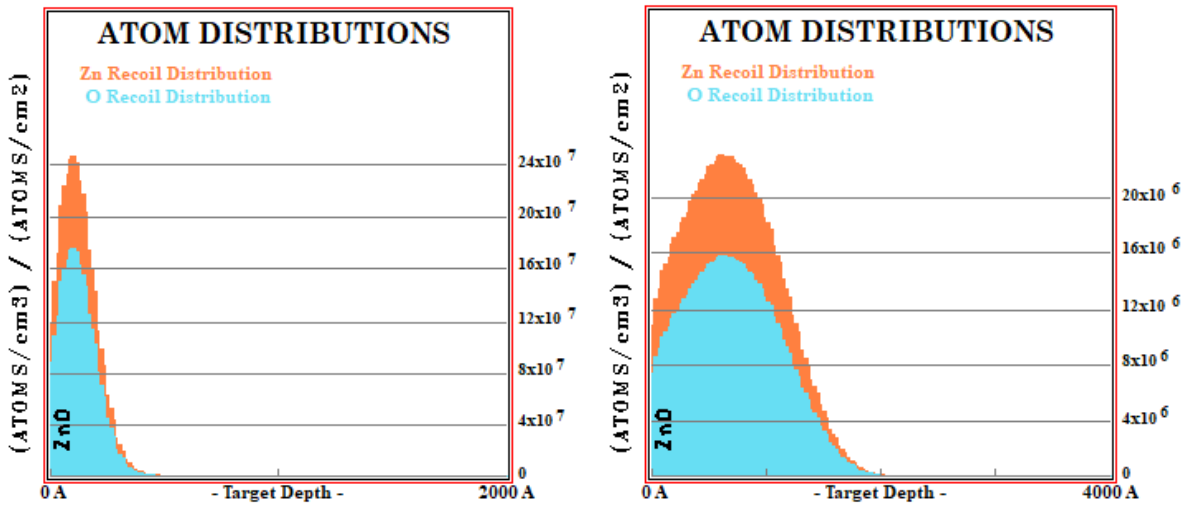


(a) **(b)**

Figure 4.4: The distribution of target phonons in ZnO films as produced by ions and recoils due to (a) Ag^+ and (b) C^+ ion implantation.

4.4.5 Ion-recoil distribution

Figure 4.5 denotes influence of the ion species on the ion-recoil distribution. The figure shows that more zinc atoms than oxygen atoms are knocked out of their lattice sites, thus creating vacancies. However, differences in the peaks are noted, showing that the ion distribution is not based entirely on target element composition but on the implanted ion species as well. The ion-recoil distribution plots are usually analysed to determine the magnitude of energy absorbed by the target material from incident ions.



(a) **(b)**

Figure 4.5: TRIM simulation of ion-recoil distribution of ZnO as induced by (a) Ag^+ and (b) C^+ ion distribution.

4.4.6 Ionization profile

Figure 4.6 shows the simulated ionization profiles of ZnO films subsequent 50 KeV Ag^+ and C^+ ion implantation. Figure 4.6a shows that upon Ag^+ ion implantation, the incident energies lost through electronic ionizations, phonon production and lattice damage are 13.5, 34.0 and 2.50 KeV/ion, respectively. This indicates that a major portion of the energy is lost through phonon production. For simulated C^+ most of the incident energy (30.3 KeV) is lost through electronic ionizations, and the remaining is lost as 18.4 and 1.26 KeV/ion for phonon production and lattice damage, respectively as shown in Figure 4.6b.

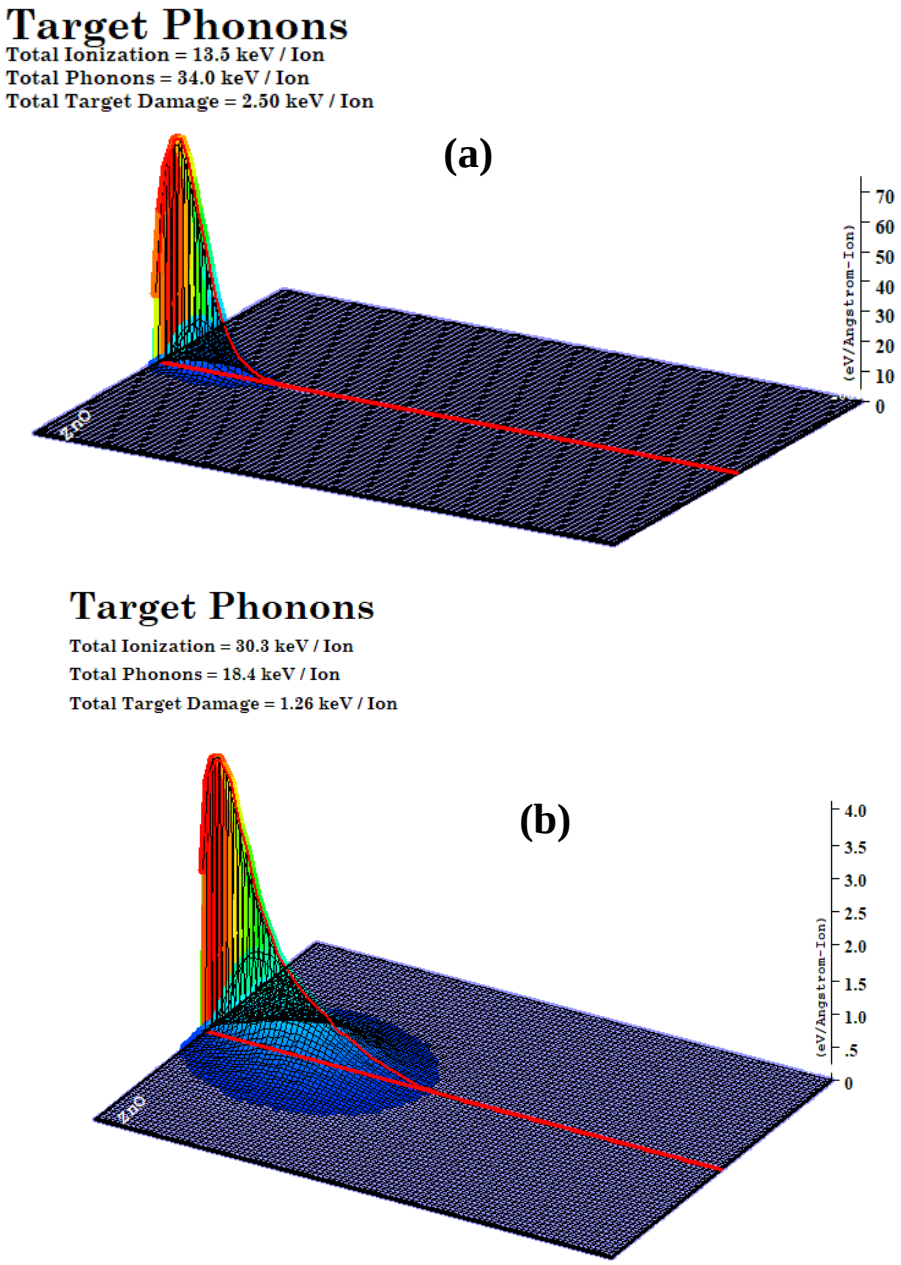


Figure 4.6: Plots of ionization of ZnO target material by (a) Ag^+ and (b) C^+ ions.

4.4.7 Collision events

Figure 4.7 shows the distribution of collision events in the ion implanted ZnO target. Each dopant element is shown separately. Indicated displacements are created by the incident ions and all the recoiling target atoms which possess sufficient energy. These displacements will result in either a target vacancy, or a replacement collision, as shown in the plots. The number of target atom displacements is equivalent to the sum of the created target vacancies and replacement collisions. Upon Ag^+ ions impingement, the ions and recoiling atoms create 859

displacements/ion. A total of 834 of these displacements results in vacancies, and only about 3% results in replacement collisions. The bombardment of ZnO with C^+ ions give 435 displacement ions of which 97 % creates target vacancies and the remaining fraction results in replacement collisions.

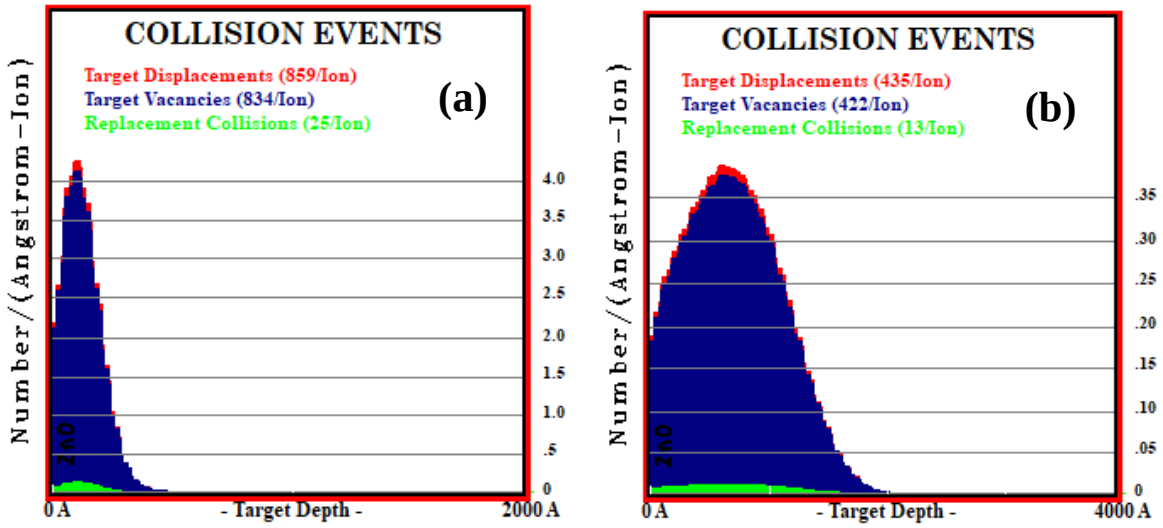


Figure 4.7: SRIM simulation of diferent collision events on ZnO target upon (a) Ag^+ ion and (b) C^+ ion implantantion.

4.4.8 Energy lost to recoil

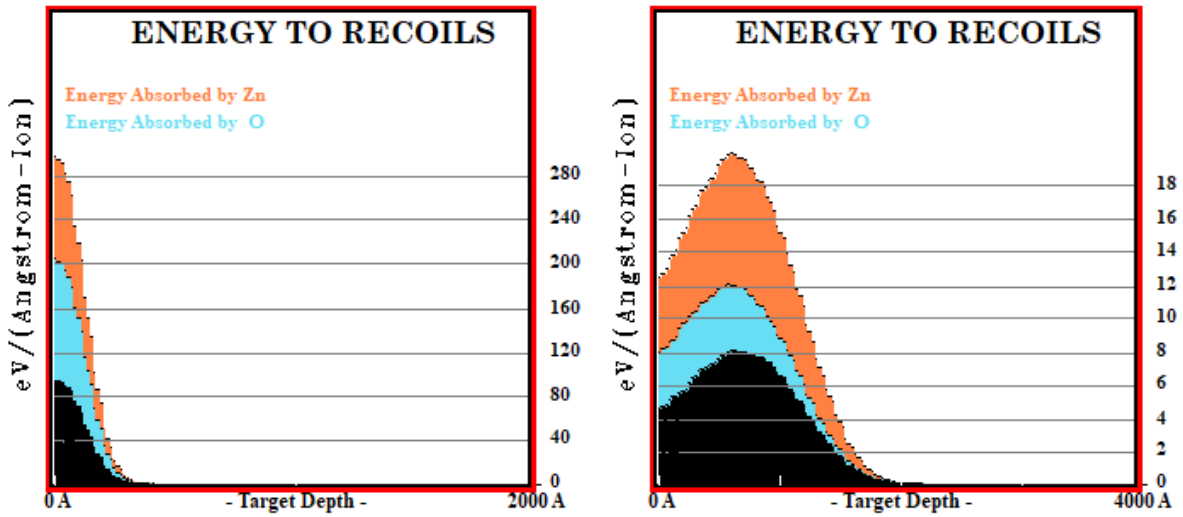
Figure 4.8 shows energy loss of incoming ions due to recoils. It is noted that Zn absorbs more energy from the impinging Ag^+ and C^+ ions as depicted in Figure 4.8a and b, respectively. This can be attributed to its highest atomic mass, thus contributing a larger quantity of energy loss compared to oxygen. Figure 4.8a shows that the energy transferred to target atoms is higher at the surface and decreases as the ions slow down within the ZnO matrix. Furthermore, the energy to recoil atom plots were used to estimate the critical energy density which is derived from the product of the maximum peak value with the implanted fluences. The equation is given as:

$$\text{critical energy density} = (\text{max. peak})(\text{fluence}) \qquad (4.7)$$

The calculated values of the critical energy density are given in column 3 of Table 4.1 and Table 4.2 for Ag^+ and C^+, respectively. The damage caused by implanting the different ion

species, (Ag and C) is compared by determining the displacement per atom (dpa). Equation 4.8 was employed to calculate the dpa. The density of ZnO was taken as 8.301 x 10^{22} atoms/cm^3. The calculated values are presented in Table 4.1 and 4.2.

$$\text{dpa} = \frac{\text{vacancy concentration}}{\text{material density}} \qquad (4.8)$$



(a) **(b)**

Figure 4.8: TRIM plot of energy transferred to the recoil cascades, (a) Ag^+ and (b) C^+ on ZnO substrate.

Table 4.1: Various calculated parameters of Ag^+ ion implantation using SRIM/TRIM simulation.

Ion fluence (x 10^{15} ions/cm^2)	**Dopant conc. (x10^{20} atoms/cm^3)**	**Vacancy conc. (x 10^{23}vac./cm^3)**	**Critical energy density (x10^{25}eV/cm^3)**	**Displacement per atom (dpa)**
1	6.0	4.10	2.0	4.94
2	12.0	8.20	6.0	9.88
3	18.0	12.3	9.0	14.8
10	60.0	41.0	30	49.4
30	180.0	123.0	90	148.2

Table 4.2: Various calculated parameters of C^+ ion implantation using SRIM/TRIM simulation.

Ion fluence (x 10^{15} ions/cm^2)	**Dopant conc. (x 10^{19} atoms/cm^3)**	**Vacancy conc. (x 10^{22} vac./cm^3)**	**Critical energy density (x10^{28} eV/cm^3)**	**Displacement per atom (dpa)**
1	9.0	3.75	2.0	0.45
2	18.0	7.50	4.0	0.90
3	27.0	11.25	6.0	1.36
10	90.0	37.50	20.0	4.52
30	270.0	112.5	60.0	13.6

CHAPTER 5: RESULTS AND DISCUSSION I- Optimization of the chemical deposition (CBD) method

The results presented in this chapter have been published in the article; **K. Lefatshe**, P. Dube, D. Sebuso, M. Madhuku, C. Muiva, "Optical dispersion analysis of template assisted 1D-ZnO nanorods for optoelectronic applications" Ceramics International 47 (6) (2021), 7407-7415.

https://doi.org/10.1016/j.ceramint.2020.11.079

5.1 Overview

Morphology and size play crucial influential roles in semiconductor nanotechnology. This chapter discusses results from the controlled fabrication of ZnO nanosized rods through the use of capping agents. Two different surfactants; ethylene glycol and polyethylene glycol were used. Another set of nanorods were fabricated in a surfactant free environment. SF-ZNR, EG-ZNR and PEG-ZNR are used to denote surfactant free grown ZnO, ethylene glycol surfactant assisted ZnO, and polyethylene glycol surfactant assisted ZnO, respectively. Freestanding, elongated one-dimensional (1D) ZnO nanorods were successfully synthesised in a simple two-step process. The surfactants were found to yield considerable effect on both the morphology and crystallinity of the nanorods. All the synthesised ZnO films portrayed a transmittance of more than 50 % in the visible range. A distinct absorption peak is also noted in the UV region, at 380 nm. Various optical parameters were calculated and their analysis indicated the presence of surfactants during nanostructure synthesis can be adopted to modify the optical response properties such as the band gap, Urbach energy and dielectric constants of ZnO nanorods, to augment their efficiency for optoelectronic devices.

5.2 Microstructural analysis

5.2.1 X-ray diffraction (XRD) Analysis

X-ray diffractograms of the synthesised ZnO films are depicted in Figure 5.1. The recorded profiles are indexed to a hexagonal wurtzite ZnO, similar to that reported on database

COD2013 2300115. No impurity or secondary peaks were observed. The (002) peak was the most dominant peak across all the grown thin films, indicating a strong preferred orientation along the c-axis. The average crystallite size (D_s), calculated from the Scherrer equation for each sample is presented in Table 5.1.

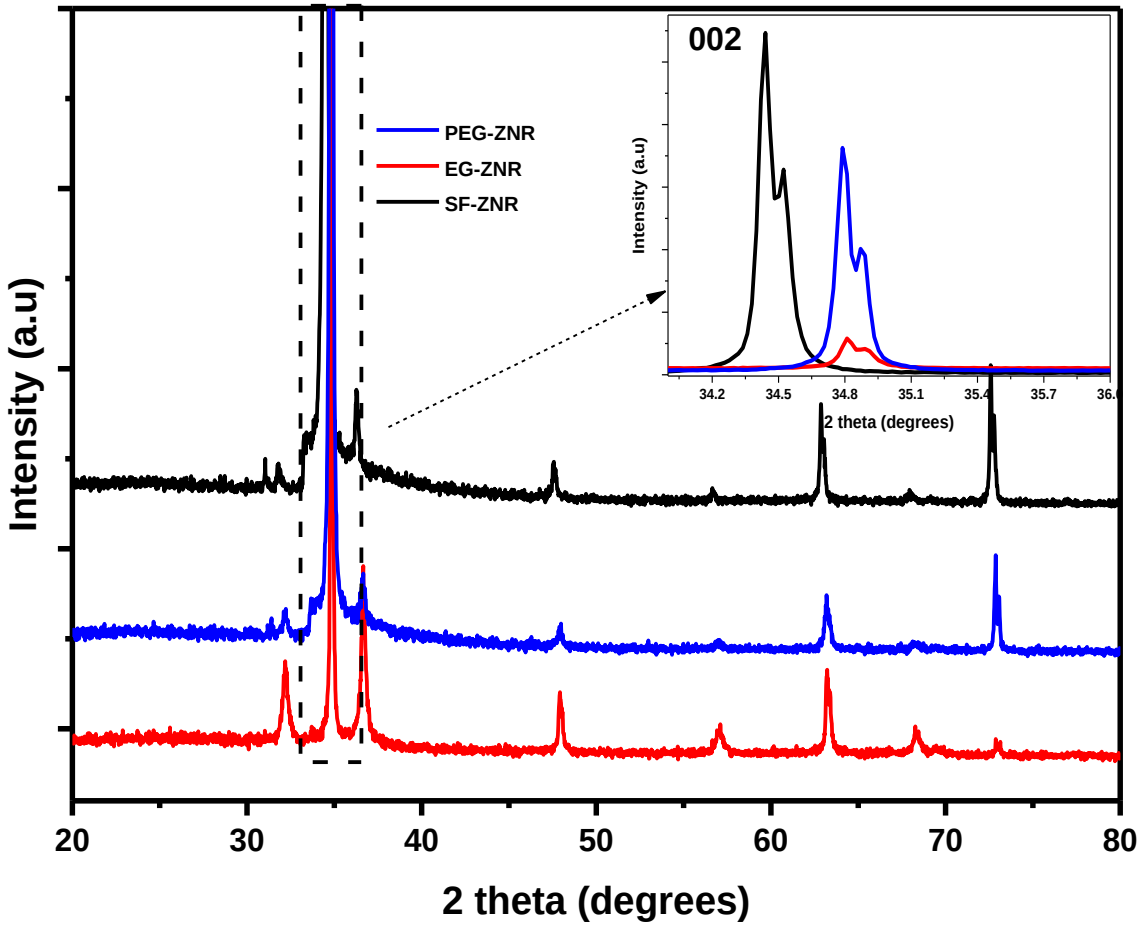


Figure 5.1: XRD Patterns of surfactant free grown (SF-ZNR ZnO), ethylene glycol surfactant assisted ZnO (EG-ZNR) and polyethylene glycol surfactant assisted ZnO (PEG-ZNR).

It was observed that the surfactant free (SF) grown ZnO nanorod film had the highest crystallite size. However; introducing ethylene glycol (EG) and polyethylene glycol (PEG) during ZnO film synthesis resulted in increased peak broadening and consequently an enormous decrease in the crystallite sizes of the nanorods, in agreement with the Scherrer equation. A possible explanation for this behaviour is that during the growth process, the molecules of the capping agents encapsulate the Zn^{2+} forming complex ions [203]. This nucleation process lowered the surface tension of the interface, resulting in decreased agglomeration which correlatively influences the reduction of particle size. In addition, it was observed that PEG and EG

surfactants affected the growth of the nanorods in divergent ways due to different binding characteristics [204]. Table 5.1 shows a disparity of calculated structural parameters; the crystallite size (D_s), the interplanar d-spacing, lattice parameters (a_p and c_p) and the lattice constant c_p/a_p. The calculated values of lattice constants are in agreement with those previously reported in literature, with the least values recorded for the ethylene grown ZnO [8, 26, 48, 70].

Table 5.1: Calculated structural parameters of ZnO films from XRD analysis.

Sample	**D_s (nm)**	**d-spacing (nm)**	**a_p (nm)**	**c_p (nm)**	**c_p/a_p**
SF- ZNR	70	0.260270	0.324940	5.20540	1.60196
EG- ZNR	43	0.257450	0.321900	5.14890	1.59953
PEG-ZNR	48	0.258860	0.323420	5.17720	1.60077

5.2.2 Raman analysis

The wurtzite structure of the films was further confirmed through Raman spectroscopic analysis. All the observed vibrational modes were assigned on the basis of the group theory which proposes eight sets of optical phonons of which only six are Raman active. The same peaks were observed across all the films. The same observations have been reported in literature [205, 206]. The 437 cm^{-1} characteristic peak, accounting for the E_2 high mode (E_{2high}) was observed as the most pronounced peak in all samples. The surfactant grown nanorods (PEG-ZNR and EG-ZNR) exhibited enhanced peaks with relatively strong intensities compared to the surfactant free (SF) grown nanorods. Other eigenmodes ascribed to the absorption band of the defects were noted at wavenumbers ~245 and 580 cm^{-1}. The appearance of these two modes confirms the presence of intrinsic defects in pure ZnO nanorods. In comparison to the SF grown ZnO, EG and PEG-ZnO showed a distinct spectral blue shift, contributed by phonon localization associated with intrinsic defects and spatial confinement within the grain boundaries due to oriented growth. Frohlich interactions contribute to the electron-phonon coupling of the ZnO nanorods [207]. Surfactant assisted ZnO showed more oxygen vacancies compared to the SF-ZNR, as noted by the stronger E_1 (LO) peaks.

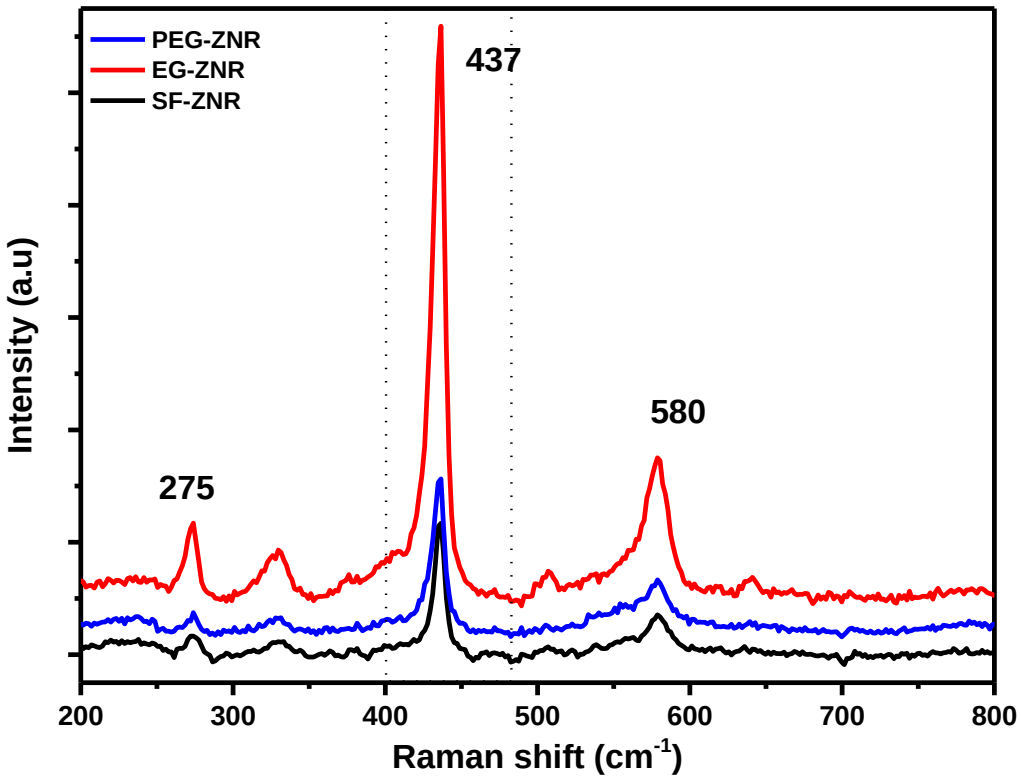


Figure 5.2: Raman spectra of surfactant free grown ZnO nanorods (SF-ZNR ZnO), ethylene glycol surfactant assisted ZnO nanorods (EG-ZNR) and polyethylene glycol surfactant assisted ZnO nanorods (PEG-ZNR).

5.3 Morphological Studies

The morphology of the grown nanorods was studied through the use of the field emission scanning electron microscope (FESEM). The observed micrographs showed distinct elongated 1D nanorods across all three samples as depicted in Figure 5.3, however, some variances were observed. The SF grown nanorods have more spherical end elongated rods of non-uniform diameters. It was observed that EG grown ZnO showed the least agglomeration, and also it is worth to note that the nanorods have screw-like ends. The PEG grown ZnO nanorods resulted in more agglomeration than the SF-ZnO. In addition, a mixture of screw-like and spherical ended nanorods are observed in the pictogram of PEG ZnO, (Figure 5.3 (C)). The diameters of the rods were noted to vary for the synthesised samples, which is attributed to the role of the growth environment.

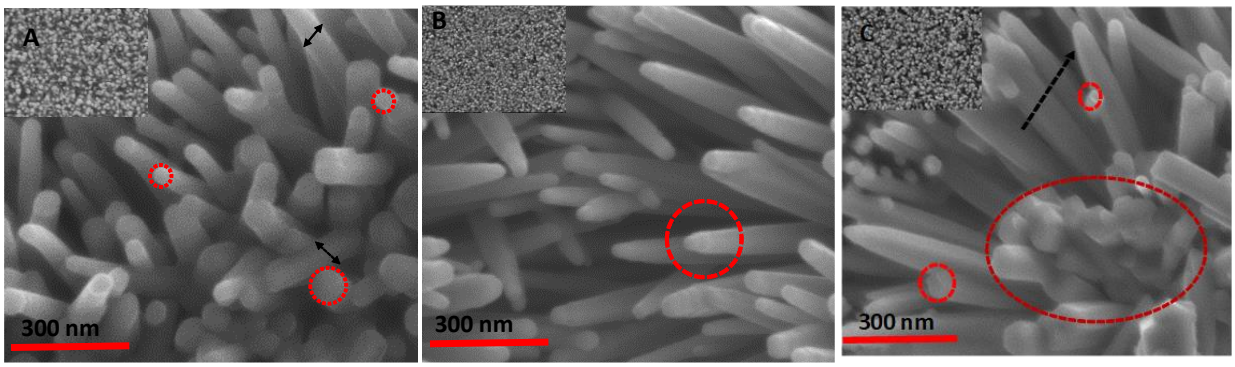


Figure 5.3: FESEM images of elongated ZnO nanorods prepared in surfactant free (A), EG (B) and PEG (C) templates.

5.4 Optical studies

5.4.1 X-ray photoelectron spectroscopy (XPS) analysis

The elemental surface analysis and chemical states identification of the synthesized ZnO NRs were examined by XPS studies. In agreement with the XRD and Raman plots, XPS showed high intensities of only the Zn and O peaks, an emphasis on the purity of the samples. The plots of intensity against binding energies are depicted in Figure 5.4. Peaks at binding energies of 1044.65, 1021.56 eV were assigned to Zn $2P_{1/2}$, and $Zn2P_{3/2}$, respectively. The oxidation state of ZnO is +2. This is elucidated by spin-orbit splitting of the core level Zn 2p peak resulting in Zn2p ½ and Zn2p3/2 peaks with an energy of approximately 23 eV, which corroborates with literature [208]. Some variation in the binding energies was noted in both the Zn and O1s narrow scans. From the chemical states chart, it is evident that the most stoichiometric film is EG-ZNR. Other than enhanced intensities, ZnO nanorods grown in ethylene glycol (EG) showed peak shifting to augmented binding energies indicating a higher positive oxidation state. This shifting is attributed to the additional Coulomb interaction of the ion core and the emitted electron, as well as possibly the variation of the texture coefficients between the different surfactants [208, 209].

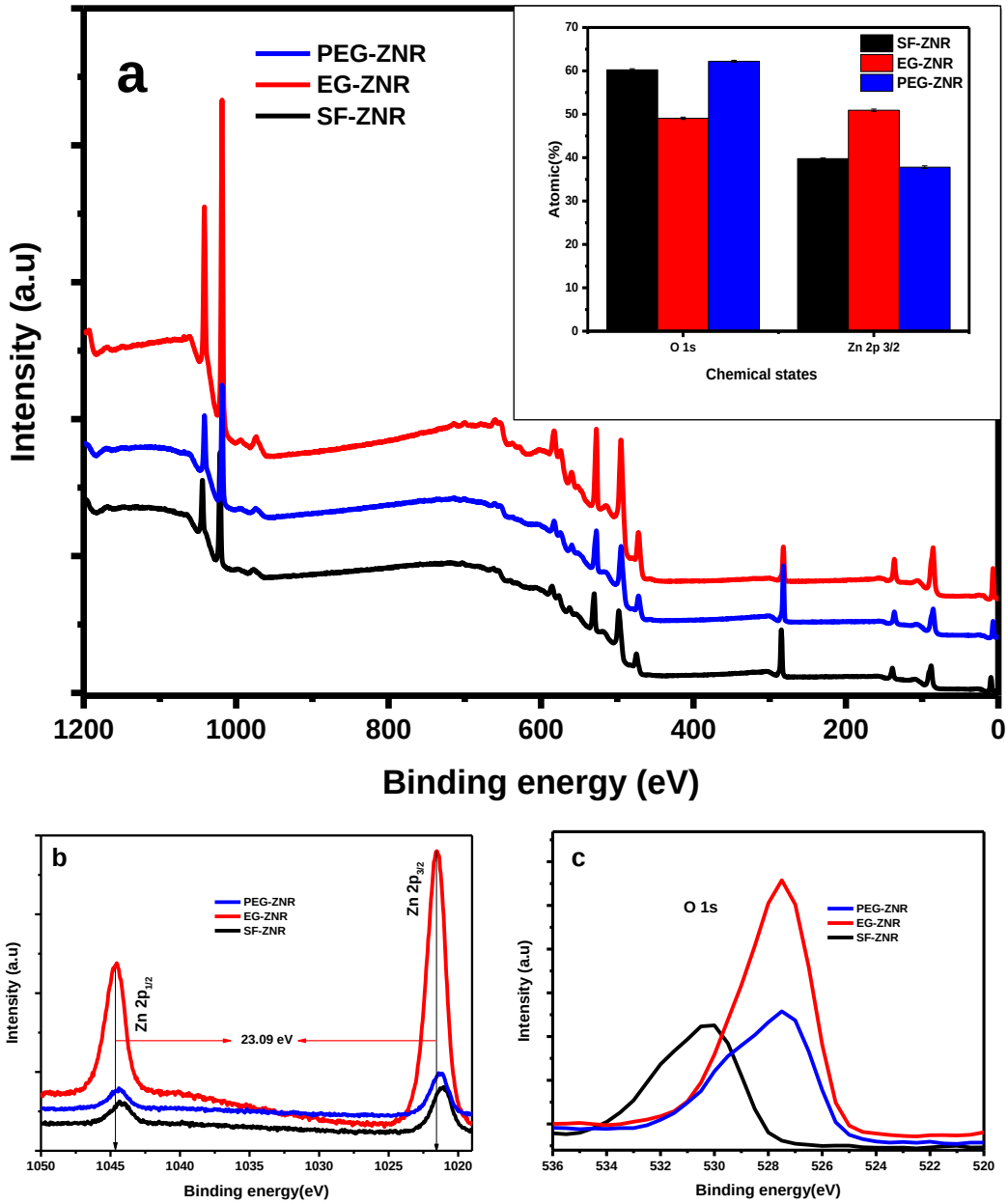


Figure 5.4: (a) XPS wide spectra of SF-ZNR, EG-ZNR and PEG-ZNR. Narrow XPS spectra of (b) 2p core shell and (c) O1s. The insert on (a) is a bar chart showing the elemental atomic percentages of Zn and O in all the three samples.

5.4.2 Transmittance

The optical analysis of the ZnO nanostructures was performed in the spectral range 300 - 800 nm. Figure 5.5 shows the transmittance spectra of the ZnO nanostructured films exhibiting excellent and high transmittance of light in the visible region. The observed sharp absorption edge for the nanostructures is in the range 380-400 nm. The intrinsic absorption energy gap of ZnO occurs in this range; a consequence of inter-band electron transitions in the film and hence ZnO nanostructures have a direct band gap energy [210, 211].

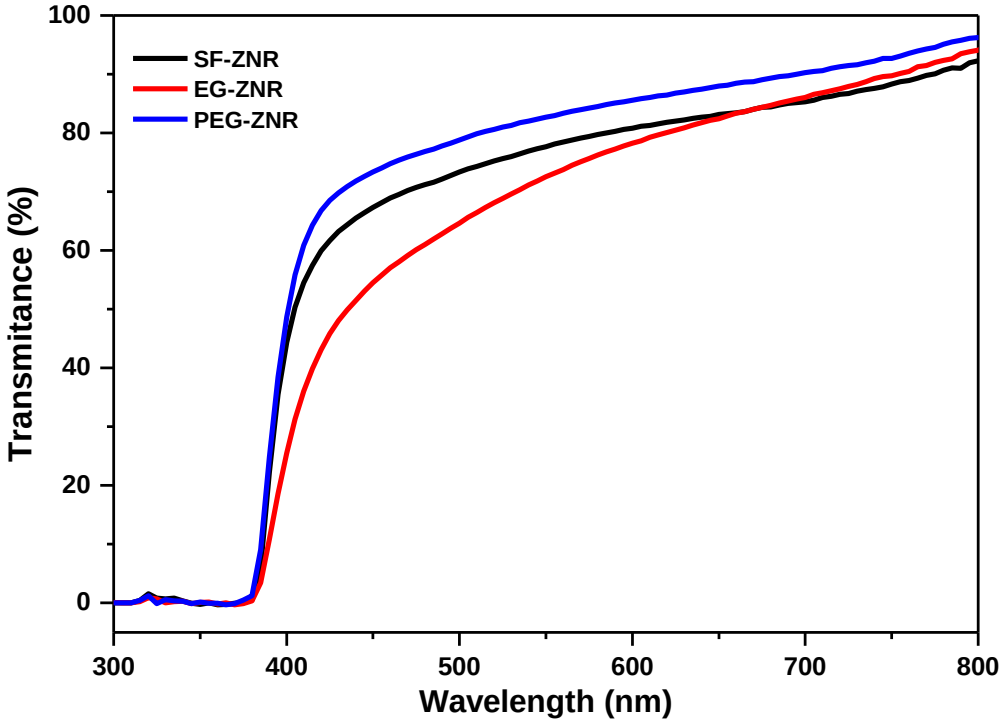


Figure 5.5: The transmittance spectra of the SF-ZNR, EG-ZNR and PEG-ZNR.

It is worth noting that the absorption edge is red shifted to higher wavelengths from the bulk (< 380 nm). The observed red shift in thin films could be attributed to quantum size effects or quantum confinements of the ZnO nanoparticles and residual strain inherent in hosted thin films [211]. Significant differences in the crystallite size as well as the morphologies as observed in the XRD data and the SEM micrographs, respectively, could well be attributed to these variations. The observed absorption shift from the bulk value of ZnO could be attributed to size effects as particle sizes change to nanosize [212].

5.4.3 Optical band gap (E_g)

Diverse methods explained in chapter 3 (section 3.4.9) were adopted to study the optical band gap of the pristine samples. The Tauc plot of $(\alpha hv)^2$ vs hv to determine the optical band gap (E_g) is shown in Figure 5.6. The curve was extrapolated to the hv axis to obtain the E_g of the ZnO nanostructures. The E_g values from this method are denoted as $E_{g(Tauc)}$ and are listed in Table 5.2.

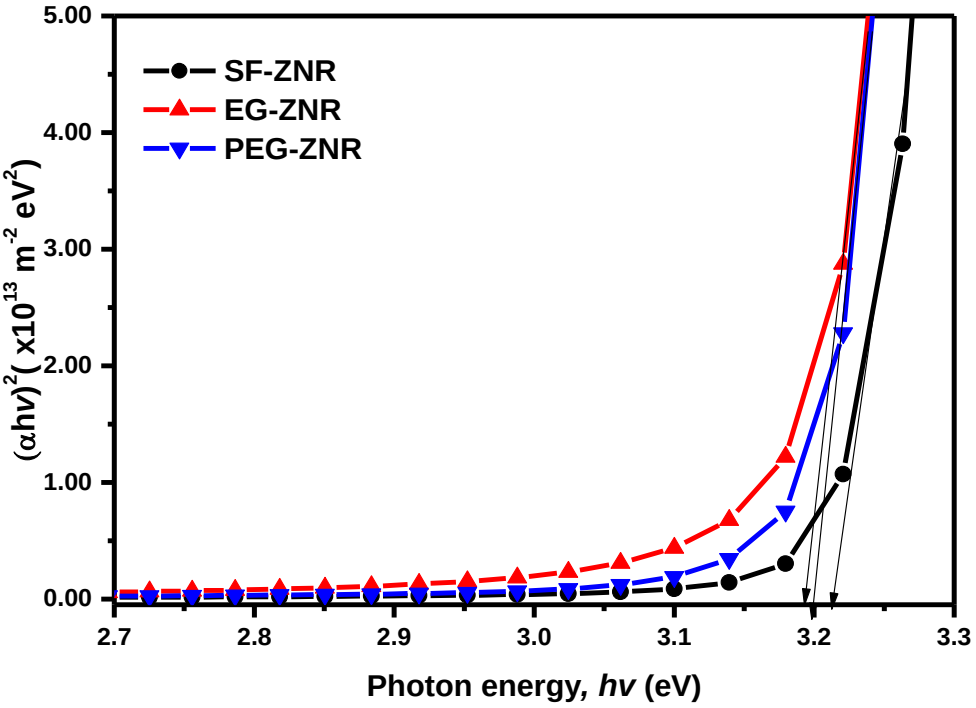


Figure 5.6: Variation of $(\alpha hv)^2$ with photon energy, hv, for SF-ZNR, EG-ZNR and PEG-ZNR.

Figure 5.7 shows the derivative spectroscopy method ($dT/d\lambda$), which was also used to estimate the band gap of ZnO nanostructures [182]. The inset shows a zoomed view of the full width at half maximum (FWHM) of the peak derivative, with the dotted line drawn to the x-axis showing the corresponding cut off wavelength (λ_{max}). The obtained λ_{max} was used to calculate the bandgap energy values using equation 3.35 (subsection 3.4.9). The values deduced from the derivative spectroscopy method are denoted as $E_{g(ds)}$ and are listed in Table 5.2.

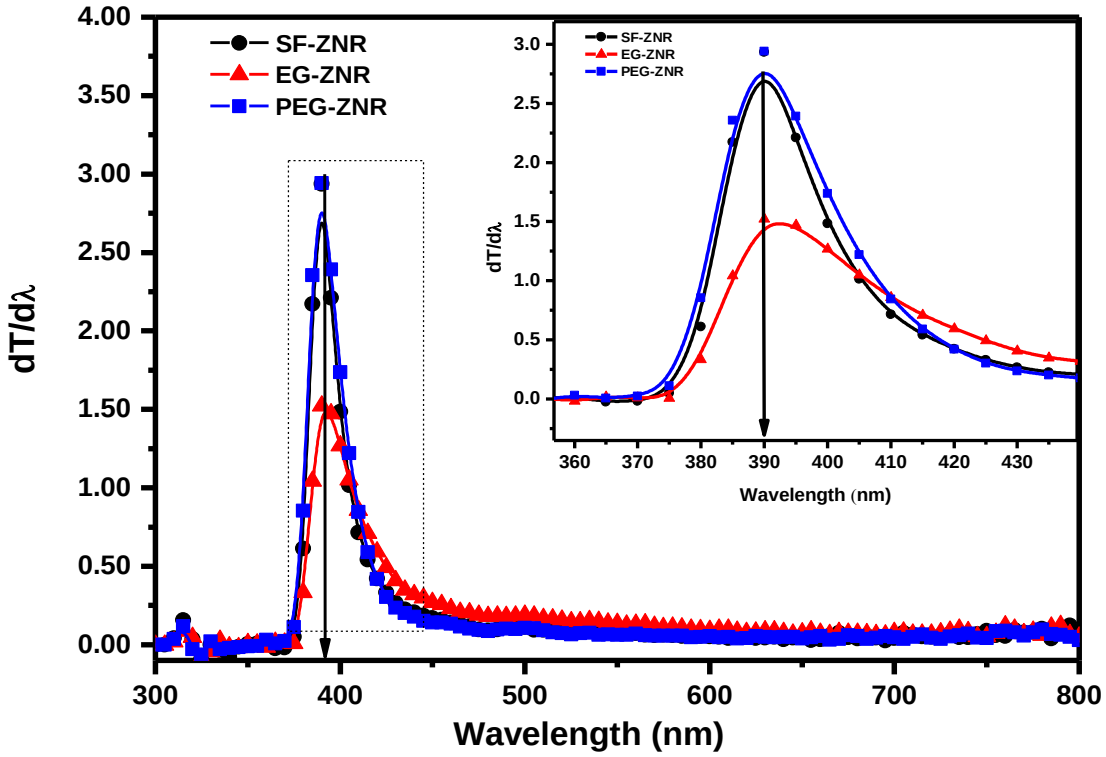


Figure 5.7: The derivative spectroscopy plot of SF-ZNR, EG-ZNR and PEG-ZNR nanorods.

Furthermore, the optical band gap was deduced through the $hv(2nk)^{1/2}$ vs photon energy (hv) curve, depicted in Figure 5.8. As expected, this plot clearly exhibits the linear, exponential and tail regions. The E_g can be deduced by extrapolating the region that is linear to the hv axis, as k_x approaches zero. The values of E_g obtained from this method were denoted as $E_{g(nk)}$ and are listed in Table 5.2.

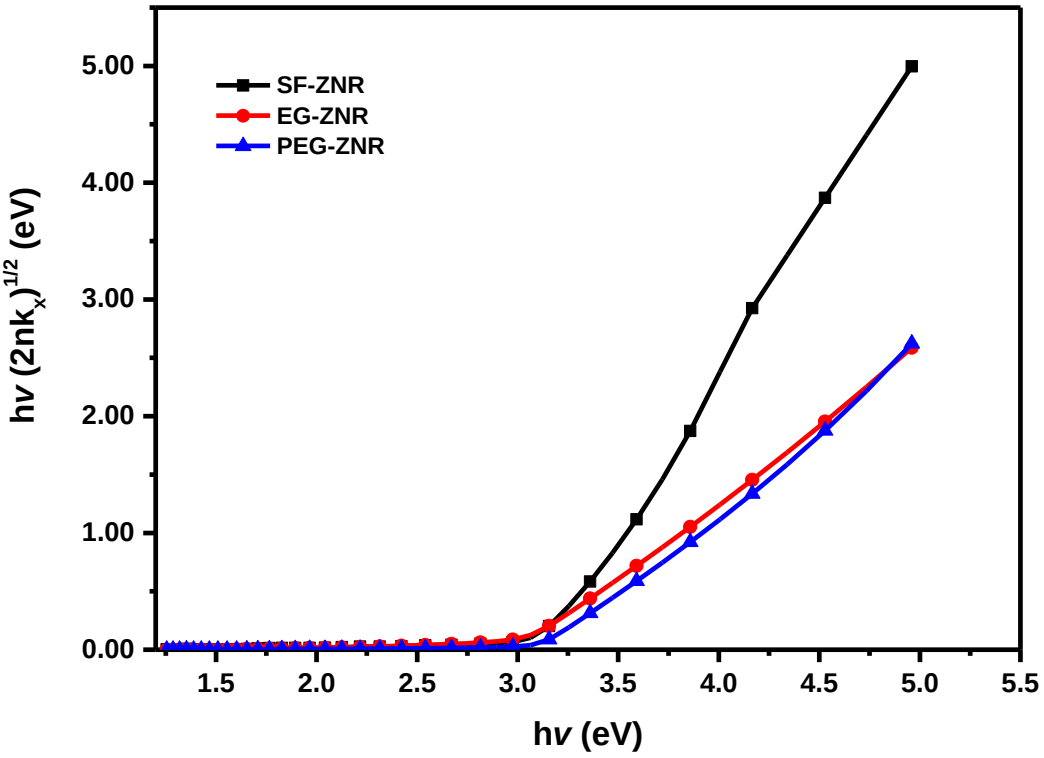


Figure 5.8: Plot of $h\nu(2nk_x)^{1/2}$ vs hv for ZnO nanorods.

There was an observed variation in the calculated E_g values, all lower than the expected value of the bulk ZnO of 3.31 eV [213, 214]. The lower values observed could be due to the use of surfactants that are non-ionic. These surfactants have the ability to reduce particle interfacial and surface tension; as a consequence, there is an alteration in the size of particles hence a red shift in the band edge. The band energy width can be estimated using equation 5.1 [181]:

$$E_n = E_b + \frac{h^2}{8R_p^2}\left(\frac{1}{m_e^*} + \frac{1}{m_h^*}\right) - \frac{1.8e^2}{4\pi\varepsilon\varepsilon_o r}, \qquad (5.1)$$

where E_n is the band gap width of the nanosized material in (eV), E_b is the band gap width of the bulk ZnO in (eV), R_p is the particle radius, h is the plank's constant, m_h* is the hole effective mass, m_e* is the electron effective mass, e is the electronic charge, ε_o is the dielectric permittivity of free space. As R_p decreases a significant value is loaded to the bulk value E_b and the value of E_n increases. For the present case E_n instead decreased relative to the bulk value pointing to microstructural defects, residual stress and strain as the cause of the band gap reduction. The peak shift in the predominant XRD peaks (002) is evidence of stress and strain in the films which is also correlated with the blue shift in the absorption edge for the PEG-ZNR and EG-ZNR relative to the SF-ZNR.

5.4.4 Urbach energies

The Urbach energy, E_u was deduced from the plot of (Ln α) vs hv in Figure 5.9, the linear part of the plot is fitted, and the reciprocal of the slope gives the E_u. The values of E_u for the ZnO nanostructures are listed in Table 5.2. As shown in Table 5.2, the E_u values are lower for the EG-ZnO and PEG-ZnO samples as compared to the SF-ZnO. This was also observed from the reduced crystallite growth, shape effects and also peak shifts in the XRD data. The observed behavior corresponds to changes in optical transition states (occupation of unoccupied states in the conduction band) [185].

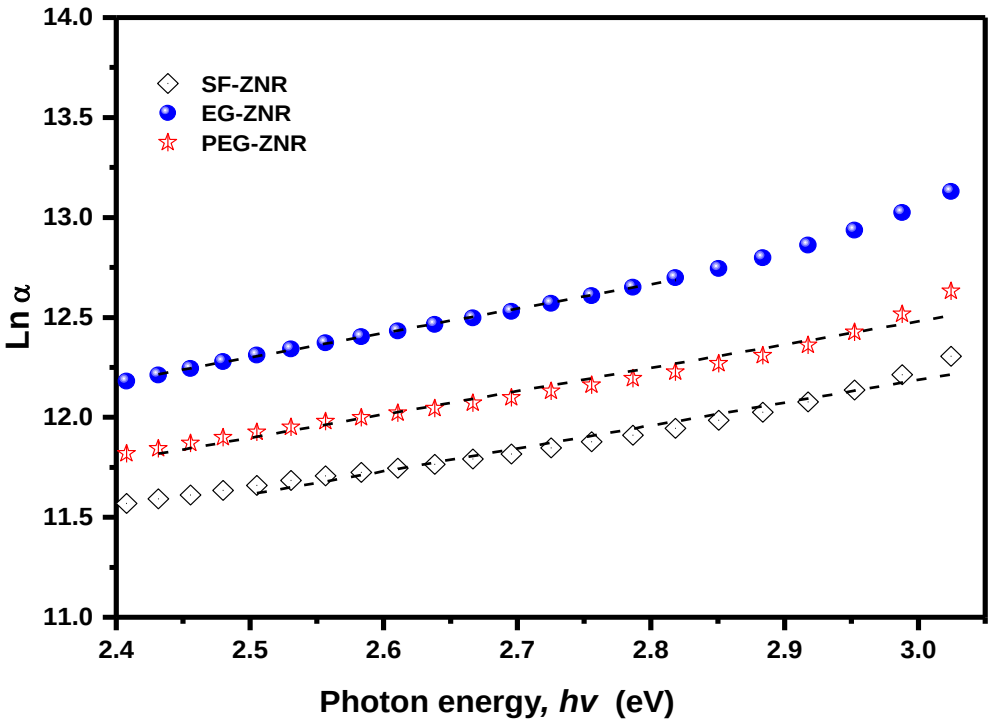


Figure 5.9: Variation of Ln α with the photon energy to determine the Urbach energies of the SF-ZNR, EG-ZNR and PEG-ZNR nanostructures. Linear fitted with Reg ≈1.

5.4.5 Spectral dispersion parameters

5.4.5.1 Refractive index (n)

The model used to evaluate the optical constants (n and k_x) was based on the physical thickness of the ZnO nanostructured films, with a presumption of a ternary layered layer model; the

substrate, the thin film and the incident medium. In the present case, the substrate was borosilicate glass, and the incident medium was air. Figure 5.10 shows the dispersion of refraction index, n, of ZnO nanostructures against the wavelength. The refractive index follows the normal dispersion of a semiconductor. The ZnO nanostructured thin films exhibit higher values of n at 400 nm < λ. However, there was an observed gradual decrease of n in the 400 – 700 nm range. The low values of n recorded could be attributed to lower packing fraction for the ZnO nanostructures during chemical bath deposition [215].

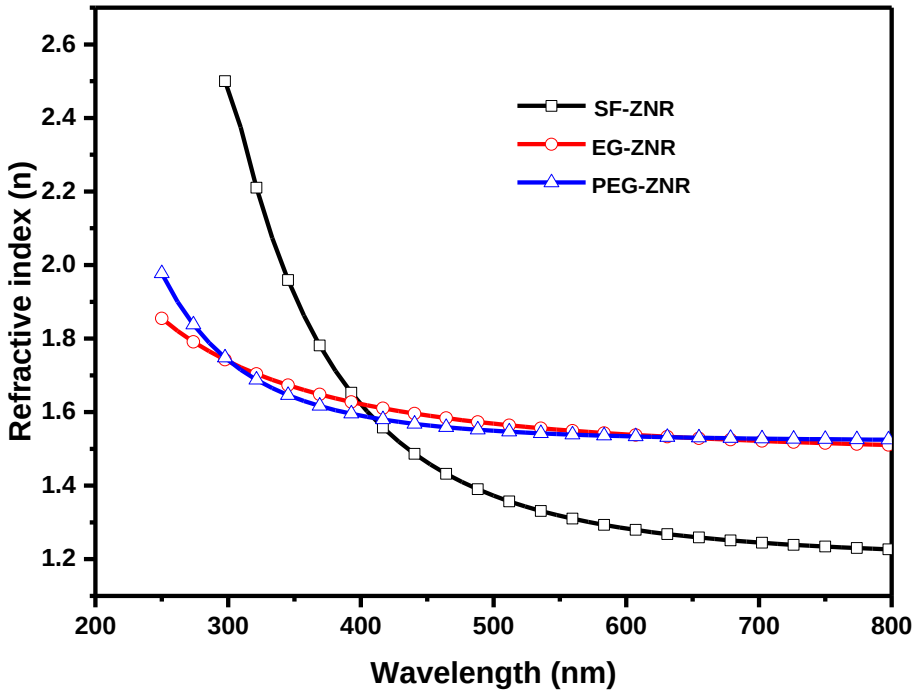


Figure 5.10: The refractive index of SF-ZNR, EG-ZNR and PEG-ZNR as a function of the wavelength.

5.4.5.2 Extinction coefficient (k_x)

The extinction coefficient (k_x) was evaluated over the spectral range of 200 - 800 nm. Figure 5.11 shows a plot of the extinction coefficient of the ZnO nanostructures as a function of wavelength. The k_x values of all samples show a decreasing trend as wavelength increases, the values almost reaching zero in the measured transparency region where λ is greater than the

absorption edge (≈ 400 nm). As expected, k_x is high in the absorption region where λ is less than the absorption edge [216].

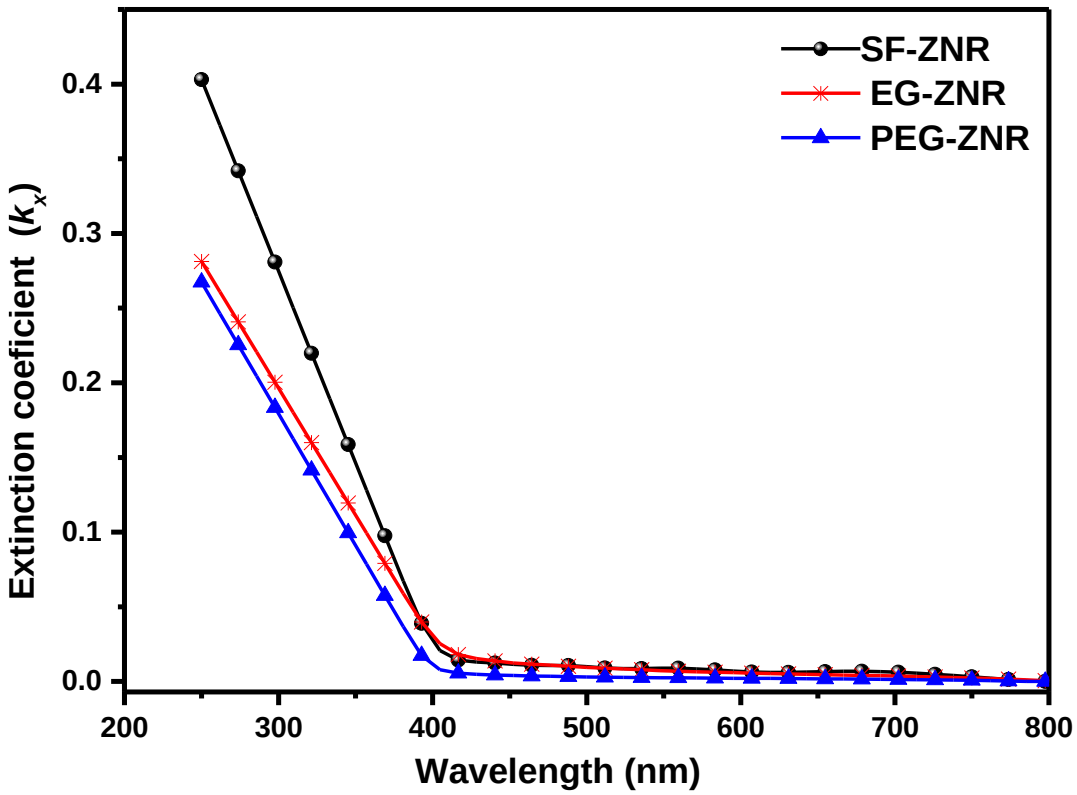


Figure 5.11: The extinction coefficient of SF-ZNR, EG-ZNR and PEG-ZNR as a function of the wavelength.

5.4.5.3 Wemple-Didomenico (WDD) single oscillator dispersion energies

To study the oscillator parameters, values of E_o (the effective oscillator energy) and E_d (quantity of dispersion energy), were evaluated using the Wemple-Didomenico (WDD) effective single oscillator model [186]. A thorough description of this model is presented in section 3.4.9. The plot of $(n^2-1)^{-1}$ vs $(hv)^2$ shown in Figure 5.12 was used to determine these two parameters. With the aid of equation 3.41, the intercept (E_o/E_d) and the gradient ($1/E_oE_d$) were solved simultaneously to give the required quantities E_o and E_d. The calculated values for E_o, E_d and $E_{g(WDD)}$ are listed in Table 5.2. With the WDD model as a basis, Tanaka [217] put forward a direct relation between the band gap energy (E_g) of a material and the effective oscillator energy (E_o), i.e., $E_o \approx 2E_g$. Values of the optical band gap, E_g obtained from this

relation are also presented in Table 5.2 and denoted as $E_{g(WDD)}$. The obtained E_g values from this model follow the same trend as those obtained through other methods used. An insignificant difference is observed for values of the diverse methods, which may be attributed to the relative approximations for each model.

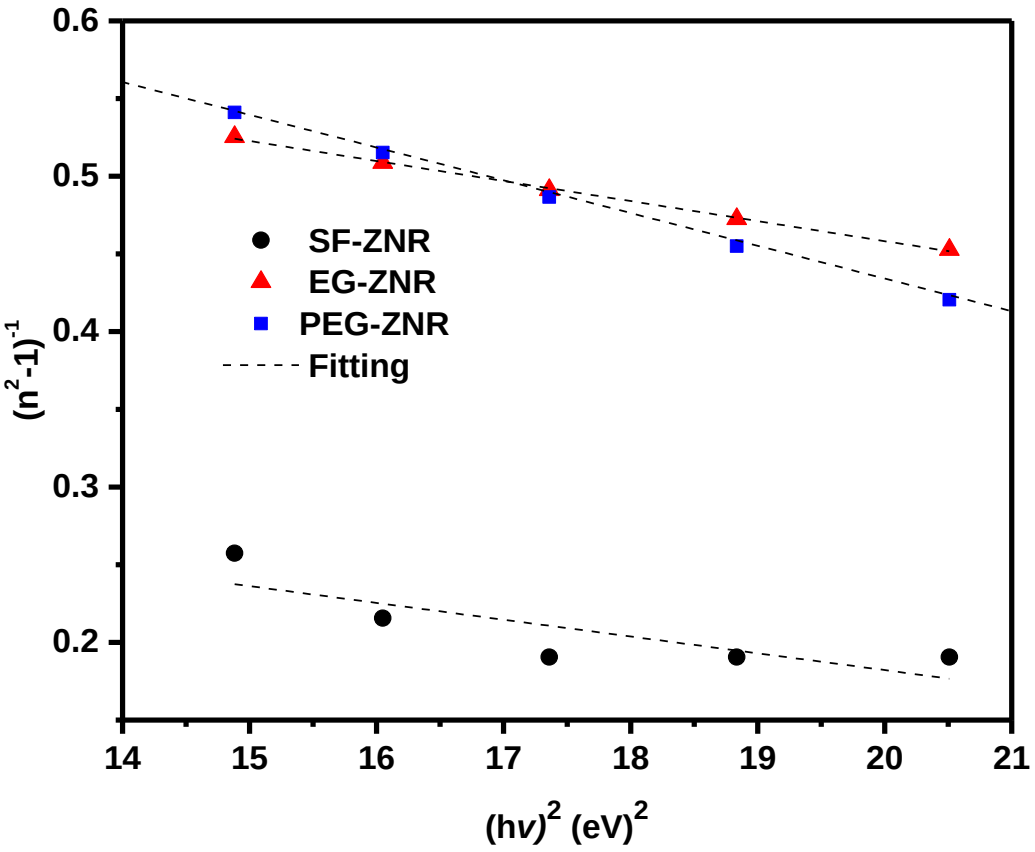


Figure 5.12: Plot of the refractive index factor (WDD), $(n^2-1)^{-1}$ vs hv^2 for ZnO nanostructured films. Linear fits with Reg. ≈ 0.8.

Table 5.2: Calculated energy gaps of the ZnO nanostructures using Tauc $[E_{g(Tauc)}]$, Derivative $[E_{g(ds)}]$, WDD $[E_{g(WDD)}]$ and 2nk $[E_{g(nk)}]$ models, single oscillator parameters (E_d and E_o) and Urbach energies $[E_u]$ of the samples.

Sample	$\mathbf{E_{g(Tauc)}}$ (eV)	$\mathbf{E_{g(ds)}}$ (eV)	$\mathbf{E_{g(WDD)}}$ (eV)	$\mathbf{E_{g(nk)}}$ (eV)	$\mathbf{E_d}$ (eV)	$\mathbf{E_o}$ (eV)	$\mathbf{E_u}$ (meV)
SF-ZNR	3.21	3.18	3.16	3.14	15.81	6.32	0.91
EG-ZNR	3.19	3.16	3.18	3.17	8.35	6.65	0.67
PEG-ZNR	3.20	3.18	3.19	3.19	7.45	6.38	0.83

5.4.6 Dielectric parameters

Figure 5.13 depicts a linear relationship of n^2 vs λ^2. The parameters ε_L and N/M*, were deduced from the vertical intercept and the slope, respectively. These values have been listed in Table 5.3. The calculated values N/M* for the ZnO nanostructures were found to be higher in the surfactant grown films, with the highest value recorded PEG-ZNR. The discrepancies in the calculated values show that the surfactants can be used to modify the dielectric constants.

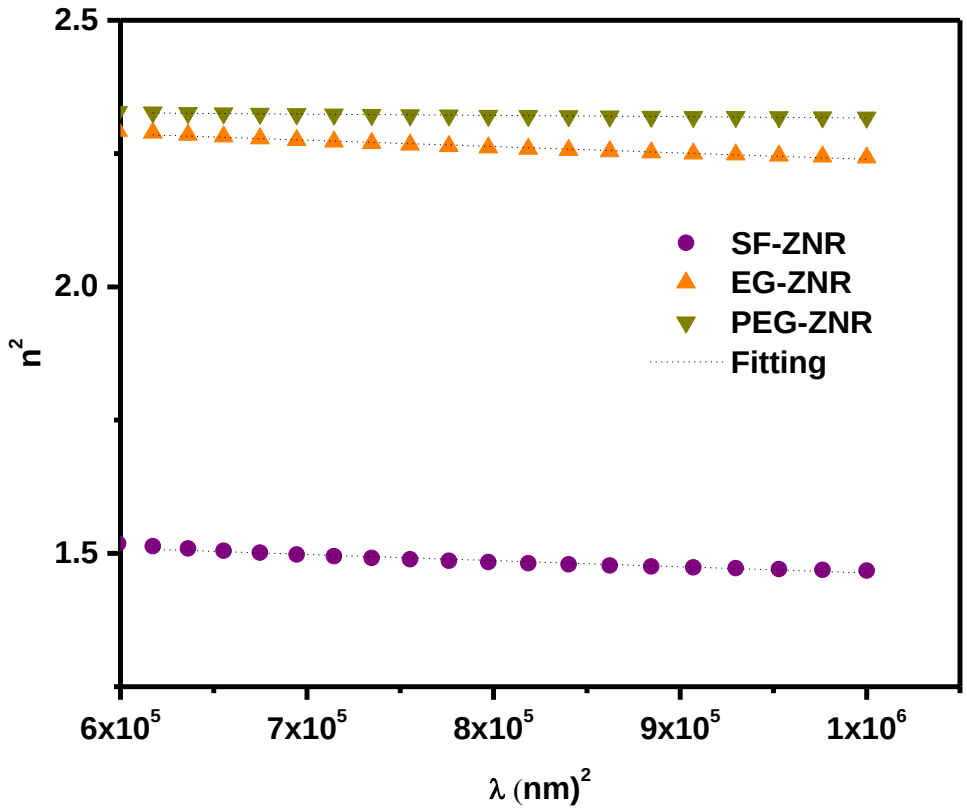


Figure 5.13: Plot of n^2 vs λ^2 for the ZnO SF-ZNR, EG-ZNR and PEG-ZNR nanostructures. Linear fitted with Reg ≈ 1.

The zero-frequency dielectric was also deduced, when hv of the WDD equation is set to zero. The calculated values of $n_{(0)}$ and $(n_{(0)}^2)$ for are listed in Table 5.3. Both $n_{(0)}$ and $(n_{(0)}^2)$ are found to be lower in the samples grown in the presence of surfactants, which is also in agreement with the refractive index values. The plasma frequency (ω_p), was also calculated based on Penn's theory as described in section 3.1. Values found from the calculation of ε_0, ε_L and the N/M^* from previous plots and respective relations were used in the calculation of ω_p using equation 3.45. The values of ω_p were found to be (51.62, 41.42, and 60.89) x 10^{13} s^{-1} for surfactant free, EG grown and PEG-grown ZnO nanorods, respectively. The results are presented in Table 5.3 and are found to have a similar trend with N/M^*. The highest value of N/M^* was obtained for PEG grown ZNR, which can be attributed to a higher charge carrier concentration as observed by a higher N/M^* ratio.

Table 5.3: Static refractive indext ($n_{(o)}$), high frequency dielectric constant ($n_{(o)}^2$), lattice dielectric constant (ε_L), plasma frequency (ω_p), carrier concentration to effective mass ratio(N/M*) and momenta (M_{-1} and M_{-3}).

Sample	$\mathbf{n_{(0)}}$	$\mathbf{(n_{(0)})^2}$	$\boldsymbol{\varepsilon_L}$	$\boldsymbol{\omega_{p\,x}\,10^{13}}$ **(s^{-1})**	$\mathbf{N/M^*x\ 10^{55}}$ **($m^{-3}\ Kg^{-1}$)**	$\mathbf{M_{-1}}$	$\mathbf{M_{-3}}$
SF-ZNR	1.80	3.24	1.60	51.62	14.74	2.24	0.060
EG-ZNR	1.50	2.25	2.40	41.42	14.24	1.26	0.028
PEG-ZNR	1.47	2.16	2.30	60.89	29.48	1.17	0.028

The excitation energy of electrons spectrum can be explained by the frequency dependence of the dielectric constant, which consists of two components according to the Krammer-Kronig theory [218]. Equations that relate the imaginary (ε_i) and real (ε_r) parts of the dielectric function to the refractive index (n) and extinction coefficient (k_x) have been discussed in section 3.4.9. Figure 5.14 shows plots of (ε_i) and (ε_r) against the incident photon energy (hv). The increase in dielectric losses (ε_i) above the band gap energy (E_g, i.e., >3.20 eV) depict poor dielectric behaviour, pointing to good conductor behaviour**.** The observed trend could be attributed to the accumulated charge carriers in the distinct regions of conductivities in the ZnO nanostructures [219]. This trend is in good agreement with the observed values of N/M* in Table 5.3. The increase in relative permittivity could be attributed to polarizations, electronic and space charge displacements. The molecule polarizations cause the field reversals to fall back resulting in dielectric losses. The calculated values of the momenta are presented in Table 5.3. Both M_{-1} and M_{-3} are found to decline for the ZnO synthesized using surfactants, similar to the trend of E_d.

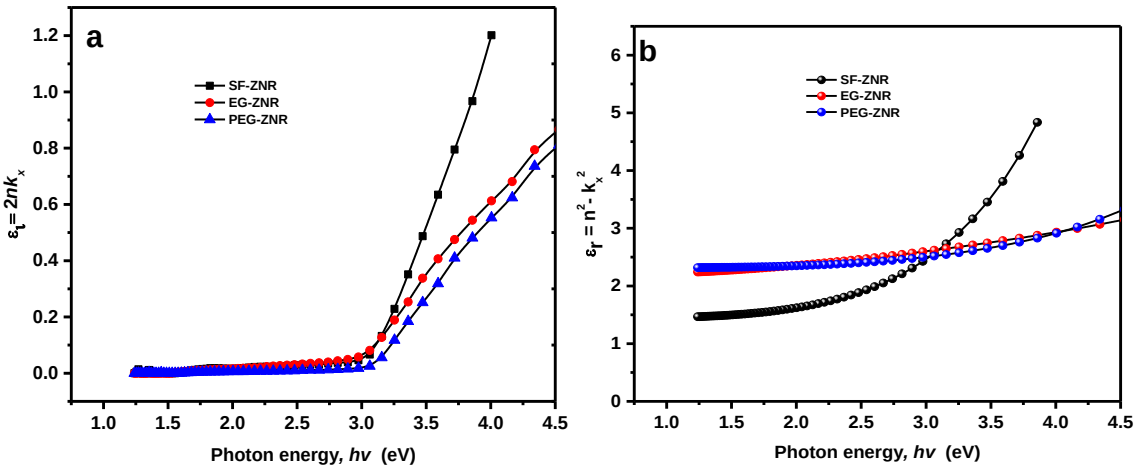


Figure 5.14: The spectral dependence of the (a) imaginary (ε_i) and (b) real components (ε_r) of the dielectric function for the ZnO NRs nanostructures.

In summary, both the XRD and Raman confirmed the wurtzite ZnO with no secondary or impurity peaks. XPS studies also indicated that c-axis oriented wurtzite ZnO nanorods were of high purity. The crystallite sizes and morphologies of the nanorods were successfully controlled by use of capping agents. Ethylene glycol grown ZnO nanorods (EG-ZNR) showed uniform dispersed elongated nanorods with screw-ends. A red shift in the optical band gap relative to the bulk for surfactant grown nanorods was observed from optical studies. The optical constants n and k_x were investigated; with n showing normal dispersion of light in the measured region. Similar to other properties, dispersive constants showed dependence on the addition of surfactants. The ratio N/M* was found to be elevated for surfactant grown samples, which sequentially triggered a surge in the values of the plasma frequency. This surge could be attributed to concentration of charge carriers in the samples. The components of the complex dielectric constant were observed to follow the trend of the refractive index (real part) and the extinction coefficient (imaginary part). In conclusion, this study has shown that utilization of surfactants during ZnO synthesis can simultaneously control the morphology and crystallinity as well as modify its optical properties without altering its wurtzite structure. The polyethylene glycol was opted as the superlative surfactant for the synthesis of the 1D nanostructures. However, few parameters were further adjusted and optimized including the concentrations of the precursor solutions, the volume as well as the spraying rate so as to reduce the diameters of the nanorods. The samples obtained from these modified steps were characterized and further used for ion implantation to modify the structure and optical properties of ZnO NRs.

CHAPTER 6: RESULTS AND DISCUSSION II-Ag^+ ion implanted ZnO nanorods

The results presented in this chapter have been published in the article: **K. Lefatshe**, C. Muiva, M. Madhuku, 'Effect of low energy Ag^+ ion implantation on ZnO nanorods for enhanced visible light absorption-structural and optical analysis' Optical Materials, 122 (2021), 111757. https://doi.org/10.1016/j.optmat.2021.111757

6.1 Overview

This chapter presents an analysis of the structural, morphological and optical response properties of ion implanted ZnO. The synthesised ZnO NRs were implanted with Ag^+ ions at low energy of 50 KeV and varying fluences of 1 $x10^{15}$, 2 $x10^{15}$, 3 $x10^{15}$, 1 $x10^{16}$, and 3 $x10^{16}$ ions/cm^2. The influence of injected Ag^+ ions on the structural and optical properties of ZnO NRs was investigated. The ion implantation-induced structural distortions in the ZnO lattice were characterized mainly through the X-ray diffraction technique. The Raman analysis and FTIR were also used as complementary techniques to the XRD. A detailed explanation on the effect of varying the silver (Ag^+) ion fluence on the structural and optical response properties of ZnO is provided.

6.2 Crystalline structure analysis

6.2.1 X-ray Diffraction (XRD) analysis

Structural identification and analysis of implanted ZnO NR films was studied through the XRD. Figure 6.1 shows XRD 2θ scans of pristine and Ag^+ ion implanted ZnO (at fluences of $1x10^{15}$, $2x10^{15}$, $3x10^{15}$, $1x10^{16}$, and $3x10^{16}$ ions/cm^2). The prominence of the 002 peak was retained post implantation, showing that the Ag^+ ion implantation did not cause amorphization of the films. The patterns were analysed for phase identification and to study the influence of Ag^+ ions. The profiles for Ag^+ ion-implanted ZnO films were all indexed to a hexagonal wurtzite crystallographic structure [220, 221]. No additional peaks of Ag, its oxides nor any other impurities or secondary phases were identified, indicating efficacious assimilation of Ag^+ ions into the ZnO lattice. A variation in the peak intensities, peak positions (2θ angles) as well

as peak broadening i.e., full width at half maximum (FWHM) is observed. As shown on the enlarged view of the most prominent (002) peak in Figure 6.1b, the change in the intensity, FWHM and the positions of the peak is strongly dependent on the Ag^+ ion fluence. An increase in peak broadening (FWHM) has been attributed to crystalline size reduction due to induced disorders within the lattice, which, as a result, degrades the degree of preferred orientation [28].

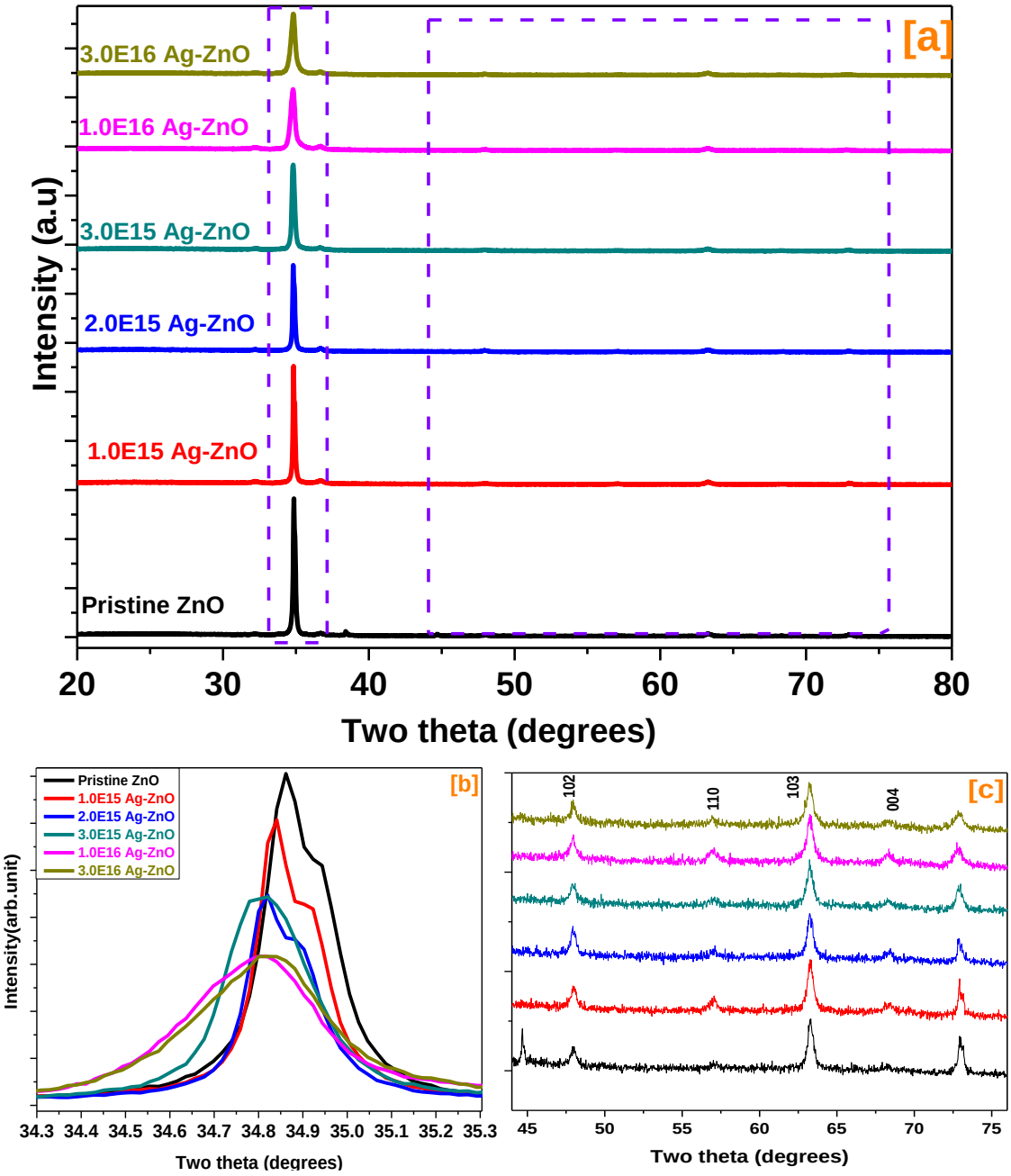


Figure 6.1: Recorded XRD [a] wide range scans, [b] enlarged 002 peak and other dwarfed peaks [c] of pristine ZnO and Ag^+ implanted ZnO at different fluences ($1x10^{15}$, $2x10^{15}$, $3x10^{15}$, $1x10^{16}$ and $3x10^{16}$ ions/cm^2).

As indicated by reduced intensities, bombardment of the ZnO films with Ag^+ metallic ions resulted in the reduction of the crystallinity of the films. Similar findings are reported in literature demonstrating that the incorporation of transition metals modifies the crystallinity of ZnO [222-224]. The reduction of the peak intensity and peak shifting to lower angles indicate an change in the crystallinity of the films and lattice expansion, which could be ascribed to the existence and concentration of structural defects caused by ion implantation [6, 7] Crystallographic parameters of Ag^+ implanted ZnO films including the peak positions and FWHM for the (002) peak, are as presented in Table 6.1. As elucidated, the increase in FWHM and negative peak shifting signal lattice expansion and induced microstrain broadening [225].

Despite observed peak shift back to higher 2θ angles for the sample implanted to ion fluence 3 x 10^{16} ions/cm^2, the evolution of the extracted parameters follows a similar trend. This attribute signals the possibility that the inclusion of more Ag^+ ions above the 1.0 x 10^{16} ions/cm^2 inhibits further lattice expansion. The impact of Ag^+ ions on the lattice of ZnO was further assessed through a calculation of various microstructural parameters using a series of equations which have been described in chapter 3, section 3.4.1 [8, 128, 129]. The interplanar spacings (d) between the 002 planes are found to increase with the Ag^+ ion fluence across all the samples. An increase in d-spacing indicates lattice expansion in the c-direction, as supported by the peak shift towards lower 2θ angles [13]. The calculated crystallite size (D_s) of the pristine and the Ag^+ ion implanted samples were also compared. The D_s was found to decrease from 56.31 to 24.29 nm after implantation with Ag^+ ions at fluence 3.0 x10^{16} ions/cm^2. Generally, some dislocations arise during crystal growth or when the crystal is said to be distorted by stress [226]. The obtained D_s values were used to determine the dislocation density (δ). A systematic increase in the dislocation densities was observed. The values of δ were found to be amplified by the intrusion of Ag^+ ions into the ZnO hexagonal lattice, demonstrating an increase in the concentration of defects and a distorted lattice. Furthermore, the increase in dislocation density confirms that the deterioration in the film's crystallinity increases with Ag^+ fluence. The calculated crystallite sizes (D_s), interplanar d-spacing (d), and dislocation densities (δ) are also all listed in Table 6.1.

Table 6.1: The 002-peak position (2θ), interplanar d-spacing (d), FWHM (β), crystallite size (D_s) and dislocation densities (δ) of pristine and Ag^+ implanted ZnO films.

Ag^+ ion fluence (ions/cm^2)	**2θ (º)**	**d (nm)**	**β (º)**	**D_s (nm)**	**δ (x10^{14} line/m^2)**
0	34.866	0.25734	0.148	56.31	3.15
1x10^{15}	34.843	0.25750	0.161	51.76	3.73
2x10^{15}	34.837	0.25754	0.172	48.45	4.26
3x10^{15}	34.815	0.25770	0.226	36.87	7.36
1x10^{16}	34.796	0.25784	0.340	24.51	16.65
3x10^{16}	34.821	0.25766	0.343	24.29	16.95

To fortify the study, lattice parameters shows that the crystallographic planes expand preferentially in the c-axis. The lattice parameter a_p was found to change in the opposite direction. A substantial lattice expansion in the perpendicular direction is observed to be proportional to the fluence of Ag^+ ions, while in the parallel direction there is no direct relationship between the lattice parameter and the ion fluence, showing that the deformation of the lattice happens primarily in the out-of-plane axis and thus the induced strain in the implanted films is perpendicular. A slight reduction in the lattice parameter c_p, at ion fluence 3 x 10^{16} ions/cm^2 corroborates the previously discussed peak shifting. This slight reduction shows that at this fluence there might be evolution of different types of defects which leads to less expansion of the lattice. The lattice parameters were plotted as a function of the calculated d-spacing as depicted in Figure 6.2, which shows that a linear relationship is established for the perpendicular lattice c_p.

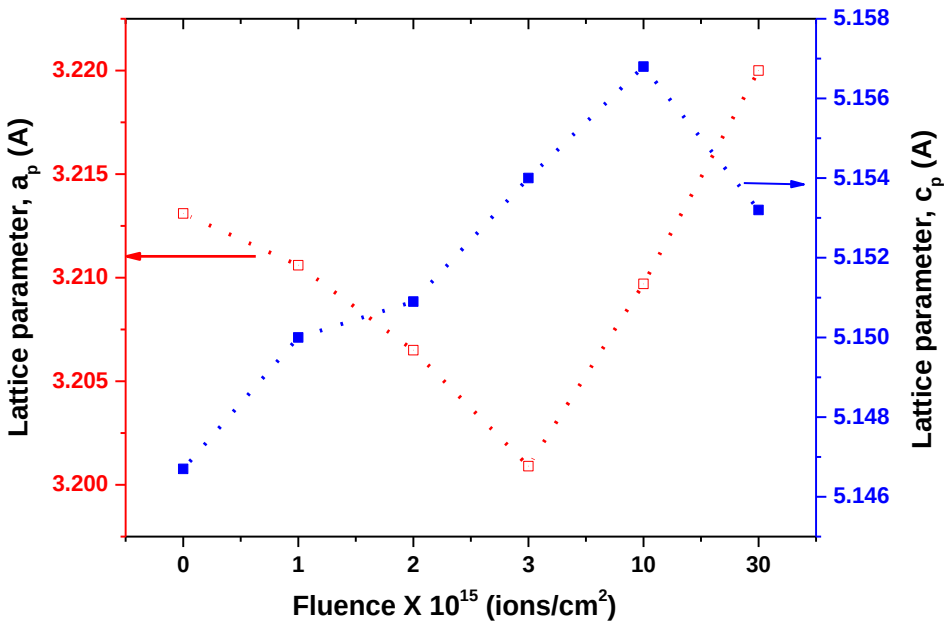


Figure 6.2: The variation of the lattice parameters a_p and c_p with fluence of Ag^+ ions (the dotted lines are to guide the eye).

As previously explained, an implanted ion interacts with the host atoms, losing its energy through electronic and nuclear collisions and consequently being forced to stop and occupy a lattice site. The ion can either settle on an interstitial site or substitute an atom of the host lattice. Substitution usually results in lattice expansion [227, 228]. Comparing the atomic radii of Ag^+ (0.114Å) and Zn^{2+} (0.074Å), Ag^+ ions are most likely to substitute the Zn atoms. But as the fluence is increased, an affinity for occupying interstitial sites may also arise, hence the possibility of both substitution and interstitial settling is predicted for the sample at 3 x10^{16} ions/cm^2. The magnitude of the microstrain was calculated using the Wilson relation. A linear proportionality of the calculated microstrain to the ion fluence was observed as expected, indicating that as Ag^+ ions are bombarded, they stretch the ZnO lattice, resulting in more induced strain. This increase is relative to ion fluence and the deterioration in the crystallinity of the samples [229].

Furthermore, strain-induced variations of the interatomic distance tend to inevitably alter the interaction between neighbouring ions. The Zn-O bond length, L and the second nearest-neighbour bond-lengths denoted L_1, L_2, and L_3 were calculated. The disparity of the calculated parameters presented in Table 6.2 alludes to some alterations to the lattice structure induced by the presence of Ag^+ ions. Similar to the FWHM and dislocation density, the microstrain, and lattice parameter c_p, were found to upsurge upon Ag^+ ion implantation. The expansion of these

listed attributes varies with Ag^+ ion fluence as expected, primarily due to the substitution of Zn^{2+} by Ag^+ ions of larger ionic radius. Disparities in d-spacing, 2θ position, and lattice parameter c_p; upon Ag ion implantation have previously been confirmed [222, 230]. The variation of d-spacing suggests the introduction of stacking faults upon Ag^+ injection. A stacking fault is a two-dimensional imperfection caused by the non-alignment of one atomic plane with another. The calculated stacking fault probability (SFP), is shown to increase with the increase in the dislocation density and lattice parameter, indicating the presence of defects in the ZnO lattice.

Table 6.2: Various calculated microstructural parameters of Pristine and Ag^+ ion implanted ZnO films.

Parameters	**Ion fluence (ions/cm^2)**					
	Pristine ZnO	**1.0x10^{15}**	**2.0 x10^{15}**	**3.0 x10^{15}**	**1.0 x10^{16}**	**3.0 x10^{16}**
Lat. parameter a_p (Å)	3.2131	3.2106	3.2065	3.2009	3.2097	3.2220
Lat parameter c_p (Å)	5.1467	5.1500	5.1509	5.1540	5.1568	5.1532
Lattice strain, ε_{zz} x 10^{-2} (%)	-	6.40	8.07	14.2	19.5	12.5
Biaxial stress, σ_z (GPa)	-	-0.290	-0.366	-0.644	-0.885	-0.567
u_c	2030560	1571691	1291412	568528	167441	162880
Positional para. μ (Å)	0.37992	0.38011	0.37980	0.37971	0.37917	0.37958
Bond length L (Å)	1.9553	1.9576	1.9563	1.9570	1.9550	1.9560
L_1 (Å)	3.1914	3.1924	3.1946	3.1970	3.2017	3.1971
L_2 (Å)	3.7613	3.7662	3.7627	3.7638	3.7580	3.7615
L_3 (Å)	3.7613	3.7662	3.7627	3.7638	3.7580	3.7615
Stacking fault (SF)	0.00117	0.00127	0.00136	0.00178	0.00267	0.00271

6.2.2 Raman analysis

Raman spectroscopy measurements of the implanted ZnO NRs were conducted out at room temperature, using the green emission 514 nm argon ion laser. Figure 6.3 shows Raman spectra of pristine and Ag^+ ion implanted ZnO samples. The presence of the E_{2high} peak in all samples is an indication that the wurtzite structure of ZnO was not altered by the implantation of Ag^+ ions, which supports the XRD analysis. However, the presence of distortions and possibly defects on the ZnO matrix can be substantiated through analysis of its intensity and other observed peaks. The decrease of the intensity of this peak is observed to be dependent on the ion fluence. This behaviour has previously been associated with the presence of lattice defects caused by Ag^+ implantation [231, 232]. Furthermore, the variation in the peak phonon frequencies is associated with stress induced in the wurtzite crystal structure during ion implantation [232]. All implanted samples show a slight decrease in the frequency thus indicating that a weak tensile stress was induced to the ZnO lattice.

Another common significant peak at 578 cm^{-1} assigned as the A1 longitudinal optical (LO) phonon mode was observed to increase upon Ag^+ ion implantation. According to Mondal et al [233], the A1 (LO) is one of the ZnO peaks that are most sensitive to O-site disorder in the ZnO lattice, and can be intensified by transition metals implantation-induced-disorder [234]. Previous researchers have ascribed the presence of this peak to intrinsic defects associated with oxygen vacancies [223]. This peak intensified and shifted to a lower Raman shift at higher Ag^+ ion fluence. Simultaneous peak broadening and shifting upon Ag^+ incorporation has been previously reported to be due to dopant-induced lattice distortions. Munawar et al [231] attribute the peak shift to be due to the surface variation activated by the charge transport between the foreign ions and host lattice. The emergence of this peak is also noted upon ion implantation of ZnO using other various metallic dopants and has been attributed to the disorder-activated Raman scattering (DARS) as induced by the presence of defects mainly oxygen vacancies and interstitials thus resulting in the breakdown of translational crystal symmetry [29, 235-237]. The development of two additional modes (AM), disorder-activated peaks at 233 and 184 cm^{-1} was observed. These peaks are ascribed to the deformation or disorder in the ZnO lattice [238, 239]. Even though peaks related to the presence of lattice defects and distortion were observed, no secondary phase peaks were indexed in the Raman spectra. Raman and XRD data confirm that structural disorder due to ion implantation is highly dependent on ion fluence.

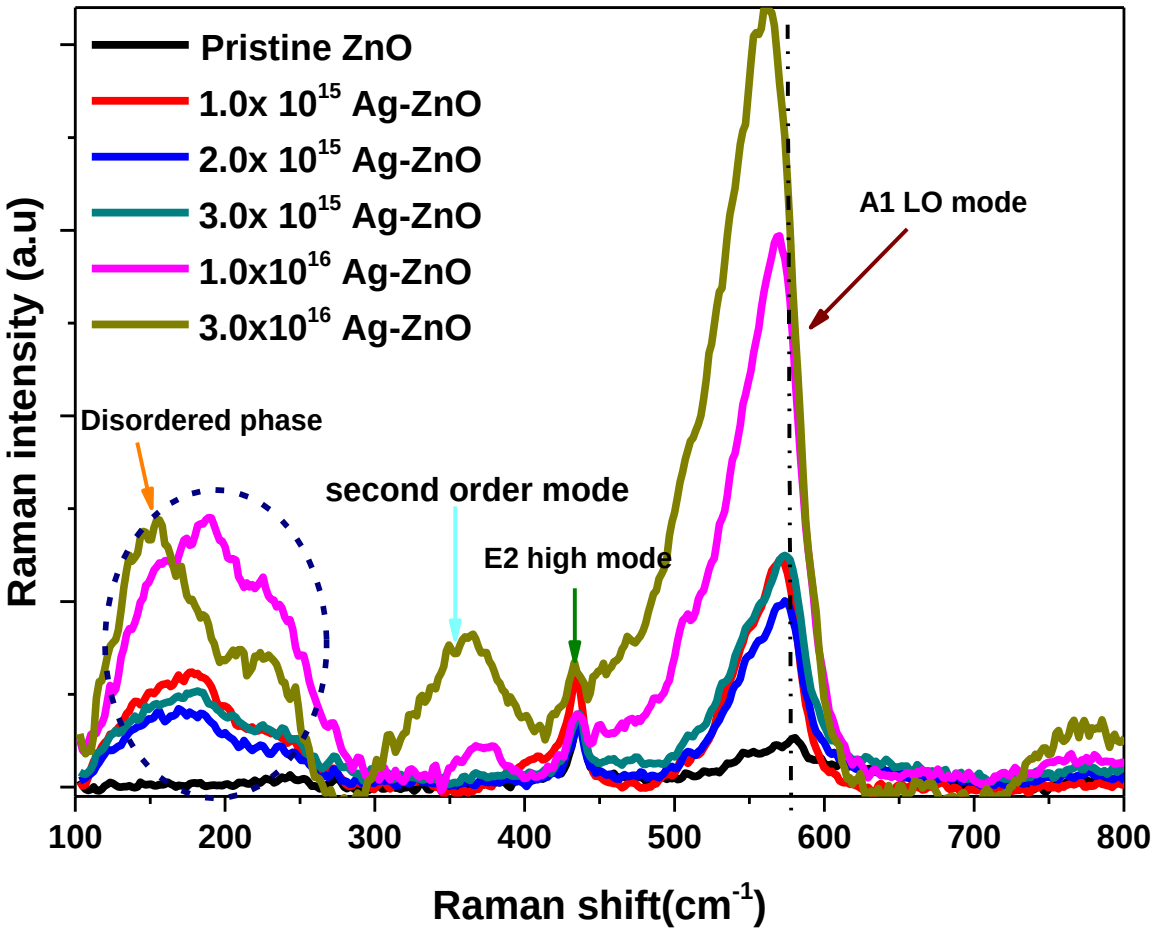


Figure 6.3: Room temperature Raman spectra of pristine and Ag^+ implanted ZnO.

6.2.3 Fourier Transform Infrared (FTIR) analysis

The presence of Ag^+ ions in the ZnO matrix has also been investigated by studying any dissimilarities in the FTIR spectra of ZnO implanted with Ag^+ cations at varying fluences. The FTIR spectra given in Figure 6.4 show multiple fingerprints frequencies lower than 400 cm^{-1} for all samples, which are described to be the metal-oxide vibrations [8]. A slight shift is observed for the band recorded at 610 cm^{-1}. Not much variation was observed in the FTIR spectra of the pristine and implanted ZnO samples except for only small shifts of the band positions and the intensity of the absorption bands. The shift may be due to the change in the band position due to the substitution of Ag^+ ions into the host matrix. Our FTIR results indicate re-arrangement of bonding through variation of the positions and intensities of the functional groups.

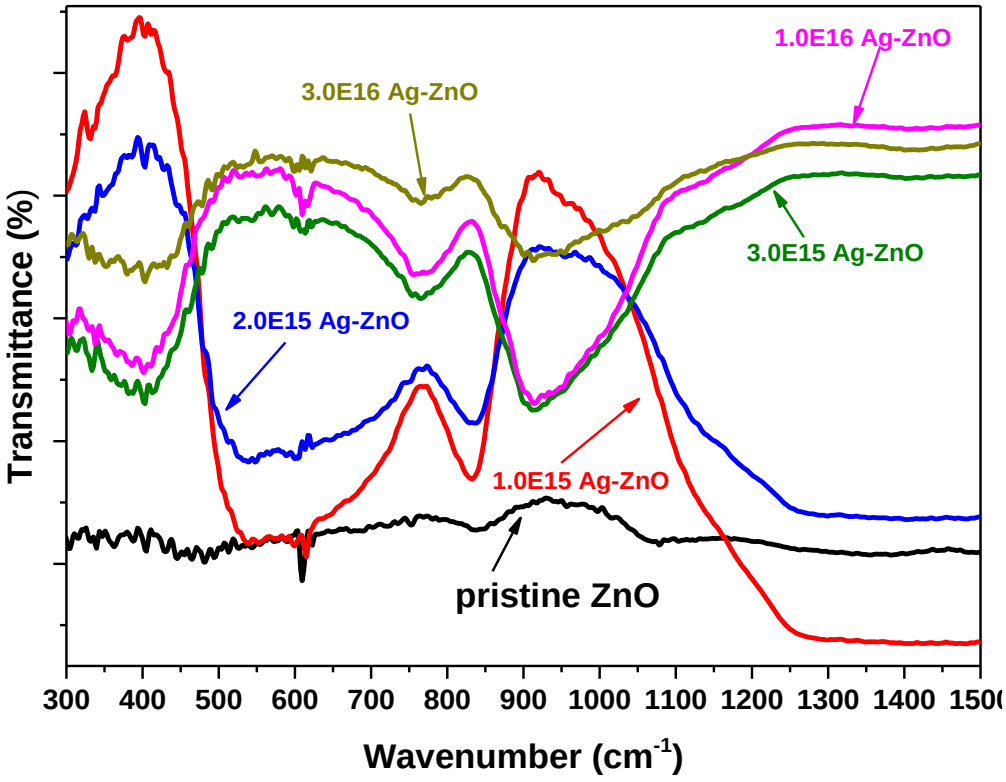


Figure 6.4: FTIR spectra of pristine ZnO and Ag^+ ion implanted ZnO films at fluences of $1x10^{15}$, $2x10^{15}$, $3x10^{15}$, $1x10^{16}$ and $3x10^{16}$ ions/cm^2.

6.3 Morphological Analysis

6.3.1 Field Emission Scanning Electron Microscopy (FESEM)

Figure 6.5 shows top surface view field emission scanning electron microscopy (FESEM) images of Ag^+ ion implanted ZnO nanorod films. The FESEM images indicate a high concentration of elongated nanostructures with varying diameters. Comparable morphologies were seen pre- Ag^+ ion implantation, signifying that the much-required 1D morphology was not ruined post- Ag^+ ion implantation. An increase in the Ag^+ ion fluence results in the distension of the nanorods as noticed in Figure 6.5e. No cracks or voids were observed. The FESEM has limited comparability since it is a surface-imaging technique, thus a tapping AFM imaging technique was implemented for further morphological analysis.

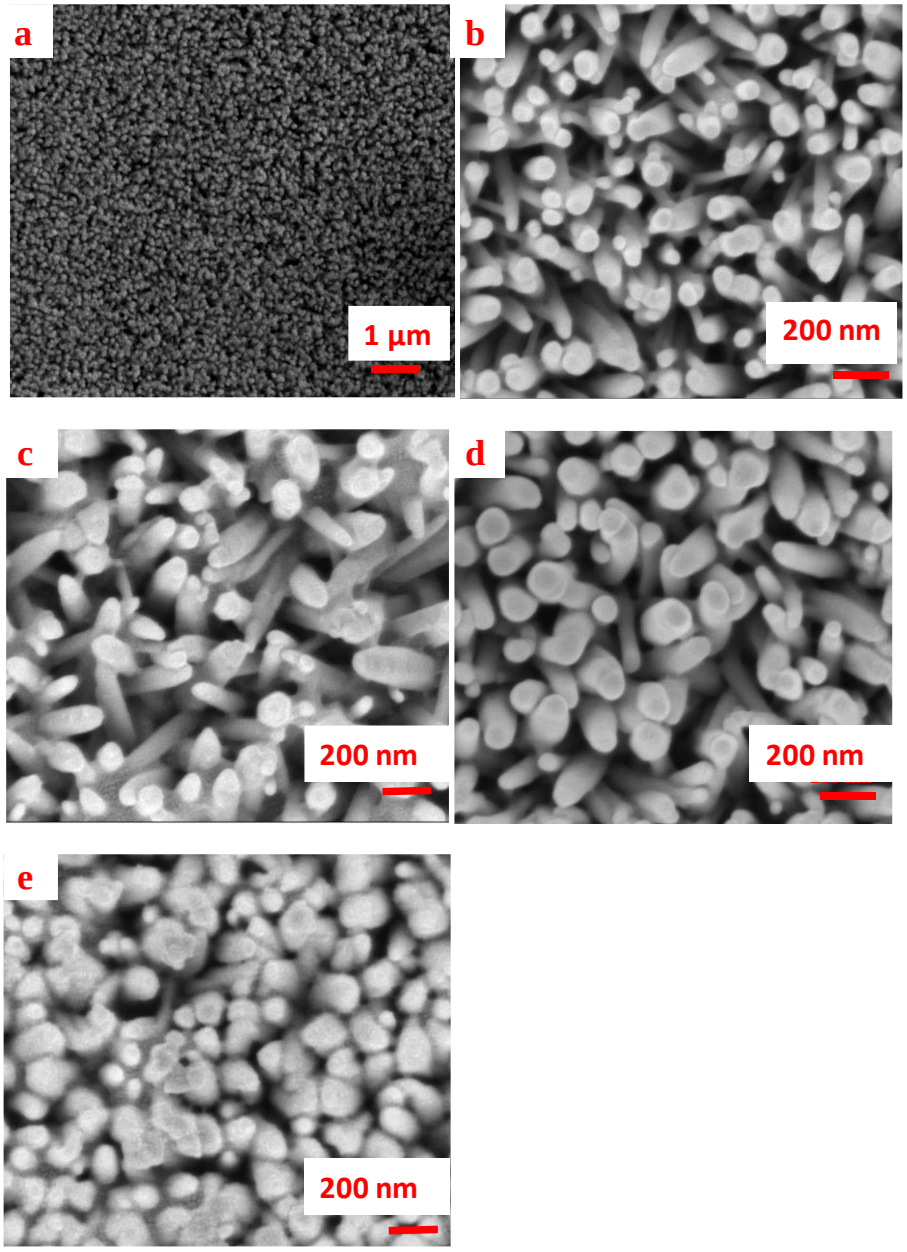


Figure 6.5: Field emission scanning electron microscopy (FESEM) images of Ag^+ ion implanted ZnO at fluences of (a, b) 2.0 x 10^{15}, (c) 3.0 x 10^{15}, (d) 1.0 x 10^{16} and (e) 3.0 x 10^{16} ions/cm^2.

6.3.2 Elemental analysis

From FESEM imaging, elemental analysis was conducted through the energy dispersive X-ray spectroscopy (EDX). Spatial distribution of Ag^+ ions over the host matrix is shown in Figure 6.6. All samples were analysed, the atomic percentages of the constituents are presented in

Table 6.3. A relative increase in the atomic percentage was noted thus also confirming a successfully incorporation of Ag^+ ions in the ZnO matrix. In combination to the EDX, the elemental mapping was conducted to study the distribution of the implanted Ag^+ ions in the ZnO matrix. All the constituent elements are shown to be uniformly dispersed within the host matrix. Furthermore, Rutherford backscattering spectroscopy (RBS) measurements were conducted to corroborate the presence of Ag on ZnO films. RBS raw data of pristine and Ag^+ ion implanted ZnO NR films were compared and the spectra (Figure A1, given in Appendix A) show Zn as the main constituent element compared to O. A very small yield is noted for the Ag peak, which was further noted to gradually increase as the ion fluence was increased.

Table 6. 3: Elemental composition of pristine and Ag^+ ion implanted ZnO.

Element	**Atomic percentage (%)**					
	ZnO	**1.0 x10^{15}**	**2.0 x10^{15}**	**3.0 x10^{15}**	**1.0 x10^{16}**	**3.0 x10^{16}**
Zn	64.81	63.19	60.38	59.58	63.57	65.44
O	18.79	20.05	21.67	17.85	30.74	23.90
C	19.41	16.73	17.85	26.10	15.04	9.84
Ag	0.00	0.03	0.09	0.38	0.59	0.82

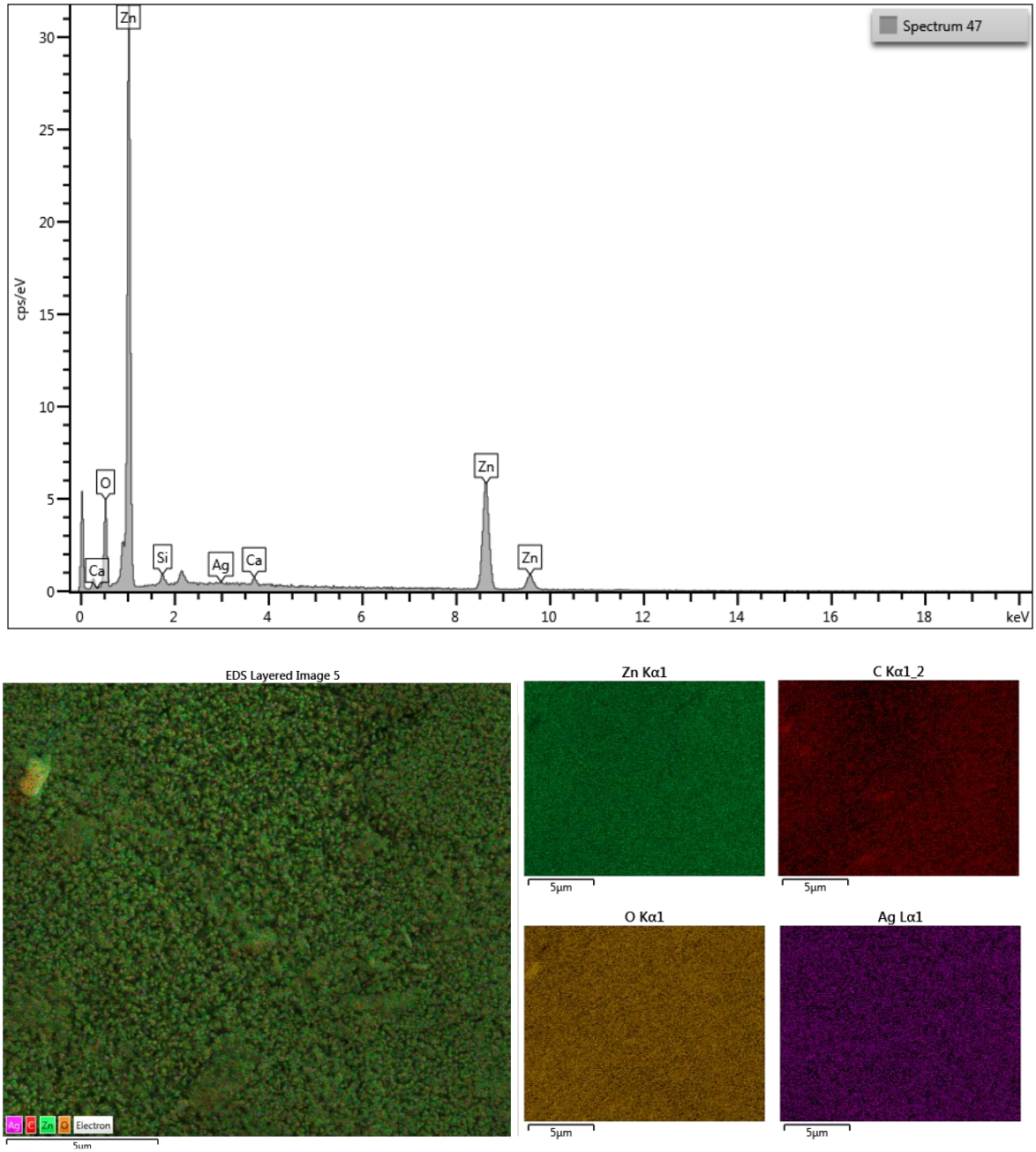


Figure 6.6: Elemental mapping images of Ag^+ ion implanted ZnO at fluence of 3.0 x 10^{15} ions/cm^2.

6.3.3 Atomic Force Microscopy (AFM)

Figure 6.7 displays 2D and 3D AFM images of ZnO films following Ag^+ ion implantation. The 1D nanorod morphology is further confirmed, and no grains or any agglomerates are noted on the surface of the nanorods, thus inferring a successful assimilation of the Ag^+ ions into the nanorods. The 1 μm^2 micrographs were statistically analysed to obtain the physical properties

such as surface roughness and grain height, which are given in Table 6.4. The surface roughness (R_{rms}) tends to considerably intensify with increase in Ag^+ ion fluence up to fluence 3 x 10^{15} ions/cm^2. Above this, there is a decline in the R_{rms}. Even though a decrease was observed beyond this fluence, the R_{rms} was still however more pronounced compared to that of the pristine ZnO film. R_{rms} can be associated with the sensitivity of the intersection angle between neighbouring grains. Its increase could show a likelihood of the creation of a micro-void structure and sputtering events on the growing films from the ion implantation process [240]. On the other hand, the decrease in the surface roughness at high fluences during ion bombardment might be due to the increase in surface diffusion processes [240, 241].

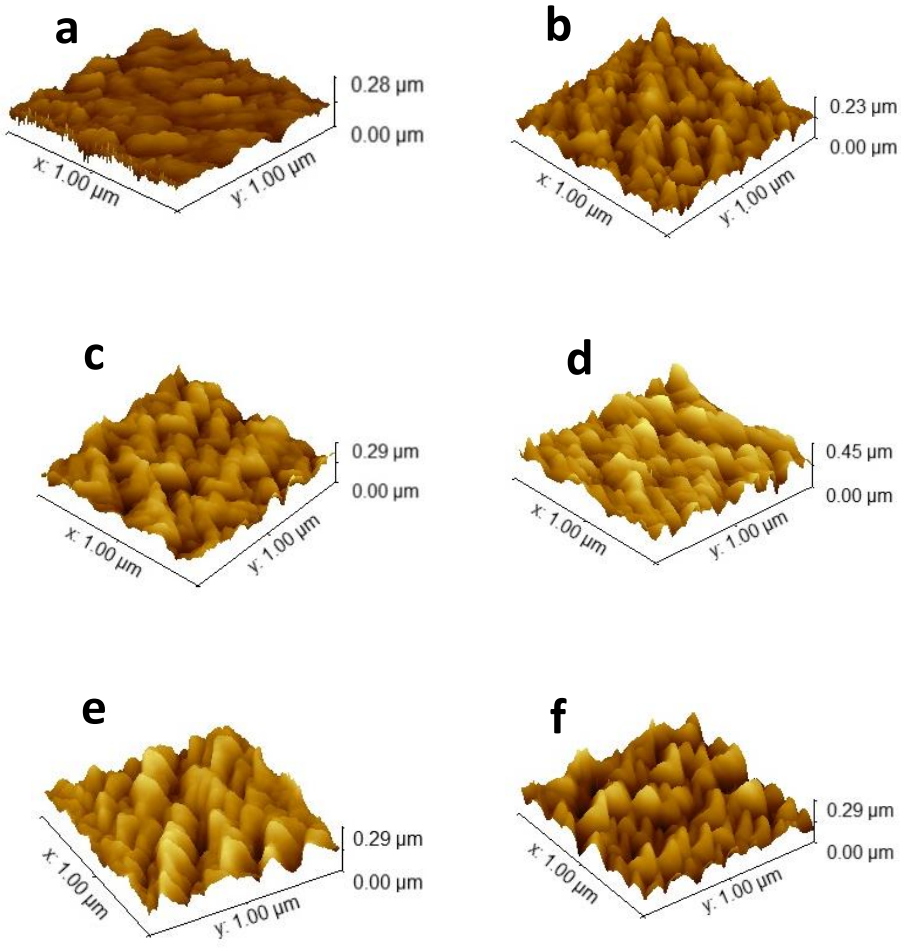


Figure 6.7: Three-dimensional (3D) AFM tapping mode images of low energy (a) pristine and Ag^+ ion implanted ZnO samples at fluences of (b) 1x 10^{15} (c) 2x 10^{15}, (d) 3x 10^{15}, (e) 1x 10^{16}, and (f) 3x 10^{16} ions/cm^2.

Table 6.4: Surface statistical AFM analysis of the Ag^+ ion implanted films.

Ag^+ ion fluence (ions/cm^2)	**R_a (nm)**	**R_{rms} (nm)**	**R_a/R_{rms}**	**Grain height (nm)**
0	122.2	18.69	6.54	278.20
1 x10^{15}	118.5	24.50	4.84	234.65
2 x10^{15}	158.8	36.55	4.34	331.81
3 x10^{15}	269.3	55.66	4.78	426.99
1 x10^{16}	175.0	39.09	4.48	292.35
3 x10^{16}	141.6	37.33	3.79	289.9

6.4 Optical Analysis

6.4.1 Absorbance

The measured absorbance spectra of the pristine and Ag^+ ion-implanted ZnO NRs samples are compared to assess the impact of Ag^+ ions on the optical response of ZnO NRs. A strong dependence of the absorbance on Ag^+ ion fluence is established. The spectra given in Figure 6.8 show significant augmentation in the visible light absorption spectra of Ag^+ ion-implanted ZnO NRs. The ZnO NR film implanted with Ag^+ ions of fluence 1.0 x10^{16} ions/cm^2 showed the highest increase in the visible region of about 42%. Moreover, a shift of the absorption edge towards the visible region was noted upon implantation of ZnO NRs with Ag^+ ions. The red-shift in the absorption edge intensifies as more Ag^+ ions are introduced onto the host lattice, indicating a clear dependence of light absorbance on the presence of Ag^+ ions. This shift signals the possibility of electronic structure alteration as instigated by Ag^+ ion implantation. Red-shifting to higher wavelengths and enhanced absorption has been reported for Ag^+ implanted ZnO [222, 242].

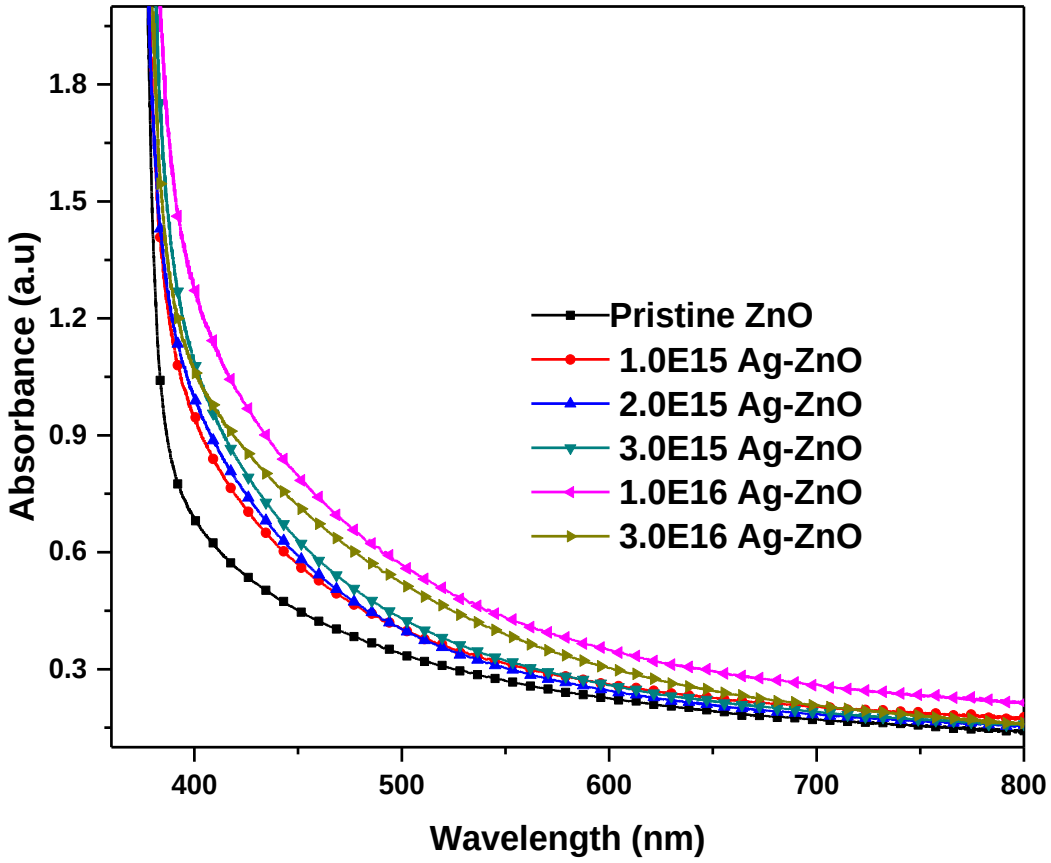


Figure 6.8: Absorbance spectra from pristine and Ag^+ ion implanted ZnO samples.

6.4.2 Extinction (k_x) coefficients

The extinction (k_x) coefficient of the pristine and Ag^+ ion implanted films was also determined. Figure 6.9 shows the dependence of k_x on the fluence of implanted Ag^+ ions. The plot shows that k_x of the Ag^+ ion implanted ZnO film is much greater than that of the pristine ZnO sample in the visible region. This distinct enhancement of the extinction coefficient in the visible light region is understood to be due to increase in impurity concentration [175].

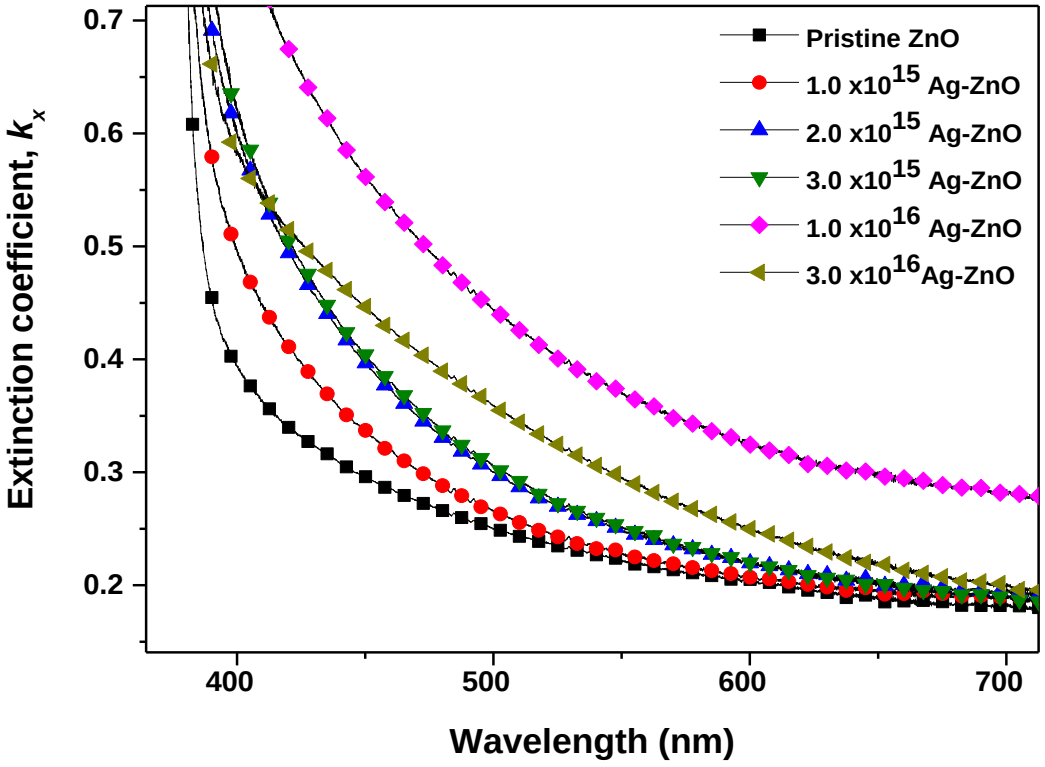


Figure 6.9: Strong dependence of the extinction coefficient (k_x) on Ag^+ ion fluence.

6.4.3 Optical band gap

Intrinsic and extrinsic defects lead to alteration of the electronic structure thus resulting in variation of the optical bandgap. The influence of impurity dopants on the optical properties of SMOs depends not only on their concentration but also on the fabrication or incorporation itinerary. Previous studies have reported an increase in the bandgap of ZnO upon Ag doping, using the wet chemical synthesis route [33]. The intensification of the Burstein-Moss effect is attributed to cause this increase, resulting in enhancement of the Fermi level in the conduction band of ZnO. Usually, the increase in the charge carrier concentration is also associated with the latter [243, 244]. The optical energy bandgaps (E_g) of pristine and Ag^+ ion-implanted ZnO NRs were estimated from the Tauc model. The extrapolation of the linear fragments of plots in Figure 6.10 gave an estimation of the bandgap, E_g. The bandgap of the undoped ZnO was estimated to be 3.25 eV, which is not much divergent from that found in the literature [239]. The calculated E_g values are given in Table 6.5. An overall decrease in the bandgap is observed, proportional to the fluence of Ag^+ ions. The red shift of the calculated bandgap is explained to be due to the creation of extra intermediate energy levels between the conduction and valence

bands [243]. Bandgap constriction upon Ag^+ ion implantation is also associated with the disturbance of the structural periodicity. According to Imran et al [222], induced-local defects due to Ag^+ ions decrease the bandgap. The donor defects levels amalgamate with the conduction band resulting in the reduction of the bandgap of ZnO. However, after ion implantation at fluence 3.0×10^{16} ions/cm^2, there was a shift towards lower wavelengths. This shows saturation type behaviour with further increase in fluence of Ag^+ ions within the ZnO matrix. Such saturation of radiation induced disorder in ZnO has been reported [245].

Xue et al have reported that the increase in the band gap of high fluence implanted ZnO films is due to the formation of agglomerates/clusters during implantation [246]. The observed variation of E_g compared to the bare ZnO NR film illustrates the creation of some imperfections or defects in the host lattice during Ag^+ ion implantation, which affects the electronic properties of the ZnO [222]. Accumulation of impurities results in impurity band formation as the localized defect states create shallow defect bands within the SMO system leading to reduced repulsion between the CB and VB band. This occurrence infers significant bandgap reduction [246, 247]. Depending on their nature, the local defects can also serve as electron sinks and trap the photoexcited negative charges thus delaying recombination, hence leading to enhancement of photocatalytic activities. The degree of induced lattice deformation is evident in the optical properties of implanted ZnO.

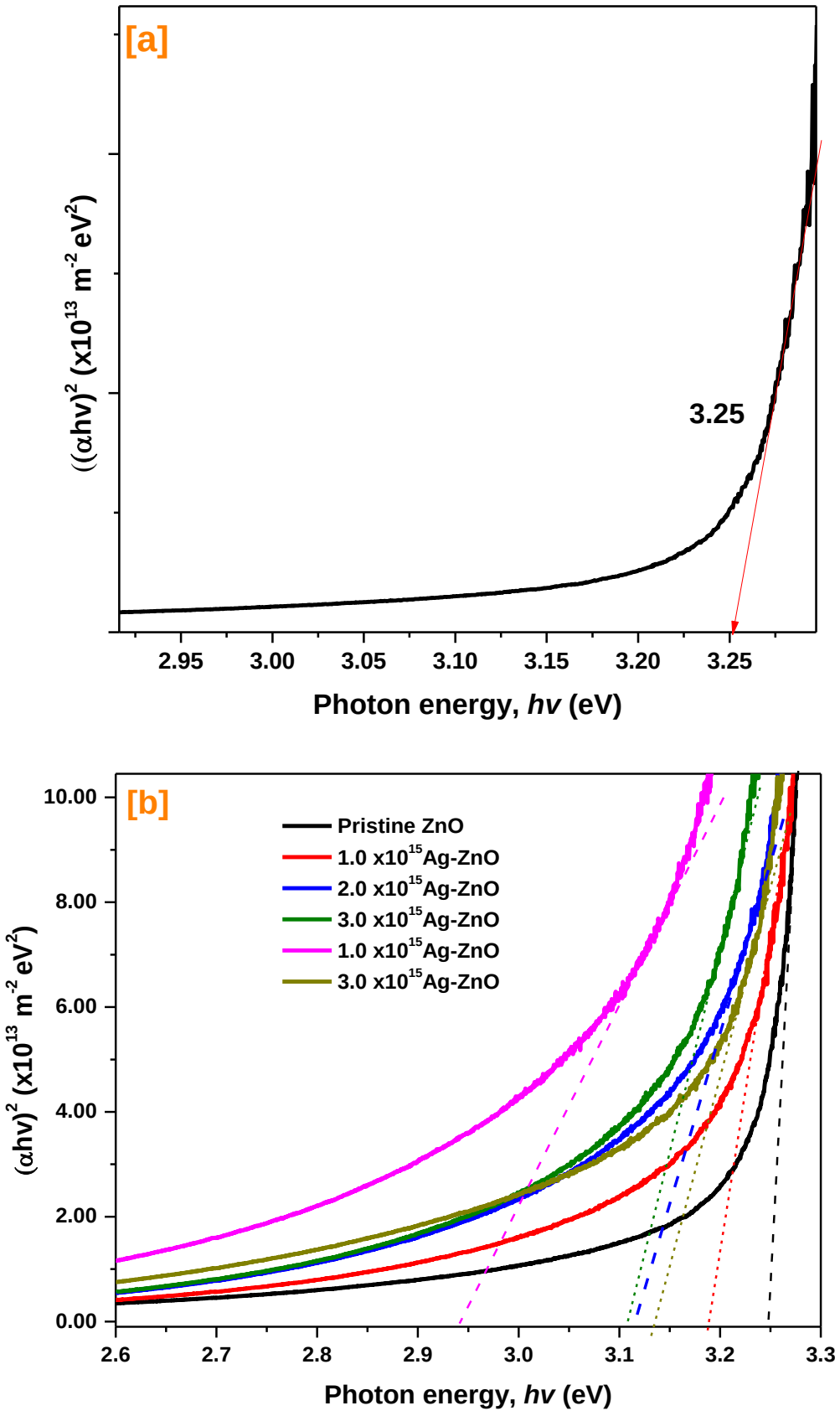


Figure 6.10: Tauc plots used to determine the optical band gap (E_g) of (a) pristine and (b) Ag^+ ion implanted ZnO films.

6.4.4 Urbach energy

A linear relationship of the exponential behaviour of the absorption coefficient (Ln α) against the photon energy (hv) for pristine and Ag^+ ion implanted ZnO nanorods is illustrated in Figure 6.11. The reciprocal of the gradient of the plot was determined as the Urbach energy, E_u. The calculated Urbach energies of each sample are presented in Table 6.4. ZnO NR film implanted at fluence of 3.0 x 10^{15} ions/cm^2 has shown to give the lowest band tail energy of 0.65 eV, though it did not show the lowest band gap reduction. Overall, both the optical band gap and Urbach energies of ZnO are observed to decrease upon Ag^+ ion implantation as shown in Table 6.5. The similarity of the observed trend of these two parameters with that of the lattice parameters and peak shifting from XRD analysis (subsection 6.2.1) suggest contribution from the induced lattice distortions.

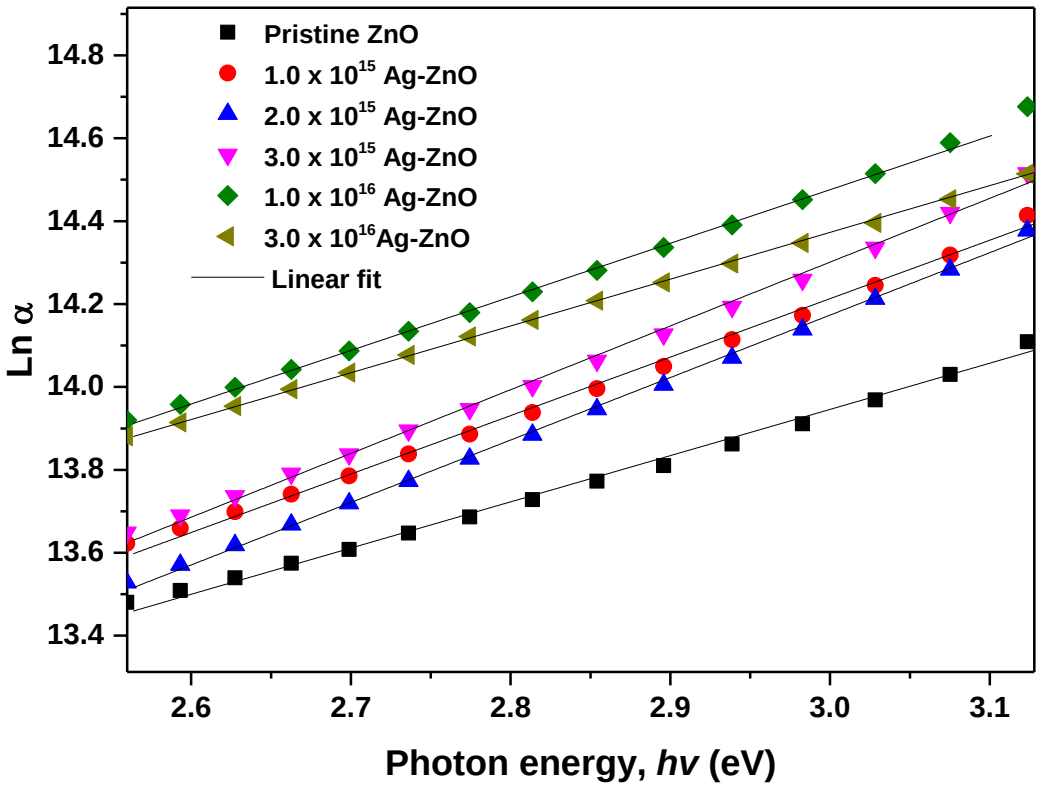


Figure 6.11: Ln α against photon energy for pristine and Ag^+ ion implanted ZnO NRs.

6.4.5 Skin depth and optical conductivity

In addition to the absorption coefficient (α), extinction coefficient (k_x) and optical band gap (E_g), the optical conductivity (σ_{opt}) and skin depth (ϕ) also play important roles and can thus be analysed to predict the efficiency of materials in photo-absorption-related applications. The spectral distribution of the skin depth and the optical conductivity are shown in Figure 6.12 and 6.13, respectively. The differences in the two parameters are noted to change as a function of the fluence of the implanted Ag^+ ions. The decrease in the skin depth (i.e the penetration depth of the photons), indicates an increase in the conductivity of the materials upon ion implantation. This variation proves that as Ag^+ ions assimilate in the ZnO matrix they enhance the photo response of the host ZnO, thus leading to increase in the optical conductivity of the implanted samples. It has been shown that the increase in photo-conductivity signals the creation of intermediary energy levels between the valence and the conduction bands [248]. These results further corroborate the alteration of the electronic structure and indicates that the implantation of Ag^+ ions is a suitable approach to modify the optical characteristics of ZnO for photo-absorption applications.

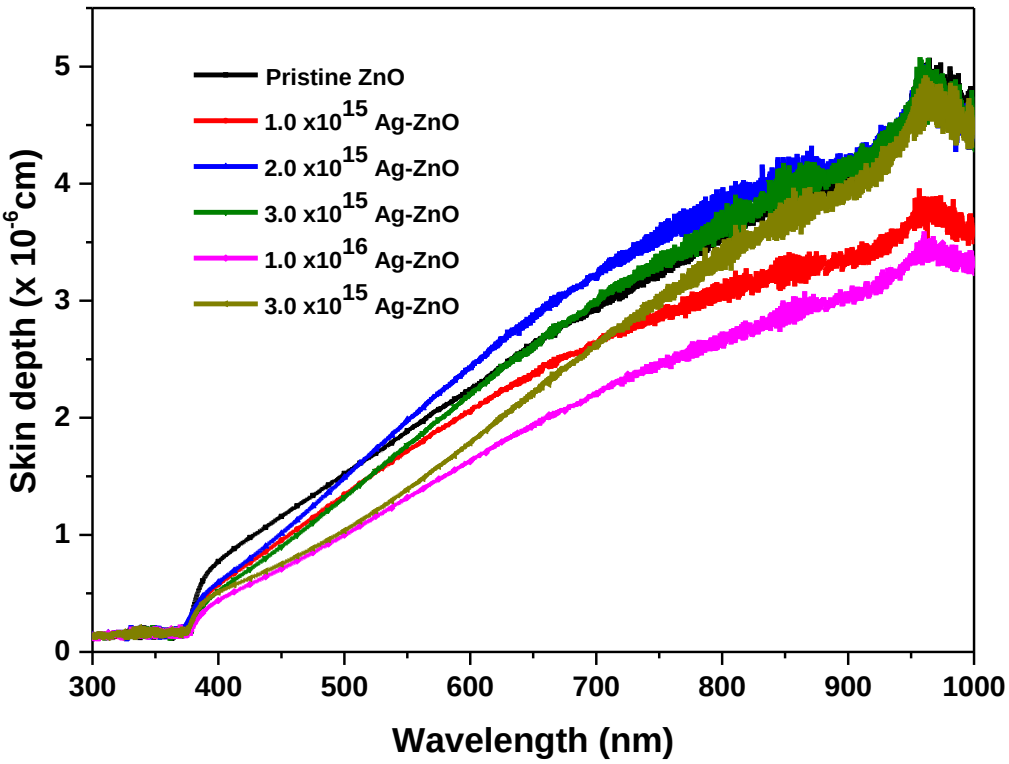


Figure 6.12: The variation of skin depth with the fluence of Ag^+ ions.

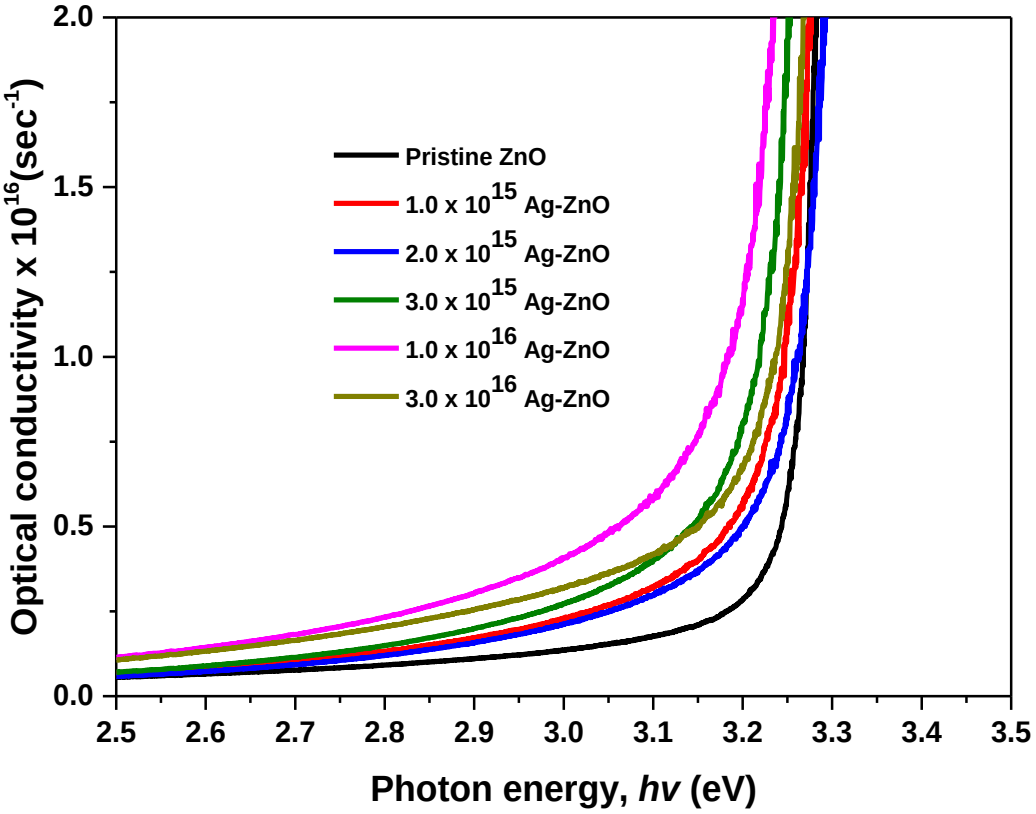


Figure 6.13: Optical conductivity as a function of the wavelength for Ag^+ ion implanted ZnO NRs.

Table 6.5: Calculated optical band gaps (E_g) and refractive index (n) of pristine and Ag^+ ion implanted samples.

Sample ID	**E_g (eV)**	**E_u (meV)**	**N**
Pristine ZnO	3.25	896	2.069
1.0 x 10^{15} Ag-ZnO	3.21	709	2.094
2.0 x 10^{15} Ag-ZnO	3.16	664	2.125
3.0 x 10^{15} Ag-ZnO	3.11	650	2.156
1.0 x 10^{16} Ag-ZnO	2.93	773	2.267
3.0 x 10^{16} Ag-ZnO	3.18	886	2.112

Ag^+ ions were successfully implanted into ZnO NRs. The structural and optical properties of ZnO were investigated and found to be both influenced by Ag^+ ion fluence. XRD and Raman analyses confirmed the hexagonal wurtzite crystallographic structure of ZnO which was not altered by the implanted Ag^+ ions. The presence of Ag^+ ions was noted by a variation in the FWHM, the peak intensity, and 2θ Bragg angles. XRD profiles indicated a higher degree of deterioration of the film's crystallinity with increase in the Ag^+ ion fluence. The crystallite size of the ZnO nanorods was found to decrease from 56 nm to 24 nm as calculated from Scherrer equation. A redshift in the optical absorbance was noticed, coupled with pronounced absorption in the visible light range. Further optical analysis showed that the reduction of the optical band gap from 3.25 eV for pristine ZnO to a lower value of 2.93 eV was achieved by implantation of 1.0 $x10^{16}$ ions/cm^2 of Ag^+ ions. However further increase in the Ag^+ fluence resulted in the increase of the band gap to 3.18 eV. The calculated energy band gap was found to contribute to the increase in the calculated refractive index. A corroboration between structural lattice deformation induced by Ag^+ ion implantation and optical response was established. The results demonstrate that low energy Ag^+ ion bombardment resulted in either substitutional or interstitial implantation with synergistical modification of the physiochemical and electronic properties of ZnO NRs as observed by reduced crystallite size for increased number of active sites; enhanced and extended spectral response of ZnO towards visible light and solar utilisation and reduced band gaps which enables rapid formation of electron/hole pairs due to minimum required energies for photoexcitation. Considering the results, it can be concluded that the implantation of Ag^+ ions can be adopted as an effective and efficient approach to modify the structural and optoelectronic properties of ZnO NRs for visible light driven photocatalytic applications.

CHAPTER 7: RESULTS AND DISCUSSION III: Carbon ion implanted ZnO NRs

7.1 Overview

In this chapter a detailed study of the structural, morphological and optical properties of carbon implanted ZnO nanorods films is presented. The degree of lattice distortion incurred during ion implantation is investigated by calculating microstructural and crystallographic parameters using a combination of mathematical models expounded in chapter 3. Raman and FTIR spectroscopy have been used to further examine the structural and chemical bonding properties of the carbon implanted ZnO nanorods. The Tauc plot method has been implemented to study the optical band gap of the samples. ZnO nanorods implanted with C^+ ions at fluence of 1×10^{15}, 2×10^{15}, 3×10^{15}, 1×10^{16} and 3×10^{16} ions/cm^2 are hereafter referred to as CIIZ1, CIIZ2, CIIZ3, CIIZ4 and CIIZ5, respectively. The results discussed in this chapter have been submitted for publication in a manuscript format in Optical materials journal.

7.2 Structural Studies of Carbon ion implanted ZnO

7.2.1 XRD analysis

The XRD profiles of the carbon ion implanted ZnO NRs are as shown in Figure 7.1. Diffraction peaks observed across all samples at 2θ angles of about 32.2, 34.8, 36.6, 47.9, 63.3 and 73.2˚ were assigned as the corresponding (100), (002), (101), (102), (103) and (004) planes. The peak positions are considered to be consistent and well matched with a hexagonal wurtzite structure [23] [249] [250] [251]. Furthermore, the acquired XRD profiles depict no secondary phase or carbon related reflections, indicating that the incorporated carbon ions do not alter the fundamental hexagonal wurtzite structure of ZnO.

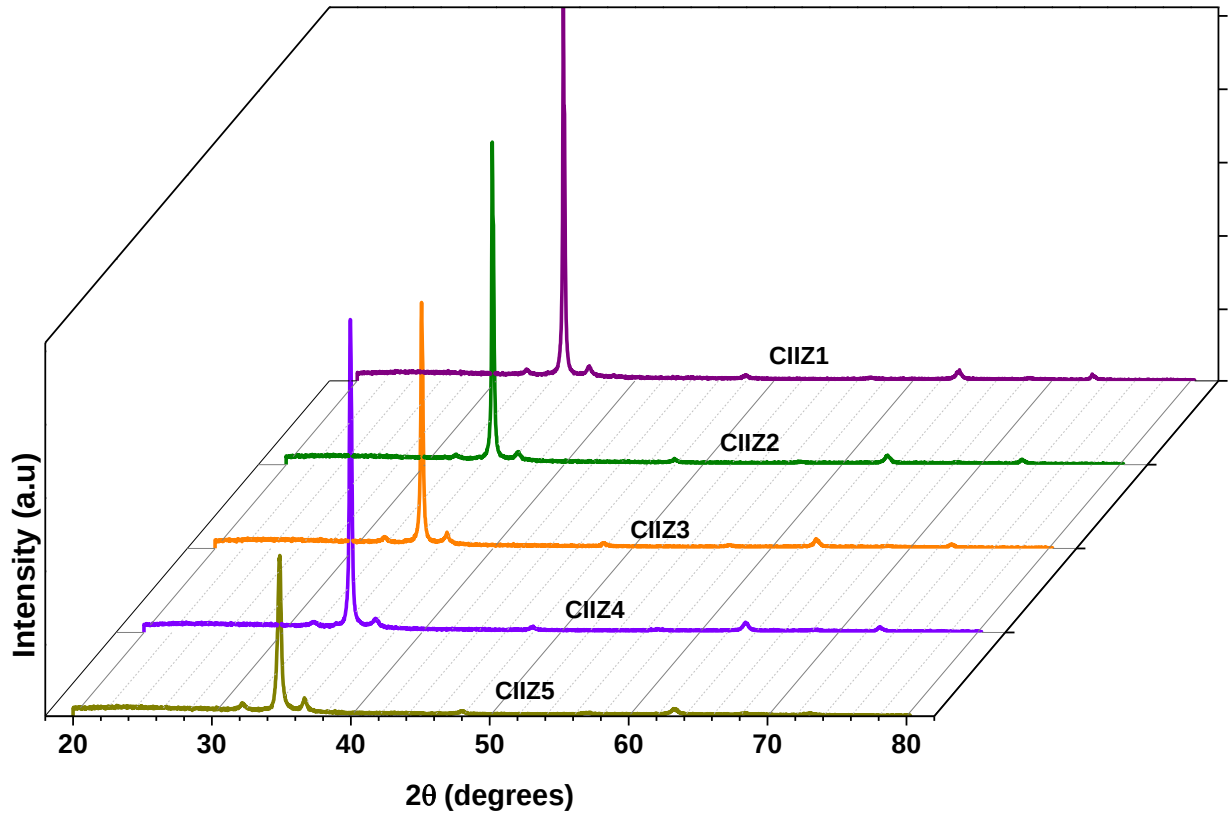


Figure 7.1: 2θ XRD profiles of carbon implanted ZnO at fluences of 1.0 x10^{15} (CIIZ1), 2.0 x10^{15} (CIIZ2), 3.0 x10^{15} (CIIZ3), 1.0 x10^{16} (CIIZ4) and 3.0 x10^{16} ions/cm^2 (CIIZ5).

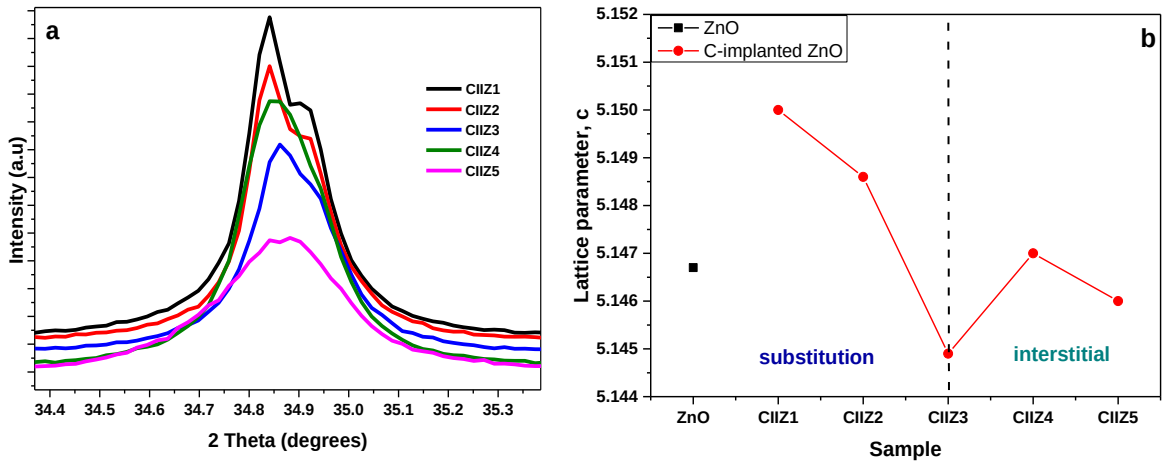


Figure 7.2: (a) Zoomed 002 peak and (b) a plot of the lattice parameter, c_p, of pristine ZnO, CIIZ1 (1.0 x10^{15} ions/cm^2) CIIZ2 (2.0 x10^{15} ions/cm^2), CIIZ3 (3.0 x10^{15} ions/cm^2), CIIZ4(1.0 x10^{16} ions/cm^2), and CIIZ5 (3.0 x10^{16} ions/cm^2).

To investigate the effect of carbon ion implantation on the crystal lattice, parameters of the prominent 002 peak were thoroughly inspected. Significant discrepancies in the peak intensity, peak broadening (FWHM) and peak position, as a function of carbon ion fluence are noted. These inconsistencies suggest lattice distortion as instigated by carbon ion implantation. Non-uniform peak shifting to both lower and higher 2θ angles is noted upon carbon ion implantation. Previous studies have explained that a shift to higher angles denotes substitutional doping, whereas interstitial doping results in the peak shifting to lower 2θ angles [252, 253]. Moreover, the shift in the peak position is an indication of the type of strain induced by the incorporation of dopant ions. Compressive and tensile strain are associated with the occurrence of lattice imperfections, with a shift towards higher angles signifying compressive strain and the latter being characterised by opposite shift towards lower angles [254]. Figure 7.2 shows variation in the peak intensity, accompanied by a noticeable peak width augmentation (FHWM). This observation reflects a reduction in the crystallinity of the films. Similar to Ag^+ ion implantation, implanted carbon ions lose their energy in the ZnO lattice through nuclear collisions and electronic energy loss, resulting in the formation of point defects such as interstitials, vacancies, etc. by displacement of the host atoms which would deteriorate the nanorod crystallinity [255].

The increase in FHWM of C^+ implanted ZnO also suggests a systematic decrease in the crystallite size. It is observed that peak broadening is proportional to the carbon fluence, thus inferring that crystallite deterioration and lattice disordering escalates linearly with an increase in carbon ion concentration. An alteration of the crystallite size of ZnO upon doping has been reported [254, 256]. The microstructural information given in Table 7.1 shows an increase in the interplanar spacing for CIIZ1, CIIZ2 and CIIZ4, showing an expansion of 0.06%, 0.04% and 0.006%, respectively. By comparing the value of the implanted ZnO with that of the pristine ZnO, it is apparent that the CIIZ1 has experienced the highest but not much augmented degree of expansion.

Quantitative estimations of the crystallite size (D_s) and lattice parameters (c) of carbon ion implanted ZnO samples were determined using a series of equations as previously discussed in chapter 3. The lattice parameter c of the C^+ ion implanted samples deviate significantly from that of the unimplanted ZnO NRs film. Expectedly, an alteration to lower angles resulted in increase of the lattice parameter c, signifying lattice expansion. On the other hand, lattice shrinkage was noted for samples which depicted a shift towards higher angles. Previous studies

involving density function theory simulations have projected that implantation of C^+ ions is most likely to result in substitution of the O-atom than Zn-atom, which consequently ensues lattice expansion attributed to the difference in atomic radii of C, O and Zn of ~0.91, 0.63 and 1.53 Å [256-261]. Nevertheless, lattice expansion can also be induced by lattice defects or interstitial occupancy of the implanted ions [257, 262]. Carbon atoms show a remarkable substitution preference at lower fluence of carbon ions [253]. The unlikely substitution of Zn^{2+} ions by implanted C^+ could disrupt the hexagonal crystalline structure.

Table 7.1: Calculated lattice parameters of pristine and C^+ ion implanted ZnO films.

Parameter	**Pristine**	**CIIZ1**	**CIIZ2**	**CIIZ3**	**CIIZ4**	**CIIZ5**
$2\theta^o$ (002)	34.866	34.846	34.853	34.879	34.864	34.871
FHWM (^{o})	0.148	0.169	0.172	0.189	0.200	0.287
D_s (nm)	56.3	49.4	48.3	44.0	41.6	29.0
d- spacing (Å)	2.57336	2.57501	2.57429	2.57244	2.57341	2.57301
a (Å)	3.2131	3.2174	3.2155	3.2171	3.2192	3.2192
c (Å)	5.1467	5.1500	5.1486	5.1449	5.1470	5.1460
δ (lin/m^2)	3.15	4.14	4.26	5.15	5.78	11.86
ε_{zz} x10^{-2} (%)	-	6.40	3.61	-3.61	5.56	-1.39
σ_z (GPa)		-0.290	-0.164	0.164	-0.252	0.631
SF	0.000117	0.000133	0.000136	0.000149	0.000158	0.000226

A negative peak shift of -0.02^o was noted at the lowest fluence (1.0 x10^{15} ions/cm^2). In contrast, at 3.0 x10^{15} ions/cm^2 the uppermost positive shift by 0.013^o resulted in the maximum observed lattice contraction; therefore, it can be suggested that injection of more carbon atoms boosts the possibility of partial substitution of lattice oxygen by carbon atoms as well as the presence of interstitial carbon atoms in the ZnO lattice. Similar trend was established by Kumar et al [253]. who reported that during implantation of C^+ ions in ZnO, at lower fluences carbon ions tend to occupy substitutional sites whereas at higher concentration they partially occupy

interstitial positions. Just like in the case of TiO_2, a stoichiometric ZnO favours the inclusion of C atoms in interstitial locations, while rich in oxygen vacancy ZnO favours the substitutional inclusion of carbon in oxygen occupied sites [263]. The variation in the extracted parameters implies the possibility of implanted C atoms being located at both the substitutional and interstitial (Ci) sites. The results also suggest the possibility of complex defects as induced by the carbon atoms. The calculated microstrain is noted to increase upon introduction of C^+ ions. This growth in the magnitude of the microstrain post implantation is assumed to be due to the generation of defects which induces crystal imperfections, dislocations as well as stacking faults within the ZnO lattice [253].

Table 7.2: The calculated bonding and crystallographic properties of pristine and C^+ ion implanted ZnO.

Parameter	**Pristine**	**CIIZ1**	**CIIZ2**	**CIIZ3**	**CIIZ4**	**CIIZ5**
Positional parameter, μ (Å)	0.3799	0.3801	0.3799	0.3802	0.3796	0.3799
nearest-neighbour bond (Å)	1.9553	1.9576	1.9560	1.9559	1.9538	1.9552
second nearest-neighbour bond-length, L_1 (Å)	3.1914	3.1925	3.1926	3.1890	3.1932	3.1909
Crystal lattice distortion, R	1.0195	1.0202	1.0195	1.0205	1.0183	1.0196
APF (%)	75.490	75.546	75.489	75.563	75.400	75.496
number of the unit cells, n	2 030 560	1 358 891	1 292 156	974 300	824 658	278 539
V	93 484 999	62 774 734	59 551 860	44 893 977	37 881 742	12 820 331

7.2.2 Raman analysis

The structural disorder, residual stress, and crystal defects in the crystal structure of the ZnO was investigated through Raman analysis. The acquired Raman spectra of the samples are as depicted in Figure 7.3. Several factors including spatial confinement, structural disorders and induced defects are known to cause significant shift in phonon frequencies. According to the group theory, a wurtzite ZnO is characterised by six Raman optical modes which are grouped as $A_1+2B_1+E_1+2E_2$ [23]. The two non-polar E_2 modes are known as the E_{2low} and E_{2high}, which are associated with the vibration mode of the Zn sub lattice and oxygen atoms, respectively [151]. Figure 7.4 (a-d) show individual enlarged parts of the spectra to illustrate the peak positions and symmetry of the observed vibrational modes. E_{2low} and E_{2high} are indicated in all samples, and were both noted to decrease in intensity upon the injection of carbon ions. This reduction confirms the existence of carbon impurities which destructs the translational crystal symmetry. In addition, peak shifting and reduction of their intensities have been ascribed to the crystal distortions or defects in the host framework, as induced by the dopant ions [264]. The existence of the E_{2low} and E_{2high} across all samples indicates that the wurtzite structure of ZnO was not destroyed. A disordered phase is noted between 120 and 200 cm^{-1}, shown in Figure 7.4a. This phase was not observed in pristine ZnO and its presence is thus associated with the presence of carbon ions. The polar mode of A1(LO) associated with the defects is shown to be amplified (intensity and FHWM) and shifted to lower Raman shift upon carbon injection. Interstitial carbon induces more complex features compared to substitution carbon [263]. Additional two distinct peaks, ascribed as the disorder (D) and graphitic (G) modes were observed at high ion fluence (CIIZ4 and CIIZ5) at ~1330 and 1600 cm^{-1}. It is hence possible that these peaks are as a result of carbon clusters in the crystal. The two modes are ascribed to the local vibrations of the sp^2 and sp^3 hybridized carbon, respectively [265]. It is also evident that the intensity of G- mode is more enhanced for the CIIZ4 and the intensity decreases for CIIZ5 film. This concurs with what has been previously reported [266]. The degree of graphitization I_D/I_G was calculated, and found to be less than 1, with values of 0.6 and 0.03 for the CIIZ4 and CIIZ5, respectively. This alludes that the carbon ion fluence used did not cause amorphization.

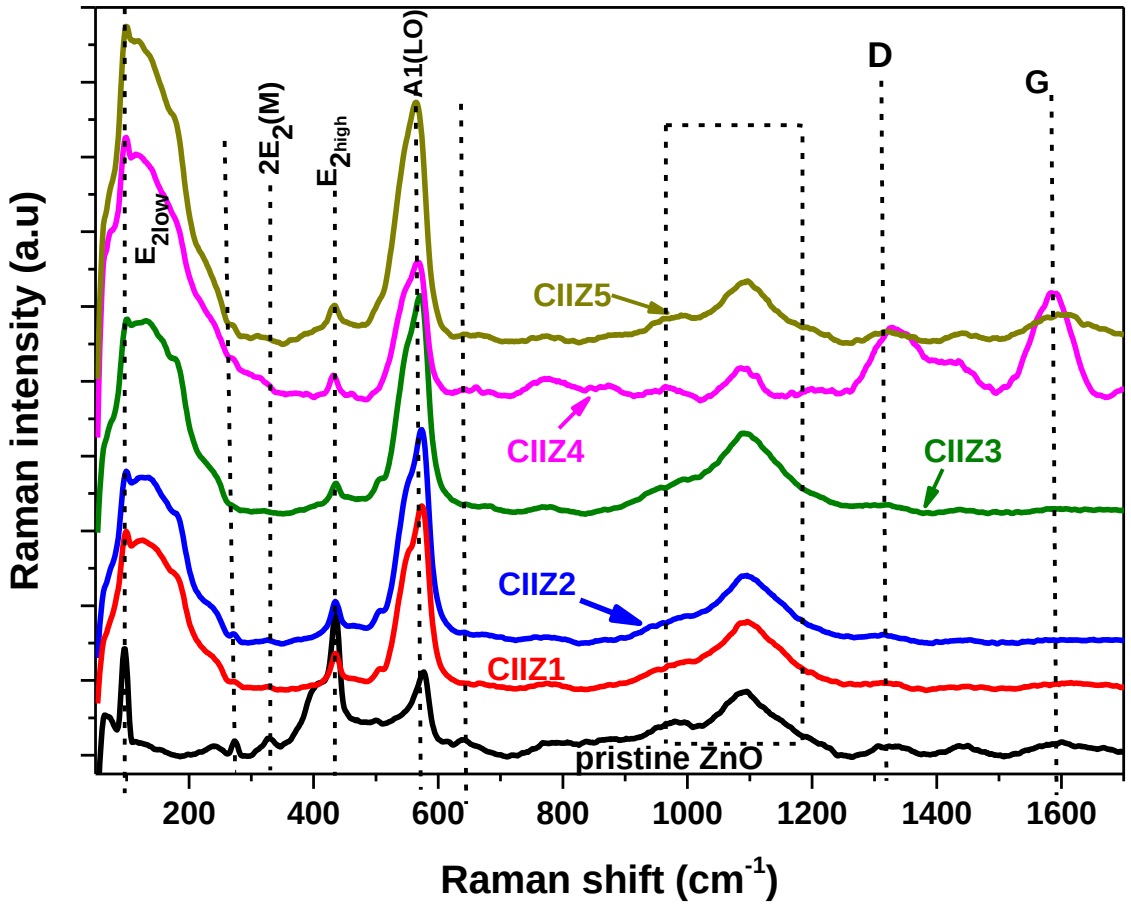


Figure 7.3: Wide range micro-Raman spectra of pristine and carbon implanted ZnO samples. (The purpose of the dotted lines is to assist in observing and tracking the changes related to peak positions and their intensities).

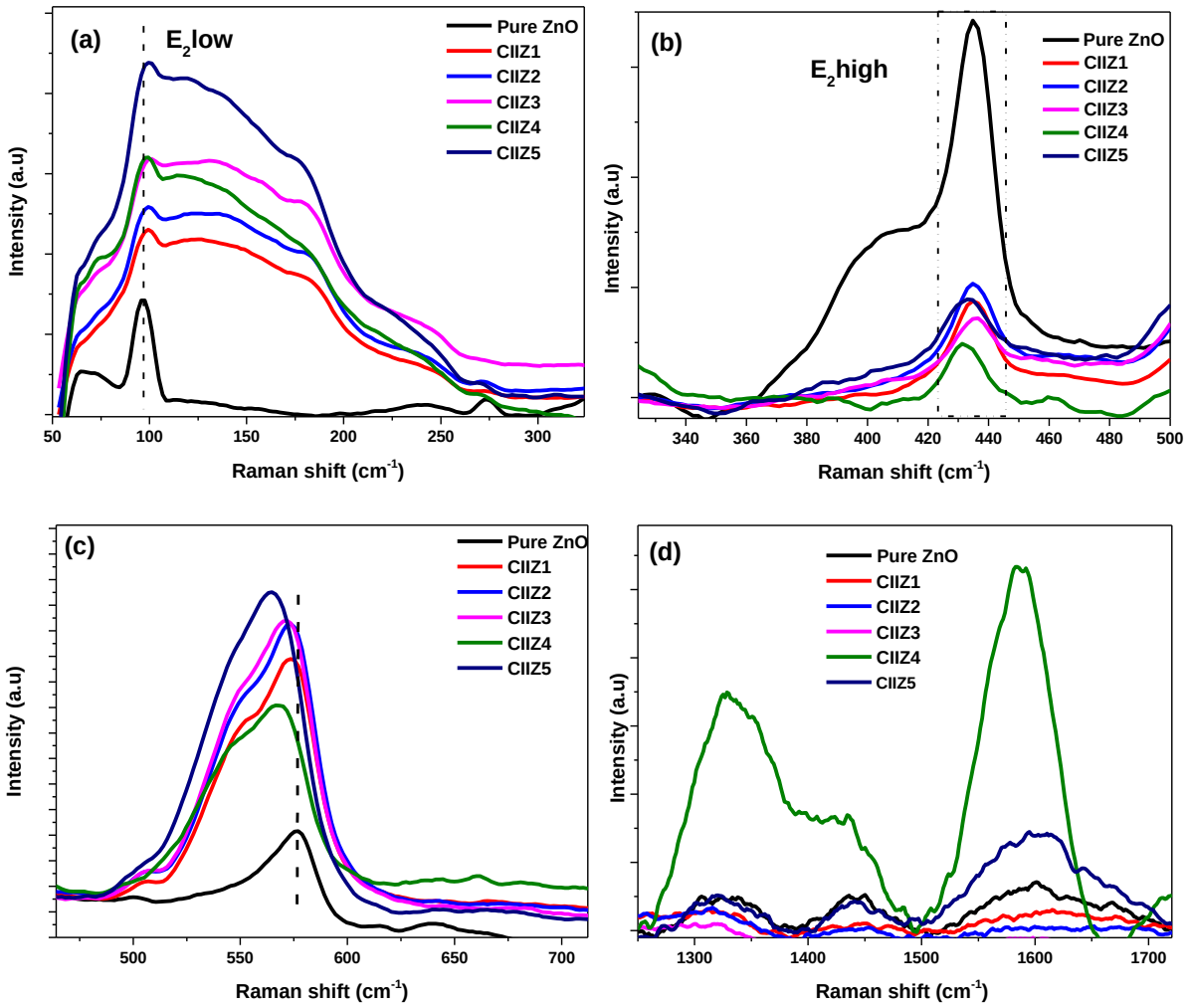


Figure 7.4: Individual enlarged parts of the Raman spectra of pristine and carbon implanted ZnO samples to illustrate the peak positions and symmetry of the observed vibrational modes.

7.2.3 FTIR

The surface chemistry and vibration modes of ZnO and their divergences as influenced by the presence of carbon ions were analysed from acquired IR spectra depicted in Figure 7.5. Several characteristic Zn-O bond peaks were observed at frequencies of below 700 cm^{-1} from all samples. The presence of the carbon implanted molecular species was confirmed through the emergence of additional absorption bands as well as a variation in intensity of the pre-existing peaks, with respect to the carbon composition. The vibration peak at 610 cm^{-1}, ascribed as the Zn-O bond, was noted to degrade substantially with carbon ion implantation and also shifted to higher frequencies at higher carbon ion fluences. Additionally, the decreased absorbances of

the Zn-O peaks with increased carbon fluence suggests the disturbance of the O-Zn-O bond and rearrangement of the chemical bonds within the ZnO films [267, 268]. This is in correlation with the XRD and Raman analysis, as they both indicated that the crystallinity of the films was reduced with increase in carbon fluence. Interestingly, residual bands are noted around 780 and 910 cm^{-1} attributed to the out-of-plane stretching vibrations of the C–O bonds [267]

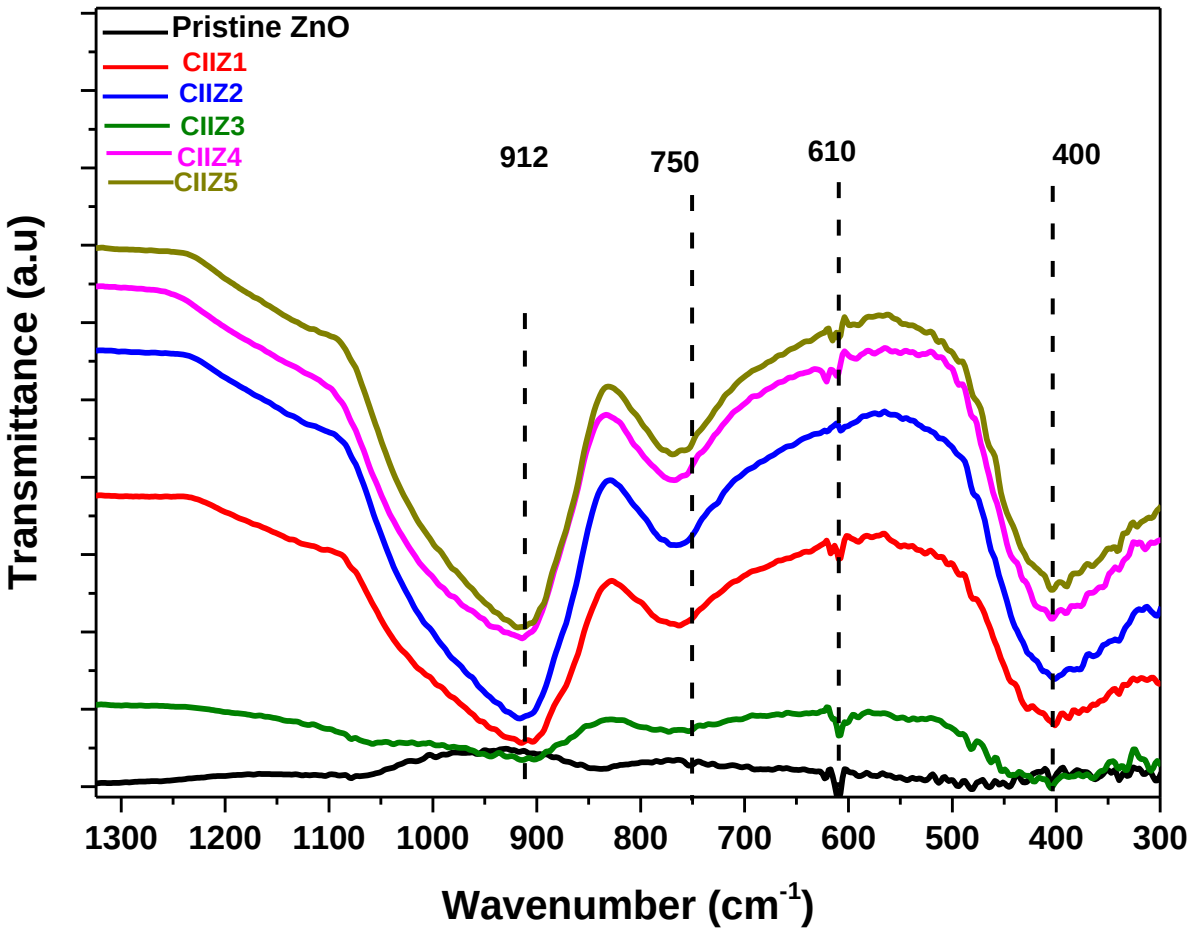


Figure 7.5: FTIR spectra showing variation of the functional groups in carbon ion implanted ZnO at different fluences.

7.3 Morphological Analysis

7.3.1 Field Emission Scanning Electron Microscopy (FESEM)

The effects of carbon ions and ion fluence on the morphology of ZnO is investigated. Figure 7.6 are images obtained using FESEM imaging. Dense vertically aligned nanorods were

observed. The diameters of the nanorods were found to be ranging between 66 and 115 nm. The compositional analysis of the samples was investigated through the EDX technique. A single EDX spectrum of the ZnO implanted with carbon ions at fluence of $1.0x10^{16}$ ions/cm^2 is given in Figure 7.7. The figure shows peaks that correspond to the Zn, O and C atoms. A Si peak is noted, which originates from the substrate. It is worth to note that palladium (Pd) was used for coating the samples to reduce charging effects. EDX analysis showed that the carbon atomic weight percentage is increasing.

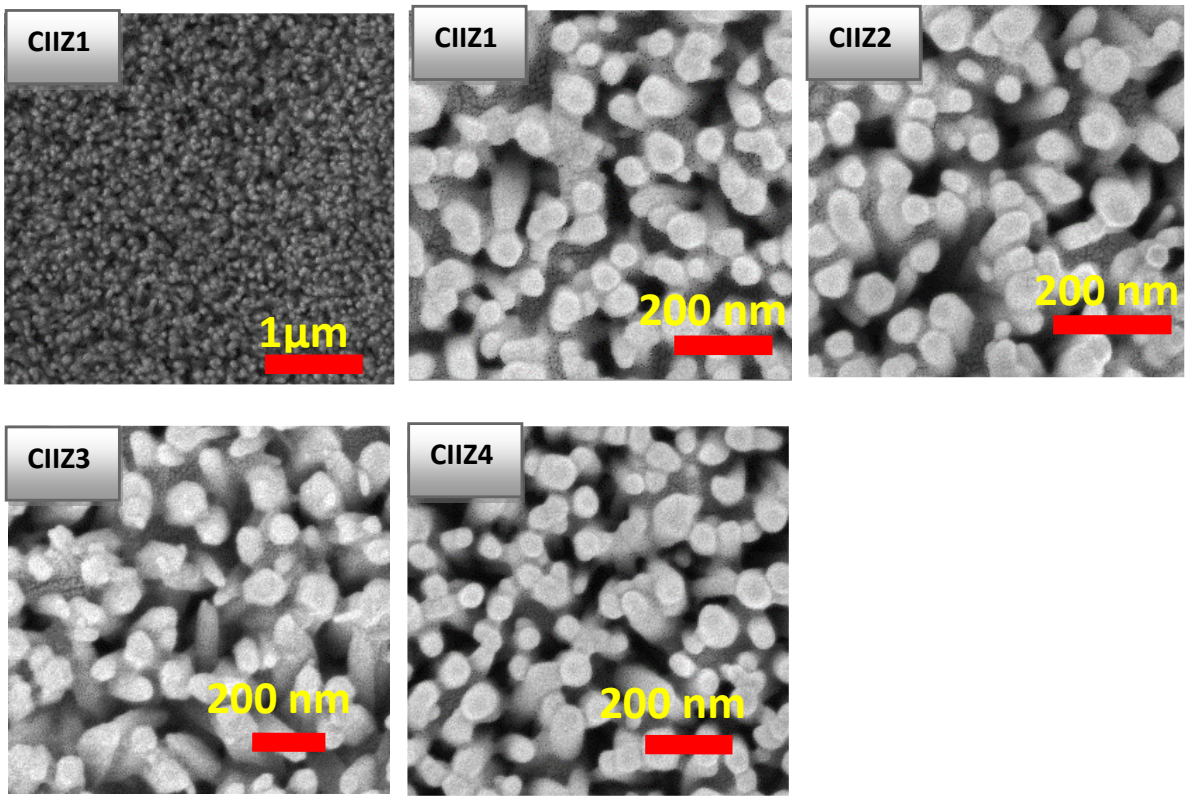


Figure 7.6: High magnification field FESEM micrographs of carbon implanted samples at 1.0 x 10^{15} (CIIZ1), 2.0 x 10^{15} (CIIZ2), 3.0 x 10^{15}(CIIZ3) and 1.0 x 10^{16} (CIIZ4).

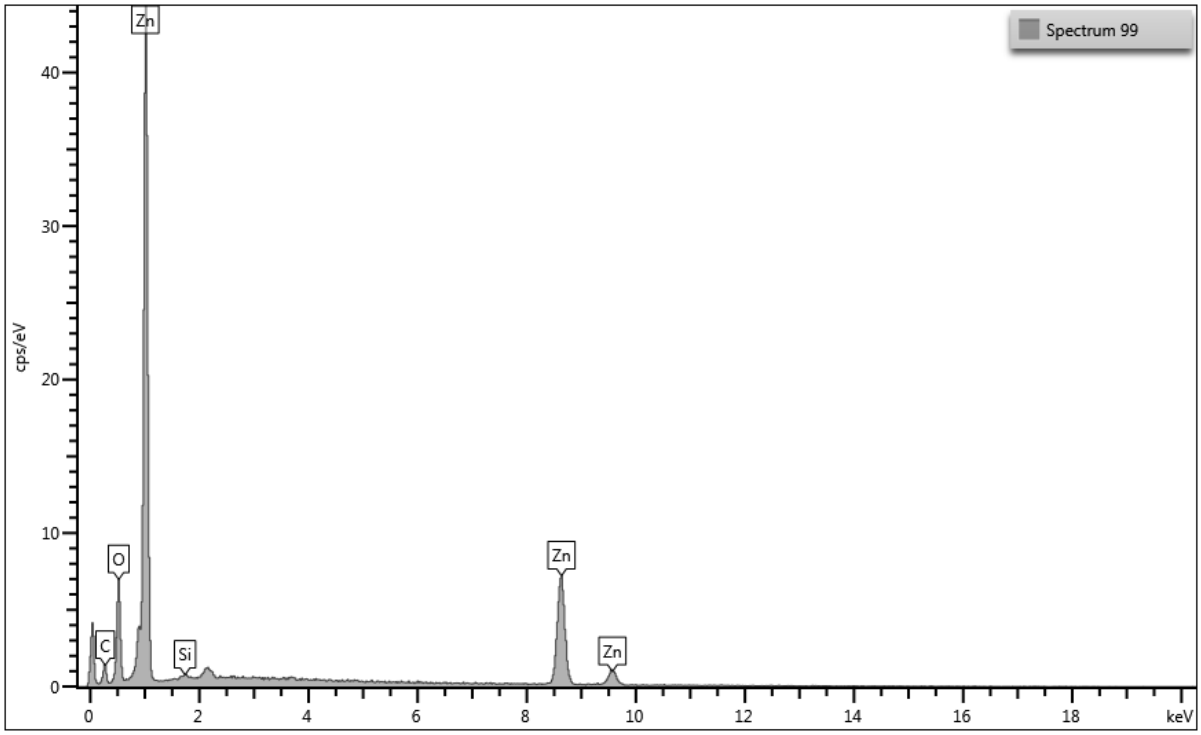


Figure 7.7: EDX spectrum and elemental mapping analysis of ZnO NRs implanted with carbon ions at fluence 1.0 x10^{16} ions/cm^2.

7.3.2 Atomic Force Microscopy (AFM)

AFM was employed to study the surface morphology of the carbon implanted ZnO films. Figure 7.8 shows 3D surface topography images of ZnO films before and after C^+ ion implantation. All the images show well defined vertically aligned structures, which is in agreement with the FESEM analysis. Some variation in the appearance of these structures is noted. CIIZ1 and CIIZ2 show very sharp tips, however the sharpness tends to decrease upon implantation of a higher fluence of carbon ions. The specific statistical analysis of the AFM micrographs (1 ×1 μm^2), given in Table 7.3 indicates a variation of morphological parameters. As the implanted carbon ion fluence increases, there is a significant decline of the surface roughness. Only the ZnO implanted at fluence 3.0 x10^{16} ions/cm^2 showed an increase in the surface roughness. This increase in R_{rms} indicates the possibility of the formation of the micro-void structure on the growing films. On the other hand, another contributing factor of increased roughness during ion bombardment could be the surface diffusion processes. The length of the nanorods is also noted to change upon ion implantation.

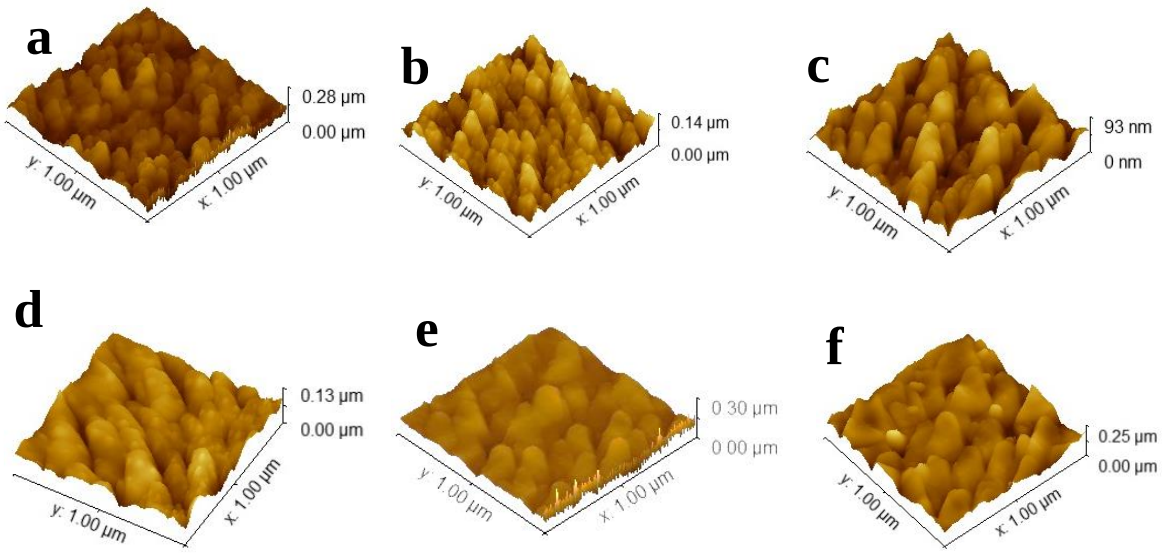


Figure 7.8: 3D topography images of (a) pristine and carbon implanted samples (from b-f) at 1.0 x 10^{15}, 2.0 x 10^{15}, 3.0 x 10^{15}, 1.0 x 10^{16} and 3.0 x 10^{16} ions/cm^2.

Table 7.3: Variation of AFM parameters of carbon ion implanted ZnO.

C^+ ion fluence (ions/cm^2)	R_a (nm)	R_{rms} (nm)	Grain height (nm)
Pristine	122.2	18.69	278.20
1 x10^{15}	57.8	16.39	234.65
2 x10^{15}	47.5	11.59	331.81
3 x10^{15}	54.1	12.78	426.99
1 x10^{16}	103.3	14.92	292.35
3 x10^{16}	104.9	22.03	345.65

7.4 Optical properties of C^+ ion implanted ZnO NRS

7.4.1 Absorbance

The efficiency of semiconducting metal oxides in photo-induced applications is influenced by the photon absorption as well as the utilization of the photogenerated charge carriers. Figure 7.9 shows the spectral dependence of the absorption and transmittance of ZnO NRs on C^+ ion films, acquired in the wavelength range of 300-1000 nm. An enhancement and strong

absorption as a result of carbon ion implantation is depicted in Figure 7.8a. A progressive shift towards longer wavelengths is also noted with the transmittance spectra due to the creation of atomic dislocations and/or structural imperfections induced by the implantation of C atoms in the ZnO matrix [269]. These observations suggest that the band gap of ZnO is reduced as a result of implantation. An average transmittance of 70% was recorded for pristine ZnO in the visible region. However, upon carbon impingement into the ZnO lattice, the transmittance is seen to exponentially decrease up to 55%.

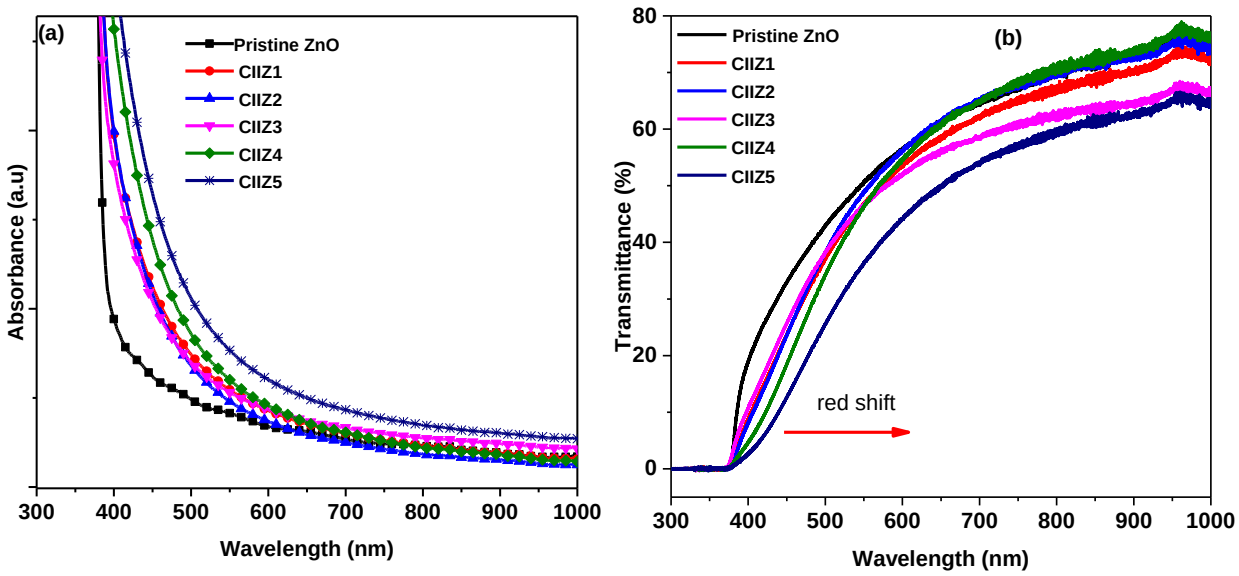


Figure 7.9: Absorbance and transmittance spectra of pristine and 50 KeV C^+ ion beam implanted ZnO thin films at various ion fluences.

The attenuation in the transmittance due to ion irradiation has been observed and associated to the presence of defects, the surface roughness and also the damage produced by ion implantation. Zhang et al [270] has summarised the poor transmittance of carbon implanted ZnO films to be as a result of increased light scattering as persuaded by the presence of crystal defects. The influence of the morphology, surface roughness and scattering from surface as well as the presence of impurities and lattice structure defects on the photon absorption rate is scrutinized. There was a noted gradual decrease of the crystallite size upon C^+ ion implantation,

and the variation of both the transmittance and absorbance spectra is not directly relative to the crystallite size, hence the possibility of the correlation of the quantum confinement effect with optical properties is ruled out for this study. However, the possibility of contributions from the lattice distortion or defects cannot be excluded.

7.4.2 Absorption (α) and extinction coefficient (k_x)

The effect of the C^+ ions was investigated through calculation of the absorption coefficient (α) and the extinction coefficient (k_x). The dependence of the absorption coefficient of the carbon implanted ZnO on the photon energy is as presented in Figure 7.10. The plots demonstrate that both α and k_x are more pronounced for carbon implanted samples compared to virgin ZnO, even though the increase is not linearly dependent on the ion fluence. The variation in the absorption and extinction coefficients reveal that the carbon ions are definitely incorporated into the ZnO lattice thus modifying its crystal and electronic structures.

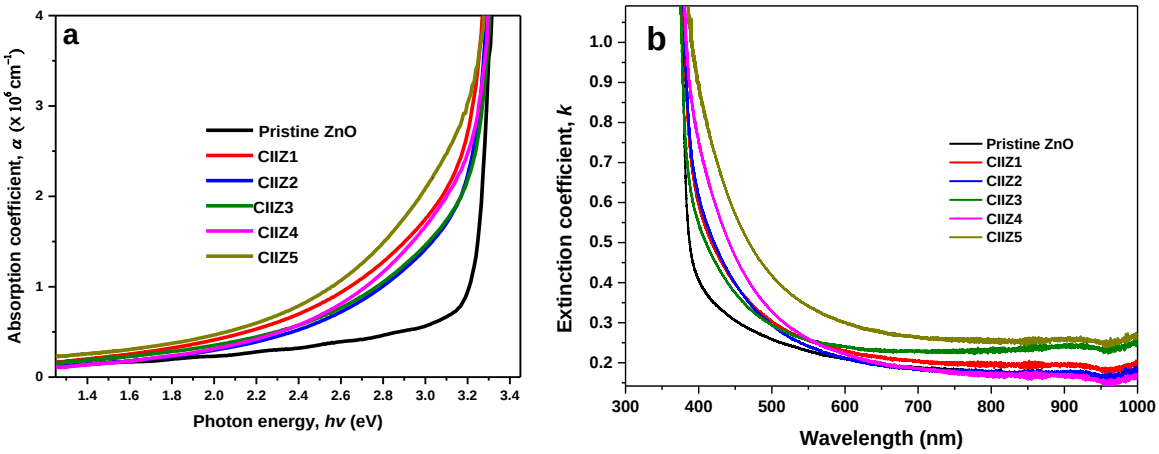


Figure 7.10: Spectral (a) optical absorption and (b) extinction coefficients of pristine and 50 KeV C^+ ion beam implanted ZnO thin films with varying ion fluence.

7.4.3 Optical band gap

The calculated absorption coefficient (α) was used to determine the optical band gap of the carbon implanted ZnO NRs. The linear part of the Tauc' plots (given in Figure 7.11) was extrapolated to estimate the optical band gap. A disparity is noted, with values of 3.20, 3.22, 3.25, 3.17 and 2.97 eV estimated as the optical band gaps of C^+ implanted ZnO at fluence of 1 $x10^{15}$, 2 $x10^{15}$, 3 $x10^{15}$, 1 $x10^{16}$ and 3 $x10^{16}$ ions/cm^2, respectively. The results show that the

band gap decreases upon carbon addition with a maximum reduction of 9% recorded at a fluence of 3 x10^{16} ions/cm^2.

The substantial difference in the optical band gap of carbon implanted ZnO can be explained by considering the C^+ induced modifications. A reduced band gap facilitates rapid photoexcitation of electrons from the conduction band, hence resulting in an increase in the electron flow [255]. Several factors are discussed as possible band gap reduction mechanisms; however, it should be noted that without further analysis it will be difficult to possibly conclude on a distinct mechanism. Substitution of carbon species into the ZnO lattice introduces isolated impurity bands of C (2p) between the conduction and valence bands, which often appear above the Fermi level [271]. These states serve as freeway for electrons to swiftly transfer into the CB upon photoexcitation. Additionally, a bandgap diminution has been attributed to oxygen vacancies generated during ion implantation [272]. The existence of free carbon and other defects present also contribute to the constriction of the band gap. CIIZ4 and CIIZ5 have the lowest band gaps, and features attributed to the graphitic carbon were noted from their Raman spectra. The optical band gap change may also be contributed by the change of the bond lengths and angles.

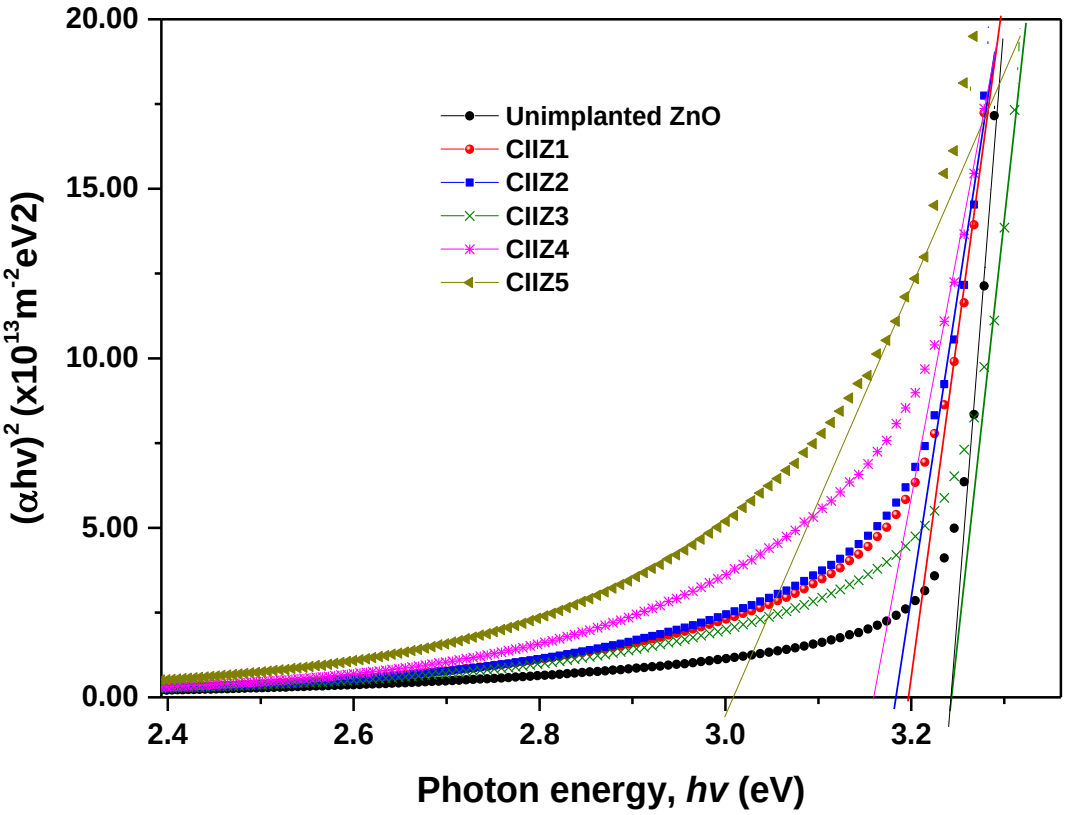


Figure 7.11: Tauc plots for optical band gap determination for pristine and ZnO NR films implanted with carbon ions of fluences of 1.0 x10^{15}, 2.0 x10^{15}, 3.0 x10^{15}, 1.0 x10^{16} and 3.0 x10^{16} denoted as CIIZ1, CIIZ2, CIIZ3, CIIZ4 and CIIZ5, respectively.

7.4.4 Urbach energy

A linear fit of the plot given in Figure 7.12 was used to determine the Urbach energy (E_u). Contrary to the expected results, the calculated E_u were found to decrease upon carbon ion implantation, however there seem to be no dependency of the E_u on the concentration of the implanted carbon ions. The reduction in E_u means a decrease in the population of surface-related defects. This may be caused by the interaction of implanted carbon atoms to the neighbouring lone O 2p states of O atoms thus creating C-O bonds by either the substitution of C atoms at the Zn-vacancies or interstitial defects of Ci. Therefore, reduced unpaired/dangling O 2p bonds or V_{Zn} means a reduction in the defects produced. The observed E_u trend is analogous to our previous studies on Ag^+ ion implantation [255].

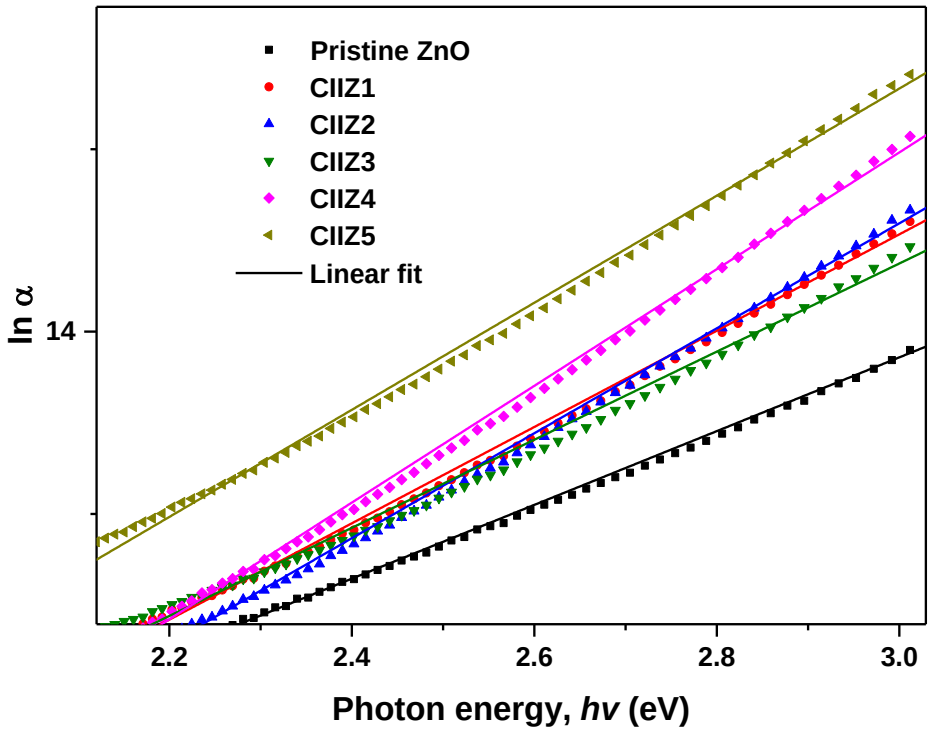


Figure 7.12: Photon energy dependence of ln α for pristine and ZnO NR films implanted with carbon ions at fluences of 1.0 x10^{15}, 2.0 x10^{15}, 3.0 x10^{15}, 1.0 x10^{16} and 3.0 x10^{16} denoted as CIIZ1, CIIZ2, CIIZ3, CIIZ4 and CIIZ5, respectively.

7.4.5 Skin depth and optical conductivity

The variation of two important parameters related to the absorption of photons within the thin films, i.e., the skin depth and optical conductivity, were investigated. As previously defined in chapter 6, the skin depth also known as the penetration depth (ϕ) is simply defined as the depth beneath the surface. This parameter is influenced by the dimensions of the frequency and the conductivity of the incident wave. Figure 7.13 illustrates discrepancies of the calculated skin depth for pristine and C^+ ion implanted ZnO NRs. The graph depicts a clear reduction of the skin depth as both the photon energy and fluence of C^+ ions increase. It is also observed that the optical conductivity, shown in Figure 7.14 increases substantially with the increase of the photon energy. With emphasis on the effect of the implanted C^+ ions, the optical conductivity is noted to be more enhanced at higher fluence of C^+ ions. The increase of the optical conductivity at higher energies is attributed to electrons excited by photon energy [273].

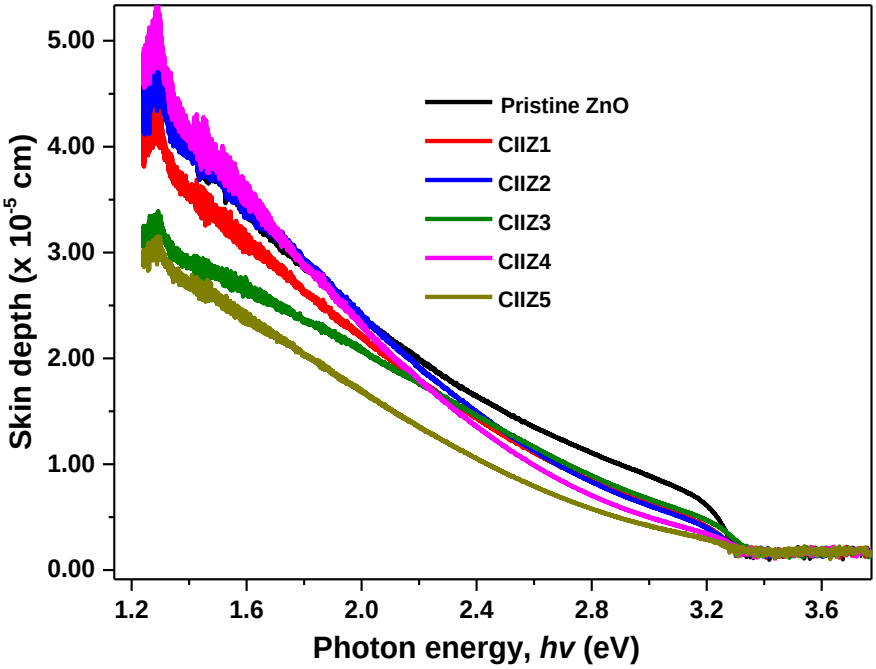


Figure 7.13: Photon energy dependence of skin depth for pristine and ZnO NR films implanted with carbon ions at fluences of 1.0 x10^{15}, 2.0 x10^{15}, 3.0 x10^{15}, 1.0 x10^{16} and 3.0 x10^{16} denoted as CIIZ1, CIIZ2, CIIZ3, CIIZ4 and CIIZ5, respectively.

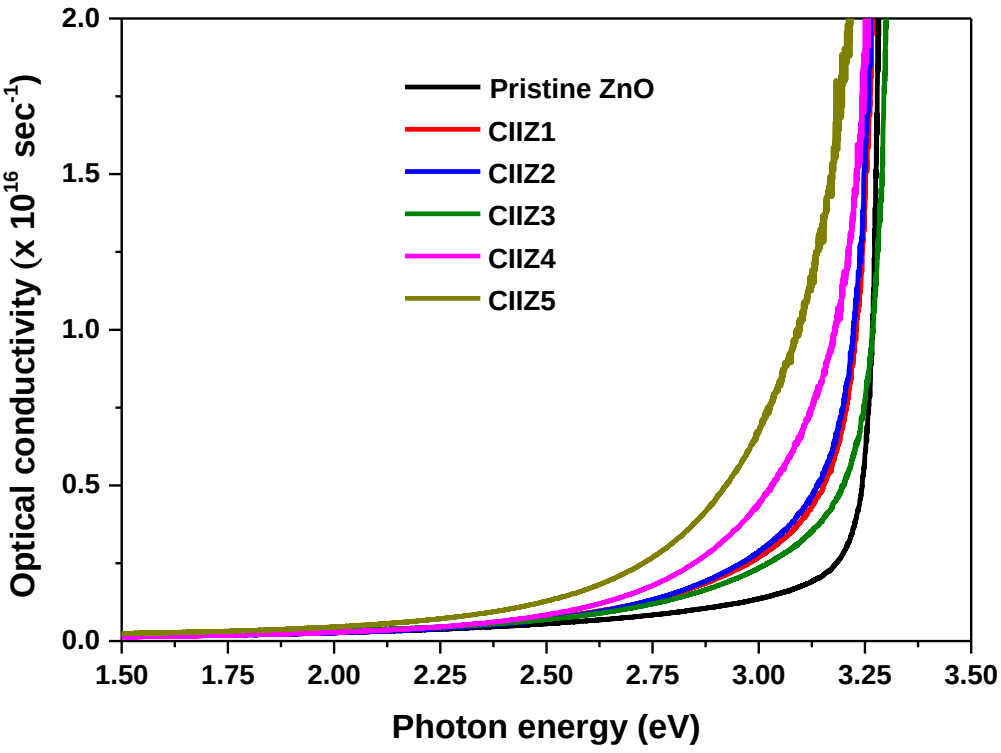


Figure 7.14: Photon energy dependence of skin depth for pristine and ZnO NR films implanted with carbon ions at fluences of 1.0 x10^{15}, 2.0 x10^{15}, 3.0 x10^{15}, 1.0 x10^{16} and 3.0 x10^{16} denoted as CIIZ1, CIIZ2, CIIZ3, CIIZ4 and CIIZ5 respectively.

Table 7.4: Calculated optical band gaps (E_g) and refractive index (n) of pristine and C^+ ion implanted samples.

Sample ID	E_g (eV)	E_u (meV)	n
Pristine ZnO	3.25	896	2.069
1.0 x 10^{15} CIIZ	3.20	759	2.100
2.0 x 10^{15} CIIZ	3.22	695	2.088
3.0 x 10^{15} CIIZ	3.25	828	2.069
1.0 x 10^{16} CIIZ	3.17	625	2.119
3.0 x 10^{16} CIIZ	2.97	681	2.174

Carbon (C^+) ions were successfully implanted onto the ZnO lattice structure. Analysis of the XRD interfaces, Raman and FTIR spectra indicate a variation in crystallographic and microstructural parameters, confirming the successful implantation of C^+ ions in the ZnO and the induced lattice damage thereof. The crystallite size was found to decrease from 56.3 to 29.0 nm. The decrease in the crystallite size is exceptionally dependent on the fluence of the impinged C^+ ions, whereas other structural parameters such as the strain and lattice constants are influenced by the location of the implanted ions in the ZnO lattice. The obtained data suggests a substitutional settling at lower fluences and interstitial settling at higher fluences, which resulted in lattice expansion and compression, respectively. Bombardment of the C^+ ions result in an enhancement of the optical absorption in the visible light region and a redshift of the optical band gap. A significant reduction of the optical band gap from 3.25 eV to 3.08 eV was also observed. The decrease was associated to the creation of the impurity band between the conduction band and the valence band. Moreover, contributions of various mechanisms for band gap variations are discussed. The results demonstrate a strong correlation between the induced lattice distortions and the optical properties. We thus conclude that ion implantation of ZnO with C^+ ions at a low energy of 50 KeV induces structural damage which leads to changes in the optoelectronic properties.

CHAPTER 8: RESULTS AND DISCUSSION IV- Silver (Ag^+) and Carbon (C^+) co-implanted ZnO nanorods

8.1 Overview

Chapters 6 and 7 have discussed the effects of mono Ag^+ and C^+ ions implantation on the structural, morphological and optical properties of ZnO nanorods. In this chapter, results on the co-implantation of the two ions are discussed. The impact of co-implantation on the structure of ZnO was studied through analysis of calculated microstructural and geometric crystallographic parameters from the measured XRD profiles. The FTIR and Raman spectroscopy were used to corroborate the microstructural analysis. This chapter further discusses the variation of morphology in ZnO thin films following 50 KeV Ag^+- C^+ co-implantation which caused substantial modification of the optical properties such as the absorbance, energy band gap and the optical conductivity.

8.2 Structural properties

8.2.1 X-ray diffraction (XRD) studies

X-ray diffraction profiles of Ag^+-C^+ co-implanted ZnO NRs are presented in Figure 8.1. The XRD profiles exhibit similarities, and the peaks are indexed to a hexagonal wurtzite structure [274-276]. This implies that co-implantation of Ag^+ and C^+ ions in the ZnO lattice did not change its wurtzite structure. Increasing the ion fluence results in a drastic decrease of the intensity of the 002-peak, indicating an alteration of the crystal quality. The observed profiles infers that the implanted fluence is less than the amorphization threshold as the preferred c-axis orientation was not totally disrupted by the presence of the co-implanted ions. Neither phase transformation nor new phase segregation is observed. The broadening of the 002 upon co-implantation of ZnO exhibits a very similar behaviour as previously reported for Ag^+ or C^+ single ion implantation [253, 255, 277]. The phenomenon signals grain size reduction and/or decrease in the lattice volume fraction.

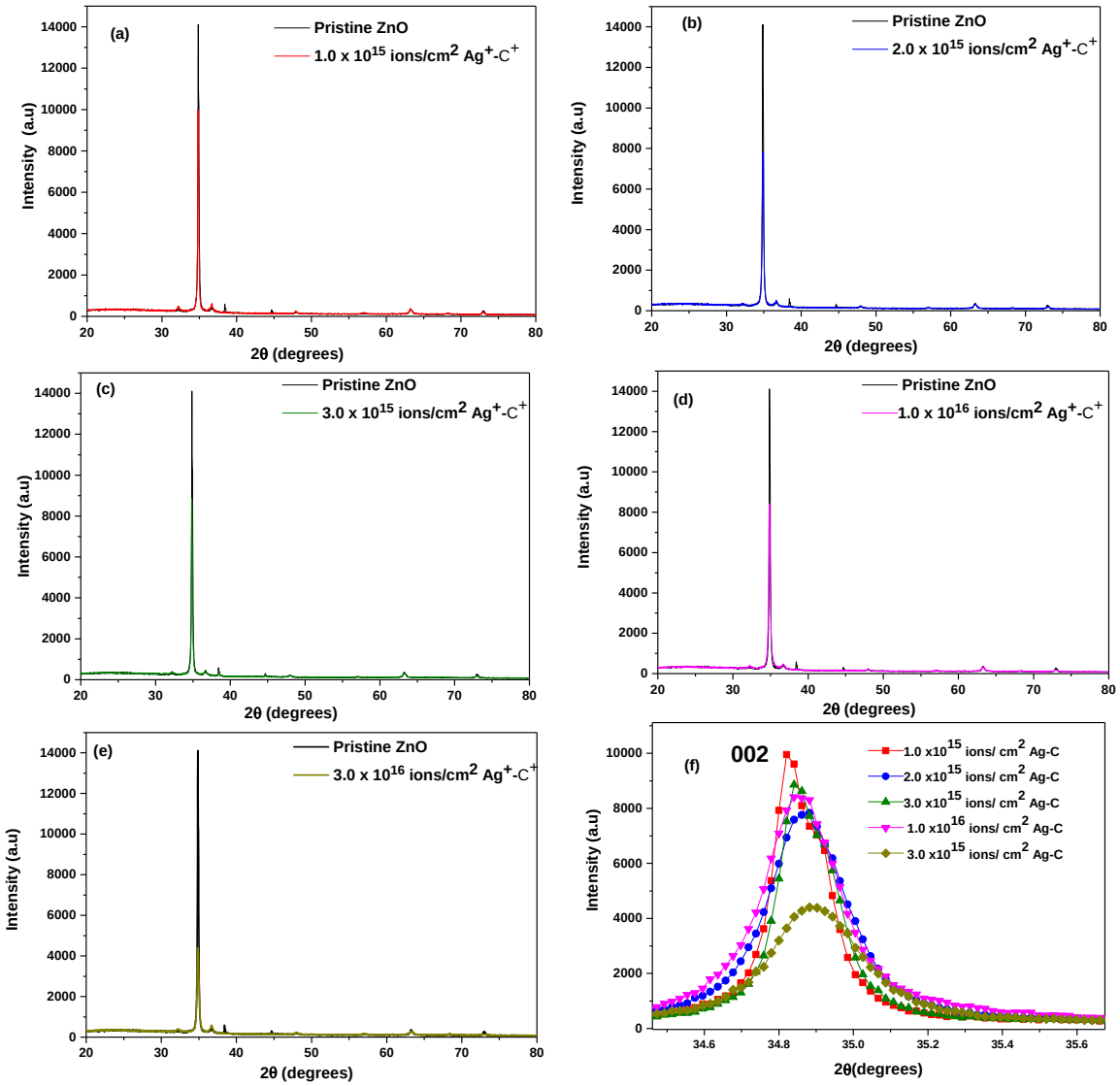


Figure 8.1: (a-e) XRD profiles of the Ag^{+}-C^{+} co-implanted ZnO films at varying fluences as labelled. (f) detailed inspection of the 002 peak of 1 x10^{15}, 2 x10^{15}, 3 x10^{15}, 1 x10^{16} and 3 x10^{16} ions/cm^2 Ag^{+}-C^{+} co-implanted ZnO film.

The observed peak shifting is strongly credited to the charge transfer happening amid edge terminated lone pairs of the ZnO and implanted ions which induces lattice distortion [278]. The contribution of the nature of the strain type and its effects on lattice distortions and defect formation are more emphasised by variation of the peak position and the interatomic d-spacing. The simultaneous broadening and shifting of the reflection planes can be measured to estimate the microstrain and lattice parameters. The change in the intensity and FWHM of the prominent 002 peak with ion fluence is illustrated in Figure 8.2.

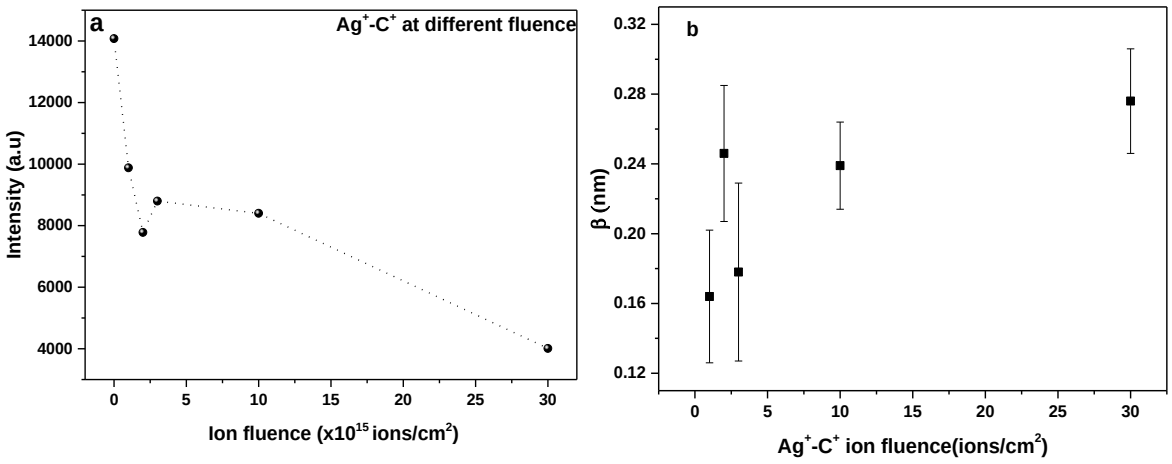


Figure 8.2: A plot to show the change of (a) the 002 peak intensity and (b) the ion fluence for ZnO NRs samples co-implanted with Ag^+ and C^+ ions at 50 KeV (dashed lines are drawn as a guide).

Lattice strain is calculated to estimate the effect of the ion implantation, hence in equation 3.13, the c_{bulk} and c_{film} were taken as the lattice parameter c_p of the pristine and implanted sample, respectively. Lattice distortion as a result of co-implantation of Ag^+ and C^+ ions is established, represented by the change of various calculated parameters from equations previously discussed in section 3.4.1. The deviation of atoms from their ideal sites in the host framework, causes change in the atomic distances relative to the pristine ZnO film. Ag^+ ions exhibit much affinity for substituting Zn^{2+}, whereas C^+ ions preferentially substitute O^{2-} or settles interstitially [253, 279]. Additionally, SRIM results have predicted that at the same energy and fluence, Ag^+ and C^+ ions have different depth penetration(range) and produce different levels of collision events. Co-implantation of these two ions results in non-uniformly distributed lattice distortion.

Results in Table 8.1 and Table 8.2 indicate that the calculated microstructural parameters of the co-implanted ZnO NRs follows a similar trend. For instance, an increase is initially noted for the bond length (L), the lattice parameter a_p, and the stacking fault probability at fluences of 1 x10^{15} and 2 x10^{15} ions/cm^2. However, at 3 x 10^{15} ions/cm^2 an opposite effect is noted as a decline is observed. Upon increasing the fluence to 1 x10^{16} ions/cm^2 and 3 x 10^{16} ions/cm^2, an increase reoccurs for the aforementioned parameters. Considering the effect of the fluence of the co-implanted ion species on the crystallite size, a decrease from 56.3 nm to 50.8 and 33.9 nm is observed at lower fluences of 1 x10^{15} and 2 x10^{15} ions/cm^2, respectively. At fluence of 3 x 10^{16} ions/cm^2 the crystallite size is noted to increase. This increase however, is still below

the crystallite size of the pristine sample. A further decrease is noted after implanting at fluences of 1 x10^{16} ions/cm^2 and 3 x 10^{16} ions/cm^2, with 30.1 nm as the lowest calculated D_s.

Table 8.1: XRD extracted crystal parameters: the position of the 002 peak, interplanar spacing (d), FWHM (β), average crystallite size (D_s), and lattice parameters (a_p and c_p) for ZnO NR films co-implanted with Ag^+ and C^+ ions.

Fluence (ions/cm^2)	**2θ (002) (º)**	**d (Å)**	**β (º)**	**D_s (nm)**	**Lattice para. a_p; c_p (Å)**	**Lattice constant (c/a)**
Pristine	34.866	2.5734	0.148	56.3	3.2131; 5.1467	1.602
1.0 x10^{15}	34.836	2.5755	0.164	50.8	3.2168; 5.1510	1.601
2.0 x10^{15}	34.873	2.5729	0.246	33.9	3.2173; 5.1457	1.599
3.0 x10^{15}	34.864	2.5735	0.178	46.8	3.2141; 5.1470	1.601
1.0 x10^{16}	34.858	2.5739	0.239	34.9	3.2158; 5.1479	1.601
3.0 x10^{16}	34.896	2.5712	0.276	30.1	3.2178; 5.1424	1.598

Table 8.2: XRD analysis microstructural parameters of Ag^{+}-C^{+} co- implanted ZnO films.

Parameters	**Ag^{+}-C^{+} co-implantation fluence (ions/cm^2)**					
	pristine	**1.0 x10^{15}**	**2.0 x10^{15}**	**3.0 x10^{15}**	**1.0 x10^{16}**	**3.0 x10^{16}**
Lattice strain, ε_{zz} x10^{-2} (%)	-	8.34	-1.95	0.556	2.22	-8.33
Biaxial stress, σz	-	-0.378	0.0845	-0.0252	-0.107	0.378
Dislocation density (x10^{14} lin/m^2)	3.15	3.87	8.71	4.56	8.22	11.01
u_c	2030560	1486633	441985	1165692	483144	313469
Positional parameter μ (Å)	0.37992	0.38000	0.38031	0.37999	0.38008	0.38052
Bond length L (Å)	1.9553	1.9574	1.9570	1.9558	1.9566	1.9568
L_1 (Å)	3.1914	3.1936	3.1888	3.1912	3.1913	3.1857
L_2 (Å)	3.7613	3.7655	3.7658	3.7624	3.7643	3.7661
L_3 (Å)	3.7613	3.7655	3.7658	3.7624	3.7643	3.7661
Stacking fault (SF)	0.00117	0.00129	0.00194	0.00140	0.00189	0.00218

8.2.2 Raman Spectroscopy

The lattice dynamics of the ZnO NRs are expounded focused on the Raman-active optical phonon modes. The identified Raman modes depicted in Figure 8.3 are classified according to the Brillouin centre theory [280]. Common Raman modes previously reported as ZnO peaks are noted on the co-implanted spectra [23, 281-283]. These observed Raman peaks confirm the hexagonal wurtzite structure which is in sync good agreement with the XRD analysis. Variations are noted in the previously observed strong scattering of the E_2 modes (E_{2low}, E_{2high}), which are considered as the Zn and O sublattices, respectively. A decrease in the phonon scattering of the E_2 modes is concurrent with an increase of the disordered region. This depiction is associated with structural disorder, grain boundaries and internal stress [284, 285]. Similarly, the A_1(LO) phonon frequency is also strongly sensitive to the presence of impurities and alteration of the free carrier concentration [233]. The displacement of the anion (O^{2-}) sublattice is the crucial derivation for the broadening and shifting of the E_{2high} mode [286]. The

intensity of both the E_{2low} and E_{2high} modes appears to be suppressed upon ion implantation, and this is observed to be dependent on the ion fluence. Similar observations for the degradation of the E_2 high mode are reported upon Li, N co implantation of ZnO [287].

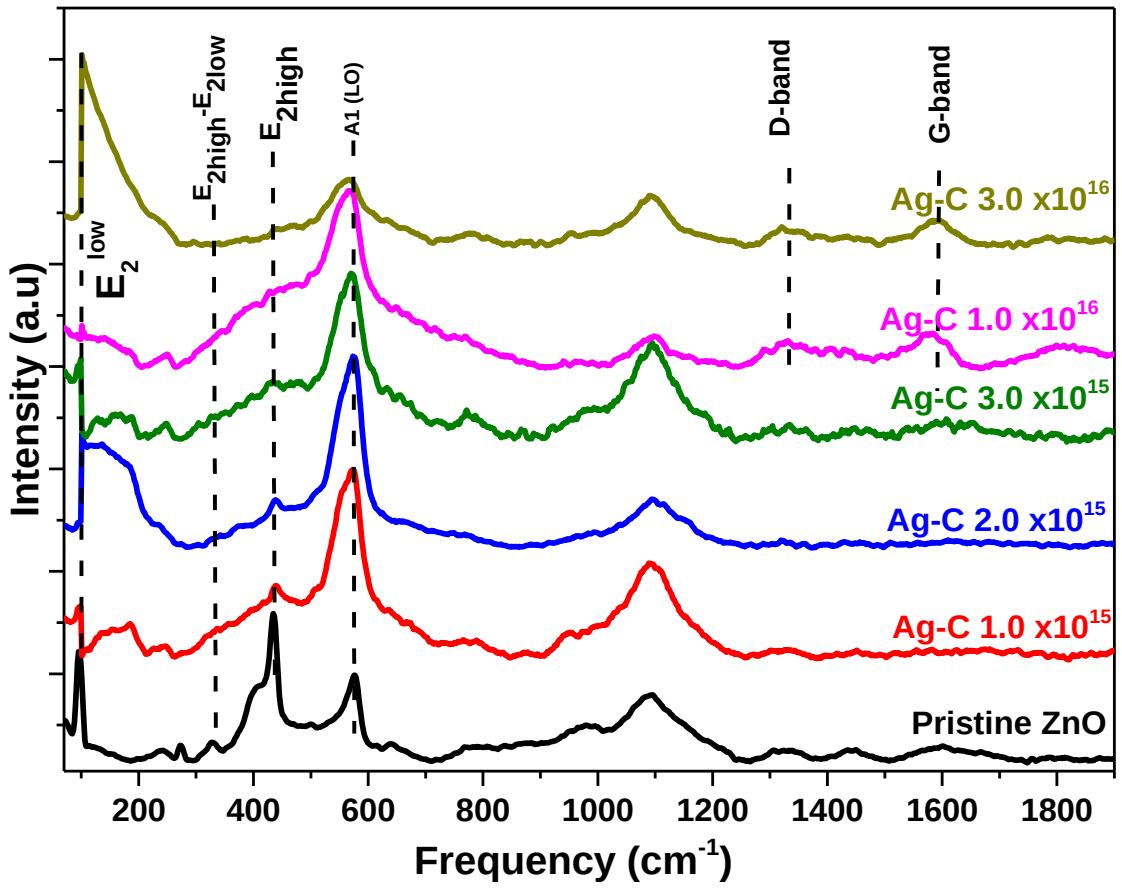


Figure 8.3: Raman spectra measurements ZnO nanorods co-implanted with Ag^+ and C^+ ions, using fluences of 1×10^{15}, 2×10^{15}, 3×10^{15}, 1×10^{16} and 3×10^{16} ions/cm^2 (energy 50 KeV). For comparison, a spectrum of pristine ZnO NRs is also shown.

Strain can possibly affect the electronic band structure, density of electronic states and phonon dispersion of lattice vibration [288]. The presence of induced strain manifest in Raman spectra through shifting and broadening of specific phonon modes. Other factors such as distortions in the lattice parameter and associated bonds strength should also be invoked for consideration of contributing to the variation in the vibrations of the Raman spectra. The strength of the A_1(LO) peak is shown to be enhanced with increasing ion fluence. Overall, lower fluence gives a higher intensity than the higher fluence used. It is observed that the peak intensity decreases with

increasing ion fluence up to 3×10^{15} ions/cm^2, then it intensifies with a further increase in the fluence. From this observation, we can argue that increasing the amount of the dopants results in adequate accumulation of lattice distortions to a certain threshold value as noted by the upsurge in the intensity of the defect peak (A1 LO) at 1 x 10^{15} ions/cm^2 and 2 x 10^{15} ions/cm^2. Introducing more ions above the threshold results in a decrease of this defect related peak, insinuating that there is a possibility of formation of defects complex.

A further increase in Ag^+ and C^+ ions result in the emergence of new peaks at higher Raman shift. These two features were not identified in the Raman spectra of either pristine or Ag^+ ion implanted ZnO. It could hence be projected that the nature of these two additional features occurring at 1319 and 1590 cm^{-1} as shown in Figure 8.3 is attributed to the presence of large quantities of carbon. Similar peaks have been observed by Sawant et al [289] who discussed their association with disorder or defects primarily due to sp^3 hybridization (D-band) and the planar configuration of the sp^2-bonded carbon structure (G-band). According to Li et al [290], implanting additional carbon ions into the ZnO matrix results in interstitial C atom bonding with an already prevailing CO defect, thus forming a C2 dimer.

Furthermore, a significant shift to lower phonon frequency was observed for the A_1(LO), highlighting that the ZnO crystal was subjected to tensile stress. Upon ion implantation, radiation damage subjects the lattice to stress. As such, the phonon frequency shifts to either a high or lower wavenumber indicating compressive or tensile stress, respectively. Ion bombardment induces defect density in the films hence distorting the host lattice as confirmed by shifting bond lengths and subsequently resulting in residual stress. This process has been theoretically revealed to induce phase transformations. Nyamukamba and his co-authors [291] reported a phase transformation of TiO_2 from anatase to rutile when co-doped with Ag and C. Jaiswal et al [292] have also reported a similar observation with phase transformation from anatase to rutile when co-doping TiO_2 with copper and nitrogen. This has been explained to be due to the reconstruction of the Ti^{4+} and O^2 ions in the adjacent planes caused by lattice distortions and oxygen deficiency in the TiO_2 lattice as Cu^{2+} and N- substitutes Ti^{4+} and O^{2-} ions, respectively. Table 8.3 gives a summary of the observed vibration peaks for pristine and ion implanted ZnO as extracted from the Raman spectra. From XRD and Raman analysis it is conclusive that co-implantation of Ag^+ and C^+ ions at higher fluences did not result in phase transformation, which has been noted on other semiconductors.

Table 8.3: Raman active phonons and their wavenumber values as observed in pristine and Ag^+ and C^+ co-implanted ZnO nanorods. BZP denotes the corresponding Brillouin zone points or lines of the processes.

Process	**Fluences**						**BZP** [293]
	Pristine	**1.0x10^{15}**	**2.0x10^{15}**	**3.0x10^{15}**	**1.0x10^{16}**	**3.0x10^{16}**	
E_{2low}	96	-	-	-	-	-	T
$B1_{(high)}$-$B1_{(low)}$	273.9	243	-	-	-	295	T
$E_{2high} - E_{2low}$	327.8	336.6	342		-	-	T
E_{2high}	434	439	439	436	437	437	T
A_1(LO)	575.7	573.6	575.9	573.0	567.9	568.4	T
TA+LO	639.4		-	-	-	-	L, H
TO + LO	1095.2	1093	1095.5	1093	1100	1096	M, L

8.2.3 FTIR

The nature of the chemical and molecular composition of ZnO films was studied by FTIR spectroscopy. This was done to confirm the presence and interactions of the implanted Ag^+ and C^+ ions as well as to understand the consequence of ion fluence on the structure of the ZnO nanorods. Figure 8.4 is a presentation of the room temperature acquired FTIR spectra of Ag^+-C^+ co-implanted ZnO NRs at varying ion fluences in the range of 400-1500 cm^{-1}. The existence of Zn-O bond is revealed at ~ 600 cm^{-1} across all samples, supporting the XRD and Raman analysis that the wurtzite structure was not destroyed. However, a shift was observed for this band which signals the presence of structural defects within the ZnO lattice. The presence of implanted ions is also noted from the emergence of some well resolved absorption shoulders/bands observed at ~400 and 900 cm^{-1}, which were previously not recorded or present in the pristine ZnO spectrum. This indicates their presence to be mediated by the bonds formed during co-implantation with of Ag^+ and C^+. A predominant variation in the strength of these bands signifies the formation of new bonding motifs between Zn, O and the implanted species. The existence of defects is established by a variation in the transmittance as well as the

disappearance of pre-existing peaks and presence of new bands and molecular vibrations. Overall, the distinctions and features observed in the given infrared spectra confirm the existence and interactions of ions in the host matrix.

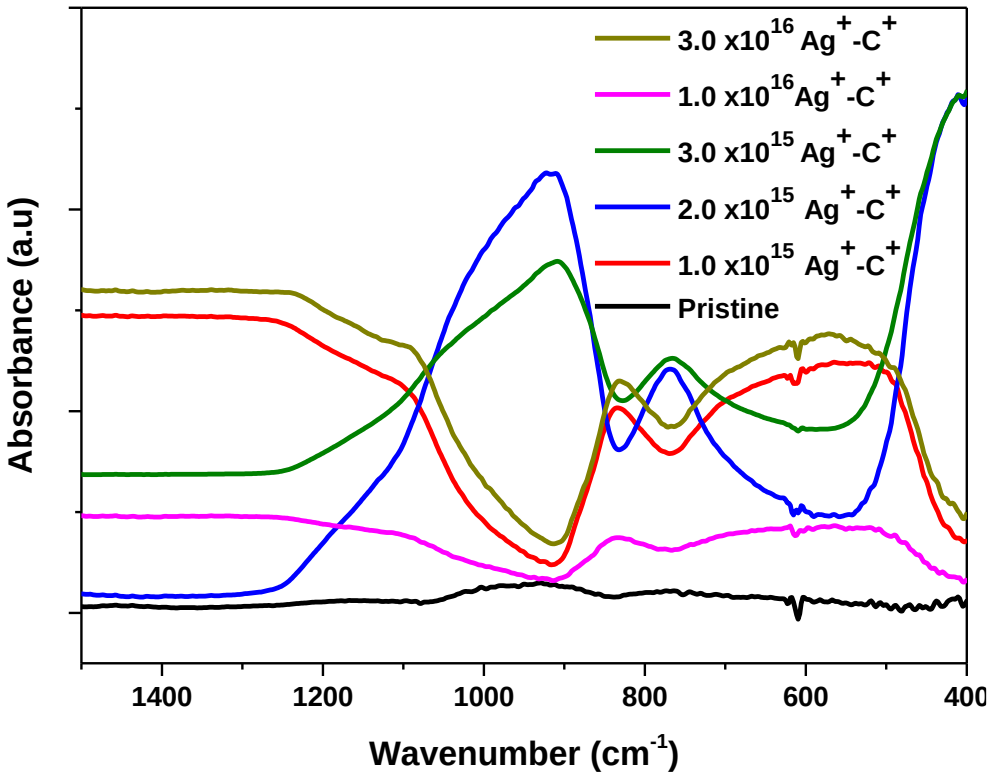


Figure 8.4: Infrared spectra of pristine and Ag^{+}-C^{+} co-implanted ZnO NR at varying fluences of 1.0 x10^{15}, 2.0 x10^{15}, 3.0 x10^{15}, 1.0 x10^{16} and 3.0 x10^{16} ions/cm^{2}.

8.3 Morphological analysis

The variation in morphology of the co-implanted ZnO nanorods films was studied through the FESEM and AFM techniques.

8.3.1 FESEM and AFM

FESEM and AFM images in Figure 8.5 show the morphology of the Ag^{+}-C^{+} co-implanted ZnO. Differences are signified in the diameters and appearance of the tips of the nanorods. The top view micrographs of the FESEM micrographs of implanted ZnO films, however, denotes a more spherical end of the nanorods, compared to the sharp pointed end before implantation.

The preserved morphology concurs with the XRD analysis which indicated that though the films crystallinity deteriorated, a c-axis preferential growth was maintained across all co-implanted samples. Calculated statistical parameters are listed in Table 8.4, and reveal the effect of the co-implanted ions on the surface morphology of ZnO. Co-implanting Ag^+ and C^+ ions lead to an interesting high increase in both Ra and (R_{rms}) of the films.

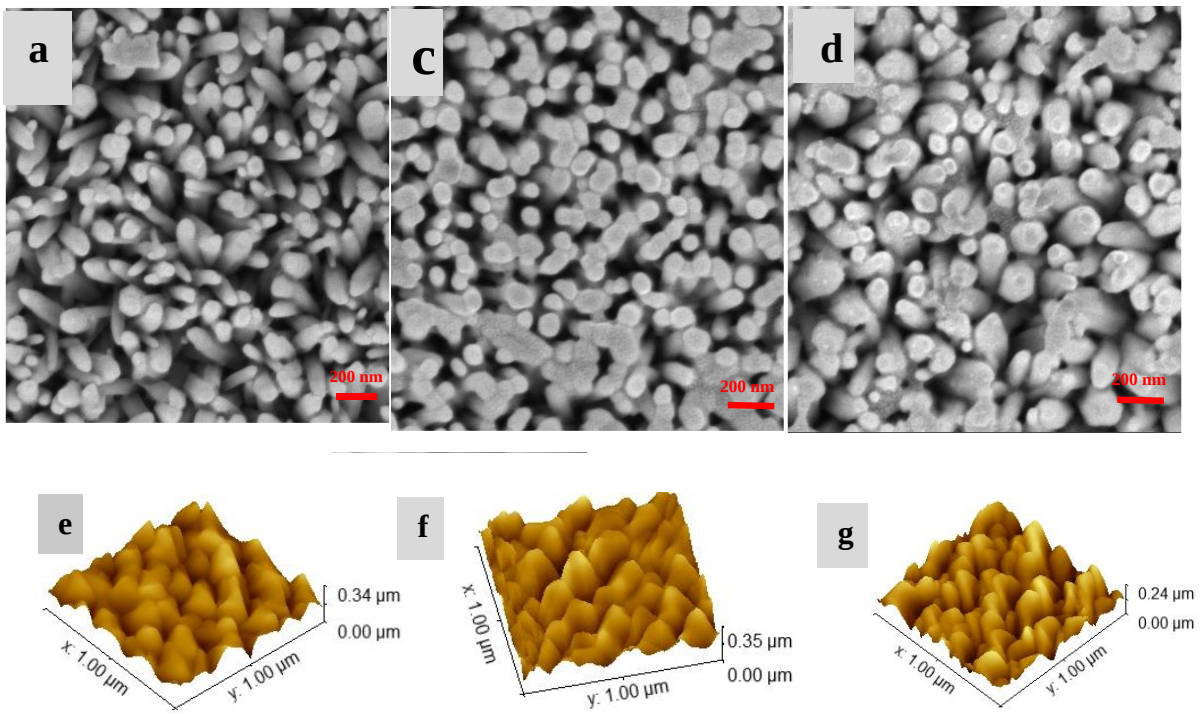


Figure 8.5: Top surface view FESEM and 3D AFM images showing the surface morphology of well-aligned ZnO nanorods implanted with varying fluences of Ag^+ and C^+ ions [(a and b)1.0 x10^{15}, (c) 3.0 x10^{15}, (d) 1.0 x10^{16}, (e) 2.0 x10^{15}, (f) 1.0 x10^{16} and (g) 3.0 x10^{16} ions/ cm^2].

Table 8.4: Surface statistical AFM analysis of the Ag^+- C^+ co-implanted films

Ion fluence (ions/cm^2)	R_a (nm)	R_{rms} (nm)	Grain height (nm)
0	122.2	18.69	278.20
1 x10^{15}	154.1	35.58	309.74
2 x10^{15}	191.9	37.76	340.82
3 x10^{15}	134.2	29.73	238.27
1 x10^{16}	197.9	37.17	346.10
3 x10^{16}	135.2	36.41	239.78

8.4 Optical Properties

8.4.1 Absorbance

Optical properties of ZnO nanostructures are solidly determined by its electronic band structure. Implantation of energetic Ag^+ and C^+ ions has been shown to induce crystal lattice modifications, which can consequently amend numerous properties including the optical properties [98]. To study the effects of Ag^+ and C^+ co-implantation, the absorbance was measured. The absorbance spectra of pristine and co-implanted ZnO NRs are shown in Figure 8.6. The figure shows a significant enhanced absorption for ZnO co-implanted with Ag^+ and C^+ ions at fluences of 1 x10^{15}, 2 x10^{15}, 3 x10^{15}, 1 x10^{16} and 3 x10^{16} ions/cm^2. Most notably, the ZnO implanted at 1 x10^{16} ions/cm^2 displays the most increased absorbance in the visible region. This broadened absorption specifies a wide distribution of localized energy states within the forbidden band [98]. Additionally, the increment of the absorbance may be associated with electronic transition from the dopant energy level to the conduction band of ZnO [98]. The optical absorption edge of pristine ZnO is situated at ≈380 nm. A shift in the absorption edge is noted upon implanting Ag^+ and C^+ ions. The absorption edge tends to shift towards longer wavelength of the visible light spectrum for all implanted samples. The noted changes are related to the effects induced by the implanted ions.

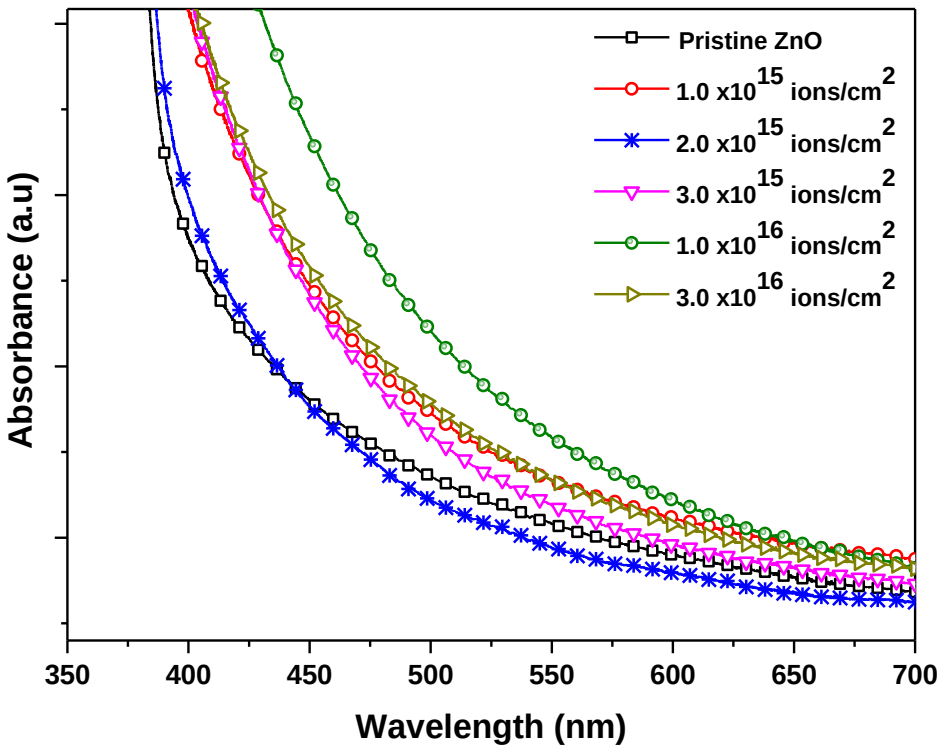


Figure 8.6: Optical absorption spectra for pristine and Ag^+- C^+ co-implanted ZnO NRs thin films at various fluences.

8.4.2 Extinction coefficient

Figure 8.7 shows the extinction coefficient of pristine and implanted films ZnO as a function of Ag^+-C^+ ion fluence. Even though samples depict higher k_x values in the UV region as compared to the visible region, a significant increase of k_x for implanted samples is noted, compared to that of pristine ZnO. This implies a higher electron concentration as possessed by Ag^+-C^+ co-implanted ZnO, which in turn facilitates enhanced light absorption.

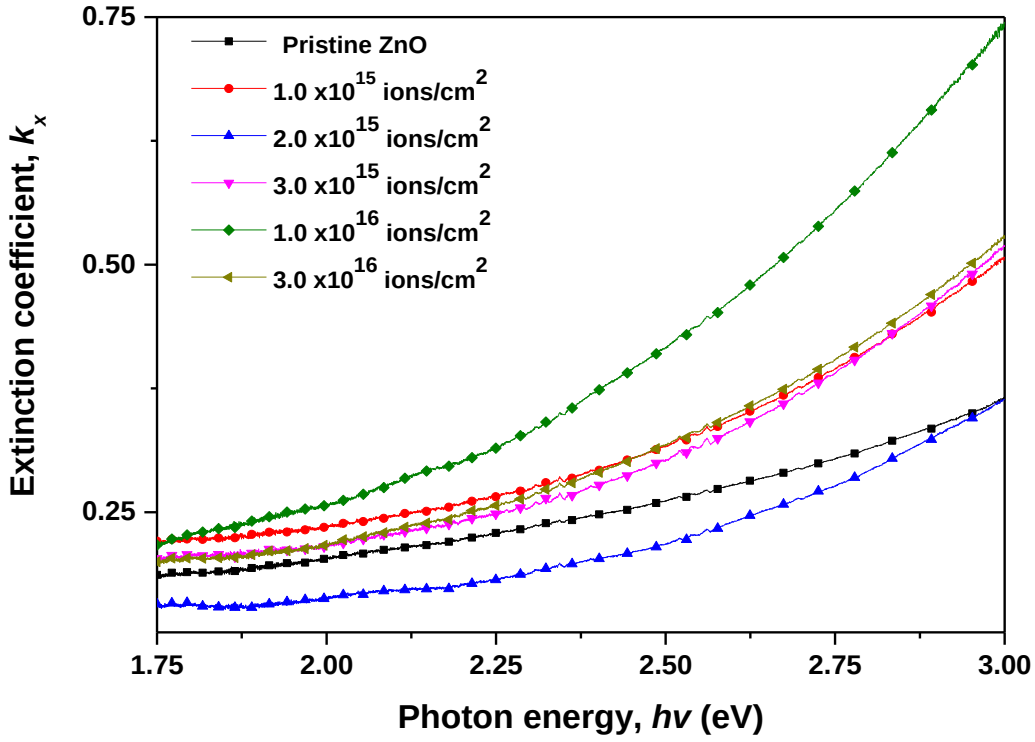


Figure 8.7: Extinction coefficient (k_x) profiles of pristine and 50 KeV Ag^+-C^+ co-implanted ZnO NRs with varying ion fluences.

8.4.3 Band gap determination

The UV-Vis transmittance spectra were used to calculate the optical band gap of the co-implanted samples. The Tauc plot method explained in section 3.49 was employed. The pristine ZnO's energy band gap was determined to be 3.25 eV, insinuating that its valence band electrons are mostly excited by UV light. Due to the strong capability of forming impurity compounds between energetic Ag^+, C^+ ions and the ZnO substrates, the band gap is altered. Figure 8.8 shows Tauc's plots used for estimation of the optical band gap. Values of E_g were found to be 3.17, 3.22, 3.11, 2.87 and 3.14 eV at fluences of 1.0 $x10^{15}$, 2.0 $x10^{15}$, 3.0 $x10^{15}$, 1.0 $x10^{16}$ and 3.0 $x10^{16}$ ions/cm^2, respectively, indicating a general decrease of the optical band gap upon co-implantation of ZnO with Ag^+ and C^+ ions. At 1.0 $x10^{16}$ ions/cm^2 the lowest optical band gap was found. The results show that the addition of Ag^+ and C^+ can adjust the band gap to a certain level as a result of the shift of the optical absorption edge in the visible region. This has also been observed upon mono Ag^+ or C^+ ion implantation. Hence, we can thus confirm the synergistic contribution of both Ag^+ and C^+ in reducing the band gap of ZnO.

Reduction of the optical band gap results in an increased photosensitivity in the visible light region as shown. It has been previously reported that a reduction in the band gap can be due to a decrease of carrier density as a result of crystal disorder as the dopant atoms act as carrier traps instead of electron donors [244].

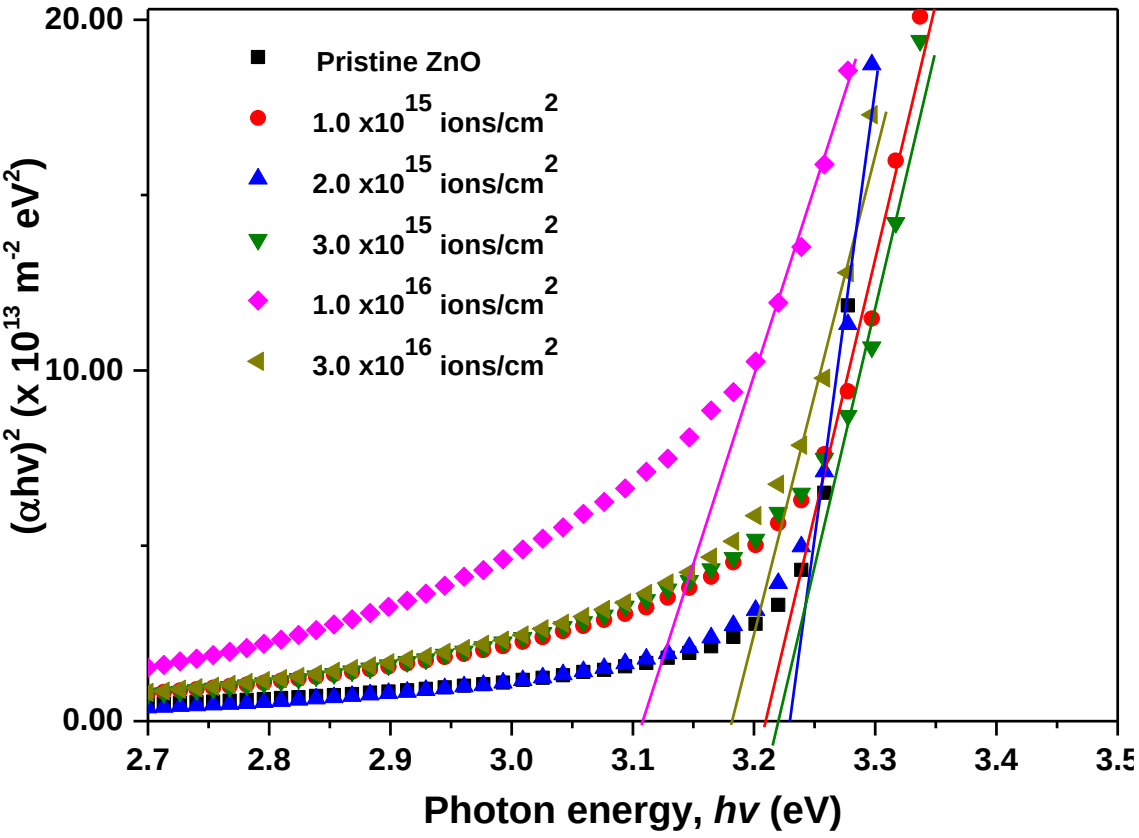


Figure 8.8: Tauc's plot for determining the optical band gap for pristine and 50 KeV Ag^+- C^+ co-implanted ZnO NRs with varying ion fluence.

8.4.4 Urbach energy

Figure 8.9 shows a plot of the Ln α vs the photon energy as a function of co-implantation ion fluence. The linear part of the plot was fitted, and the slope of the fit was used to determine the Urbach energy (E_u) and recorded in Table 8.4. The values of the E_u were found to be decreasing following ion implantation; however, this decrease is noted not to be proportional to the implanted ion fluence. The least E_u value of 758 meV was found for the ZnO film co-implanted

at a fluence of 1.0 x10^{16} ions/cm^2. Contrary to previous findings showing that a higher E_u gives the most reduction in the band gap, our values indicate that the least E_u gave the lowest calculated band gap. However; the association of higher Urbach energies to lower band gap is still a big debate in literature.

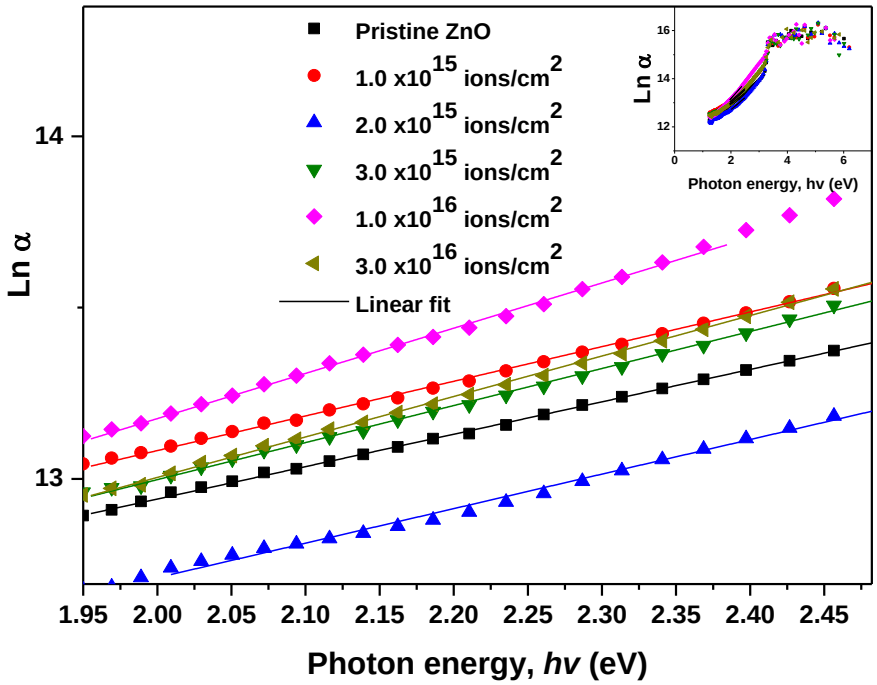


Figure 8.9: Ln α plots for Pristine and Ag-C co-implanted ZnO NRs at ion fluence of 1.0 x10^{15}, 2.0 x10^{15}, 3.0 x10^{15}, 1.0 x10^{16} and 3.0 x10^{16} ions/cm^2.

8.4.5 Skin depth and Optical conductivity

Figure 8.10 is an illustration of the influence of the co-implanted Ag^+ and C^+ ions on the skin depth and optical conductivity (σ_{opt}) parameters. The skin depth is noted to be decreasing, with increase in the fluence of the co-implanted ions. A much-augmented increase of the optical conductivity is noted for samples implanted at higher fluences as shown in Figure 8.11. This sharp increase suggests a very high photo-response of the samples thus emphasising a strong excitation of the electrons as induced by the presence of Ag^+ and C^+ ions [295]. Furthermore, the graph elucidates a noticeable decrease in the optical conductivity beyond fluence of 1.0 x 10^{16} ions/cm^2, indicating an inhibition in the escalation of charge carriers, noted by the

reduction of the optical conductivity. This sample is also observed to record the maximum optical conductivity in the visible region. The increment of the optical conductivity is associated with the decrease in the band gap and decrease in electron density in the conduction band when absorption occurred at near ultra violet region.

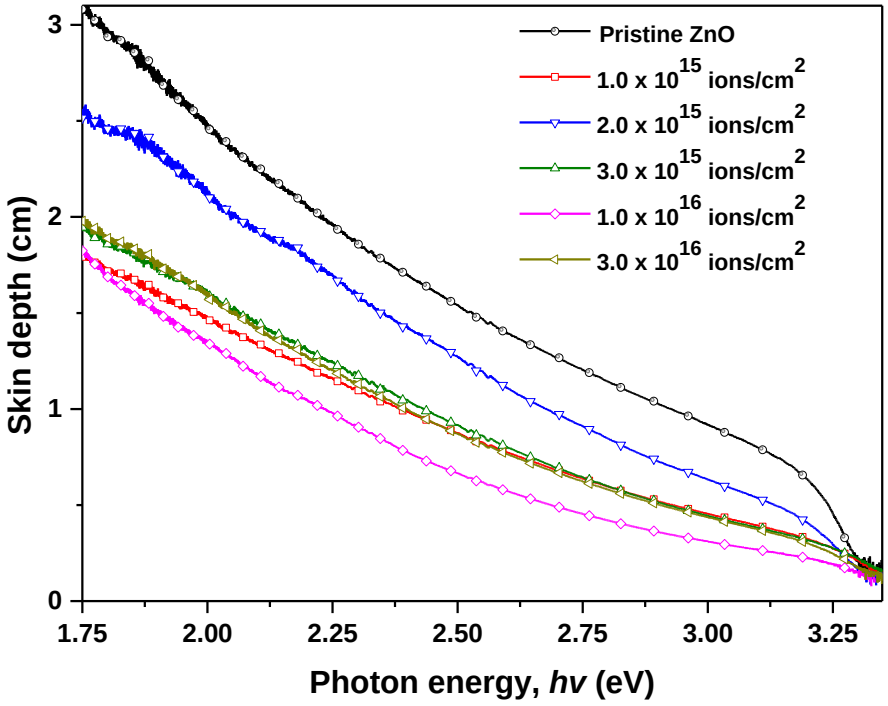


Figure 8.10: Variation of the skin depth parameter of Ag^{+}-C^{+} co-implanted ZnO NRs.

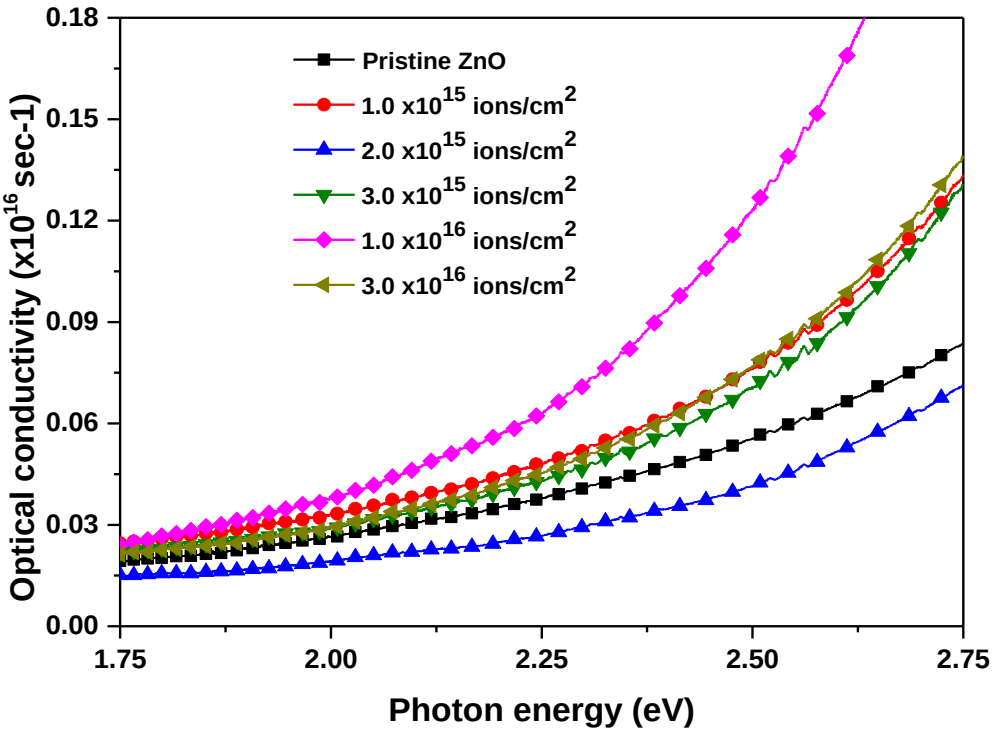


Figure 8.11: A plot showing enhanced optical conductivity of Ag^{+}-C^{+} co-implanted ZnO NRs.

Table 8.4: Direct optical band gap (E_g), and Urbach energy (E_u) for pristine and implanted samples.

Sample ID	**E_g (eV)**	**E_u (meV)**	n_{RG}
Pristine ZnO	3.25	896	2.069
1.0 x 10^{15} Ag^{+}-C^{+} ZnO	3.17	989	2.1186
2.0 x 10^{15} Ag^{+}-C^{+} ZnO	3.22	992	2.0876
3.0 x 10^{15} Ag^{+}-C^{+} ZnO	3.11	925	2.1558
1.0 x 10^{16} Ag^{+}-C^{+} ZnO	2.87	758	2.3046
3.0 x 10^{16} Ag^{+}-C^{+} ZnO	3.14	847	2.1372

In brief, this chapter investigated the co-implantation of Ag^+ and C^+ ions into ZnO nanorods. XRD analysis revealed that the nanorods maintained a hexagonal wurtzite structure, post implantation. However, increased ion fluence resulted to a notable decrease in the intensity of the 002-peak, indicative of reduced crystal quality, albeit without reaching amorphization. Microstructural parameters, such as bond length, lattice parameter, and stacking faults probability, exhibited intricate trends with varying ion fluence. Additionally, the crystallite size decreased at lower fluences but increased at higher fluences, suggesting a balance between lattice distortion and crystalline order. Raman spectroscopy corroborated the preservation of the hexagonal wurtzite structure while revealing phonon scattering variations, signifying the presence of structural irregularities, grain boundaries, and internal stress. The A1(LO) peak intensity was enhanced with escalating ion fluence to a specific threshold, beyond which it diminished, possibly due to defect complex formation. New peaks at higher Raman shifts emerged, attributed to the presence of carbon. Infrared spectra revealed shifts in phonon frequencies, indicating tensile stress in the ZnO crystal caused by radiation damage and lattice distortion from ion bombardment. The emergence of absorption bands at ~400 and 900 cm^{-1} suggested the formation of new bonds between Zn, O, and the implanted ion. Overall, these spectroscopic differences confirmed the presence and interactions of ions in the ZnO matrix.

Optical studies showed that the absorption shifted towards longer wavelengths in the visible spectrum, indicating the influence of the implanted ions. The optical band gap decreased upon co-implantation, with the lowest value of 2.87 eV observed at 1.0×10^{16} ions/cm^2. The optical conductivity was noted to increase with ion fluence up to a certain point, followed by a decrease, signifying the inhibition of charge carriers at higher fluences. The sample co-implanted at 1.0×10^{16} ions/cm^2 displayed the highest optical conductivity in the visible region. In summary, the co-implantation of Ag^+ and C^+ ions into ZnO nanorods resulted in complex changes in crystal structure, morphology, and optical properties, offering valuable insights into the effects of ion implantation on semiconductor materials.

CHAPTER 9: SUMMARY, CONCLUSIONS AND RECOMMENDATIONS

The work presented herein focused on selectively inducing lattice distortions into ZnO nanorods with an intention to modify the optical response of the ZnO towards the visible light region. ZnO NRs have been successfully synthesised on seeded glass substrates through the chemical bath deposition (CBD) technique. X-ray diffraction of the pristine ZnO films confirmed a hexagonal wurtzite structure with a preferential growth on the c-axis (002). The ion implantation method has been found to be an essential technique through which properties of semiconductors can be modified without affecting other properties such as morphology. The depth and impact of implanted ions in semiconductors can be controlled via varying several parameters such as ion fluence, implantation energy, implantation time and post-implantation treatment. Ion implantation was adopted to induce structural modifications on ZnO NRs and thus alter their optical properties.

The key findings are as summarised below:

- XRD analysis of the implanted samples indicated that the wurtzite structure of the ZnO was not damaged by any of the implanted ions. The 002 peak was maintained as the most dominant for implanted samples, however a deterioration of the crystallinity was noted upon implantation with either Ag^+, C^+ or co-implantation with Ag^+ and C^+ ions. Ag^+ ion implantation resulted in the peaks shifting to lower 2θ angles, signifying unidirectional induced tensile strain. Non-uniform peak shifting to both lower and higher 2θ angles was noted upon carbon ion implantation, confirming the type of strain induced by the incorporation of C^+ ions. Another major observation was the broadening of the peaks (FWHM), signalling the crystallite size reduction which was confirmed through calculations. The crystallite size was found to be affected by ion fluence. Crystallite size values of 24.29, 29.0 and 30.13 nm were found for ZnO implanted at 3.0 x 10^{16} ions/cm^2 with Ag^+, C^+ and Ag^+-C^+ ions, respectively. A variation of the microstructural parameters of the implanted ZnO NRs also indicated that lattice modification was induced. Due to the differences in the ionic radii of Ag, Zn and O, implantation with Ag^+ ions resulted in increase in the lattice parameter c_p. Upon C^+ and co-implantation with Ag^+ and C^+ ions, the non- linear correlation of structural damage with ion fluence and c_p was observed, suggesting synergy between the two ions, albeit dominated by the influence of carbon ions.

- Raman spectroscopy showed the presence of distortions through a variation of vibrational modes. Most notably, the E_1 and E_2 modes were noted to degrade upon implantation. An intensification of the A_1 longitudinal optical (LO) phonon mode was observed, indicating the accumulation of induced defects across all implanted samples. Additional peaks were detected on samples implanted with C^+ ions and Ag^+-C^+ co-implanted samples. Raman spectra indicated that the existence of implanted ions disrupted the translational crystal symmetry. The presence of Ag^+ and C^+ on ZnO NRs was further confirmed by a variation of the FTIR spectra.

- FESEM images showed preserved nanorod morphology. Ag^+ and C^+ ion implantation had noticeable effect on the surface roughness of the films as observed from AFM surface topographies. All of the above-mentioned structural variations confirm that the ions were successful incorporated into the ZnO framework and that the incorporation of Ag^+ and C^+ ions into interstitial sites or the displacement of the target atoms by substitution induced lattice distortion, however the degree of distortion is dependent on the type of ion, its occupancy in the host lattice as well as ion fluence.

- The influence of the induced lattice distortion on the optical response properties of the ZnO NRs was investigated. Augmented absorbances were recorded for implanted ZnO films. Implantation of ZnO NRs with Ag^+ and C^+ ions resulted in disparities, specifically a shift of the absorption edges towards longer wavelengths. A range of optical parameters were determined and pronounced differences were observed. A progressive overall decrease of the bandgap is observed. Upon Ag^+ implantation, the decrease was relative to the fluence of Ag^+ ions. This red shift was associated with the disturbance of the structural periodicity. The substantial decrease in the optical band gap of C^+ implanted ZnO was ascribed to the substitution of carbon species into the ZnO lattice, which introduces isolated impurity bands of C (2p) between the conduction and valence bands. The existence of graphitic carbon and other defects noted by the additional Raman features were also considered to contribute to the constriction of the band gap. Synergistic contribution of both Ag^+ and C^+ in attenuating the band gap of ZnO was noted upon co-implantation. Other than increased absorption of the visible light, a reduced band gap also facilitates rapid photoexcitation of electrons from the

conduction band, hence resulting in increase in the electron flow. A general increase in the calculated optical conductivity as a result of ion implantation was noted.

In conclusion, this study has shown that ion implantation of Ag^+ and C^+ ions through mono and dual implantation can be used to modify the ZnO lattice without destroying the significantly desired 1D nanorod morphology as well as the hexagonal wurtzite structure. The induced lattice distortions instigated modification of the optical response properties of ZnO NRs, i.e., enhanced absorption of the visible light spectrum. The effects of ion fluence and type of ion species have been observed.

REFERENCES

[1] K. Shingange, Z.P. Tshabalala, B. P. Dhonge, O. M. Ntwaeaborwa, D. E. Motaung and G. H. Mhlongo, "0D to 3D ZnO nanostructures and their luminescence, magnetic and sensing properties: Influence of pH and annealing,"," *Materials Research Bulletin,* vol. 85, pp. 52-63, 2017 .

[2] K. Lefatshe, G. Mola and C. Muiva, "Reduction of hazardous reactive oxygen species (ROS) production of ZnO through Mn inclusion for possible UV-radiation shielding application," *Heliyon,* vol. 6, pp. 1-8, 2020.

[3] O.Oluwaleye, M.Madhuku, B.Mwakikung and S.J.Moloi, "Studies of lattice structure, electrical properties, thermal and chemical stability of cobalt ion implanted Indium Tin Oxide (ITO) thin films on polymer substrates," *Nuclear Instruments and Methods in Physics Research Section B: Beam Interactions with Materials and Atoms,* vol. 450, pp. 267-273, 2019.

[4] K. Huang, Y. H. Li, S. Lin, C. Liang, H. Wang, C. Ye, Y. Wang, R. Zhang, D. Fan, H. Yang and Y. a. M. Lei, "A facile route to reduced graphene oxide–zinc oxide composites with enhanced photocatalytic activity," *Powder Technology,* vol. 257, pp. 113-119, 2014.

[5] S. Adhikari, D. Madra and G. Sarkar, "Highly efficient WO3–ZnO mixed oxides for photocatalysis," *Advances,* vol. 5, pp. 11895-11904, 2015.

[6] K. Asha, N. K. Biswas, S. Saxena, V. R. Satsangi, R. Shrivastav, R. Kant and S. Das, "Effect of 100 KeV Ar+ ion beam irradiation on ZnO thin films – Influence of morphology vis-a-vis electrode/electrolyte interface and its impact on photoelectrochemical water splitting," *International Journal of Hydrogen,* vol. 46, pp. 20858-20870, 2021.

[7] Y. S. Chaudhary, S. A. Khan, C. Tripathi and R. Shrivastav, "A study on 170 MeV Au13+ irradiated nanostructured metal oxide (Fe2O3 and CuO) thin films for PEC

applications," *Nuclear Instruments and Methods in Physics Research B,* vol. 244, pp. 128-131, 2006.

[8] K. Lefatshe, C. Muiva and L. Kebaabetswe, "Extraction of nanocellulose and in-situ casting of ZnO/cellulose nanocomposite with enhanced photocatalytic and antibacterial activity," *Carbohydrate Polymers,* vol. 164, pp. 301-308, 2017.

[9] K. Lefatshe, L. Kebaabetswe and C. Muiva, "Visible-Light Driven Photocatalytic and Antibacterial Assessment of Ag/ZnO/Cellulose Nanocomposite," *Advanced Science, Engineering and Medicine,* vol. 12, pp. 844-852, 2020.

[10] Q. Wang, L. Zhang, X. Liu and S. Li, "Two-Dimensional Semiconductor Heterojunctions for Optoelectronics and Electronics," *Front. Energy Res,* vol. 20, pp. 1-5, 2021.

[11] Y. Li, L. Yue, Y. Luo, W.Liu and M. Li, "Light harvesting of silicon nanostructure for solar cells application," *Optics Express,* vol. 24, pp. A1075-A1082, 2016.

[12] B. Setera and A. Christou, "Challenges of Overcoming Defects in Wide Bandgap Semiconductor Power Electronics-a review," *Electronics,* vol. 11, pp. 1-6, 2022.

[13] Y. Weilai, I.Moreno-Hernandez, K.Papadantonakis, B. Brunschwig and N. Lewis, "Understanding the Surface Corrosion Chemistry Towards Sustainable Semiconductor Photoelectrochemistry," *ECS Meeting Abstracts* , vol. 36, p. 2135, 2018.

[14] T. Tsuzuki, R. He, Dodd and M. Saunders, "Challenges in Determining the Location of Dopants, to Study the Influence of Metal Doping on the Photocatalytic Activities of ZnO Nanopowders," *Nanomaterials,* vol. 9, pp. 1-19, 2019.

[15] E.Karaköse and H.Çolak, "Structural and optical properties of ZnO nanorods prepared by spray pyrolysis method," *Energy,* vol. 140, pp. 92-97, 2017.

[16] B.Subash, B. Krishnakumar, M. Swaminathan and M.Shanthi, "Highly Efficient, Solar Active, and Reusable Photocatalyst: Zr-Loaded Ag–ZnO for Reactive Red 120 Dye Degradation with Synergistic Effect and Dye-Sensitized Mechanism," *Langmuir,* vol. 29, pp. 939-949, 2013.

[17] A. Xiong, T. Yoshinaga, T. Ikeda, M. Takashima, T. Hisatomi, K.Maeda, T. Setoyama, T.Teranishi and K. Domen, "Effect of Hydrogen and Oxygen Evolution Cocatalysts on Photocatalytic Activity of GaN:ZnO," *European Journal of Chemistry,* vol. 2014, pp. 767-772, 2014.

[18] H. S. Jung, Y. J. Hong, Y.Li, J.Cho, Y. Kim and G. Yi, "Photocatalysis using GaN nanowires," *ACS Nano,* vol. 2, pp. 637-642, 2008.

[19] S. Sato, "Photocatalytic activities of indium oxide powder prepared from indium hydroxide," *Journal of Photochemistry and Photobiology A: Chemistry,* vol. 45, pp. 361-367, 1988.

[20] D. Yu, D. Wang and Y. Qian, "Synthesis of metastable hexagonal In2O3 nanocrystals by a precursor-dehydration route under ambient pressure," *Journal of Solid State Chemistry,* vol. 177, pp. 1230-1234, 2004.

[21] E. Libman, "Some properties of zinc oxide bodies," *Journal of the American Ceramic Society,* vol. 5, pp. 488-491, 1922.

[22] L.Yu, F.Qu and X.Wu, "Facile hydrothermal synthesis of novel ZnO nanocubes," *Journal of Alloys and Compounds,* vol. 504, pp. L1-L4, 2010.

[23] K. Lefatshe, P. Dube, D. Sebuso, M. Madhuku and C. Muiva, "Optical dispersion analysis of template assisted 1D-ZnO nanorods for optoelectronic applications," *Ceramics International,* vol. 47, pp. 7407-7415, 2021.

[24] B. Sun and H. Sirringhaus, "Solution-Processed Zinc Oxide Field-Effect Transistors Based on Self-Assembly of Colloidal Nanorods," *Nano Letters,* vol. 5, pp. 2408-2413, 2005.

[25] R. Singhal, D. Agarwal, Y. Mishra, D. Kabiraj, G. Mattei, J. Pivin, R. Chandra and D. Avasthi, "Synthesis, characterizations, and thermal induced structural transformation of silver-fullerene C60 nanocomposite thin films for applications in optical device," *Journal of Applied Physics,* vol. 107, p. 103504, 2010.

[26] S. Singh and R. Singhal, "Structural and optical investigations of 120 KeV Ag implanted ZnO thin films," *Thin Solid Films,* vol. 653, pp. 377-383, 2018.

[27] X. Hou, H. Maa, F. Liu, J. Deng, Y. Ai, X. Zhao, D.Mao, D. Li and B. Liao, "Synthesis of Ag ion-implanted TiO2 thin films for antibacterial application and photocatalytic performance," *Journal of Hazardous Materials,* vol. 299, pp. 59-66, 2015.

[28] A. Jafari, K. Tahani, D. Dastan, S. Asgary, Z. S.-T. Yin, W.-D. Zhou, H. Garmestani and Ş. Ţălu, "Ion implantation of copper oxide thin films; statistical and experimental results," *Surfaces and Interfaces,* vol. 18, pp. 1-9, 2020.

[29] Li.Cai, F.Ren, M.Wang, G.Cai, Y.Chen, Y.Liu, S.Shen and L.Guo, "V ions implanted ZnO nanorod arrays for photoelectrochemical water splitting under visible light," *International Journal of Hydrogen Energy,* vol. 40, pp. 1394-1401, 2015.

[30] R. Singhal, D. Kabiraj, P. Kulriya, J. Pivin, R. Chandra and D. Avasthi, "Blueshifted SPR of Au nanoparticles with ordering of carbon by dense ionization and thermal treatmen," *Plasmonics,* vol. 8, pp. 295-305, 2013.

[31] V. Parihar, M. Raja and R. Paulose, "A brief review of structural, electrical and electrochemical properties of zinc oxide nanoparticles," *Reviews on Advanced Material Science,* vol. 53, pp. 119-130, 2018.

[32] V. Kumar, O.M. Ntwaeaborwa, T. Soga, V. Dutta and H.C. Swart, "Rare earth doped zinc oxide nanophosphor powder: A future material for solid state lighting and solar cells.," *ACS Photonics,* vol. 4, pp. 2613-2637, 2017.

[33] I. Ayoub, V. Kumar, R. Abolhassani, R. Sehgal, V. Sharma, R. Sehgal, H. C. Swart and Y. K. Mishra, "Advances in ZnO: Manipulation of defects for enhancing their technological potentials," *Nanotechnology Reviews,* vol. 11, pp. 575-619, 2022.

[34] M.A. Johar, R. Afzal, A. Alazba and U. Manzoor, "Photocatalysis and Bandgap Engineering Using ZnO Nanocomposites," *Advances in Materials Science and Engineering,* vol. 2015, pp. 1-22, 2015.

[35] A. Pérez-Larios, R. Lopez, A. Hernández-Gordillo, F. Tzompantzi, R. Gómez and L.M. Torres-Guerra, "Improved hydrogen production from water splitting using TiO2–ZnO mixed oxides photocatalysts," *Fuel,* vol. 100, pp. 139-143, 2012.

[36] X. Lu, G. Wang, S.Xie, J. Shi, W.Li, Y.Tong and Y. Li, "Efficient photocatalytic hydrogen evolution over hydrogenated ZnO nanorod arrays," *Chemical Communications,* vol. 48, pp. 7717-7719, 2012.

[37] Y. Chan, S. Y. Pung and S. Sreekantan, "Degradation of organic dye using ZnO nanorods based continuous flow water purifier," *Journal of Sol-Gel Science and Technology,* vol. 66, pp. 399-405, 2013.

[38] R. Ullah and J. Dutta, "Photocatalytic degradation of organic dyes with manganese-doped ZnO nanoparticles," *Journal of Hazardous Materials,* vol. 156, pp. 194-200, 2008.

[39] F. Zhang, Y.H. Li, M.Y. Qi, Z.R. Tang and Y.J. Xu, "Boosting the activity and stability of Ag-Cu2O/ZnO nanorods for photocatalytic CO2 reduction," *Applied Catalysis B: Environmental,* vol. 268, pp. 1-7, 2020.

[40] C. Xin, M. K.Wang and X. Wang, "Significant Enhancement of Photocatalytic Reduction of CO2 with H2O over ZnO by the Formation of Basic Zinc Carbonate," *Langmuir,* vol. 33, pp. 6667-6676, 2017.

[41] E. Libman, "Some properties of zinc oxide bodies," *Journal of the American Ceramic Society,* vol. 5, pp. 488-491, 1922.

[42] A. Srivastava, R. Gakhar, P. Dua, K. Senthil, J.S.Tawale, K. Sood and K. Yong, "Structural determination of Zn-O dumbbells in facetted nano-particles," in *Microscopy, Science, Technology, Applications and Education,* Formatex Research Center, 2010, pp. 1820-1823.

[43] K. Lee, C. W. Lai, K. S. Ngai and J. Juan, "Recent developments of zinc oxide based photocatalyst in water treatment technology: A review," *Water Research 88,* pp. 428-448, 2016.

[44] L. Shi, Z. Li, W. Zheng, Y. Zhao, Y. Jin and Z. Tang, "Synthesis, antibacterial activity, antibacterial mechanism and food applications of ZnO nanoparticles: a review," *Food Additives & Contaminants: Part A 31,* pp. 1-15, 2014.

[45] L. Wang, “Zinc oxide nanostructures: growth, properties and applications; Topical review,” *Journal of Physics: Condensed Matter 16,* vol. 16, pp. R829-R858, 2004.

[46] K. Babu, A. Reddy, C. Sujatha and K. Reddy, “Synthesis and optical characterization of porous ZnO,” *Journal of Advanced Ceramics 2,* vol. 2, pp. 260-265, 2013.

[47] V. A. Coleman and C. Jagadish, “Basic properties and applications of ZnO,” in *Zinc oxide bulk, thin films and nanostructures,* New York, Elsevier Limited, 2006, pp. 1-21.

[48] M.Asadian, “Thermodynamic analysis of ZnO cystal growth from the melt,” *Journal of Crystallization Process and Technology,* vol. 3, pp. 75-80 , 2013.

[49] S.Slavin, K.McEwan and D.M.Haddleton, “3.09 - Cobalt-Catalyzed Chain Transfer Polymerization: A Review,” *Polymer Science A comprehensive Reference,* vol. 3, pp. 249-275, 2012.

[50] K.Shingange, Z.P.Tshabalala, B.P.Dhonge, O.M.Ntwaeaborwa, D.E.Motaung and G.H.Mhlongo, “0D to 3D ZnO nanostructures and their luminescence, magnetic and sensing properties: Influence of pH and annealing,” *Materials Research Bulletin,* vol. 85, pp. 52-63, 2017.

[51] K.Lefatshe, L.Kebaabetswe and C.Muiva, “Visible-Light Driven Photocatalytic and Antibacterial Assessment of Ag/ZnO/Cellulose Nanocomposite,” *Advanced Science, Engineering and Medicine,* vol. 12, pp. 844-852, 2020.

[52] Z. L. Wang, “Zinc oxide nanostructures: growth, properties and applications-a topical review,” *Journal of Physics: Condensed Matter,* vol. 16, p. R82958, 2004 .

[53] Z. H. Azmi, S. Aris, S.Abubakar, S. Sagadevan, R.Siburian and S. Paiman, “Effect of seed layer on the growth of zinc oxide nanowires by chemical bath deposition method,” *Coatings 2022, 12,* vol. 12, pp. 1-12, 2022.

[54] A. H. Jaafar, A. Gee and N. T. & Kemp, “Nanorods vs Nanoparticles: A Comparison Study of Au/ZnO-PMMA/Au Non-volatile Memory Devices showing the importance of Nanostructure Geometry on Conduction Mechanisms and Switching Properties,” *IEEE Transactions on Nanotechnology,* vol. 19, pp. 236-246, 2020.

[55] D. H. Al-Weally, A. Holi and A. A.AL-Zahran, “Structural, Optical, Morphological Properties of ZnO Nanoparticle/ZnO Nanorods,” *Journal of Physics: Conference. Series* , vol. 1294, p. 022030, 2019.

[56] D. Phan and G. Chung, “Effects of different morphologies of ZnO films on hydrogen sensing properties,” *Journal of Electroceramics,* vol. 32, pp. 353-360, 2014.

[57] N. Alvi, S. Hussain, J. Jensen, A. Nur and M. Willander, “Influence of helium-ion bombardment on the optical properties of ZnO nanorods/p-GaN light-emitting diodes.,” *Nanoscale Research Letters,* vol. 6, p. 628, 2011.

[58] M. T. Thein, S.Y. Pung, L. S. Chuah and Y.-F. Pung, “Photodegradation behavior of ZnO nanorods on various types of organic dyesl,” *Advances in Materials and Processing Technologies,* vol. 4, pp. 272-280, 2018.

[59] F. H. Alkallas, A. B.G.Trabelsi, R. Nasser, S. Fernandez, J. Song and H. Elhouichet, “Promising Cr-Doped ZnO Nanorods for Photocatalytic Degradation Facing Pollution,” *Applied Surfaces,* vol. 12, pp. 1-16, 2022.

[60] C. Rodwihok, S. Choopun, P. Ruankham, A.Gardchareon, S. Phadungdhitidhada and D. Wongratanaphisan, “UV sensing properties of ZnO nanowires/nanorods,” *Appllied Surfurce Science,* vol. 477, pp. 159-165, 2019.

[61] K. Huang, Y.H. Li, S.Lin, C. Liang, H. Wang, C. Ye, Y. Wang, R. Zhang, D. Fan, H. Yang, Y.G. Wang and M. Lei, “A facile route to reduced graphene oxide–zinc oxide nanorod composites with enhanced photocatalytic activity,” *Powder Technology 257,* pp. 113-119, 2014.

[62] L. Cai, W. Zhou, F. Ren, J. Chen, G. Cai, Y. Liu, X. Guan and S. Shen, “W ion implantation boosting visible-light photoelectrochemical water splitting over ZnO nanorod arrays,” *Journal of Photonics for Energy,* vol. 7, pp. 1-11, 2017.

[63] K. Lefatshe, P. Dube, D. Sebuso, M. Madhuku and C. Muiva, “Optical dispersion analysis of template assisted 1D-ZnO nanorods for optoelectronic applications,,” *Ceramics International,* vol. 47 , pp. 7407-7415, 2021.

[64] D. Montenegro, V. Hortelano, O. Martínez, M. Martínez-Tomas, V. Sallet, V. Muñoz-Sanjosé and J. Jiménez, "Influence of metal organic chemical vapor deposition growth conditions on vibrational and luminescent properties of ZnO nanorods.," *Journal of Applied Physics,* vol. 113, pp. 143513-143519, 2013.

[65] J. Choi, H. Tabata and T. Kawai, "Initial preferred growth in zinc oxide thin films on Si and amorphous substrates by a pulsed laser deposition," *Journal of Crystal Growth,* vol. 226, pp. 493-500, 2001.

[66] P. Yang, H. Yan, S. Mao, R. Russo, J. Johnson, R. Saykally, N. Morris, J. Pham, R. He and H. Choi, "Controlled growth of ZnO nanowires and their optical properties.," *Advanced Functional Materials,* vol. 12, pp. 323-331, 2002.

[67] B. Liu and H. C. Zeng, "Hydrothermal Synthesis of ZnO Nanorods in the Diameter Regime of 50 nm," *Journal of the American Chemical Society,* vol. 125, pp. 4430-4431, 2003.

[68] G. An, Z. Sun, Y. Zhang, K. Ding, Y. Xie, R. Tao, H. Zhang and Z. Liu, "CO2-Mediated Synthesis of ZnO Nanorods and Their Application in Sensing Ethanol Vapor," *Journal of Nanoscience and Nanotechnology,* vol. 11, pp. 1252-1258, 2011.

[69] Y. Ni, X.Wei, J.Hong and Y.Ye, "Hydrothermal preparation and optical properties of ZnO nanorods," *Materials Science and Engineering B* , vol. 121, pp. 42-47, 2005.

[70] L. Wu, Y. Wu, Y. Shi and H. Wei, "Synthesis of ZnO nanorods and their optical absorption in visible-light region," *Rare Metals,* vol. 25, pp. 68-73, 2006.

[71] A. F. Abdulrahman, S. M. Ahmed, N. Ahmed and M. Almessiere, "Enhancement of ZnO nanorods Properties Using Modified Chemical Bath Deposition Method: Effect of Precursor Concentration," *Crystals,* vol. 10, pp. 1-24, 2020.

[72] C. Lausecker, B. Salem, X. Baillin and V. Consonni, "Implementing the Reactor Geometry in the Modeling ofChemical Bath Deposition of ZnO Nanowires," *Nanomaterials* , vol. 12, pp. 1-13, 2022.

[73] E. Pourshaban, H. Abdizadeh and M. R. Golobostanfard, “ZnO Nanorods Array Synthesized by Chemical Bath Deposition: Effect of Seed Layer Sol Concentration,” *Procedia Materials Science,* vol. 11, pp. 352-358, 2015.

[74] Z. Azmi, S. M. Aris, S. Abubakar, S. Sagadevan, R. Siburian and S.Paiman, “Effect of Seed Layer on the Growth of Zinc Oxide Nanowires by Chemical Bath Deposition Method,” *Coatings,* vol. 13, p. 474, 2022.

[75] R. A. Rahman, M. A. Zulkefle, S. H. Herman and R. I. Alip, “Seed Layer Assisted Growth of Chemical Bath Deposited ZnO Nanorods : Influence of Seed Layer Thickness,” *Journal of electrical and electronic systems research,* pp. 81-86, 2020.

[76] T. Park, K. Lee, N. Kim, Y. Oh, J. Yoo and M. Um, “Aspect ratio-controlled ZnO nanorods for highly sensitive wireless ultraviolet sensor applications,” *Jounal of Materials Chemistry ,* vol. 5, pp. 12256-12263, 2017.

[77] S. Yunus, M. Sahdan, M. Ichimura, A. Supee and S. Rahim, “Structural studies of ZnO nanostructures by varying the deposition parameters,” *AIP Conference Proceedings,* vol. 1788, pp. 1-6, 2017.

[78] A. F. Abdulrahman, S. M. Ahmed, S. M. Hamad and A. A. Barzinjy, “ Effect of Growth Temperature on Morphological, Structural, and Optical Properties of ZnO Nanorods Using Modified Chemical Bath Deposition Method.,” *Journal of Electronic Materials,* vol. 50, pp. 1482-1495, 2021.

[79] A. F.Abdulrahman, S. M.Ahmed, S. M.Hamad, M. A.Almessiere, N. M.Ahmed and S. M.Sajadi, “Effect of different pH values on growth solutions for the ZnO nanostructures,” *Chinese Journal of Physics,* vol. 71, pp. 175-189, 2021.

[80] N. Rosli, M. M. Halim, M. R. Hashim and W. Maryam, “Influence of concentration on the geometry of ZnO nanostructures prepared by chemical bath deposition,” *Journal of Physics: Conference Series,* vol. 1371 , pp. 1-7, 2019.

[81] M. F. Esfahani, “Synthesis of ZnO nanorods via chemical bath deposition method: The effects of physicochemical factors,” *Ceramics International,* vol. 42, pp. 173-184, 2016.

[82] S. D. Shinde, G. E. Patil, D. D. Kajale, D. V. Ahire, V. B. Gaikwad and G. H. Jain, "Synthesis of zno nanorods by hydrothermal method for gas sensor applications," *International Journal on Smart Sensing and Intelligent Systems* , vol. 5, pp. 57-70, 2012.

[83] M.G. Ghoniem, S. A. Talab, A. Modwi and K. K. Taha, "Exploration of Methylene Blue Degradation over ZnO Nanorods Mechanism using Scavenging Reagents.," *Oriental Journal of Chemistry,* vol. 37, pp. 609-618, 2021.

[84] T. Munawar, F. Iqbal, S. Yasmeen, K. Mahmood and A. Hussain, "Multi metal oxide NiO-CdO-ZnO nanocomposite–synthesis, structural, optical, electrical properties and enhanced sunlight driven photocatalytic activity," *Ceramics International,* vol. 46, pp. 2421-2437, 2020.

[85] D. Lin, H. Wu, R. Zhang and W. Pan, "Enhanced Photocatalysis of Electrospun Ag−ZnO Heterostructured Nanofibers," *Chemistry of Materials,* vol. 21, p. 3479–3484, 2009.

[86] B. Subash, B. Krishnakumar, M. Swaminathan and M. Shanthi, "Highly Efficient, Solar Active, and Reusable Photocatalyst: Zr-Loaded Ag–ZnO for Reactive Red 120 Dye Degradation with Synergistic Effect and Dye-Sensitized Mechanism," *Langmuir,* vol. 29, pp. 939-949, 2013.

[87] F. Mukhtar, T. Munawar, M. Nadeem, M.N. Rehman, K. Mahmood, S. Batool, M. Hasan, K. Rehman and F. Iqbal, "Enhancement in carrier separation of ZnO-Ho2O3-Sm2O3 hetrostuctured nanocomposite with rGO and PANI supported direct dual Z-scheme for antimicrobial inactivation and sunlight driven photocatalysis," *Advanced Powder Technology,* vol. 32, pp. 3770-3787, 2021.

[88] M. Ikram, S. Hayat, M. Imran, A. Haider, S. Naz, A. Ul-Hami, I. Shahzadi, J. Haider, A. Shahzadi, W. Nabgan and S. Ali, "Novel Ag/cellulose-doped CeO2 quantum dots for efficient dye degradation and bactericidal activity with molecular docking study," *Carbohydrates Polymers,* vol. 269, pp. 1-12, 2021.

[89] L. Z. Yahiya and M. K. Dhahir, "Enhanced Physical Absorption Properties of ZnO Nanorods by Electrostatic Self-Assembly with Reduced Graphene Oxide and Decorated

with Silver and Copper Nanoparticles," *Iraqi Journal of Physics,* vol. 19, pp. 66-78, 2021.

[90] M. Rashid, M. Ikram, A.Haider, S. Naz, J.Haider, A.Ul-Hamid, A.Shahzadie and M. Aqeela, "Photocatalytic, dye degradation, and bactericidal behavior of Cu-doped ZnO nanorods and their molecular docking analysis," *Dalton Transactions,* vol. 49, pp. 8314-8330, 2020.

[91] M. Ikram, S. Aslam, A. Haider, S. Naz, A. Ul-Hamid, A. Shahzadi, J. H. S. A. M. Ikram and A. R. Butt, " Doping of Mg on ZnO Nanorods Demonstrated Improved Photocatalytic Degradation and Antimicrobial Potential with Molecular Docking Analysis.," *Nanoscale Research Letters,* vol. 16, p. 78, 2021.

[92] M. Wang, F. Ren, G. Cai, Y. Liu, S. Shen and L. Guo, "Activating ZnO nanorod photoanodes in visible light by Cu ion implantation," *Nano Research,* vol. 7, pp. 353-364, 2014.

[93] X. Hou, F. L. J. D. Huiyan Maa, Y. A. X. Zhao, D. M. D. Li and B. Liao, "Synthesis of Ag ion-implanted TiO2thin films for antibacterialapplication and photocatalytic performance," *Journal of Hazardous Materials ,* vol. 299, pp. 59-66, 2015.

[94] T. Tsuzuki, R. He, A. Dodd and M.Saunders, "Challenges in determining the location of dopants, to study the influence of metal doping on the photocatalytic activities of ZnO nanopowders," *Nanomaterials ,* vol. 9, pp. 1-19, 2019.

[95] K. Lefatshe, G. T. Mola and C. M. Muiva, "Reduction of hazardous reactive oxygen species (ROS) production of ZnO through Mn inclusion for possible UV-radiation shielding application," *Heliyon,* vol. 6, pp. 1-8, 2020.

[96] M. Lesnik, D. Verhovsek, N. Veronovski, M. Grancer, G. Drazic, K. Soderznik and M. Drofenik, "Hydrothermal synthesis of Mn-doped TiO2 with a strongly suppressed photocatalytic activity," *Materials and Technology,* vol. 52, pp. 411-416, 2018.

[97] T. Tsuzuki, R. He, J. Wan, L. Sun and X. Wang, "Reduction of the photocatalytic activity of ZnO nanoparticles for UV protection applications," *International Journal of Nanotechnology ,* vol. 9, pp. 1017-1029, 2012.

[98] X. Song, W. Li, D. He, H. Wu, Z. Ke, C. Jiang, G. Wang and X. Xiao, "The "Midas Touch" Transformation of TiO2 Nanowire Arrays during Visible Light Photoelectrochemical Performance by Carbon/Nitrogen Coimplantation," *Advanced Energy Materials,* vol. 8, pp. 1-8, 2018.

[99] G. Perillat-Merceroz, P. Gergaud, S. P. Marotel, P. Jouneau and G. Feuillet, "Formation and annealing of dislocation loops induced by nitrogen implantation of ZnO," *Journal of Applied Physics,* vol. 109, p. 023513, 2011.

[100] F. Otieno, M. Airo, E. Njoroge, R. Erasmus, T. Ganetsos, A. Quandt, D. Wamwangi and D. G. Billing, "Effect of implantation of Sm+ions into RF sputtered ZnO thin film," *AIP Advances,* vol. 9, pp. 1-7, 2019.

[101] S.H. Park, S.H. Kim and S.W. Han, "Structural Properties of Nitrogen-Ion Implanted ZnO Nanorods," *Journal of the Korean Physical Society,* vol. 50, pp. 1557-1560, 2007.

[102] M. Wang, F. Ren, J. Zhou, G. Cai, L. Cai, Y. Hu, D. Wang, Y. Liu, L. Guo and S. Shen, "N Doping to ZnO Nanorods for Photoelectrochemical Water Splitting under Visible Light: Engineered Impurity Distribution and Terraced Band Structure," *Scientific Reports,* vol. 5, pp. 1-13, 2015.

[103] B. Pergolese, M. Muniz-Miranda and A. Bigotto, "Catalytic activity of Ag/Pd bimetallic nanoparticles immobilized on quartz surfaces," *Chemical Physics Letters 438,* vol. 438, pp. 290-293, 2007.

[104] A. Macková, A. Jagerová, P. Malinský, a. J. F. M. Cutroneo, P. Nekvindová, A. Michalcová, V. Holýef and T. Košutová, "Nanostructures in various Au ion-implanted ZnO facets modified using energetic O ions," *Physical Chemistry Chemical Physics,* vol. 22, pp. 23563-23573, 2020.

[105] C. I. Park, Z. Jin, E. S. Jeong, I. H. Hwang and S. W. Han, "Local structural properties of Co-ion-implanted ZnO nanorods," *Journal of the Korean Physical Society,* vol. 63, pp. 2165-2169, 2013.

[106] V. Gurylev, Nanostructured Photocatalyst via Defect Engineering: Basic Knowledge and Recent Advances, Switzerland: Springer, 2021.

[107] T. Wu, A. Wang, L. Zheng, G. Wang, Q. Tu, B. Lv, Z. Liu, Z. Wu and Y. Wang, "Evolution of native defects in ZnO nanorods irradiated with hydrogen ion," *Scientific Reports*, vol. 9, p. 17393, 2019.

[108] A. Y. Azarov, A. Hallén, X. L. Du, P. Rauwel, A. Y. Kuznetsov and B. G. Svensson, "Effect of implanted species on thermal evolution of ion-induced defects in ZnO.," *Journal of Applied Physics*, vol. 115, pp. 1-12, 2014.

[109] T. Shimogaki, K. Okazaki, D. Nakamura, M. Higashihata, T. Asano and T.Okada, "Effect of laser annealing on photoluminescence properties of Phosphorus implanted ZnO nanorods," *Optics Express*, vol. 20, pp. 15247-15252, 2012.

[110] K. Ip, R. Frazier, Y. Heo, D. Norton, C. Abernathy, S. Pearton, J. Zavada, J. Kelly, R. Rairigh, A. Hebard and R. Wilson, "Ferromagnetism in Mn- and Co-implanted ZnO nanorods," *IEEE-NANO* , vol. 2, pp. 16-19, 2003.

[111] D. Li, D. Li, H. Wu, F. Liang, W. Xie, C. Zou and L. Shao, "Defects related room temperature ferromagnetism in Cu-implanted ZnO," *Journal of Alloys and Compounds*, vol. 591, pp. 80-84, 2014.

[112] L. Cai, F. Ren, M. Wang, G. Cai and Y.Chen, "V ions implanted ZnO nanorod arrays for photoelectrochemical water splitting under visible light," *International Journal o f Hydrogen Energy*, vol. 40, pp. 1394-1401, 2015.

[113] M. Chakraborty, R. Thangavel and K. Asokan, "N doped ZnO and ZnO nanorods based p-n homojunction fabricated by ion implantation," *AIP Conference Proceedings 1953*, vol. 050047, pp. 1-4, 2018.

[114] K. S. R. Dharman Ranjith Kumar, Y. Haldorai and A.Kandasami, "Nitrogen-Implanted ZnO Nanorod Arrays for Visible Light Photocatalytic Degradation of a Pharmaceutical Drug Acetaminophen," *ACS Omega*, vol. 4, pp. 11973-11979, 2019.

[115] Z. Azmi, S.N. Aris, S. Abubakar, S.Sagadevan, R.Siburian and S.Paiman, "Effect of seed layer on the growth of Zinc xide nanowires by cemical deposition method," *Coatings*, vol. 12, p. 474, 2022.

[116] Y. Tong, Y. Liu, L. Dong, D.Zhao, J. Zhang, Y. Lu, D.Shen and X.Fan, “Growth of ZnO Nanostructures with Different Morphologies by Using Hydrothermal Technique,” *Journal of Physical Chemistry,* vol. 110, pp. 20263-20267, 2006.

[117] A. Juma, L. Lepodise, K. Maabong, D. Letshoathebe and C. Muiva, “Surfactant assisted chemical bath deposition-based synthesis of 1-D nanostructured CuO thin films from alkaline baths,” *Materials Science in Semiconductor Processing,* vol. 67, pp. 69-74, 2017.

[118] K. Lefatshe, P. Dube, D. Sebuso, M. Madhuku and C. Muiva, “Optical dispersion analysis of template assisted 1D-ZnO nanorods for optoelectronic applications,,” *Ceramics International,,* vol. 47, no. 6, pp. 7407-7415, 2021.

[119] A. Kiruthiga, T.Krishnakumar and R.Kannan, “The effect of surfactant on structural and optical properties of ZnO nanorods by wet chemical synthesis,” *AIP Conference Proceedings,* vol. 2142, pp. 6-14, 2019.

[120] M. Precision. [Online]. Available: https://www.matsusada.com/application/ps/ion_implantation/.

[121] I. N. Draganic, C. Leibman, L. J. Rybarcyk, T.M.Bronson and K. W. Dudeck, “Hot filament performance in a Freeman ion source,” in *AIP Conference Proceedings*, USA, 2011.

[122] C. P. H. Rose and G. Ryding, “Concept and design of ion implantation equipment for semiconductor processing,” *Review of Scientific Instruments,* vol. 77, pp. 1-12, 2006.

[123] C. M. McKenns, “Faraday cup designs,” in *Springer series in elctrophysics,* Berlin, 1982.

[124] B.D.Cullity, Elements of X-ray diffraction. 2nd ed., Reading: Addison-Wesley, 1978.

[125] “Anton Paar,” [Online]. Available: https://wiki.anton-paar.com/at-de/roentgendiffraktion-xrd/. [Accessed 27 04 2022].

[126] M. Khanlary and S.Isazadeh, “Structural and optical properties of ZnO thin films prepared by sol-gel method,” *Micro Nano Letters,* vol. 6, pp. 767-769, 2011.

[127] M. Moram and M. Vickers, “X-ray diffraction of III-nitrides.,” *Reports on Progress in PhysicS,* vol. 72, p. 036502, 2009.

[128] C. Moditswe, C. M. Muiva and A. Juma, “Highly conductive and transparent Ga-doped ZnO thin films deposited by chemical spray pyrolysis,” *Optik,* vol. 127, pp. 8317-8325, 2016.

[129] C. Muiva, L. Lepodise, R. Bosigo and A. Juma, “Structural analysis and temperature dependent conductivity of LaxCu1-xO shrimp-like nanostructures synthesised via wet chemical precipitation,” *Materials Characterization,* vol. 170, pp. 1-9, 2020.

[130] K. Piętak, S. Złotnik, E. Rozbiegała, P. P. Michałowski, M. Wójcik, J. Gaca and M. Rudziński, “Phosphorus implantation of Mg-doped (Al)GaN heterostructures: structural examination and depth profiling,” *Journal of Materials Science: Materials in Electronics,* vol. 31, p. 17892–17902, 2020.

[131] T. C.Paul, J. Podder and M. H. Babu, “Optical constants and dispersion energy parameters of Zn-doped TiO2 thin films prepared by spray pyrolysis technique,” *Surfaces and Interfaces,* vol. 21, pp. 1-12, 2020.

[132] S. Manzoor, S. Husain, A. Somvanshi, M. Fatema and N. Zarrin, “Exploring the role of Zn doping on the structure, morphology, and optical properties of LaFeO3,” *Applied Physics A, ,* vol. 125, p. 509, 2019.

[133] Q. He and Y. Yang, “On Lattice Distortion in High Entropy Alloys,” *Frontiers in Materials,* vol. 5, pp. 1-8, 2018.

[134] S. Venkatachalam, D. Mangalaraja, S. K. Narayandass, K. Kim and J. Yi, “Structure, optical and electrical properties of ZnSe thin films,” *Physica B: Condensed Matter,* vol. 358, pp. 27-35, 2005.

[135] R. Ghosh, D. Basak and S. Fujihara, “Effect of substrate-induced strain on the structural, electrical, and optical properties of polycrystalline ZnO thin films,” *Jornal of Applied Physics,* vol. 96, pp. 2689-2692, 2004.

[136] J.-I. C. f. D. Data, “Search Manual for Selected Powder Diffraction Data for Metals and Alloys. T,” International Centre for Diffraction Data, 1978.

[137] M. Nadeem, T.Munawar, F.Mukhta, M. R. M.Naveed ur Rahman, A.Hussain and F.Iqbal, "Hydrothermally derived Co, Ni co-doped ZnO nanorods; structural, optical,and morphological study," *Optical Materials,* vol. 111, pp. 1-11, 2021.

[138] K. K. Taha, A. Modwi and L. Khezami, "ZnO nanoparticles: Surface and X-ray profile analysis," *Journal of Ovonic Research,* vol. 14, pp. 1-11, 2018.

[139] M. Herman, "Applications of Rutherford backscattering spectrometry to refractory metal," *Journal of Vacuum Science & Technology B ,* vol. 2, p. 748, 1984.

[140] I. A. E. AGENCY, "Surface modification of materials by ion implantations for industrial and medical applications," IAEA-TECDOC-1165, Vienna, 2000.

[141] H. R. Verma, "Rutherford Backscattering Spectroscopy," in *Atomic and Nuclear Analytical Methods*, Springer, 2007, pp. 91-141.

[142] M. Mayer, *Rutherford Backscattering Spectrometry (RBS),* Germany: Max-Planck-Institut f¨ur Plasmaphysik, EURATOM Association, 2003.

[143] P. M. V. Raja and A. R. Barron, *Rutherford Backscattering of Thin Films,* Rice University., 2021.

[144] S. H. Al-Shamma, "Simulation of Rutherford backscattering cross section of atoms," *Journal of Education and Science,* vol. 25, pp. 88-107, 2012.

[145] Y. Peng, W. Wei, M. F. Saleem, K.Xiao, Y. Yang, Y.Yang, Y. Wang and W. Sun, "Resonant Raman Scattering in Boron-Implanted GaN," *Micromachines,* vol. 13, pp. 1-11, 2022.

[146] D. Baer and S. Thevuthasan, "Characterization of Thin Films and Coatings," in *Handbook of Deposition Technologies for Films and Coatings (Third Edition)*, William Andrew Publishing, 2010, pp. 749-864.

[147] A. Chaichi, A. Prasad and M. Gartia, "Raman Spectroscopy and Microscopy Applications in Cardiovascular Diseases: From Molecules to Organs-review," *Biosensors ,* vol. 8, pp. 1-19, 2018.

[148] C. Charpentier, P. Prod'homme, L. Maurin, M. Chaigneau and P. Cabarrocas, “X-ray diffraction and raman spectroscopy for better undestanding of ZnO:Al growth process,” *EPJ Photovoltaics,* vol. 2, pp. 1-8, 2011.

[149] S. Singh, R.S. Srinivas and S.S. Major, “Effect of substrate temperature on the structure and optical properties of ZnO thin films deposited by reactive rf magnetron sputtering,” *Thin Solid Films,* vol. 515, pp. 8718-8722, 2007.

[150] D. Song, “Effects of rf power on surface-morphological, structural and electrical properties of aluminium-doped zinc oxide films by magnetron sputtering,” *Applied Surface Science,* vol. 254, pp. 4171-4178, 2008.

[151] K. A. Alim, V. A. Fonoberov, M. Shamsa and A. A. Balandin, “Micro-Raman investigation of optical phonons in ZnO nanocrystals,” *Journal of Applied Physics,* vol. 97, pp. 1-5, 2005.

[152] K. Fahelelbom, A. Saleh, M. M. A. Al-Tabakha and A. Ashames, “Recent applications of quantitative analytical FTIR spectroscopy in pharmaceutical, biomedical, and clinical fields: A brief review,” *Reviews in Analytical Chemistry,* vol. 41, pp. 21-33, 2022.

[153] M. J. Baker, J. Trevisan, P.Bassan, R. Bhargava, H. Butler, K. Dorling, P. Fielden, S. W. Fogarty, N. J. Fullwood, K. A.Heys, C. Hughes, P.Lasch, P. L. Martin-Hirsch, B.Obinaju, G. D. Sockalingum, J. Sulé-Suso, R. J. Strong, M. Walsh, B.R.Wood, P.Gardner and F. L. .Martin, “Using Fourier transform IR spectroscopy to analyze biological materials,” *Nat Protoc,* vol. 9, pp. 1771-1791, 2014.

[154] B. Giechaskiel and M.Clairotte, “Fourier Transform Infrared (FTIR) Spectroscopy for Measurements of Vehicle Exhaust Emissions: A Review,” *Applied Science,* vol. 11, pp. 1-35, 2021.

[155] O. Faix, “Fourier Transform Infrared Spectroscopy,” in *Methods in Lignin Chemistry. Springer Series in Wood Science,* Berlin, Springer, 1992, pp. 83-109.

[156] T. N. Corporation, *Introduction to Fourier Transform Infrared Spectrometry,* 2001.

[157] F. A. Settle, Handbook of Instrumental Techniques for Analytical Chemistry, New Jersey: Upper Saddle , 1997.

[158] Y. Kim. and C. Park, “Principle of Field Emission-Scanning Electron Microscopy (FE-SEM) and its Application to the Analysis of Carbon Nanostructures,” *Carbon Letters*, vol. 2, pp. 202-211, 2001.

[159] C. Suryanarayana, “Microstructure: An Introduction,” in *Aerospace Materials and Material Technologies*, Singapore, Springer, 2017, pp. 105-123.

[160] R. S. Prabhu, R. Priyanka, M. Vijay and G. K. Vikashini, “Field emissionscanning electron microscopy (FESEM) with A very big future in pharmaceutical research,” *International Journal of Pharmacy and Biological Sciences*, vol. 11, pp. 183-187, 2021.

[161] B. Lewczuk and N. Szyryńska, “Field-Emission Scanning Electron Microscope as a Tool for Large-Area and Large-Volume Ultrastructural Studies,” *Animals*, vol. 11, pp. 1-21, 2021.

[162] R. W. Welker, “Chapter 4 - Size Analysis and Identification of Particles,” in *Developments in Surface Contamination and Cleaning*, William Andrew Publishing, 2012, pp. 179-213.

[163] Y. F. Dufrêne, T. Ando, R. Garcia, D. Alsteens, D. Martinez-Martin, A.Engel, C. Gerber and D. J. Müller, “Imaging modes of atomic force microscopy for application in molecular and cell biology,” *Nature Nanotechnology*, vol. 12, pp. 295-307, 2017.

[164] F. Stevie and C. L. Donley, “Introduction to x-ray photoelectron spectroscopy,” *Journal of Vacuum Science and Technology; A*, vol. 38, pp. 1-20, 2020.

[165] J. Moulder, W. Stickle, P. Sobol and K. Bomben, Handbook of X-ray Photoelectron Spectroscopy, Minnesota: Perkin-Elmer Corporation, 1992.

[166] J. Hook and H. Hall, Solid state physics, Wiley, 2001.

[167] P. V. Raja and A. R. Barron, “X-ray Photoelectron Spectroscopy,” in *Physical Methods in Chemistry and Nano Science*, OpenStax CNX, Midas Green Innovations, Ltd, 2020.

[168] T. Spectronic, *Basic UV-Vis Theory, Concepts and Applications*, Thermo Spectronic.

[169] J. Roberts, J. Chapman, S.Chandra and D.Cozzolino, “The Use of UV-Vis Spectroscopy in Bioprocess and Fermentation Monitoring,” *Fermentation* , vol. 4, p. 18, 2018.

[170] D. L. Pavia, G. M. Lampman, G. S.Kriz and L. R.Vijaan, Spectroscopy Third ED, CBS Publishers and Distributors, 1997.

[171] M. Picollo, M. Aceto and T. Vitorino, "UV-Vis spectroscopy," *Physical Sciences Reviews,* vol. 2018, pp. 1-14, 2018.

[172] C. Burgess, "Chapter 1 The basics of spectrophotometric measurement," in *UV-Visible Spectrophotometry of Water and Wastewater*, Elsevier, 2007, pp. 1-19.

[173] D. Swinehart, "The Beer- Lambert's law," *Journal of Chemical Education,* vol. 39, p. 333, 1962.

[174] L.D.S.Yadav, "Ultraviolet (UV) and Visible Spectroscopy," in *Organic Spectroscopy*, Dordrecht, Springer, 2005.

[175] F. Rocha, A. Gomes, C. N. Lunardi, S.Kaliaguine and G. S. Patience, "Experimental methods in chemical engineering: Ultraviolet visible spectroscopy—UV-Vis," *UV-Vis. The Canadian Journal of Chemical Engineering,* vol. 96, pp. 2512-2517, 2018.

[176] S. Xue, X. Zu, L. Shao, Z. Yuan, W. Zheng, X. Jiang and H. Deng, "Effects of annealing on optical properties of Zn-implanted ZnO thin films," *Journal of Alloys and Compounds,* vol. 458, pp. 569-573, 2008.

[177] M. Kahouli, A. Barhoumi, A. Bouzit, A. Al-Hajry and S. Guermazi, "Structural and optical properties of ZnO nanoparticles prepared by direct precipitation method," *Superlattices and Microstructures,* vol. 85, pp. 7-23, 2015.

[178] H. Bolarinwa, M. Onuu, A. Fasasid, S. Alayande, L. Animasahun, I. Abdulsalami, O. Fadodun and ". I. Egunjobi, "Determination of optical parameters of zinc oxide nanofibre deposited by electrospinning technique," *Journal of Taibah University for Science,* vol. 11, pp. 1245-1258, 2017.

[179] F. A.Mir, "Transparent wide band gap crystals follow indirect allowed transition and bipolaron hopping mechanism," *Results in Physics,* vol. 4, pp. 103-104, 2014.

[180] P. Dube, A. Juma and C. Muiva, “Dispersive optical constants and electrical properties of nanocrystalline CuInS2 thin films prepared by chemical spray pyrolysis,” *Ceramics International,* vol. 46, pp. 7396-7402, 2020.

[181] C. Gumus, O. Ozkendir, H. Kavak and Y. Ufuktepe, “Structural and optical properties of zinc oxide thin films prepared by spray pyrolysis method.,” *Journal of optoelectronics and advanced materials,* vol. 8, pp. 299-303, 2006.

[182] L. E. Brus, “Electron–electron and electron-hole interactions in small semiconductor crystallites: The size dependence of the lowest excited electronic state,” *The Journal of Chemical Physics,* p. 4403, 1984.

[183] I. Mehmet and G. Nisami, “Composition-tuned band gap energy and refractive index in GaSxSe1-x,” *Material Chemistry and Physics,* vol. 190, pp. 74-78, 2017.

[184] C. Belkhaoui, F. Mzabi, H. Smaoui and P. Daniel, “Enhancing the structural, optical and electrical properties of ZnO nanopowders through (Al + Mn) doping,” *Results in Physics,* pp. 1686-1696, 2019.

[185] C. Mrabet, O. Kamoun, A. Boukhachem, M. Amlouk and T. Manoubi, “Some physical investigations on hexagonal-shaped nanorods of lanthanum-doped ZnO,” *Journal of Alloys and Compounds,* vol. 648, pp. 826-837, 2015.

[186] R. Mimouni, O. Kamoun, A. Yumak, A. Mhamdi, K. Boubaker, P. Petkova and M. Amlouk, “Effect of Mn content on structural, optical, opto-thermal and electrical properties of ZnO: Mn sprayed thin films compounds,” *Journal of Alloys and Compounds,* vol. 645, pp. 100-111, 2015.

[187] S. Wemple and M. DiDomenico, “Behavior of the electronic dielectric constant in covalent and ionic materials,” *Physical Review B,* vol. 3, pp. 1338/-1351, 1971.

[188] A.M.A. Shamekh, A.Z. Mahmoud and M.A. Abdel-Rahim, “Assessment of linear/nonlinear optical constants and dispersion parameters of Se85− xTe15 Sbx glasses for photonic applications,” *Optical Materials,* vol. 114, p. 111008, 2021.

[189] M. Wakkad, E. Shokr and S. Mohamed, “Optical and calorimetric studies of Ge–Sb–Se glasses,” *Journal of Non-Crystalline Solids,* vol. 265, pp. 157 - 166, 2000.

[190] C. Muiva, J. Mwabora, T. Sathiaraj and J. King, "Optical properties of amorphous Se90-xIn1oSbx thin film alloys," *Journal of Alloys and Compounds,* vol. 689, pp. 432-438, 2016.

[191] P. L. Sant'Ana, J. R. Bortoleto, N. C.Cruz, E. C.Rangel and S. F.Durrant, "Stopping and Range of Ions in Matter data for polymeric materials simulating the process of plasma immersion íon implantation," *Brazillian Journal of Vacuum Apllications,* vol. 39, pp. 2-13, 2020.

[192] F. Umarov and A. Dzhurakhalov, "Ion Bombardment-Induced Surface Effects in Materials," in *Radiation Effects in Materials,* Intechopen, 2016.

[193] M. Robinson and I. Torrens, "Computer simulation of atomic displacement cascades in solids in the binary-collision approximation," *Physical Reviews B ,* vol. 9, p. 5008, 1974.

[194] J. F. Ziegler, "SRIM-2003," *Nuclear Instruments and Methods in Physics Research B,* vol. 219, p. 1027, 2004.

[195] G. J. Caporaso, Y.-J. Chen and S. E. Sampayan, "The dielectric wall accelerator," *Reviews of Accelerator Science and Technology ,* vol. 02, pp. 253-263, 2009.

[196] P. Sigmund, "Stopping power in perspective," *Nuclear Instruments and Methods in Physics Research B,* vol. 135, pp. 1-15, 1998.

[197] H. Xue, "Ion irradiation induced damage and dynamic radiation induced damage and dynamic recovery in single crystal silicon carbide and strontium titanate," in *PhD dissertation,* University of Tennessee, 2015.

[198] J. F. Ziegler, J. P. Biersack and U. Littmark, The Stopping and Range of Ions in Matter, New York: Pergamon, 1985.

[199] G. S. Was, Fundamentals of Radiation Materials Science: Metals and Alloys, Springer, 2007.

[200] J. Tesmer and M. Nastasi, Handbook of modern ion beam materials analysis, USA: Materials Research Society, 1995.

[201] J.P. Crocombette and C. V. Wambeke, “Quick calculation of damage for ion irradiation: implementation in Iradina and comparisons to SRIM,” *EPJ Nuclear Sciences and Technologies* , vol. 5, no. 7, pp. 1-9, 2019.

[202] J. Lindhard and M. Scharff, *Physical Review* , vol. 124, pp. 128-130, 1961.

[203] H. Bethe, *Annalen der Physik,* vol. 397, pp. 325-400, 1930.

[204] S. Campisi, M. Schiavoni, C. E. Chan-Thaw and A. Villa, “Untangling the Role of the Capping Agent in Nanocatalysis: Recent Advances and Perspectives- A review,” *Catalysts,* vol. 6, pp. 1-21, 2016.

[205] H. Heinz, C. Pramanik, O. Heinz, Y. Ding, R. K. Mishra, D. Marchon, R. Flatt, I. Estrela-Lopis, J. Llop, S. Moya and R. F. Ziolo, “Nanoparticle decoration with surfactants: Molecular interactions, assembly, and applications,” *Surface Science Reports,* vol. 72, pp. 1-58, 2017.

[206] J. Kennedy, B. Sundrakannan, R.S. Katiyar, A. Markwitz, Z. Li and W. Gao, “Raman scattering investigation of hydrogen and nitrogen ion implanted ZnO thin films,” *Current Applied Physics,* vol. 8, pp. 291-294, 2008.

[207] J. Kennedy, P.P. Murmu, J. Leveneur, A. Markwitz and J. Futter, “Controlling preferred orientation and electrical conductivity of zinc oxide thin films by post growth annealing treatment,” *Applied Surface Science,* vol. 367, pp. 52-58, 2016.

[208] V.G. Plekhanov, “Chapter 6 Exciton-phonon interaction,” *Semiconductors and Semimetals,* vol. 68, pp. 135-180, 2001.

[209] R. Al-Gaashani, S. Radiman, A.R. Daud, N. Tabet and Y. Al-Douri, “XPS and optical studies of different morphologies of ZnO nanostructures prepared by microwave methods,” *Ceramics International,* vol. 39, pp. 2283-2292, 2013.

[210] H. Verma, Atomic and Nuclear Analytical Methods, New York: Springer, 2007.

[211] A. Zak, R. Razali, W. Majid and M. Darroudi, “Synthesis and characterization of a narrow size distribution of zinc oxide nanoparticles,” *International Journal of nanomedicine,* vol. 6, pp. 1399-1403, 2011.

[212] A. Zak, A. Hashim and M. Darroudi, “Optical properties of ZnO/BaCO3 nanocomposites in UV and visible region,” *Nanoscale Research Letters* , p. 399, 2014.

[213] B. Wei, K. Zheng, Y. Ji, Y. Zhang and X. Han, “Size-dependent bandgap modulation of ZnO nanowires by tensile strain,” *Nano Letters,* vol. 12, pp. 4595-4599, 2012.

[214] F. Paraguay, W. Estrada, D. Acosta, E. Andrade and M. Yoshida, “Growth,structure and optical characterization of high quality ZnO thin films obtained by spray pyrolysis,” *Thin solid films,* p. 192, 1999.

[215] A. Duzynska, V. D. R. Hrubiak, H. Teisseyre, W. Paszkowicz, A. Reszka, A. Kaminska, S. Saxena and J. Fidelus, “The structural and optical properties of ZnO bulk and nanocrystals under high pressure,” *High pressure Research,* vol. 32, pp. 354-363.

[216] S. H. Mohamed, “Synthesis, structural and ellipsometric evaluation of oxygen-deficient and nearly stoichiometric zinc oxide and indium oxide nanowires/nanoparticles,” *Philosophical Magazine A,* vol. 91, pp. 3598-3612, 2011.

[217] M. Kahouli, A. Barhoumi, A. Bouzit, A. Al-Hajry and S. Guermazi, “Structural and optical properties of ZnO nanoparticles prepared by direct precipitation method,” *Superlattices and Microstructures,* vol. 85, pp. 7-23, 2015.

[218] K. Tanaka, “Optical properties and photoinduced changes in amorphous AsS films,” *Thin Solid Films,* vol. 66, pp. 271-279, 1980.

[219] J. Solyom, Fundamentals of the physics of solids II: Electronic properties, Berlin Heidelberg: Springer, 2009.

[220] P. Ahmad, A. Rao, K. Babu and G. Rao, “Particle size effect on the dielectric properties of ZnO nanoparticles,” *Materials Chemistry and Physics,* vol. 224, pp. 79-84, 2019.

[221] K. Lefatshe, P. Dube, D. Sebuso, M. Madhuku and C. Muiva, “Optical dispersion analysis of template assisted 1D-ZnO nanorods for optoelectronic applications,,” *Ceramics International,,* vol. 47, no. 6, pp. 7407-7415, 2021.

[222] F.Zahedi, R.S.Dariani and S.M.Rozati, "Effect of substrate temperature on the properties of ZnO thin films prepared by spray pyrolysis," *Materials Science in Semiconductor Processing,* vol. 16, pp. 245-249, 2013.

[223] M. Imram, R.Ahmad, N.Afzal, M. Rafique, M.A.Raza and Z.Khaliq, "Structural, optical and electrical characteristics of silver ions irradiated ZnO film on flexible substrate," *Superlattices and Microstructures,* vol. 144, pp. 1-8, 2020.

[224] R. S. Zeferino, M. B. Flores and U. Pal, "Photoluminescence and Raman Scattering in Ag-doped ZnO Nanoparticles," *Journal of Applied Physics,* vol. 109, pp. 014308 -1-6, 109, 014308 2011.

[225] L.Wang, L.Meng, V.Teixeir, S.Song, Z.Xu and X.Xu, "Structure and optical properties of ZnO:V thin films with different doping concentrations," *Thin Solid Films,* vol. 517, pp. 3721-3725, 2009.

[226] I.Ahmad, M.Madhuku, A.Sadaf, S.Khan, J.Hussain, A.Ali, D.Wan, S.Z.Ilyas, G.Mola, A.Waheed and M. A.Rasheed, "Tailoring the structural and optical characteristics of InGaN/GaN multilayer thin films by 12 MeV Si ions irradiations," *Materials Science in Semiconductor Processing,* vol. 64, pp. 95-100, 2017.

[227] Q. He and Y. Yang, "On Lattice Distortion in High Entropy Alloys," *Frontiers in Materials,* vol. 5, pp. 1-8, 2018.

[228] T.Chen, C. Foo and S. Tsang, "Interstitial and substitutional light elements in transition metals for heterogeneous catalysis," *Chemical science,* vol. 12, pp. 517-532, 2021.

[229] T. Fa, L. Lin, Y. Shu-De, W. Ming-Fang and Z. Sheng-Qiang, "Unidirectional expansion of lattice parameters in GaN induced by ion implantation," *Chinese Physical Society B,* vol. 20, pp. 1-4, 2011.

[230] C. Charpentier, P. Prod'homme, I. Maurin, M. Chaigneau and R. i. Cabarrocas, "X-Ray diffraction and Raman spectroscopy for a better understanding of ZnO:Al growth process," *EPJ Photovoltaics ,* vol. 2, pp. 1-8, 2011.

[231] R. S. Zeferino, M. B. Flores and U. Pal, "Photoluminescence and Raman Scattering in Ag-doped ZnO Nanoparticles," *Journal of Applied Physics,* vol. 109, pp. 1-6, 2011.

[232] T. Munawar, S. Yasmeen, F.Mukhtar, M. S.Nadeem, K.Mahmood, M. Saif, M.Hasan, A.Ali, F.Hussain and F.Iqba, "Zn0.9Ce0.05M0.05O (M = Er, Y, V) nanocrystals: Structural and energy bandgap engineering of ZnO for enhancing photocatalytic and antibacterial activity," *Ceramics International,* vol. 46, pp. 14369-14383, 2020.

[233] E.Wendler, Th.Bierschenk, F.Felgenträger, J.Sommerfeld, W.Wesch, D.Alber, G.Bukalis, L.C.Prinsloo, N. d. Berg, E.Friedland and J.B.Malherbe, "Damage formation and optical absorption in neutron irradiated SiC," *Nuclear Instruments and Methods in Physics Research Section B: Beam Interactions with Materials and Atoms*, vol. 286, pp. 97-101, 2012.

[234] A. Mondal, S.Pal, A.Sarkar, T.S.Bhattacharya, A. Das, N.Gogurla, S.K.Ray, P. Kumar, D.Kanjilal, K.D.Devi, A.Singha, S.Chattopadhyay and D.Jana, "Raman spectroscopic analysis on Li, N and (Li,N) implanted ZnO," *Materials Science in Semiconductor Processing*, vol. 80, pp. 111-117, 2018.

[235] M. Schumm, M. Koerdel, S. Müller, H. Zutz and C. Ronning, "Structural impact of Mn implantation on ZnO," *New Journal of Physics* , vol. 10, pp. 1-14, 2008.

[236] J.Kennedy, B.Sundrakannan, R.S.Katiyar, A.Markwitz, Z.Li and W.Gao, "Raman scattering investigation of hydrogen and nitrogen ion implanted ZnO thin films," *Current Applied Physics,* vol. 8, pp. 291-294, 2008.

[237] M. Wang, F.Ren, G.Cai, Y.Liu, S.Shen and L.Guo, "Activating ZnO nanorod photocatalyst in visible light by Cu ion implantation," *Nano Research,* vol. 7, pp. 1-14, 2014.

[238] K. S. Ranjith, L. Nivedita, K. Asokan, S. Krishnamurthy, R.Pandian, M. Kamruddin, D. Avasthi and R. T. Kumar, "Robust water repellent ZnO nanorod array by Swift Heavy Ion Irradiation: Effect of Electronic Excitation Induced Local Chemical State Modification," *Scientific Reports* , vol. 7, pp. 1-10, 2017.

[239] J. Wang, H. Zhong, Z. Li and Wei Lu, "Raman study of N+-implanted ZnO," *Applied Physical Letters,* vol. 88 , 2006.

[240] P. Zhang, C. Kong, W. L. G. Qin, Q. Xu, H. Zhang, H. Ruan, Y. Cui and L. Fang, "The origin of the ∼274 cm−1additional Raman mode induced by theincorporation of N

dopants and a feasible route to achieve p-typeZnO:N thin films," *Applied Surface Science,* vol. 327, pp. 154-158, 2015.

[241] R.Alipour, A. Khani, R.Mohammadi and S.Rostami, "The effect of formation of titanium nitride thin film on surface characteristics of titanium by nitrogen ion implantation," *Journal of chemical research,* vol. 40, pp. 12-15, 2016.

[242] Z.Dou, Y.Guo, F.Zhang and D.Zhang, "Effect of low-energy nitrogen ion implantation on friction and wear properties of ion-plated TiC coating," *Coating,* vol. 11, 2021.

[243] N. M. Lyadov, A. I. Gumarov, V. F. Valeev, V. I. Nuzhdin, R. I. Khaibullin and I. A. Faizrakhmanov, "Optical and electrical studies of ZnO thin films heavily implanted with silver ions," *Journal of Physics: Conference Series* , vol. 572, pp. 1-6, 2014.

[244] Z. Bahşi and A. YavuzOral, "Effects of Mn and Cu doping on the microstructures and optical properties of sol–gel derived ZnO thin films," *Optical Materials,* vol. 29, pp. 672-678, 2007.

[245] B. Houng, C. C. Liu and M. T. Hung, "Structural, electrical and optical properties of molybdenum-doped TiO2 thin films," *Ceramics International,* vol. 39, pp. 3669-3676, 2013.

[246] S.Chattopadhyay, S. Dutta, D. Jana, S. Chattopadhyay, A. Sarkar, P. Kumar, D. Kanjilal, D. K. Mishra and S. K. Ray, "Interplay of defects in 1.2 MeV Ar irradiated ZnO," *Journal of applied physics,* vol. 107, pp. 1-8, 2010.

[247] S.W.Xue, X.T.Zu, L.X.Shao, Z.L.Yuan, W.G.Zheng, X.D.Jiang and H.Deng, "Effects of annealing on optical properties of Zn-implanted ZnO thin films," *Journal of Alloys and Compounds,* vol. 458, pp. 569-573, 2008.

[248] V. R. Akshay, B. Arun, G. Mandal and M. Vasundhara, "Visible range optical absorption, Urbach energy estimation and paramagnetic response in Cr-doped TiO 2 nanocrystals derived by a sol-gel method," *Physical Chemistry,* vol. 21, pp. 12991-13004, 2019.

[249] E. M. Hussein, W. M. Desoky, M. F. Hanafy and O. W. Guirguis, "Effect of TiO2 nanoparticles on the structural configurations and thermal, mechanical, and optical

properties of chitosan/TiO2 nanoparticle composites," *Journal of Physics and Chemistry of Solids,* vol. 152, pp. 1-15, 2021.

[250] M. Wang, F. Ren, G. Cai, Y. Liu, S. Shen and L. Guo, "Activating ZnO nanorod photoanodes in visible light by Cu ion implantation," *Nano Research,* vol. 7, pp. 353-364, 2014.

[251] N. Rohith, P. Kathirvel, S. S and M. Lakshmi, "Influence of Ag doping on the structural, optical, morphological and conductivity characteristics of ZnO nanorods," *Optik,* vol. 172, pp. 940-952, 2018.

[252] M. Ginting, S. Taslima, K. Sebayang, D. Aryanto, T. Sudiro and P. Sebayang, "Preparation and characterization of zinc oxide doped with ferrite and chromium," *AIP Conference Proceedings* , vol. 1862, pp. 1-5, 2017.

[253] L. Ntozakhe and R. T. Taziwa, "Pyrolysis of Carbon-Doped ZnO Nanoparticles for Solar Cell Application," in *Zinc Oxide Based Nano Materials and Devices*, 2018.

[254] P. Kumar, H. K. Malik and K. Asokan, "Tuning of optical bandgap and magnetization of C-implanted ZnO thin films," *Europhysics Letters,* vol. 110, pp. 1-5, 2015.

[255] R.Kumari, A.Sahai and N.Goswami, "Effect of nitrogen doping on structural and optical properties of ZnO nanoparticles," *Progress in Natural Science: Materials International,* vol. 25, pp. 300-309, 2015.

[256] K.Lefatshe, C.Muiva and M.Madhuku, "Effect of low energy Ag+ ion implantation on ZnO nanorods for enhanced visible light absorption-structural and optical analysis," *Optical materials,* vol. 122B, 2021.

[257] S. Gautam, P. K.Thakur, S. Kumar, R. Singh, D.-J. Huang, Y. Kim and K. HwaChae, "Evidence of ZnCO3 interstitial phase in carbon implanted ZnO(002) thin films and room temperature ferromagnetism," *Vacuum,* vol. 184, p. 109897, 2021.

[258] S. Zhou, Q. Xu, K. Potzger, G. Talut, R. Grötzschel, J. Fassbender, M. Vinnichenko, J. Grenzer, M. Helm, H. Hochmuth, M. Lorenz, M. Grundmann and H. Schmid, "Room temperature ferromagnetism in carbon-implanted ZnO," *Applied Physics Letters,* vol. 93, pp. 1-13, 2008.

[259] H. Pan, J. Yi, L. Shen, R. Wu, J. Yang, J. Lin, Y. Feng, J. Ding, L. Van and J. Yin, "Room-temperature ferromagnetism in carbon-doped ZnO," *Physical Review Letters*, vol. 99, p. 127201, 2007.

[260] F. Li, D. Wei, P. Zhang, X. Chen, F. Ding, S. Wang, R. Zhao and Z. Wang, "Effects of Zr ion implantation on crystal structure and nanoindentation behavior of TC18 titanium alloy," *Materials Research Express*, vol. 6, pp. 5-13, 2019.

[261] Y.-P. Zhu, M. Li, Y.-L. Liu, T.-Z. Ren and Z.-Y. Yuan, "Carbon-Doped ZnO Hybridized Homogeneously with Graphitic Carbon Nitride Nanocomposites for Photocatalysis," *Journal of Physical Chemistry C*, vol. 118, pp. 10963−-0971, 2014.

[262] X. Zhang, J. Qin, R. Hao, L. Wang, X. Shen, R. Yu and S. Limpanart, "Carbon-Doped ZnO Nanostructures: Facile Synthesis and Visible Light Photocatalytic Applications," *Journal of Physical Chemistry C*, vol. 119, pp. 20544-20554, 2015.

[263] X.J.Ye, C.S.Liu, W.Zhong, H.A.Song, C.T.Au and Y.W.Du, "Experimental and theoretical studies on the magnetic property of carbon-doped ZnO," *Physics Letters A*, vol. 374, pp. 496-500, 2010.

[264] C. D. Valentin, G. Pacchioni and A. Sellon, "Theory of carbon doping of titanium dioxide," *Chemical materials*, vol. 17, pp. 6656-6665, 2005.

[265] T. Munawar, S. Yasmeen, F. Mukhtar, M. Nadeem, K. Mahmood and M. S. Saif, "Zn0.9Ce0.05M0.05O (M = Er, Y, V) nanocrystals: Structural and energy bandgap engineering of ZnO for enhancing photocatalytic and antibacterial activity," *Ceramics International*, vol. 46, pp. 4369-14383, 2020.

[266] H. Zhang, W. Li, G. Qin, H. Ruan, L. Ye and C. Kong, "Understanding the thermal evolution of defects in carbon-implanted ZnO," *Ceramics International*, vol. 46, pp. 672-677, 2020.

[267] P. Kumar, P. Kumar, A. Kumar, I. Sulania and F. Chand, "Structural, optical and magnetic properties of N ion implanted CeO2 thin films," *RSC Advances*, vol. 7, pp. 9160-1968, 2017.

[268] J.Betrain, C.Barrero and A.Punnoose, “Relationship between ferromagnetism and formation of complex carbon bonds in carbon doped ZnO powders,” *Physical Chemistry-Chemical Physics,* vol. 21, pp. 8808-8819, 2019.

[269] S.Ito, H.Kobayashi, K.Araki, K.Suzuki, N.Sawaki, K.Yamashita, Y.Honda and H.Amano, “Resonant Raman and FTIR spectra of carbon doped GaN,” *Journal of Crystal Growth,* vol. 414, pp. 56-61, 2015.

[270] Y. F. Wang, Y. C. Shao, S. H. Hsieh, Y. K. Chang, P. H. Yeh, H. C. Hsueh, J. W. Chiou, H. T. Wang, S. C. Ray, H. M. Tsai, C. W. Pao, C. H. Chen, H. J. Lin, J. F. Lee, C. T. Wu, J. J.Wu, Y. M.Chang, K. Asokan, K. H. Chae, T.Ohigashi, Y.Takagi, T. Yokoyama, N.Kosugi and W. F. Pong, “Origin of magnetic properties in carbon implanted ZnO nanowires,” *Scientific Reports*, vol. 8, pp. 1-13, 2018.

[271] H. Zhang, W. L. G. Q. H. Ruan, L.Ye and C. Kong, “Understanding the thermal evolution of defects in carbon-implanted ZnO single crystal,” *Ceramics International,* vol. 46, pp. 672-677, 2020.

[272] V. Sharma, M.Prasad, S.Jadkar and S.Pal, “Influence of carbon and phosphorus doping on electronic properties of ZnO,” *Journal of Materials Science: Materials in Electronics,* vol. 27, pp. 12318-12322, 2016.

[273] H. Liu, F. Zeng, Y. Lin, G. Wang and F. Pan, “Correlation of oxygen vacancy variations to band gap changes in epitaxial ZnO thin films.,” *Applied Physical Letters,* vol. 102, pp. 18-22, 2013.

[274] Y.Caglar, S. Ilican and M.Caglar, “Single-oscillator model and determination of optical constants of spray pyrolyzed amorphous SnO2 thin films,” *The European Physical Journal B,* vol. 58, pp. 251-256, 2007.

[275] D.Aryanto, E.Hastuti, M. Taspika, I. I. K. Anam, W. B. Widayatno, A. S. Wismogroho, P.Marwoto, B. W. Nuryadin, A. Noviyanto and S. Sugianto, “Characteristics and photocatalytic activity of highly c-axis-oriented ZnO thin films,” *Journal of Sol-Gel Science and Technology,* vol. 96, pp. 226-235, 2020.

[276] M. Arif, A.Sanger, P. Vilarinho and A.Singh, “Effect of annealing temperature on structural and optical properties of sol-gel-derived ZnO thin films,” *Journal of Electronic Materials,* vol. 47, pp. 3678-3684, 2018.

[277] K.S.Ranjith, L. R. Nivedita, K. Asokan, S. Krishnamurthy, R. Pandian, M. Kamruddin, D.K.Avasthi and R. Kumar, “Robust water repellent ZnO nanorod array by Swift Heavy Ion Irradiation: Effect of Electronic Excitation Induced Local Chemical State Modification,” *Scientific Reports* , vol. 7, p. 3251, 2017.

[278] A. Kozlovskiy, M. Zdorovets, I. Kenzhina, A. Berguzinov, D. TishKeVich, T. Zubar and A. Trukhanov, “The study of the applicability of ionizing radiation to increase the photocatalytic activity of TiO2,” *Journal of Nanostructure in Chemistry,* vol. 10, pp. 331-346, 2020.

[279] F.Hofman, E.Tarleton, R.J.Harder, N.Phillips, P.Ma, J. Clark, I.Robison, B.Abbey, W.Liu and C.Beck, “3D lattice distortions and defect structures in ion implanted nano-crystals,” *Scientific reports,* vol. 7, pp. 1-8, 2017.

[280] X.B.Wang, C.Song, W. Geng, F. Zeng and P. F, “Luminescence and Raman scattering properties of Ag-doped ZnO films,” *Journal of Physics D: Applied Physics,* vol. 39, pp. 4992-4996, 2006.

[281] W. Shen, J.Wang, Q. Y. Wang, Y. Duan and Y. P. Zeng, “Structural and optical properties of ZnO films on Si substrates using a γ-Al2O3 buffer layer,” *Journal of Physics D: Applied Physics,* vol. 39, pp. 269-274, 2006.

[282] G.G.Miranda, R. L. S. e. Silva, H. S. Pessoni and A.FrancoJr, “Raman spectroscopy study of Ga-doped ZnO ceramics: An estimative of the structural disorder degree,” *Physica B: Condensed Matter,* vol. 606, pp. 1-6, 2021.

[283] E.Muchuweni, T. S. Sathiaraj and C. Shonhiwa, “Raman spectroscopy and optical properties of GAZO thin films deposited at various substrate temperatures,” *The European Physical Journal Plus,* p. 133, 2018.

[284] K.Mosalagae, D.M.Murape and L.M.Lepodise, “Effects of growth conditions on properties of CBD synthesized ZnO nanorods grown on ultrasonic spray pyrolysis deposited ZnO seed layers,” *Heliyon,* vol. 6, pp. 1-10, 2020.

[285] S. B.Yahia, L.Znaidi, A.Kanaev and J.P.Petitet, “Raman study of oriented ZnO thin films deposited by sol–gel method,” *Spectrochimica Acta Part A: Molecular and Biomolecular Spectroscopy,* vol. 71, pp. 1234-1238, 2008.

[286] Y.Huang, M.Liu, Z.Li, Y.Zeng and S.Liu, “Raman spectroscopy study of ZnO-based ceramic films fabricated by novel sol–gel process,” *Materials Science and Engineering: B,* vol. 97, pp. 111-116, 2003.

[287] O.Marin, T.Soliz, J. A.Gutierrez, M.Tirado, C.Figueroa and D.Comedi, “Structural, optical and vibrational properties of ZnO:M (M=Al3+ and Sr2+) nano and micropowders grown by hydrothermal synthesis,” *Journal of Alloys and Compounds,* vol. 789, pp. 56-65, 2019.

[288] A.Mondal, S. Pal, A. Sarkar, T. Bhattacharya, A. Das, N. Gogurl, S. Ray, P. Kumar, D. Kanjilal, K. Devi, A. Singh, S. Chattopadhyay and D. Jana, “Raman spectroscopic analysis on Li, N and (Li,N) implanted ZnO,” *Materials Science in Semiconductor Processing,* vol. 80, pp. 111-117, 2018.

[289] Y.-P. Mia, F.Ma, Y.-H. Huang and K.-W. Xu, “Strain effects on electronic states and lattice vibration of monolayer MoS2,” *Physica E: Low-dimensional Systems and Nanostructures,* vol. 71, pp. 1-6, 2015.

[290] S.Y.Sawant, K.J.Yeol, H.Han and S.Ansari, “Electrochemically active biofilm-assisted biogenic synthesis of Ag-decorated ZnO@C-core shell ternary plasmonic photocatalyst with enhanced visible-photocatalytic efficiency,” *New journal of chemistry,* vol. 47, pp. 1995-2005, 2017.

[291] P. Li and W.Luo, “Properties of carbon impurities in ZnO: A hybrid functional study,” *Physics Review,* vol. 94, pp. 1-5, 2016.

[292] P.Nyamukamba, L.Tichagwa, S.Mamphhweli and L.Petrik, “Silver/carbon codoped titanium dioxide photocatalyst for improved dye degradation under visible light,” *International Journal of Photoenergy,* vol. 2017, pp. 1-9, 2017.

[293] R.Jaiswal and A.Miotello, “Copper and nitrogen co-doped TiO2 photocatalyst with enhanced absorption and catalytic activity,” *Applied Catalysis B: Environmental,* Vols. 168-169, pp. 333-341, 2015.

[294] M. Schumm, “ZnO-based semiconductors studied by Raman spectroscopy: Semimagnetic alloying, doping, and nanostructures- PhD thesis,” Julius–Maximilians university, 2008.

[295] N. Alian, A. T. Kaffi, S. Abdalskhi and S. Ahmed, “The Effect of Silver Doping on Optical Properties of TiO2,” *Journal of Applied Physics,* vol. 11, pp. 14-19, 2019.

APPENDIX A: SUPPLEMENTARY DATA

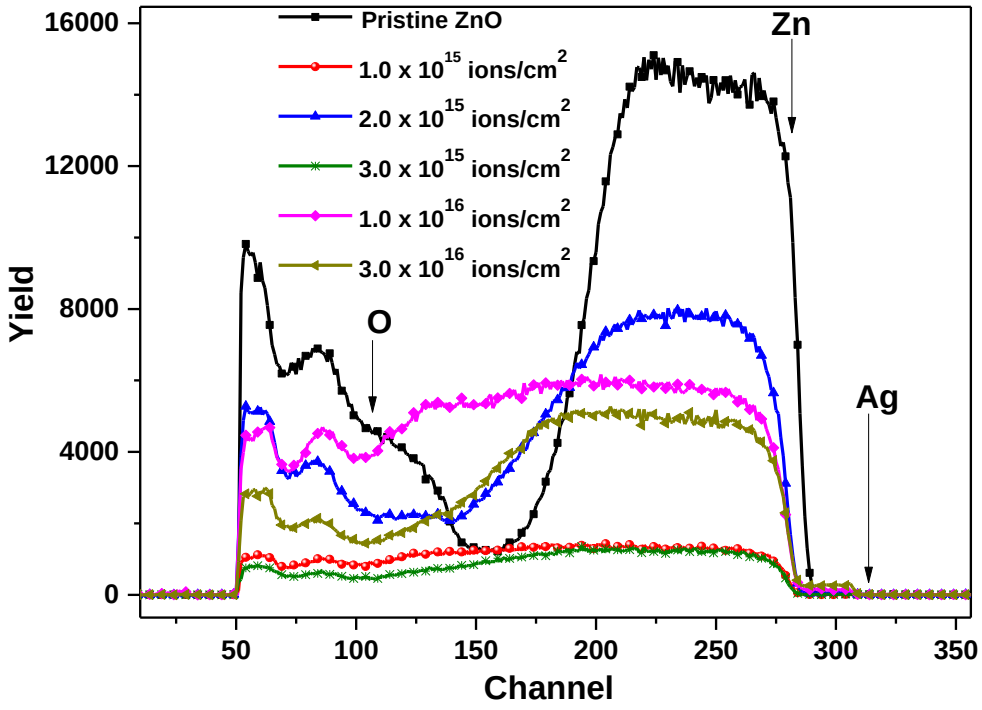


Figure A1: Rutherford backscattering spectra of pristine and Ag^+ ion implanted ZnO NRs.

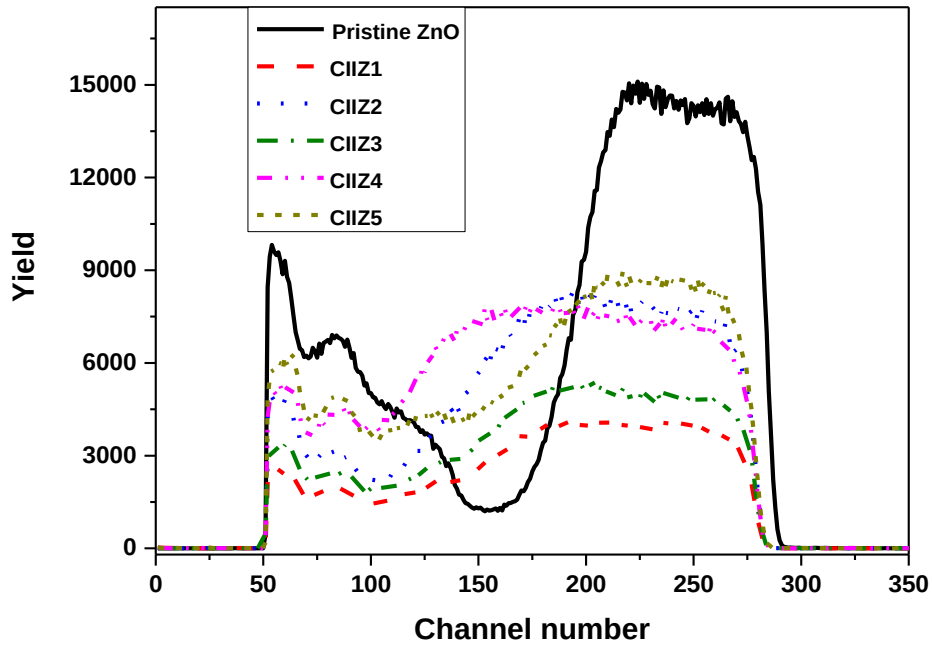


Figure A2: Rutherford backscattering spectra of pristine and C^+ ion implanted ZnO NRs.

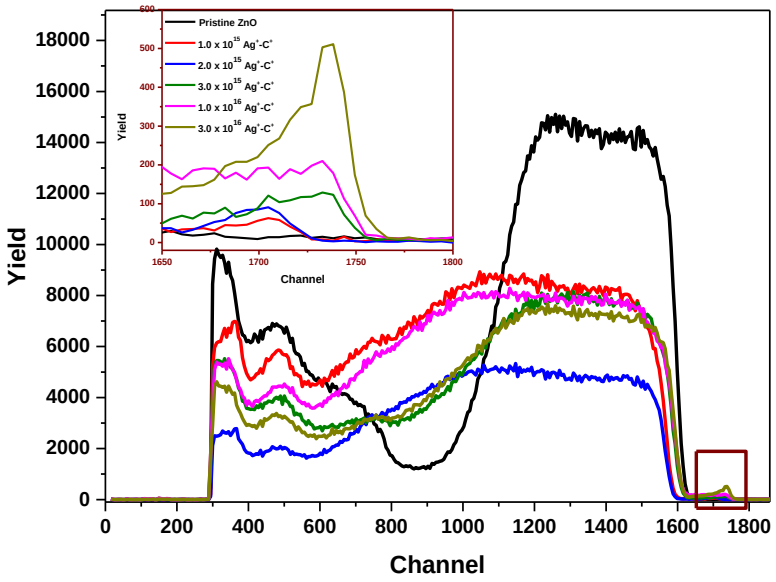


Figure A3: Rutherford backscattering spectra of pristine and Ag^{+}- C^{+} co-implanted ZnO NRs.

APPENDIX B: PHOTOGRAPHS OF SOME OF THE USED EQUIPMENT



Figure B.1: The Varian-Extrion 200-20A2F Ion implanter.



Figure B.2: The Bruker dimension edge scan analyst for atomic force measurements.



Figure B.3: A picture of the Bruker D8 Advance XRD equipment used.



Figure B.4: A Zeiss MERLIN FESEM used for the examination of the surface morphology and elemental composition analysis.

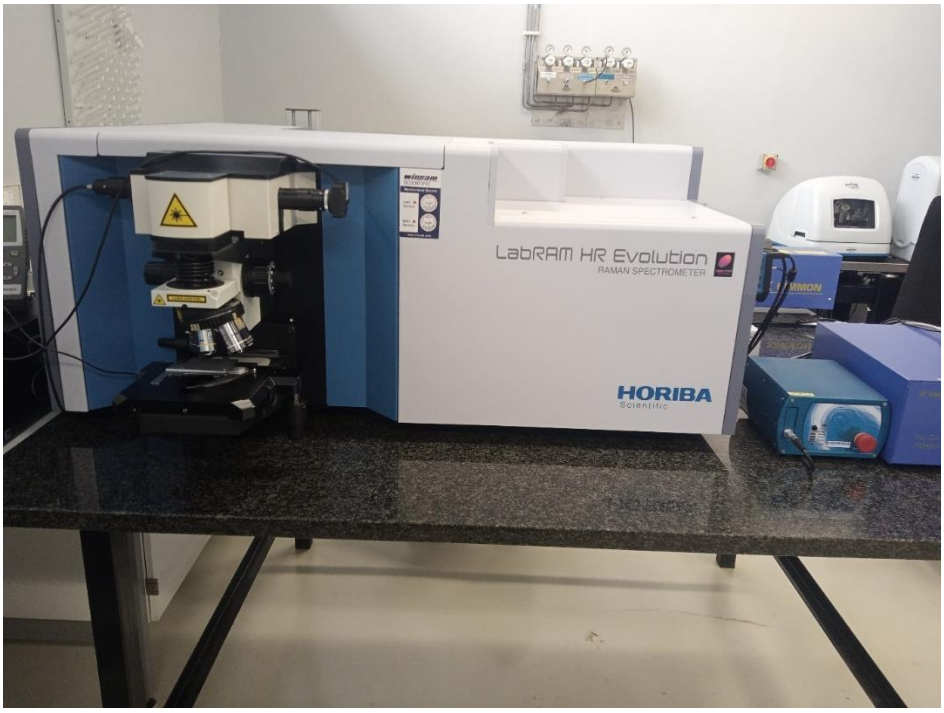


Figure B.5: The Horiba Labram HR evolution Raman spectrometer.



Figure B.6: The Bruker Vertex 70v FTIR spectrophotometer.

APPENDIX C: PUBLICATIONS

Optical Materials 122 (2021) 111757

Contents lists available at ScienceDirect

Optical Materials

journal homepage: www.elsevier.com/locate/optmat



Effect of low energy Ag^{+} ION implantation ON ZnO nanorods for enhanced visible light absorption- structural and optical analysis

Kebadiretse Lefatshe [a,*], Cosmas Muiva [a], Morgan Madhuku [b]

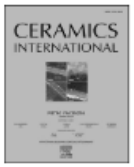
[a] Botswana International University of Science and Technology, P. Bag 16, Palapye, Botswana
[b] iThemba LABS, Tandem and Accelerator Mass Spectrometry Department, P. Bag 11, Wits, 2050, South Africa

Ceramics International 47 (2021) 7407–7415

Contents lists available at ScienceDirect

Ceramics International

journal homepage: www.elsevier.com/locate/ceramint



Optical dispersion analysis of template assisted 1D-ZnO nanorods for optoelectronic applications

Kebadiretse Lefatshe [a,*], Phindani Dube [a], Dineo Sebuso [a], Morgan Madhuku [b], Cosmas Muiva [a]

[a] Botswana International University of Science and Technology, P. Bag 16, Palapye, Botswana
[b] i Themba LABS, P. Bag 11, WITS 2050, South Africa

Heliyon 6 (2020) e04186

Contents lists available at ScienceDirect

Heliyon

journal homepage: www.cell.com/heliyon

Research article

Reduction of hazardous reactive oxygen species (ROS) production of ZnO through Mn inclusion for possible UV-radiation shielding application

Kebadiretse Lefatshe [a,*], Genene T. Mola [b], Cosmas M. Muiva [a]

[a] Department of Physics and Astronomy, Botswana International University of Science and Technology, Private Bag 16, Palapye, Botswana
[b] School of Chemistry & Physics, University of KwaZulu Natal, Pietermaritzburg Campus, Private Bag X01, Scottsville 3209, South Africa